

Analysis of plane problems with defects of different geometric shapes

Student: Yifeng Chen (Somerville College)

Supervisor: Prof. John Huber (Oriel College)

Prof. David Anthony Hills (Lincoln College)

Prof. Lifeng Ma (University of Nottingham)

Solid Mechanics and Materials Engineering Group

Department of Engineering Science

University of Oxford

A thesis submitted for the degree of Doctor of Philosophy

Hilary Term 2024

“我走到湖边，天上飘着雪，上下苍茫，我立在堤岸上，心里突然起了一阵奇异的感动，那种感觉，似喜似悲，是一种天地悠悠之念，二十五岁的那个自己，变成一团模糊，逐渐消隐，我感到脱胎换骨，骤然间，心里增添了许多岁月。“

————《蓦然回首》白先勇

"I walked to the lakeside, where snow drifted in the sky. The vast expanse stretched above and below, and as I stood on the embankment, a strange emotion suddenly stirred within me. It was a feeling both joyous and sad, a sense of the enduring passage of time. The twenty-five-year-old me turned into a blur, gradually fading away. I felt as though I had undergone a profound transformation; suddenly, my heart seemed to have gained many years."

——*《Suddenly Looking Back》Bai Xianyong*

Abstract

This thesis presents research on a plate with defects of various geometric shapes, including a circular hole, a 'finite-height crack,' a notch, and a parabolic notch. The primary focus of the entire work is to produce analytical solutions for the stress state of a plate containing one of these defects, subjected to different loading modes. Additionally, the thesis explores the unique situation where the plane problem extends into the third dimension, forming a 3D body, and examines the end effects.

While the stress state within a plate with a circular hole is a classical problem with a fully solved solution, this thesis delves into the shakedown phenomenon under cyclic loading, offering insights of practical importance.

Defects containing one or more singular features are also worth investigating. Singular features are defined as areas where stress is concentrated and tends to infinity in elastic analysis, such as cracks or sharp notches. The general approach to these problems typically involves using asymptotic or approximate solutions, like Williams' solution. However, this thesis aims to produce a non-approximated, closed-form solution for the stress field of a wedge (with angles ranging from zero to 2π) interacting with a singularity (singular force or dislocation) under the anti-plane loading. This methodology can be extended to a parabolic notch, which is also discussed.

The 'finite-height crack' is another example involving singular features, but it has two singularities at a 'short' distance apart. Therefore, the thesis discusses the interaction of the stress state around the two singularities and predicts the location of fracture initiation in a 'finite-height' crack case.

Finally, the thesis explores a scenario where a plane problem extends into the third dimension, becoming a 3D problem. An example is presented using plane contact as a reference, employing numerical methods to analyse the 3D end effect. This work provides a clear

explanation of how the end effect generalizes at the free end and the distance it propagates in terms of the geometric feature length.

Acknowledgement

I would like to express my gratitude to my supervisor, Professor David Anthony Hills, for providing me with the opportunity to be part of his theoretical solid mechanics group. He is the most intelligent person I have ever met. When I encountered challenges, his insights always guided me through the intricacies of the true physics world. Special thanks are also due to my second supervisor, Professor Lifeng Ma, for his assistance with my work. In my opinion, his mathematical prowess surpasses that of any engineer I have known; I would readily refer to him as a mathematician rather than an engineer.

I extend my appreciation to Professor George Adams from North-Eastern University, USA, for his invaluable assistance with my 'Finite-height-crack' paper. This paper could never have been completed without his support.

I would also like to express my gratitude to Professor John Huber, who generously took me on as his student after Professor Hills' retirement. He provided constructive advice on my academic work and thesis.

A special mention goes to my colleague and friend, Dr. Hendrik Andresson, for his academic and technical support in my research. Thanks also to Dr. Nills Ciewakala, Dr. Daniel Riddoch, and Mr. James Truelove for their kind assistance and constant support.

I wouldn't be in this position without the love and support of my friends in Oxford. Special thanks to Mr. Peihao Song and Dr. Huanming Chen, who not only treated me as a family member but also provided valuable academic suggestions. We have shared many moments of camaraderie over beers. Special thanks also go to Dr Fay Pu, who has been there for me in the very last step of my DPhil journey.

Finally, and most importantly, I want to express my deepest gratitude to my parents, Yu Yi and Shibao Chen. They have been with me every step of the way – bearing, raising, teaching, encouraging, and loving me.

Table of Contents

Abstract I

Acknowledgement III

Table of Contents IV

1. Introduction 1

1.1. Motivation 1

1.2. Objectives 2

1.3. Thesis scope 3

1.4. Publications 5

Bibliography 6

2. Background and Literature review 7

2.1. Modes of loading 7

2.2. Plane elasticity 7

2.3. General law for elasticity 8

2.4. Wedge problem 11

2.4.1. Asymptotic solution 11

2.3. Complex variable potential for elastic problem 18

2.3.1. Plane complex potential 19

2.4.2. Anti-plane complex potential 19

2.3.3. Complex potential for singularities 20

2.5. Parabolic notch problem 21

2.6. Plane contact problem 24

2.7.1. Contact classification 26

2.7.1. Airy stress function and analytical plane contact solution. 28

2.7.3. Subsurface contact stress 31

2.8. Circular hole problem 32

2.8.1. Plane solution 32

2.8.2. Anti-plane solution 33

2.9. Shakedown 34

2.10. Mathematical essentials for a general complex variable method 36

2.10.1. Analytical function and entire function 36

2.10.2. Liouville's theorem 36

2.10.3. A generalized complex variable problem 36

2.12. Effective Convergence Checks 39

Bibliography 42

3. Shakedown of a plate with a circular hole 47

3.1 Introduction 47

3.2 Paper: Shakedown of a plate with a circular hole 49

Abstract 49

1. Introduction 49

2. Formulation 51

3. Residual Stress Field 55

4. Load-unload Case Analysis....58

5. Marching in Time Solution....67

6. Varying Degrees of Load Reversal....70

7. Conclusion....79

3.3 Limitations of the paper....80

4. Finite height-crack problem....83

4.1 Introduction....83

4.2 Paper: Investigation of stress state around a finite-height crack....85

Abstract....85

1. Introduction....86

2. Heavy load case: sharp crack problem approximation....92

3. Light Load case: Notch problem approximation....99

4. Non small scale yielding: intermediate state analysis....106

5. Application to an example problem: an infinite plate with a rectangular shaped crack....108

6. Critical stress intensity factor of the notch mode 1 loading approximation....111

7. Conclusion....113

4.3 Clarification....114

5. Anti-plane wedge interacting with a singularity....119

5.1. Introduction....119

5.2. Paper: A generalized anti-plane singularity within a semi-infinite wedge of arbitrary angle....121

Abstract 121

1. Introduction 121

2. The complex framework and its form for a generalized anti-plane singularity 124

3. Formulation 126

4. Solution 129

5. Solutions for typical cases 130

6. The image force on a screw dislocation due to the configuration of the wedge 133

7. Application: formulation for a slip band under anti-plane loading 135

8. Concluding remarks 139

6. Parabolic Notch interacting with anti-plane singularity 144

6.1. Introduction 144

6.2. Paper：A Parabolic Notch Interacting with a Generalized Anti-plane Singularity 145

Abstract 145

1. Introduction 145

2. The complex framework and its form for a generalized anti-plane singularity 149

3. Formulation 153

4. Solution 155

5. Examples: Analytical solution for the parabolic notch interacting with singularities 157

6. Concluding remarks 162

6.3. Validation of the results 168

7. Analysis of elastic prismatic contact of finite length 171

7.1. Introduction 171

7.2. Paper: Analysis of a Prismatic Elastic Contact of Finite Length 173

Abstract 173

1. Introduction 174

2. Theoretical background 176

3. Finite length, common-edge contact 182

4. Finite length, Hertzian contact 190

6. Conclusion 199

Acknowledgement 200

Appendix: Nonlinear fitting algorithm 200

8. Conclusion and Future Work 205

Declaration of Competing interesting 210

1. Introduction

1.1. Motivation

The term 'plane problem' refers to a simplified scenario where the deformation of a solid primarily occurs within a single plane. The analysis for it is often two-dimensional, with the effect in the third dimension considered negligible. Analysing the plane problem has the advantage of simplifying three-dimensional complexity, making it easier to solve using mathematical models. These advantages enable more tractable solutions and a better understanding of fundamental principles. Although structures and mechanical bodies are now widely analysed using numerical methods such as finite element analysis, the plane problem remains a benchmark for validation, allowing researchers to compare results.

The study of the plane problem is integral to the development of elasticity theory, forming the basis for understanding the mechanical behaviour of materials and solving practical engineering problems. However, the difficulty of the plane problem often arises with the introduction of defects. These defects can be characterized as singular or non-singular features. Singular features include cracks and sharp notches, where the stress is infinitely large at the singularity in pure elastic analysis. A significant amount of work is dedicated to analysing singular features, with the classic and general approach using asymptotic methods to provide an approximated solution, although the closed-form solution remains unknown. Non-singular features include non-sharp holes and parabolic notches. Even though the stress remains finite in the analysis, these features still perturb the stress field distribution and are thus valuable to study.

Research on the plane problem has constantly improved and evolved over the past decades, especially with the development of finite element solutions. Analytical solutions for such problems remain fundamental for understanding the real mechanism. As a result, this

thesis aims to contribute to the analytical results for a specific type of problem: a plane containing defects, providing either new or improved methods to study such problems.

The analytical methods, together with Finite Element Analysis (FEA), allow for flexible application to both simple and complex geometries. The analytical methods developed in this thesis provide quick insights and solutions for simple problems. For complex geometries that contain simple geometrical defects, these defects can be treated as isolated features and studied locally. This approach enables scientists and engineers to quickly gain knowledge of stress distribution and ensure the safety and reliability of the mechanical part.

The theoretical methods for plane elastic problems with defects are also highly relevant to industrial applications. Defects are an important factor in the prediction of the life expectancy of mechanical parts. These theoretical methods support predictive maintenance strategies by identifying critical stress regions and potential failure points. This enables industries to implement timely maintenance and reduce maintenance costs. Additionally, industries are continually developing new materials with tailored properties. The ability to predict and manage defects in these materials accelerates their adoption and integration into commercial products.

1.2. Objectives

This thesis aims to investigate the mechanical behaviour of a plate with defects and provide general analytical results. The defects under consideration are characterized by one of four geometric shapes: a circular hole, a 'finite-height' crack, a sharp notch, or a parabolic notch. While Kirsch's solution (Kirsch, 1898) has already yielded analytical results for both Mode 1 and Mode 2 loading in the context of a circular hole, this thesis will primarily focus on the shakedown phenomenon under cyclic loads, a topic of both educational and practical

engineering significance. For sharp and parabolic notches, a novel method using a complex variable tool has been developed to derive a closed-form solution.

Additionally, this thesis presents a specific analysis of a finite-height crack, which is a crack that has an opening height at its tip, forming a ‘letterbox’ shape. The method of analysis is applicable to the interaction between notches and solid inclusions. Furthermore, instead of using asymptotic methods, this thesis will also discuss the closed form solution of a sharp and parabolic notch under anti-plane loading, inspired by the complex variable method developed by Hills and Ma (2022 & 2023) for the cases of plane loading. This thesis also aims to extend the plane problem to a more practical situation: a plane that has the extension in the third dimension to form a three dimensional body. In this 3D case, the thesis will discuss the end-effect using contact problem examples.

1.3. Thesis scope

A summary of the contents of this thesis is as follows:

Chapter 1 gives the motivation, objectives, scope, and work outline of this thesis.

Chapter 2 provides a background for this thesis, covering classic methods and math tools applied to the plane problem.

Chapter 3 discusses the shakedown problem for a plane containing a circular hole. The shakedown limit is calculated by both analytical and numerical methods via a finite element model; the results of both methods are compared to demonstrate the use of Melan’s lower bound theory in engineering. This chapter has been published as a journal paper: https://doi.org/10.1177/03093247231163205

Chapter 4 provides a specific analysis of a 'finite-height' crack loaded mode 1 and mode 2 loading. The analysis again combines the numerical and analytical approaches, aiming to

determine the specific places for crack initiation around crack height. The results were further applied to a rectangular-shaped imbedded crack to demonstrate the practical use. This chapter has also been published as the following journal paper:

https://doi.org/10.1016/j.ijsolstr.2023.112499

Chapter 5 & Chapter 6 discuss a complex variable method used for analyzing a featured plane, wedge, or parabolic notch containing singularities (either a dislocation or a singular force), under anti-plane loading. The advantage of this complex variable method is that it can obtain closed-form solutions. We also validate the developed method by comparing with classic results, and practical applications of the results obtained by this method are also discussed. In these two chapters, Chapter 5 illustrates the method used in wedge cases, and Chapter 6 extends the methodology and applies it to the parabolic notch case. These chapters have been published as the following journal papers:

Chapter 5: https://doi.org/10.1177/03093247231190684;

Chapter 6: https://doi.org/10.1115/1.4054865.

Chapter 7 discusses the case when the plane problem is extended in the third dimension to form a 3D prismatic body, and uses two types of plane contact problem, Hertzian contact and plane common edge contact, to demonstrate the difference with plane analytical results. The analysis is done through finite element modelling, and the stress state of each plane is extracted along the length in the prismatic case to observe the difference. The analytical explanations are also provided for how the difference is created and the free end effect propagation is investigated in the prismatic body. This chapter is prepared for publication as an academic journal paper.

Chapter 8 concludes the achievements of this work and some recommendations for further investigation are given.

1.4. Publications

First Author publications.

1. Chen, Y., Adams, G. G., & Hills, D. A. (2023). Investigation of stress states around a finite-height crack. International Journal of Solids and Structures, 284, 112499. **This paper forms chapter 4**
2. Chen, Y., & Hills, D. A. (2023). Shakedown of a plate with a circular hole: An educational problem. The Journal of Strain Analysis for Engineering Design, 03093247231163205. **This paper forms chapter 3**
3. Chen, Y., Hills, D. A., Huber, J.E., Ma, L. (2023). Analysis of elastic prismatic contact of finite length. Paper submitted to European Journal of Mechanics A/Solids. **This paper forms chapter 7**

Publications led by collaborators.

4. Ma, L., Chen, Y., & Hills, D. A. (2023). A generalized anti-plane singularity within a semi-infinite wedge of arbitrary angle. The Journal of Strain Analysis for Engineering Design, 03093247231190684. **This paper forms chapter 5**
5. Ma, L., Chen, Y., & Hills, D. A. (2022). A Parabolic Notch Interacting With a Generalized Anti-plane Singularity. Journal of Applied Mechanics, 89(9), 091001. **This paper forms chapter 6**

Bibliography

1. Kirsch. E. G. (1898). Die Theorie der Elastizität und die Bedürfnisse der Festigkeitslehre. Zeitschrift des Vereines deutscher Ingenieure, 42, 797–807.
2. Ma, L., Hills, D. A. (2022). Interaction of a parabolic notch with a generalized singularity. International Journal of Engineering Science, 176, 103685.
3. Ma, L., Hills, D. A. (2023). A wedge of arbitrary angle interacting with a generalized singularity. International Journal of Solids and Structures, 262, 112062.

2. Background and Literature review

2.1. Modes of loading

All stress systems in the vicinity of opening defects (such as notches, cracks, etc.) can be derived from three modes of loading (see Ewalds and Wanhill, 1984; Hills et al., 2013), as shown in Figure 2-1. The predominant stress situation in most cases is the mode 1 opening load, followed by the mode 2 sliding load and the mode 3 tearing load. In plane theory, mathematical models are usually confined to either in-plane (modes 1 and 2) or anti-plane (mode 3) situation. Therefore, it is necessary to distinguish these modes of loading first.

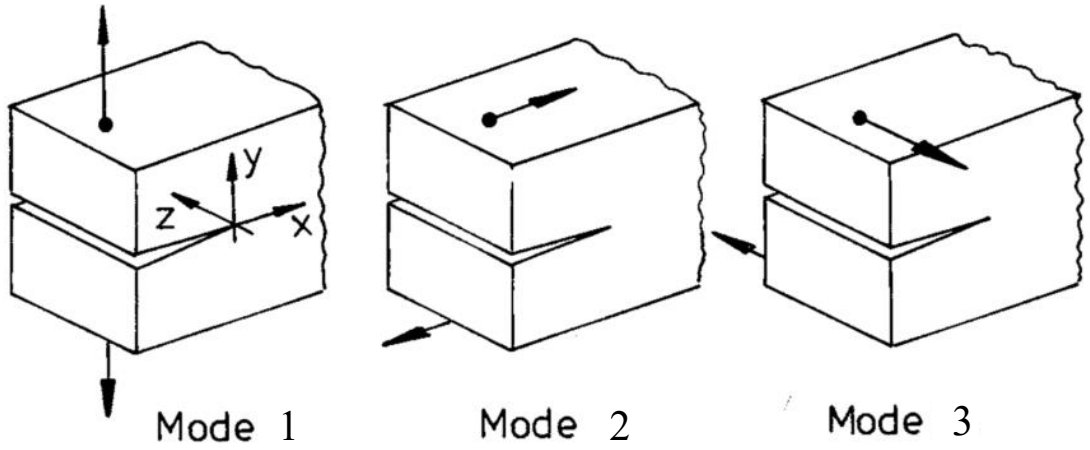


Figure 2-1. Modes of loading: Mode 1 opening, Mode 2 shearing and Mode 3 Tearing. (Hills *et al*., 2013)

2.2. Plane elasticity

It is natural for engineers and researchers today to rely on numerical tools for solving the traction and stress of mechanical bodies due to their convenience. However, caution must be exercised when dealing with defects, especially singular defectes, and analytical solutions are still essential for understanding the underlying physics of a mechanical body under various loading circumstances.

Plane elastic theory is foundational in the development of numerical methods. The idealization in plane elastic theory is to treat the problem as a 'plane,' which means no gradient of any stress or strain component in the through thickness direction. We start by distinguishing between the plane stress and the plane strain cases. We denote the in-plane dimensions as x and y, and the out-of-plane dimension as z. Plane stress implies that all the through thickness stresses are assumed to vanish, i.e., $\sigma_{zx} = \sigma_{zy} = \sigma_{zz} = 0$, this often applies when the third dimension dimension is negligible compared to the plane dimensions. Another assumption, considered more useful, is the plane strain case, where the out-of-plane strain is zero, i.e., $\epsilon_{zx} = \epsilon_{zy} = \epsilon_{zz} = 0$. Unlike the plane stress case, plane strain is often applied to thick bodies where the out-of-plane dimension is significant enough to support moments of the x and y dimensions. The following sections will review the classic plane problems that has been investigated in previous literature.

2.3. General law for elasticity

The concepts of equilibrium, compatibility, and Hooke's law form the foundational principles for elastic analysis of material behaviours. The combination of these three leads to the powerful airy stress function. In this section we will briefly introduce the above:

Equilibrium

The principle of equilibrium is fundamental in mechanics. It states that a body is in equilibrium if the sum of forces and the sum of moments acting on it are zero. Mathematically, this can be expressed as:

$$\sum F = 0$$

$$\sum M = 0$$

Where F and M represent force and moment respectively.

In a two-dimensional plane problem, these conditions can be rewritten as:

$$\frac{\partial \sigma_{xx}}{\partial x} + \frac{\partial \tau_{xy}}{\partial y} + fx = 0$$

$$\frac{\partial \sigma_{yy}}{\partial y} + \frac{\partial \tau_{xy}}{\partial x} + fy = 0$$

where σ_{xx} and σ_{yy} are normal stresses, τ_{xy} is the shear stress, and f_x and f_y are body forces per unit volume in the x and y directions, respectively.

Compatibility

While equilibrium ensures that the forces are balanced, compatibility ensures that the material deforms in a continuous manner without any gaps or overlaps. Compatibility conditions are geometric constraints, it must be satisfied for a deformation to be physically possible. For a two-dimensional plane, the compatibility equation is given by:

$$\frac{\partial^2 \varepsilon_{xx}}{\partial y^2} + \frac{\partial^2 \varepsilon_{yy}}{\partial x^2} = 2\frac{\partial^2 \varepsilon_{xy}}{\partial x \partial y}$$

where $\varepsilon_{xx}, \varepsilon_{yy}$, and ε_{xy} are the normal and shear strains, respectively.

Hooke's Law

Hooke's law relates the stresses and strains in a linear elastic material. It states that the strain in a material is directly proportional to the applied stress, given that the stress is within the elastic limit. For a two-dimensional plane strain problem, Hooke's law can be written as:

$$\varepsilon_{xx} = \frac{1-\nu^2}{E}\left(\sigma_{xx} - \frac{\nu}{1-\nu}\sigma_{yy}\right)$$

$$\varepsilon_{yy} = \frac{1-\nu^2}{E}\left(\sigma_{yy} - \frac{\nu}{1-\nu}\sigma_{xx}\right)$$

$$\varepsilon_{xy} = \tau_{xy}/\, G$$

where E is Young's modulus, ν is Poisson's ratio, and $G = \frac{2(1+\nu)}{E}$ is the shear modulus.

Airy stress function

The equilibrium and compatibility equations, along with Hooke's law, provide a complete

description of the stress and strain states in an elastic body. However, solving these equations simultaneously can be complex. The Airy stress function, φ, is introduced to simplify this process. By substituting Hooke's law into the compatibility equation and incorporating the equilibrium conditions, one arrives at a single biharmonic equation in terms of φ:

$$\nabla^4 \varphi = 0$$

In terms of the Airy stress function, the stress components in a two-dimensional state can be expressed as:

$$\sigma_{xx} = \frac{\partial^2 \varphi}{\partial y^2}$$

$$\sigma_{yy} = \frac{\partial^2 \varphi}{\partial x^2}$$

$$\tau_{xy} = -\frac{\partial^2 \varphi}{\partial x \partial y}$$

By using the Airy stress function, the problem of finding the stress distribution in a body reduces to solving a single partial differential equation.

Although the Airy stress function helps simplify the equations of equilibrium by reducing the number of variables involved, it can only be applied with certain restrictions. Firstly, the Airy stress function is primarily used in two-dimensional elastic problems, where the material is assumed to be continuous, isotropic, and homogeneous. Therefore, it does not apply to nonlinear materials. Secondly, the biharmonic equation is solved by applying suitable boundary conditions. For complex boundary conditions or geometries, it is challenging to propose a suitable Airy stress function.

2.4. Wedge problem

2.4.1. Asymptotic solution

The classic method to solve the plane wedge problem is by using Williams' solution. The wedge is defined generally, with its internal angle, 2α, ranging from zero up to 2π, as shown in Figure 2-2. The position of any point on the wedge is defined in polar coordinates (r, θ). The starting point of this solution is to utilize the concept of the scalar stress function. Assuming there is no body force and the stress component is independent of the z dimension, we know that the traction on the boundary varies in a power sense, $r^{\lambda-1}$, where λ is the eigenvalue. The stress potential will have the form $\Phi = r^{(\lambda+1)} f(\theta)$, and the biharmonic equation can be further simplified to the following expression (Barber, 2002):

$$\Phi = r^{\lambda+1}[A_1 \cos(\lambda+1)\theta + A_2 \cos(\lambda-1)\theta + A_3 \sin(\lambda+1)\theta + A_4 \cos(\lambda-1)\theta] \quad (2.1)$$

where A_1, A_2, A_3, A_4 are arbitrary constants. From the traction free condition on the flanks of the wedge:

$$\sigma_{r\theta} = \sigma_{\theta\theta} = 0 \qquad \text{when } \theta = \alpha \quad (2.2)$$

The stress $\sigma_{r\theta}$ and $\sigma_{\theta\theta}$ are found from the differentiation of the stress function and substituted back to equation (2.2) to solve the arbitrary constants:

$$\begin{bmatrix} (\lambda_1+1)\sin(\lambda_1+1)\alpha & (\lambda_1-1)\sin(\lambda_1-1)\alpha \\ (\lambda_1+1)\cos(\lambda_1+1)\alpha & (\lambda_1+1)\cos(\lambda_1-1)\alpha \end{bmatrix} \begin{bmatrix} A_1 \\ A_2 \end{bmatrix} = 0 \quad (2.3)$$

and

$$\begin{bmatrix} (\lambda_2+1)\cos(\lambda_2+1)\alpha & (\lambda_2-1)\cos(\lambda_2-1)\alpha \\ (\lambda_2+1)\sin(\lambda_2+1)\alpha & (\lambda_2+1)\sin(\lambda_2-1)\alpha \end{bmatrix} \begin{bmatrix} A_3 \\ A_4 \end{bmatrix} = 0 \quad (2.4)$$

Where λ_i is the eigenvalue and the subscript i represent its in Mode i loading case. This equation has solution only if the determinant of matrix is zero, hence we require:

$$\lambda_1 \sin(2\alpha) + \sin(2\lambda_1\alpha) = 0 \quad (2.5)$$

$$\lambda_2 \sin(2\alpha) - \sin(2\lambda_2\alpha) = 0 \quad (2.6)$$

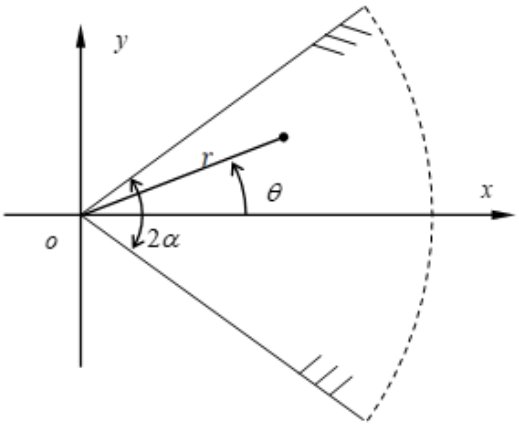


Figure 2-2: The configuration of a wedge with internal angle 2α.

Note that the stress and strain vary with r^{λ_i-1}, as we approach to the wedge tip the strain energy will be in the form of

$$U = \frac{1}{2}\int_0^{2\pi} \sigma_{ij}\epsilon_{ij} r dr d\theta = C\int_0^r r^{2\lambda-1} dr \tag{2.7}$$

and this integral is bounded if $\lambda > 0$. These eigenvalues are plotted with the variation of α in Figure 2-3. Notice that the mode 2 eigenvalue is only sufficient to cause a singularity for $2\alpha > 257.4°$. The eigenvalues can substitute back to equation (2.3) and (2.4) to solve A_1, A_2, A_3 and A_4. Stress components can be expressed in the form of asymptotic solution:

$$\sigma_{ij}(r,\theta) = K_1 r^{\lambda_1-1} f_{ij}^1(\theta) + K_2 r^{\lambda_2-1} f_{ij}^2(\theta) \tag{2.8}$$

Where K_i are the stress intensity factors for a notch in mode i loading and can be found from:

$$K_1 = \lim_{r\to 0} \sqrt{2\pi}\, r^{1-\lambda_1} \sigma_{\theta\theta} \text{on} \theta = 0 \tag{2.9}$$

$$K_2 = \lim_{r\to 0} \sqrt{2\pi}\, r^{1-\lambda_2} \sigma_{r\theta} \text{on} \theta = 0 \tag{2.10}$$

$\theta = 0$ indicates the bisector of the wedge and $f_{ij}^n(\theta)$ are the related eigenfunctions in mode n loading. The expressions for these eigenfunctions can be found in the literature, such as Hills and Dini (2011). It is important to note that Williams' solution is deduced through pure elastic analysis, but the singular stress state at the root of the notch will always induce plastic deformation due to the finite yield stress of the material. One way of approximating the plastic

front radius is by calculating the distance from the notch tip that the Von Mises stress exceeds its yielding stress in elastic analysis, and Von Mises stress σ_v is defined as:

$$\sigma_v^2 = \frac{1}{2}[(\sigma_{11} - \sigma_{22})^2 + (\sigma_{22} - \sigma_{33})^2 + (\sigma_{11} - \sigma_{33})^2 + 6(\sigma_{23}^2 + \sigma_{13}^2 + \sigma_{12}^2)].$$

For a sharp notch loaded under both mode 1 and mode 2 loading, the characteristics of the approximated plastic front are discussed in Hills and Dini (2011), in which it plots the contour of non-dimensional plastic radius r_p/d_0 shown in Figure 2-4, where r_p is the approximated plastic front, and d_0 is the mode mixity that has length dimension, defined as $d_0 = \left|\frac{K_2}{K_1}\right|^{\frac{1}{\lambda_1-\lambda_2}}$ with a non-dimensional loading parameter $\frac{G_0}{k}$, where $G_0 = K_1^{\frac{\lambda_2-1}{\lambda_2-\lambda_1}} K_2^{\frac{\lambda_1-1}{\lambda_1-\lambda_2}}$ and k is the yield stress. The contour shows that when the value of $\frac{G_0}{k}$ is smaller than a certain value, the plastic radius contour shape will be the same as that in the mode 1 loading, hence we assume the notch is in mode 1. As $\frac{G_0}{k}$ gradually increase, the contour will gradually change to the mode 2 loading contour shape and we can assume that the crack is loaded under mode 2.

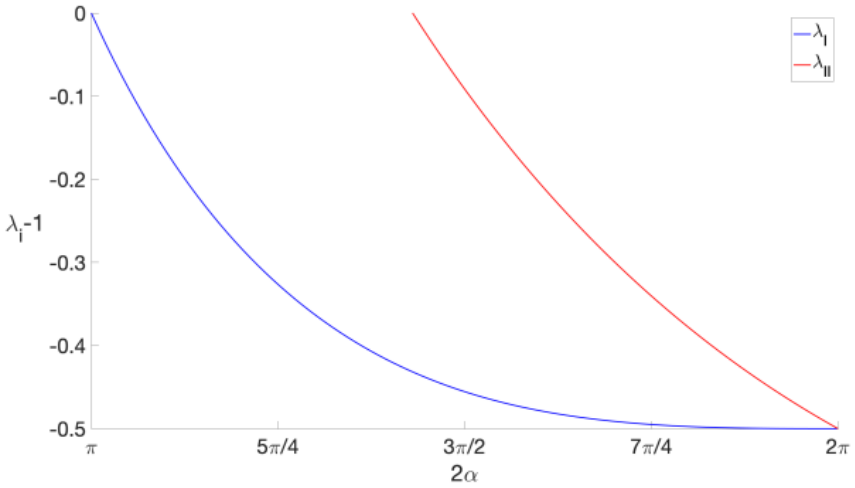


Figure 2-3: Variation of the eigenvalues of the Williams solution with wedge opening angle.

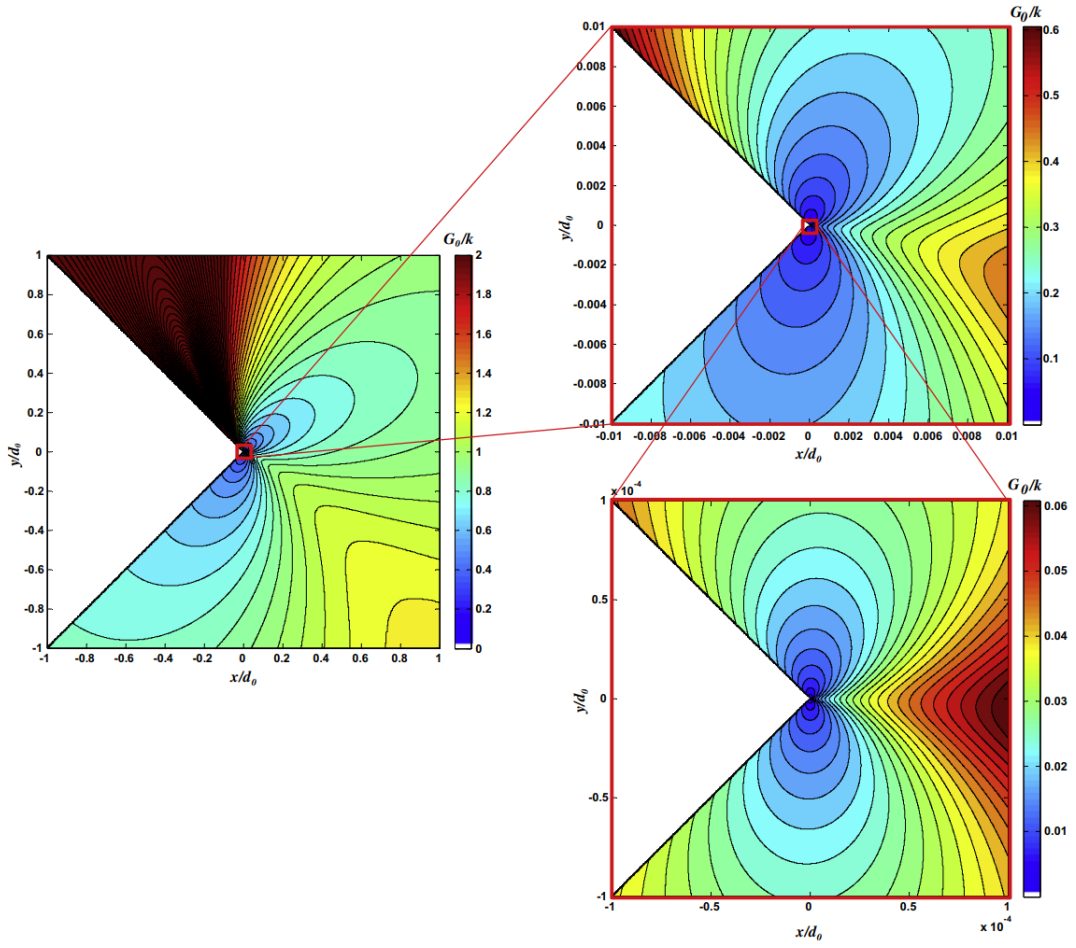


Figure 2-4: Contours of the estimated size of the plastic fronts r_p/d_0, as a function of the dimensionless load G_0/k, at three different levels of magnification for a $2\alpha = 3\pi/2$ wedge. (Hills and Dini, 2011)

Numerous textbooks on basic fracture mechanics discuss the relationship between the energy release rate and the stress intensity factors (Broek, 2012; Anderson, 2017, etc.). If the plastic behavior of the material is not available, to evaluate the energy release rate and hence the stress intensity factors, contour integral methods are often used. Examples include Sanders' integral (Sanders, 1960) and the J-integral (Rice et al., 1973). To accomplish this, the local stress field near the crack needs to be evaluated, and finite element analysis of the geometry is commonly performed to determine a calibration matrix between the external loads and the stress intensity factors.

$$\begin{bmatrix} K_1 l^{\lambda_1 - 1} \\ K_2 l^{\lambda_2 - 1} \end{bmatrix} = \begin{bmatrix} a & b & c & d \\ e & f & g & h \end{bmatrix} \begin{bmatrix} \frac{P}{2l} \\ \frac{Q}{2l} \\ \frac{M}{2l^2} \\ \frac{\Delta\sigma}{2} \end{bmatrix} \tag{2.11}$$

Where the external loads are a normal force P, a shear force Q, a moment M, and a differential bulk tension $\Delta\sigma$; l is a characteristic length to adjust the dimension of the equation.

It's important to note that such path-independent integral methods for singularities owe their origin to Eshelby's work (Eshelby, 1951), which defines several contour integrals that are path-independent by virtue of the energy conservation theorem, as evaluated by Knowles and Sternberg (1972). The following review focuses on a specific path-independent integral that is easily adopted for numerical methods, namely, the H-integral.

H-integral

The advantage of using a path-independent integral for analysing singular elasticity problems lies in its precision: the only errors incurred are those associated with numerical calculations during the application of the chosen algorithm for numerical approximation. This approach eliminates additional sources of error, such as those arising from the expansion of eigenfunctions around singularities. Furthermore, this section will briefly introduce an easily adoptable procedure applied within the Finite Element Method, known as the 'H-integral' (Sinclair, G.B. *et al*., 1984). It proposes a practical computational method to estimate stress intensity factors accurately with minimal computational effort. For a contour chosen around a sharp re-entrant corner or notch shown such as the one shown in Figure 2-5, the stress intensity factor can be recovered as follows:

$$K_{1(2)} = \int_{\Sigma} \left(\sigma_{ij} u_i^* - \sigma_{ij}^* u_i\right) \eta_j \, ds \tag{2.12}$$

where σ_{ij} represents the two-dimensional stress components on a given contour, and these

stresses can be extracted from the FE (Finite Element) results; u_i represents the corresponding displacements; σ_{ij}^* and u^*represent the complementary stress and displacement fields, which satisfy the same equilibrium and constitutive equations as σ_{ij} and u; η_j is an outward-pointing unit vector normal to the contour surface; and ds is the infinitesimal contour length. According to Eq. (2.8) and the constitutive law, stress and strain along the contour will behave as follows:

$$\sigma_{ij} = O\left(r^{\lambda-1}\right); u = O\left(r^{\lambda}\right) \tag{2.13}$$

As the contour radius shrinks to zero, the integrand in Eq. (2.12) needs to behave as $O(r^{-1})$ so that the integral can recover the stress intensity factor as a constant. Hence, we must have:

$$\sigma_{ij}^* = O\left(r^{-\lambda-1}\right); u^* = O\left(r^{-\lambda}\right) \tag{2.14}$$

Notice that on the flanks of this contour, the integral will diverge because of the r^{-1} term when r goes to zero. However, if λ satisfies equations (2.5) or (2.6) then -λ also does, and the complementary fields can be further required to be the eigenfunction themselves so that both $\sigma_{ij}u_i^*$ and $\sigma_{ij}^*u_i$ will be equal to zero on the flanks. Under the above conditions, the integral around the contour is equal to the integral performed only on a circular arc, and appropriate participation factors are chosen in the complementary fields to recover the stress intensity factors $K_{1(2)}$. These complementary fields are defined differently for modes 1 and 2 loadings and are listed in Sinclair *et al.* (1984). This integral method will be further discussed in Chapter 4.

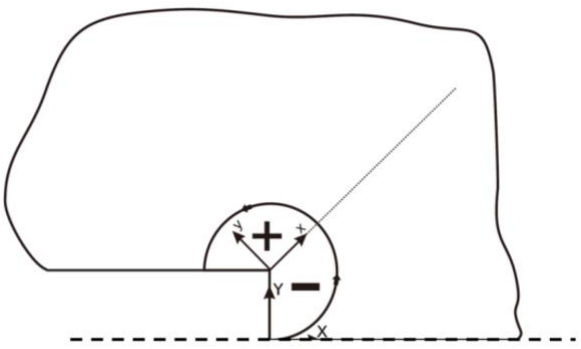


Figure 2-5: a close contour around a sharp notch feature.

Alternative methods

The methods mentioned above provide insights into wedge-related problems, but challenges remain. For instance, in Williams' asymptotic approach, approximations are made because only the dominant term in the series expansion is used. Additionally, these methods struggle to cover all loading conditions, such as discrete force or non-uniform far-field loading. For a given geometry of the wedge, the external load can always be classified as force or displacement loads, and these two types of loads can be further seen as the superposition of singular loads or singular dislocations. Alternative formulations for the wedge problem are studied, starting not from the Airy stress function but from the Kolosov-Muskhelishvili potential (Muskhelishvili, 1953), combined with Neuber's conformal mapping (Neuber, 1958). This forms a unified approach to analyse notch problems (Lazzarin and Tovo, 1996; Filippi *et al*., 2002). The conformal mapping formula used to transform a wedge (in the z-plane) into a semi-infinite half-plane (in the ξ-plane) is shown as follows (Ma and Hills, 2023):

$$\begin{cases} z = x + iy = re^{i\theta} = w(\zeta) = (-i\zeta)^q = \left(e^{-i\frac{\pi}{2}}\zeta\right)^q, \theta \in (-\alpha, \alpha), \\ \zeta = u + iv = \rho e^{i\varphi} = w^{-1}(z) = iz^{\frac{1}{q}} = e^{i\frac{\pi}{2}}z^{\frac{1}{q}}, \varphi \in (0, \pi) \end{cases}, \begin{cases} (z \neq 0), \\ q = \frac{2\alpha}{\pi}, 0 < q \leq 2 \end{cases} \tag{2.15}$$

The mapping between two planes is illustrated in Figure 2-6, notice that the free surface of the wedge has been mapped as the u-axis of the ξ plane. Based on the mapping geometry, Ma and Hills (2023) use complex analysis technique through the argument of analytical continuation (see Section 2.9 for more details) on the boundary of the wedge to calculate Muskhelishvili's potential function (see section 2.3 for details):

$$\begin{cases} \varphi(z) = A\, ln\left(z^{\frac{1}{q}} - z_0^{\frac{1}{q}}\right) - \bar{B}\, ln\left(z^{\frac{1}{q}} + \bar{z}_0^{\frac{1}{q}}\right) - \dfrac{z^{\frac{1}{q}}}{qe^{i\pi q}} \dfrac{\bar{A}}{\left(z^{\frac{1}{q}} + \bar{z}_0^{\frac{1}{q}}\right)} \\ \psi(z) = B\, ln\left(z^{\frac{1}{q}} - z_0^{\frac{1}{q}}\right) - \bar{A}\, ln\left(z^{\frac{1}{q}} + \bar{z}_0^{\frac{1}{q}}\right) + \dfrac{\bar{A}z^{\frac{1}{q}}\bar{z}_0^{\frac{1}{q}}}{q^2\left(z^{\frac{1}{q}} + \bar{z}_0^{\frac{1}{q}}\right)^2} + \dfrac{e^{i\pi q}}{q} \dfrac{\bar{B}z^{\frac{1}{q}}}{\left(z^{\frac{1}{q}} + \bar{z}_0^{\frac{1}{q}}\right)} \end{cases} \tag{2.16}$$

Where z_0 is the location of the singularity, constants A and B are related to the loading conditions:

$$\begin{cases} A = \dfrac{1}{(1+\kappa)}\left[\dfrac{\mu}{i\pi}\left(b_x + ib_y\right) - \dfrac{1}{2\pi}\left(F_x + iF_y\right)\right] \\ B = \dfrac{1}{(1+\kappa)}\left[\dfrac{\kappa}{2\pi}\left(F_x - iF_y\right) - \dfrac{\mu}{i\pi}\left(b_x - ib_y\right)\right] \end{cases} \tag{2.17}$$

And μ is the shear modulus, the Kolosov constant $\kappa = 3 - 4\nu$ for plane strain and $\kappa = \frac{(3-\nu)}{(1+\nu)}$ for plane stress, ν is Poisson's ratio. This method has been extended to two further works in anti-plane scenario in this thesis, see chapters 5 and 6.

Another method, mentioned in numerous pieces of literature for solving the wedge problem, is Mellin's transformation technique (see Erdogan and Arin, 1976; Hanson and Keer, 1989). Although Mellin's transformation differs from the asymptotic approach, which can produce closed-form, exact solutions, the analytical solution derived from it is limited to several simple cases and applying this method is extremely laborious.

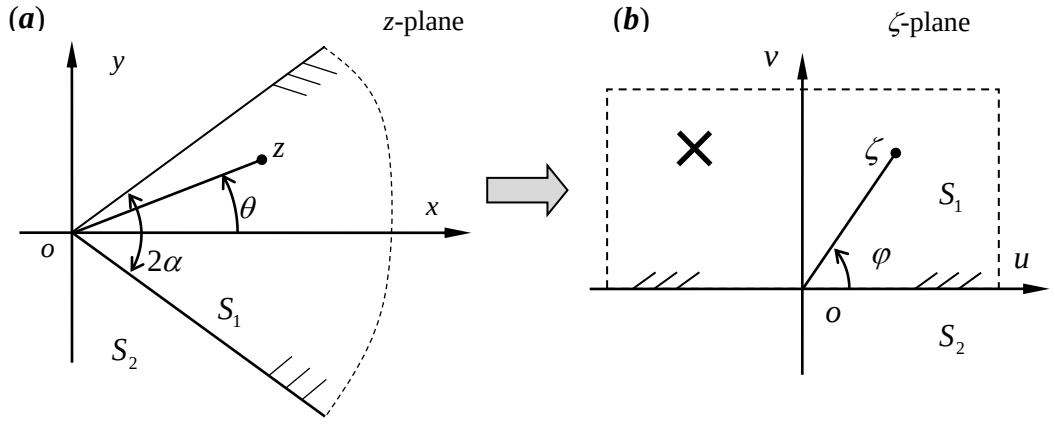


Figure 2-6: (a) wedge model; (b) auxiliary plane after mapping

2.3. Complex variable potential for elastic problem

For elastic problems, complex potentials provide a powerful method to generate stress fields. The plane and anti-plane potentials are detailed in the following sections:

2.3.1. Plane complex potential

The plane elastic problem can be characterized using Muskhelishvili's complex potential, where all stresses and displacements can be expressed in terms of two complex potentials $\varphi(z)$ and $\psi(z)$:

$$\sigma_{11} + \sigma_{22} = 2\left[\varphi'(z) + \overline{\varphi'(z)}\right]$$

$$\sigma_{22} + i\sigma_{12} = \varphi'(z) + \overline{\varphi'(z)} + \bar{z}\varphi''(z) + \psi'(z)$$

$$2\mu(u_1 + iu_2) = \kappa\varphi(z) - z\overline{\varphi'(z)} - \overline{\psi(z)}$$

$$T_1 + iT_2 = -i\left[\varphi(z) + z\overline{\varphi'(z)} + \overline{\psi(z)}\right]|_A^B \tag{2.15}$$

where, $i = \sqrt{-1}$, $z = x_1 + ix_2 (= x + iy)$, u_1, u_2 are displacements in *x*- and *y*- directions $\sigma_{ij}(i, j = 1,2)$ are stress components, T_1 and T_2 are the resultant forces in *x*- and *y*- directions acting on an arc $\widehat{AB}$, which are related to the stresses by

$$\sigma_{22} = -T_{2,1}, \sigma_{12} = -T_{1,1}$$
$$\sigma_{11} = T_{1,2}, \sigma_{21} = T_{2,2}, \tag{2.16}$$

$\varphi'(z) = \frac{d\varphi(z)}{dz}$, the comma followed by a subscript *i* indicates differentiation with respect to x_i, and the bar over a function denotes its complex conjugate.

2.4.2. Anti-plane complex potential

For an anti-plane elastic problem (Mode 3 loading), the only two non-zero stress components are σ_{13} and σ_{23}. By applying the constitutive and equilibrium equations, it is found that the through thickness displacement satisfies the Laplace equation:

$$\frac{\partial^2 w}{\partial^2 x} + \frac{\partial^2 w}{\partial^2 y} = 0 \tag{2.17}$$

The potential function is detailed in Bower (2009) and the stress function can be expressed in terms of an analytic function, $f(z)$, as the following:

$$\begin{cases}\sigma_{23} + i\sigma_{13} = \mu f^{'}(z) \\ \phi + i\mu w = \mu f(z)\end{cases} \tag{2.18}$$

The two stress components are derived for the stress function can be expressed as:

$$\sigma_{13} = -\phi_{,2} \quad \sigma_{23} = \phi_{,1} \tag{2.19}$$

The resultant force acting on an arc $\widehat{AB}$ can be expressed as

$$T_3 = -\frac{\mu}{2}\left[f(z) + \bar{f}(\bar{z})\right]|_A^B = -\phi|_A^B \tag{2.20}$$

2.3.3. Complex potential for singularities

The general complex potential around a singularity can be express as (Bower, 2009)

$$F(z) = A\, ln(z - z_0) \tag{2.21}$$

Where z_0 indicates the location of the singularity, this formula can be extended to both the case where the singularity is in the plane (such as edge dislocation or plane singular force) or the case where the singularity is in the anti-plane (like screw dislocation or anti-plane singular force):

Plane singularity:

For a plane singularity, two complex potentials, $\varphi(z)$ and $\psi(z)$, are required in Muskhelishivili potentials. Therefore, around the singularity they can be adjusted as follows:

$$\begin{cases}\varphi_0(z) = A\, ln(z - z_0) \\ \psi_0(z) = B\, ln(z - z_0)\end{cases} \tag{2.22}$$

The constants A and B are determined by the following boundary conditions of the loads:

$$\begin{cases} b_x + ib_y = \oint_{z_0} d(u_1 + iu_2) \\ F_x + iF_y = -\oint_{z_0} d(T_1 + iT_2) \end{cases} \tag{2.23}$$

The contour of integration encloses the singularity, and b_x,b_y are Burger's vector components, F_x,F_y are concentrated force components. By Substituting equation (2.22) into (2.15), and combining with (2.23), the potentials can be expressed as:

$$\begin{cases} \varphi_0(z) = A\,ln(z-z_0) = \frac{1}{(1+\kappa)}\left[\frac{\mu}{i\pi}\left(b_x + ib_y\right) - \frac{1}{2\pi}\left(F_x + iF_y\right)\right] ln(z-z_0) \\ \psi_0(z) = B\,ln(z-z_0) = \frac{1}{(1+\kappa)}\left[\frac{\kappa}{2\pi}\left(F_x - iF_y\right) - \frac{\mu}{i\pi}\left(b_x - ib_y\right)\right] ln(z-z_0) \end{cases} \quad (2.24)$$

In a case of displacement loading only, the singular force term is zero, so the equation can be further simplified by omitting all force-related terms. A similar approach applies in the case of force loading only.

Anti-plane singularity:

There is only one potential required in the anti-plane case:

$$f_0(z) = A\,ln(z-z_0) \quad (2.25)$$

The constant A is determined by the following condition of the loads:

$$\begin{cases} b_z = \oint_{z_0} dw \\ F_z = -\oint_{z_0} dT_3 = \oint_{z_0} d\phi \end{cases} \quad (2.26)$$

Where b_z is the Burgers vector, F_z is the anti-plane concentrated force. By substituting equation (2.25) into the last equation in (2.18), and considering (2.26), we obtain:

$$f_0(z) = \frac{(F_z + i\mu b_z)}{2\pi\mu i} ln(z-z_0) \quad (2.27)$$

In a case of displacement loading only, the singular force is zero, so the equation can be further simplified by omitting all force-related terms. A similar approach applies in the case of force loading only.

It should be noted that the above singular potentials (equations (2.24) and (2.27)) apply locally around the singular loadings. For the complete potential functions, perturbation terms are also required, depending on other features of the plane, such as its geometry and global loadings.

2.5. Parabolic notch problem

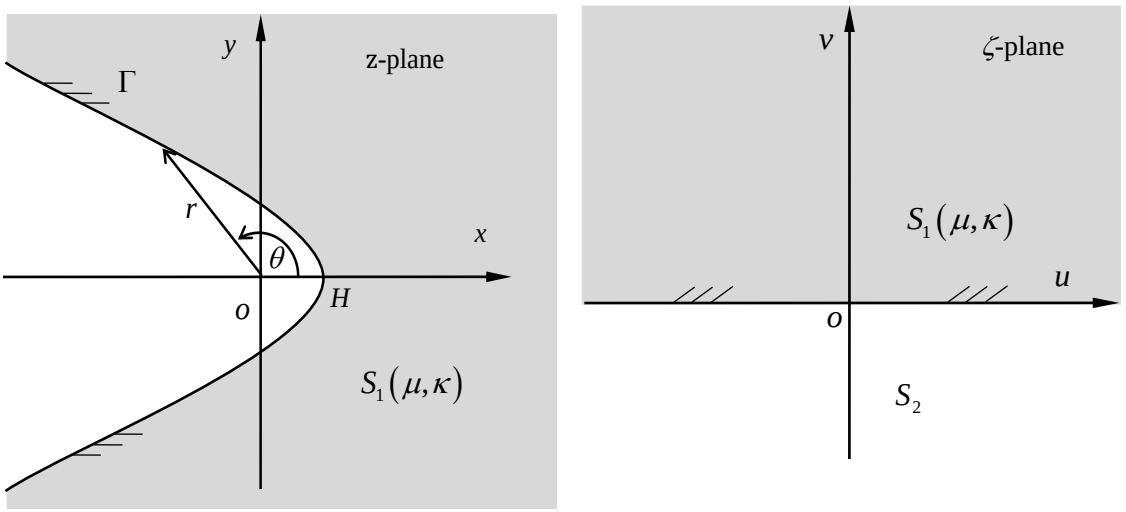
When the internal angle of a wedge falls within the range between π and 2π, the wedge

can also be referred to as a sharp notch. Another fundamental type of notch, which has received considerable research attention, is the ‘smooth’ or ‘blunt’ notch. Engineers tend to avoid sharp features in designs due to the singular stress that arises around such features. Therefore, research on the mechanical behaviour of a ‘blunt’ notch holds more practical value, including in the contexts of component assembly and power transmission.

The Asymptotic method still plays a useful role in calculating the stress concentration for a blunt notch, Neuber (1958) made use of the first term of the Airy biharmonic expansion to give an approximation of the stress concentration factor, and this factor has been further adopted by others works that target on characterizing the stress field (see, e.g., Savruk and Kazberuk, 2006; Kim and Cho, 2012; Bahrami *et al*., 2019). Even though the results are simple, information is lost in the asymptotic approach such as gradient of stress and spatial distribution.

The complex potential method, reminiscent of a sharp notch approach and utilizing Muskhelishvili's formula, has also been applied to 'blunt' notches, using Neuber’s conformal mapping technique (see, e.g., Lazzarin and Tovo, 1996; Ma and Hills, 2022). The conformal mapping formula is crucial for the process, and a suitable mathematical description of the blunt notch is required. In Neuber (1937), the Cartesian coordinates of the notch plane were transformed into an auxiliary curvilinear system. The key parameter of this transformation is the sharp notch angle 2α to which the blunt notch can be approximated. Thus, this method can only be applied in cases where the free edges of the blunt notch coincide with those of a sharp notch in the far field. Ma and Hills (2022) describe a blunt notch tip as a parabolic surface, with its shape characterized by the function set out by Zappalorte *et al* (1998). The geometry of the parabolic notch, as shown in Figure 2-7(a), defines a length parameter H. The corresponding expression of the Cartesian coordinate is as follows:

$$x = H - \frac{y^2}{4H} \tag{2.28}$$



(a) (b)

Figure 2-7. A parabolic notch (a) physical model in Cartesian coordinate with a length parameter H at the crack tip, (b) mapping auxiliary half-plane.

Another constant related to conformal mapping is h, expressed as

$$h = \sqrt{H} = \sqrt{r}\cos\frac{\theta}{2} \tag{2.29}$$

The conformal mapping formula that maps the parabolic notch (Figure 2-7(a)) onto an auxiliary half-plane (Figure 2-7(b)) is:

$$\begin{cases} z = x + iy = re^{i\theta} = w(\zeta) = (-i\zeta + h)^2 \\ \zeta = w^{-1}(z) = i\left(z^{\frac{1}{2}} - h\right) = u + iv \end{cases} \tag{2.30}$$

The auxiliary coordinate system can be expressed as

$$v = \sqrt{r}\cos\frac{\theta}{2} - h, \;\; u = -\sqrt{r}\sin\frac{\theta}{2}. \tag{2.31}$$

Note that the free edge of the parabolic notch is mapped onto the u-axis of the ξ-plane. The conformal mapping technique transfers the parabolic notch problem to a half-plane problem which is comparatively easier to analyze. The conformal mapping formula (2.29) - (2.31) will be further applied in chapter 6.

Ma and Hills (2022) utilized the conformal mapping scheme described above to map a parabolic notch onto a half-plane. Subsequently, they performed a complex analysis through the argument of analytical continuation (see Section 2.9 for more details) on the boundary of the parabolic notch. This analysis addressed a specific problem: the interaction of a parabolic notch with a plane singularity. They proposed potential functions compatible with the Muskhelishvili potential as follows:

$$\begin{cases} \varphi(z) = A\,ln(z-z_0) - A\,ln\left(\sqrt{z}+\sqrt{z_0}\right) - \bar{B}\,ln\left(2-\sqrt{\bar{z}_0}-\sqrt{z}\right) + \dfrac{\bar{A}z}{2\sqrt{\bar{z}_0}\left(\sqrt{\bar{z}_0}+\sqrt{z}-2\right)} \\ \psi(z) = B\,ln(z-z_0) - B\,ln\left(\sqrt{z}+\sqrt{z_0}\right) - \bar{A}\,ln\left(2-\sqrt{\bar{z}_0}-\sqrt{z}\right) + \dfrac{A\left(\sqrt{z}-2\right)^2}{2\sqrt{z}\sqrt{z_0}} \\ \qquad + \dfrac{\bar{B}\left(\sqrt{z}-2\right)^2}{2\sqrt{z}\left(\sqrt{\bar{z}_0}+\sqrt{z}-2\right)} - \bar{A}\dfrac{\left(\sqrt{z}-2\right)^2}{4\sqrt{\bar{z}_0}}\dfrac{\left(2\sqrt{\bar{z}_0}+\sqrt{z}-4\right)}{\left(\sqrt{\bar{z}_0}+\sqrt{z}-2\right)^2} \end{cases}$$

Where constants A, B are defined in equation (2.17) and z_0 is the location of the dislocation.

2.6. Plane contact problem

The study of contact problems dates back to the nineteenth century when Hertz investigated the optical interference occurring between two glass lenses in contact (Hertz, 1881). Hertz postulated that the contact was frictionless and that the contacting bodies had quadratic profiles. Contact mechanics is of practical interest in various engineering fields, a notable example being the fretting fatigue issues in aircraft engine blades. Contemporary researchers aim to devise a general solution for all types of contacts, endeavoring to overcome the limitations of Hertz's original work.

In the advancement of contact mechanics theory, it is often assumed that the contact area is small relative to the size of the contacting bodies. This implies that the stress field distant from the contact area is negligible (Barber, 2018). Such an assumption leads to the approximation of a half-plane, analogous to the plane fracture mechanics problem. The correlation between contact mechanics and fracture mechanics was explored by

Giannakopoulos *et al*. (1998). They suggest that one method of analyzing contact problems is to conceive the contact pair as a single monolithic body and to examine the traction along the interface. Consequently, an asymptotic wedge analogue is employed to model the contact edge and address fretting issues.

The plane contact problem is a type of elastic plane problem, where the stress field can be characterized by the Muskhelishvili potential. However, research interest often centres more on the stress behaviour along the contact surface—such as contact pressure and shear stress—rather than on the general stress field distribution across the entire plane or near geometric features. This thesis will not focus on the development of analytical solutions, as they are well-documented in numerous textbooks, including those by Johnson (1987) and Hills (2021).

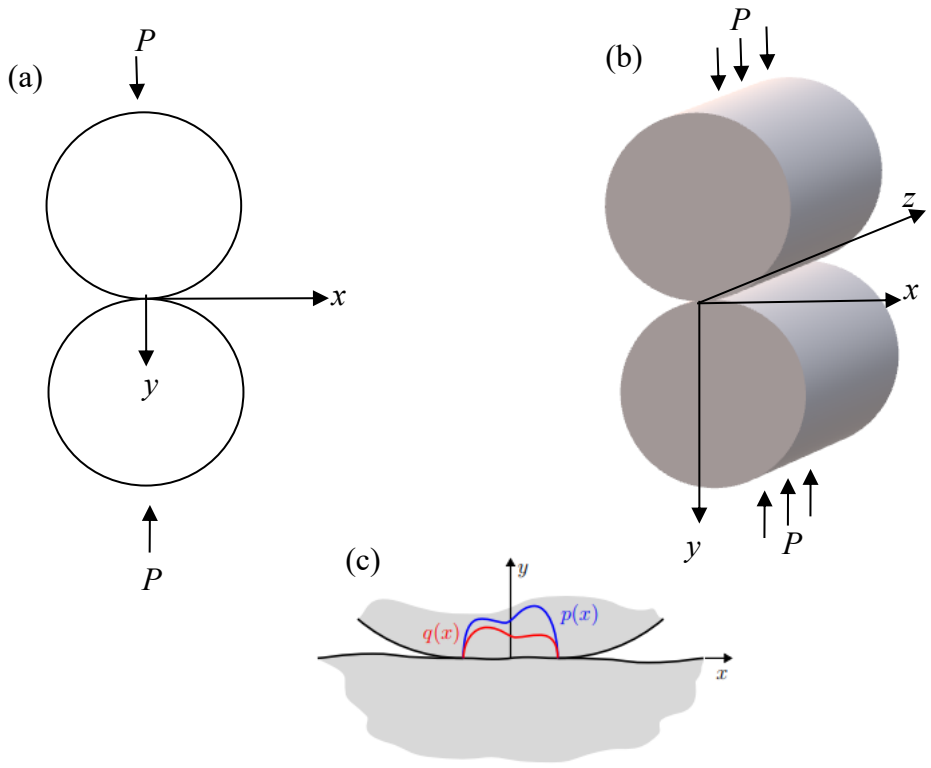


Figure 2-8: Illustration of contact geometries: (a) plane contact; (b) plane contact that has been extended in the in-plane direction; (c) contact pressure and shear stress along the contacting surface.

In this work, we will use the plane contact problem as a case study to examine how the

contact profile changes when a plane (depicted in Figure 2-8(a)) that extends in the anti-plane direction is modelled as a prismatic body (illustrated in Figure 2-8(b)). This three-dimensional body retains properties that are locally 'plane' and can be conceptualized as layers 'grouped' together in the through-thickness direction. The aim is to evaluate how the stress field changes between these layers along the extended contact direction. The choice of the contact problem as the reference for plane problems is advantageous because the stress along the contact interface serves as an indicator to assess how the general stress field varies with extent. For this inquiry, it is essential to first discuss the fundamentals of the contact problem.

2.7.1. Contact classification

Different geometries of the contact bodies lead to variations in the stress field along the contact interface. Generally, the contact problem can be categorized into four distinct types, as illustrated in Figure 2-9 (Hills and Anderson, 2022). Throughout this thesis, our consideration will be confined to two-dimensional scenarios. As previously mentioned, our focus will be primarily on the stress behavior at the contact edge, and we will assume that the contacting bodies extend infinitely in the direction perpendicular to the contact plane.

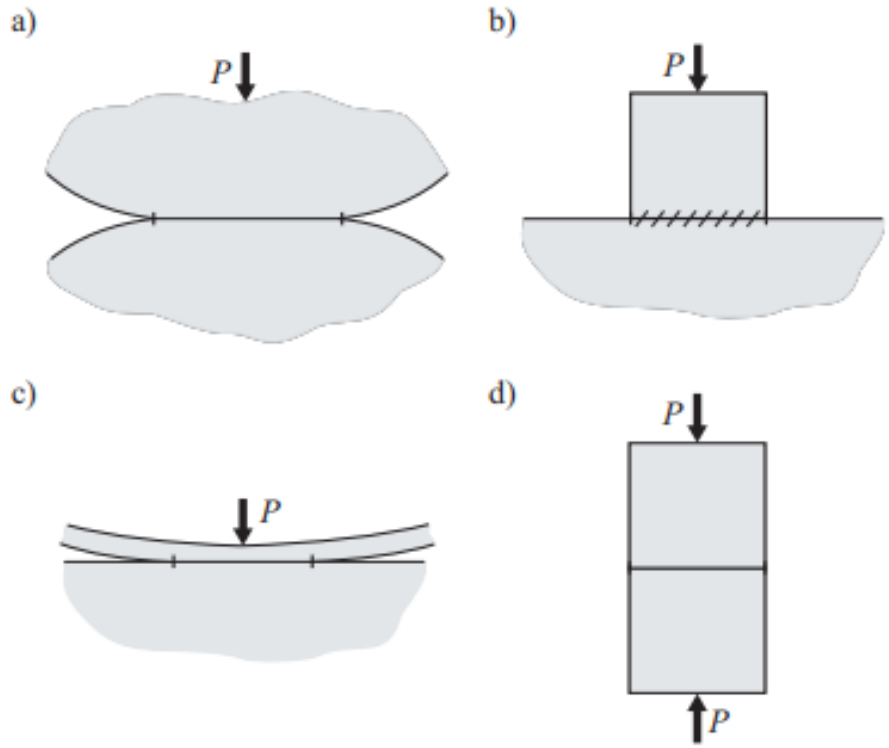


Figure 2-9: Contact classification (a) an incomplete contact; (b) a complete contact; (c) a receding contact; (d) a common edge contact.

An incomplete contact, depicted in Figure 2-9(a), arises when bodies with convex surfaces are pressed together. This configuration is characterized by the contact area increasing as the applied pressure increases. The contact pressure decreases smoothly to zero at both edges in a square root bounded manner. Conversely, a complete contact occurs when the size of the contact area remains fixed regardless of the applied load, such as when a square block is pressed into an elastic half-plane, as shown in Figure 2-9(b). Assuming that there is no slip at the contact interface, that is, the contact is fully adherent, the problem is analogous to a $\frac{3}{2}\pi$ wedge, and Williams' solution is applicable. From Williams' analysis, it can be inferred that the contact pressure $p(s)$ behaves as $s^{\lambda-1}$, and is therefore singular.

Imagine stepping on a stiff board that lies flat on the floor. Due to the force applied by your foot, the contact area between the board and the floor will diminish as the applied load increases. Contacts in which the application of force reduces the contact area are characterized

as receding contacts. In such receding contacts, the contact pressure decreases to zero at the contact edge, and if the bodies are of similar elasticity $p(s)$ behaves as $\sqrt{s}$ (Hills and Andresen, 2020).

The final type of contact, termed common edge contact, occurs when the contacting sides are collinear, forming a straight line. The analysis of this type of contact is analogous to Williams' analysis of a π wedge. Consequently, the contact pressure $p(s)$ behaves as s^0, indicating a uniform pressure distribution.

2.7.1. Airy stress function and analytical plane contact solution.

The analytical solution of contact problems begins with the consideration of a line load applied to an elastic half-plane, as depicted in Figure 2-10(a). Flamant (1892) discovered the solution to this problem, which he identified as a special case of Boussinesq's (1885) three-dimensional solution. The stress in polar coordinates can be expressed as follows:

$$\sigma_{rr}(r,\theta) = \frac{2P}{\pi r} sin(\theta), \qquad \sigma_{\theta\theta} = \sigma_{r\theta} = 0. \tag{2.32}$$

The corresponding Airy stress function was given by Timoshenko and Goodier (1951):

$$\varphi(r,\theta) = -\frac{P}{\pi} r\theta \, cos(\theta) \tag{2.33}$$

The state of stress can be expressed in Cartesian coordinates by

$$\sigma_{xx}(x,y) = \frac{2P}{\pi}\frac{x^2 y}{(x^2+y^2)^2}$$

$$\sigma_{yy}(x,y) = \frac{2P}{\pi}\frac{y^3}{(x^2+y^2)^2}$$

$$\sigma_{xy}(x,y) = \frac{2P}{\pi}\frac{xy^2}{(x^2+y^2)^2} \tag{2.34}$$

The corresponding strain can be found using Hooke's law, and integrated to give the expression of the displacement:

$$u(x) = -\frac{P}{4}\frac{\kappa - 1}{2\mu} sgn(x) + \frac{C_1}{2\mu}$$

$$v(x) = \frac{P}{2\pi}\frac{\kappa + 1}{2\mu} ln|x| + + \frac{C_2}{2\mu} \tag{2.35}$$

where the $sgn(x)$ function is defined as -1 for x < 0 and 1 for x > 0, C_1 and C_2 are arbitrary constants involved in the integration of the strain.

We now extend the Flamant solution to a distributed normal force, shown in Figure 2-10(b), simply by superimposing a set of point loads with magnitude $p(\xi)d\xi$. it is convenient to work with displacement derivatives, thereby eliminating the arbitrary constants C_1 and C_2. The displacement derivatives can be expressed as:

$$\frac{\partial u(x)}{\partial x} = -\frac{\kappa - 1}{4\mu} p(x)$$

$$\frac{\partial v(x)}{\partial x} = \frac{\kappa + 1}{4\pi\mu} \int_{Contact} \frac{p(\xi)}{x - \xi} d\xi \tag{2.36}$$

Considering two elastic bodies that are not necessarily elastically similar brought into contact having the displacement along the contact surface u_1, v_1 and u_2, v_2. We can write down the relative change in surface slope $h(x) = u_1(x) - u_2(x)$ and $g(x) = v_1(x) - v_2(x)$ as:

$$\frac{1}{\alpha}\frac{\partial h(x)}{\partial x} = \beta p(x)$$

$$\frac{1}{\alpha}\frac{\partial g(x)}{\partial x} = \frac{1}{\pi} \int_{Contact} \frac{p(\xi)}{x - \xi} d\xi \tag{2.37}$$

The composite compliance α, and Dunders' constant (Dunders, 1967), β, depend solely on the elastic properties of the contacting bodies:

$$\alpha = \frac{\kappa_1 + 1}{4\mu_1} + \frac{\kappa_2 + 1}{4\mu_2}$$

$$\beta = \frac{\mu_2(\kappa_1 - 1) - \mu_1(\kappa_2 - 1)}{\mu_2(\kappa_1 + 1) + \mu_1(\kappa_2 + 1)} \tag{2.38}$$

Equation (2.37) can characterize a wide range of plane contact problem, the solution by

inversion of a singular integral equation of this kind is given by (Hills *et al.* 2013):

$$p(x) = -\frac{w(x)}{\pi\alpha}\int_{Contact}\frac{g'(\xi)}{w(\xi)(\xi - x)}d\xi + Cw(x) \tag{2.39}$$

The constant C and the fundamental function $w(x)$ depend on the end behaviour of the contact and are listed in Hills $et\ al.$ (2013).

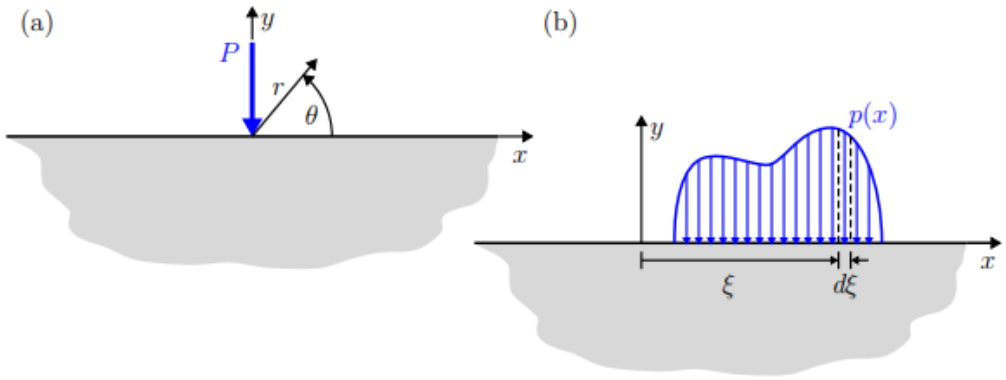


Figure 2-10. Half-plane loaded with (a) a line load applied at its origin; (b) an arbitrary distributed pressure $p(x)$.

Hertzian contact

Consider two infinitely long parallel cylinders with radii R_1 and R_2 brought into contact. The condition of being infinitely long ensures that plane strain conditions can be applied. If the contact area, denoted as $[-aa]$, is relatively small compared to the cylinders' geometries, we can approximate the surface profile in the contact with a parabolic form. By taking the first term of the binomial expansion, we obtain:

$$2Rg(x) \cong x^2 \tag{2.40}$$

where

$$\frac{1}{R} = \frac{1}{R_1} + \frac{1}{R_2} \tag{2.41}$$

We assume the bounded end condition hence the fundamental function $w(x)$ is given by

$$w(x) = \sqrt{a^2 - x^2} \tag{2.42}$$

And the constant C is zero. By applying the inversion formula (2.39) gives

$$p(x) = \frac{\sqrt{a^2 - x^2}}{\pi\alpha R}\int_{-a}^{a} \frac{\xi}{\sqrt{a^2 - \xi^2}(\xi - x)}\, d\xi = \frac{1}{\alpha R}\frac{1}{\sqrt{a^2 - x^2}} \tag{2.43}$$

By the equilibrium condition:

$$P = \int_{a}^{a} p(\xi) d\xi = \frac{\pi a^2}{2\alpha R} \tag{2.44}$$

Substituting equation (2.43) into (2.44) we can find the expression of the contact profile as:

$$p(x) = \frac{2P}{\pi a}\sqrt{1 - \left(\frac{x}{a}\right)^2} \tag{2.45}$$

We note that the peak pressure is at $x = 0$ and $p_0 = \frac{2P}{\pi a}$.

2.7.3. Subsurface contact stress

For contact bodies that can be idealized as a half-plane, the subsurface stress can be derived from the Muskhelishvili potential. If the contact surface experiences arbitrary traction, denoted by $p(x)$ and $q(x)$ (as shown in Figure 2-6(c)), the potential is given by:

$$\varphi^n(z) = \frac{1}{2\pi i}\oint_{Contact} \frac{p(x)}{x - z}\, dx$$

$$\varphi^t(z) = \frac{1}{2\pi}\oint_{Contact} \frac{q(x)}{x - z}\, dx \tag{2.46}$$

In equation (2.46), z is defined as the complex variable $z = x + iy$, $\varphi^n(z)$ and $\varphi^t(z)$ refer to the potential corresponding to the normal and shear traction respectively. The stress field can be further evaluated by using equations (2.15), another potential $\psi(z)$ involved in the second equation of (2.15) can be further evaluated using the analytical continuation at the contact interface (Hills *et al.*, 2013):

$$\psi'^{(z)} = -\varphi(z) - \bar{\varphi}(z) - z\varphi'(z)$$

Hence the second equation of (2.15) can be further simplified for the plane elastic contact problem, shown as follows:

$$\left(\sigma_{yy} - \sigma_{xx}\right) + 2i\tau_{xy} = 2[\bar{z}(z - \bar{z})\varphi'(z) - \varphi(z) - \bar{\varphi}(\bar{z})] \tag{2.47}$$

2.8. Circular hole problem

The stress concentration around a circular hole represents a classical problem in mechanics. Unlike sharp notches, where stress tends towards infinity in elastic analysis, the stress concentration factor around a circular hole is finite. This factor, defined as the ratio of the stress near the hole to the remote applied stress, is equal to three in homogeneous, isotropic, and linear elastic materials. The material around the hole is often considered underutilized due to stress concentration, leading to significant research efforts aimed at enhancing the material strength near the hole. Examples include inserting a layer of incompressible material (refer to Nie and Batra, 2019; Sburlati, 2013; Kubair and Bhanu-Chandar, 2008). However, methods for strengthening the material around the circular hole fall outside the scope of this thesis. Instead, this problem will be analyzed analytically, as closed-form solutions are attainable. Consequently, our focus will be on studying the problem in the context of elasto-plasticity to determine if the structure can reach a shakedown state (see section 2.10) under a given loading history. Closed form analytical solution for the plate that contains a circular hole is listed in this section.

2.8.1. Plane solution

Consider a plate that contains a circular hole subject the remote stress σ_0 and $n\sigma_0$ in vertical and horizontal direction, where $-1 < n < 1$, shown in Figure 2-11(a). We align the polar axis set with the one of the principal directions. The state of stress, usually solved by Airy stress function, gives the famous Kirsch's solution (Kirsch, 1989):

$$\sigma_{rr} = \frac{1}{2}\left[\left(1-\frac{a^2}{r^2}\right)+cos(2\theta)\left(\frac{3a^4}{r^4}-\frac{4a^2}{r^2}+1\right)\right] + \frac{n}{2}\sigma_0\left[\left(1-\frac{a^2}{r^2}\right)-cos(2\theta)\left(\frac{3a^4}{r^4}-\frac{4a^2}{r^2}+1\right)\right]$$

$$\sigma_{\theta\theta} = \frac{1}{2}\left[\left(1+\frac{a^2}{r^2}\right)-cos(2\theta)\left(\frac{3a^4}{r^4}-\frac{4a^2}{r^2}+1\right)\right] + \frac{n}{2}\sigma_0\left[\left(1+\frac{a^2}{r^2}\right)+cos(2\theta)\left(\frac{3a^4}{r^4}-\frac{4a^2}{r^2}+1\right)\right]$$

$$\sigma_{r\theta} = \frac{1}{2}\left[-sin(2\theta)\left(\frac{3a^4}{r^4}-\frac{2a^2}{r^2}-1\right)\right]+\frac{n}{2}\sigma_0\left[-sin(2\theta)\left(\frac{3a^4}{r^4}-\frac{2a^2}{r^2}-1\right)\right] \quad (2.48)$$

The severest stress state lies on the surface of the hole, where the traction vanishes and the remaining stress component is given by:

$$\sigma_{\theta\theta}(a,\theta) = \sigma_0(1+n) - 2\sigma_0(1-n)\,cos\,2\theta \quad (2.49)$$

The exact location of maximum stress is found by taking the derivatives of equation (2.49) with respect to θ, and the maximum stress is at $\theta = \frac{\pi}{2}$ and the minimum stress is at $\theta = 0$, as follows:

$$\sigma_{\theta\theta}\left(a,\frac{\pi}{2}\right) = \sigma_0(3-n)$$

$$\sigma_{\theta\theta}(a,0) = \sigma_0(3n-1) \quad (2.50)$$

2.8.2. Anti-plane solution

Now consider a plane that contains a hole subject to remote anti-plane shear τ shown in Figure 2-11(b). The anti-plane stress field can be derived from the complex potential method, i.e., equation (2.18) - (2.20), by purposing a suitable complex potential to satisfy the boundary condition $\tau_{yz} = \tau, \tau_{xz} = 0$ as $z \to \infty$. The complex potential is expressed as the follows:

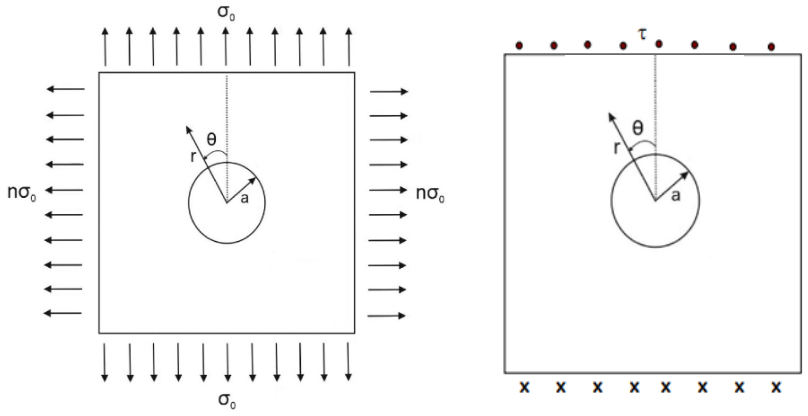
$$f(z) = \tau/\mu\left(z-\frac{a^2}{z}\right) \quad (2.51)$$

where again, $z = x + iy$ is the complex coordinate. substituting equation (2.51) into equation (2.18) and (2.19), the stress field can be represented as:

$$\tau_{yz} = -\tau\left(1 - \frac{a^2}{2r^2} cos\, 2\theta\right)$$

$$\tau_{xz} = \tau\frac{a^2}{2r^2} sin\, 2\theta \tag{2.52}$$

The severest anti-plane shear stress again lies at the circular hole, specifically, at $\theta = \frac{\pi}{2}$ and at $\theta = \frac{\pi}{4}$.



(a) (b)

Figure 2-11: Geometry of a plate with a circular hole (a) plane loading; (b) anti-plane loading.

2.9. Shakedown

When a mechanical body is subjected to cyclic loading, it may exhibit responses other than consistent elastic behavior throughout the entire loading history. The residual stress induced by plastic deformation can strengthen the material, potentially increasing its load-bearing capacity. In the context of cyclic loading, the plastic response can lead to either shakedown or steady state plasticity. Shakedown occurs when the applied load, combined with

residual stress, remains within the elastic limit for the entire loading history. Steady state plasticity, on the other hand, can lead to the collapse of the structure. This failure can manifest in two forms: cyclic plasticity, where the structure experiences fully reversing plastic deformation in a steady state; and ratcheting, characterized by the accumulation of plastic strain with each load cycle.

The study of shakedown can be traced back to Bleich's early work in the 1930s, and Koiter later provided the foundational concepts and theories. Civil engineering design codes now invariably center around plastic design rules, and implicit in these codes is the shakedown theorem. Melan, in 1936, proposed a lower bound theorem that helps to quantify the shakedown limit of a structure, which is presented here:

Melan's theorem

Melan's theorem provides a sufficient condition for shakedown in elastic-perfectly plastic structures under prescribed loading histories (Peigney, 2016). The theorem posits that *'if a residual stress state can be found which, combined with the applied stress, always remains within the yield boundary, shakedown to an elastic condition will occur'* (Melan, 1936). In simpler terms, as Barber (2016) succinctly put it, 'the system will shake down if it can'. It's crucial to note that for Melan's theorem to be fully applicable, all points within the structure must remain within the elastic limit during the cyclic load. Therefore, a full-field calculation for every point is necessary, making the finite element method a common choice for assessing the stress field. However, analytical calculations can also be employed in a conservative manner by focusing on areas subjected to the most severe stress and proposing a corresponding residual stress field. The shakedown limit determined through this approach can provide a rough estimate of the safe load .

2.10. Mathematical essentials for a general complex variable method

The complex variable method, based on the complex potential discussed in Section 2.3, serves as the foundation for solving plane elastic problems and yields accurate, closed-form solutions. This section introduces a valuable tool in complex analysis based on the argument of complex continuation for boundary value problems in the field of solid mechanics. Understanding the application of this tool is essential for Chapters 5 and 6. We will begin with basic mathematical concepts and then illustrate the development of this tool.

2.10.1. Analytical function and entire function

A function $f(z)$ of a complex variable z is a mapping from one complex number to another complex number, this function is differentiable if $\frac{f(\xi)-f(z)}{\xi-z}$ approaches to the same value for any direction of approach of ξ to z. This limit is called the derivative of the function $f'(z)$. If $f(z)$ is differentiable at z_0 and at each point in the neighbourhood of z_0, then $f(z)$ is said to be analytic at z_0. The term *holomorphic, monogenic,* and *regular* are also used (Carrier *et al*., 2005). An entire function is a complex-valued function that is analytical on the whole complex plane.

2.10.2. Liouville's theorem

Liouville's theorem states that every bounded entire function must be a constant (Nelson, 1961). This also implies that if the function $f(z)$ is not a constant for all $z \in \mathbb{C}$, then the function is unbounded (singular) in the complex plane. The proof of the Liouville's theorem can be conducted by using Cauchy's integral formula, see Fine and Rosenberger (1997).

2.10.3. A generalized complex variable problem

Consider a complex plane that is divided by a boundary Γ into domains S_1 and S_2, shown in Figure 2-12. We can examine two functions, $f_1(z)$ and $f_2(z)$. Here, $f_1(z)$ is bounded in S_1, conventionally it will be singular in S_2 according to the Liouville's theorem. Conversely,

$f_2(z)$ is defined as bounded in S_2 but singular in S_1. If the following equation holds true on the boundary:

$$f_1(z) + f_2(z) = 0 \ \text{for} z \in \Gamma \tag{2.53}$$

Then we must have

$$f_1(z) = -f_2(z) \ \text{for} z \in \Gamma \tag{2.54}$$

We could use continuation agreement to construct another function $f(z)$ so that

$$\begin{cases} f(z) = f_1(z) & \text{for } z \in \mathrm{S}_1 \\ f(z) = -f_2(z) & \text{for } z \in \mathrm{S}_2 \end{cases} \tag{2.55}$$

Notice that function $f(z)$ is a bounded entire function, according to Liouville's theorem it is a constant for the whole complex plane, i.e.,

$$\begin{cases} f_1(z) = C & \text{for } z \in \mathrm{S}_1 \\ -f_2(z) = C & \text{for } z \in \mathrm{S}_2 \end{cases} \tag{2.56}$$

If $f_1(z)$ and $f_2(z)$ comprise the complex potential mentioned in section 2.3 for plane elastic problem, it is convenient to take the constant C as zero, because the stress will be in the order of the first derivative of the potential function. In conclusion,

$$\begin{cases} f_1(z) = 0 & \text{for } z \in \mathrm{S}_1 \\ -f_2(z) = 0 & \text{for } z \in \mathrm{S}_2 \end{cases} \tag{2.57}$$

The application of this principle to generalized complex variable problems can be extended to a semi-infinite plane containing a singularity (such as a singular force or dislocation) with a traction-free boundary of any shape (a sharp notch, a parabolic notch, a circular hole, etc.) and under any type of loading mode, provided that a suitable conformal mapping strategy is developed. Examples of applications for in-plane wedges and parabolic notches can be found in Ma and Hills (2023) and Ma and Hills (2022), respectively. Additionally, the verification of this complex variable tool for generalized complex variable problems has also been demonstrated in Ma and Hills (2023) by applying Cauchy's singular integral formula.

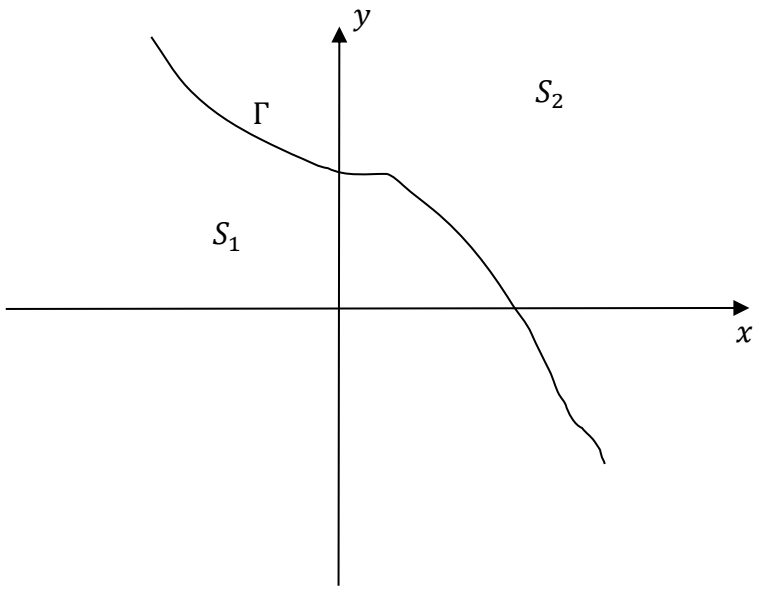


Figure 2-12. Illustration of a complex plane that is divided into two domains S_1 and S_2.

2.11. Numerical tools for dealing with singular problem

Singular features, such as stress concentrations, cracks, or other discontinuities, present significant challenges to traditional numerical methods. Various advanced numerical tools have been developed to address these challenges effectively, such as the Meshfree Galerkin method, Collapsed Elements, and the Extended Finite Element Method (XFEM).

Unlike traditional finite element methods that predefined mesh is required, Meshfree Galerkin method use a set of points distributed over the domain and employ shape functions to solve the stress. This allows Meshfree Galerkin method to adaptively refine the point distribution in regions with high gradients or singularities, such as crack tips (Nagevadiya *et al.,* 2019).

Collapsed Elements deal with the geometric singularities by collapsing elements in regions of high stress concentration. As a result, it captures the local behaviour more accurately without the necessity for an extremely fine mesh throughout the entire domain. Additionally, special numerical integration techniques are often employed to handle the complexities

associated with the collapsed elements, enhancing their efficiency and accuracy (Fu, 2009).

Additionally, XFEM introduces additional degrees of freedom and applies enrichment functions to represent the discontinuous nature of the problem. This method can accurately capture stress intensity factors and other singular behaviours without requiring a highly refined mesh. By allowing the mesh to remain independent of the discontinuities. It can integrate with existing FEM infrastructure, with modifications to include enrichment functions and additional degrees of freedom. This provides a balanced approach that enhances computational efficiency while maintaining high accuracy. (Moës *et al*., 1999)

In summary, each of these advanced numerical tools—Meshfree Galerkin methods, Collapsed Elements, and XFEM—offers unique advantages for dealing with singular problems in computational mechanics. The choice of method depends on the specific nature of the singularity, the desired accuracy, computational resources, and the complexity of the domain. Meshfree Galerkin methods excel in handling highly irregular domains and evolving discontinuities, while Collapsed Elements are ideal for localized singularities with high gradients. Finally, XFEM provides a robust solution for problems with well-defined discontinuities.

2.12. Effective Convergence Checks

In verifying finite element stresses at two-dimensional stress concentrations, ensuring convergence is critical for controlling discretization errors and achieving reliable results. The methodology applied in this thesis involves mesh refinement and specific convergence criteria, developed by Sinclair *et al.* (2016).

Initially, the process starts with a coarse mesh which is successively refined by halving the element size, and sub-modelling is used to manage computational effort on finer meshes. Stress increments are calculated by defining the stress of interest determined by FEA (Finite Element Analysis) on mesh m as σ_m and then calculating the stress increment attending mesh

refinement from $m-1$ to m as:

$$\Delta\sigma_m = \sigma_m - \sigma_{m-1}$$

For convergence, stress increments must comply with the conditions:

$$\Delta\sigma_{m-1}\Delta\sigma_m > 0$$

$$|\Delta\sigma_{m-1}| > |\Delta\sigma_m|$$

The true error for mesh m is $e_m = \sigma - \sigma_m$ where σ is the true value of the stress. The error is assumed to converge asymptotically as:

$$e_m \approx \frac{e_0}{h_m}\left(\frac{h_0}{h_m}\right)^c$$

where e_0 is the error for the normalizing mesh size h_0, and c is the theoretical rate of convergence. The observed convergence rate c_m is defined so that:

$$e_m \approx e_{m-1}\left(\frac{h_m}{h_{m-1}}\right)^{c_m}$$

The estimated convergence rate $\widehat{c_m}$ is calculated using:

$$k^{\widehat{c_m}} = \frac{\Delta\sigma_{m-1}}{\Delta\sigma_m}$$

The error estimate $\widehat{e_m}$ is given by:

$$\widehat{e_m} = \frac{\Delta\sigma_m}{k^{\widehat{c_m}} - 1}$$

A conservative approach is taken when $\widehat{c_m} < 1$ by increasing the error estimate.

Convergence is judged based on the percentage error estimate $\widehat{e_m}$:

- $1\% < \widehat{e_m} \leq 5\%$: Satisfactory
- $0.2\% < \widehat{e_m} \leq 1\%$: Good
- $0 \leq \widehat{e_m} \leq 0.2\%$: Excellent

In Sinclair *et al.* (2016), the above convergence checks methods were applied to seven benchmark problems with exact solutions for their peak stresses, covering a wide range of stress concentration factors. The convergence checks resulted in 91 error assessments for these

benchmark problems, with errors assessed at the same level as true exact errors on 83 occasions and one level worse for the other 8, ensuring conservative error estimation with a 91% accuracy rate and 9% modest conservatism.

2.13. Remaining Challenges

The work described above represents progress in our understanding of planes with defects of different geometric shapes. However, some challenges still exist. First, strictly speaking, the analyses have mostly been conducted in an asymptotic or approximate sense. Solutions lose their accuracy at points far from the geometric features. Second, it is difficult to treat various load conditions, including spatially varying far-field loads, and near-field loads such as body forces or imposed displacement loads around notches. Third, when considering a wedge with dislocations, micromechanics analysis in the literature focuses tightly on dislocation-wedge interaction problems. These analyses are very powerful in specific applications but lack a generic approach for developing solutions to generalized singularity-wedge problems, such as when the singularity represents a force or a more complex strain nucleus like point-wise defined residual strain. Lastly, the analysis of plane problems mainly focuses on in-plane stress states. When the third dimension is introduced, neither anti-plane analysis nor full three-dimensional analysis is well explored.

In this thesis, these challenges are addressed by either improving current methods or developing new ones. The aim of this thesis is to propose a generic approach to treating plane problems with defects and to develop a fundamental solution for each case.

Bibliography

4. Anderson, T. L. (2017). Fracture mechanics: fundamentals and applications. CRC press.
5. Bahrami, B., Ayatollahi, M. R., and Mirzaei, A. M. (2019). Analysis of stresses and displacements in the vicinity of blunt V-notches by considering higher order terms. Fatigue & Fracture of Engineering Materials & Structures, 42(8), 1760-1774.
6. Barber, J. R. (2002). Elasticity. Dordrecht: Kluwer academic publishers.
7. Barber, J. R. (2016). Nominally static frictional contacts under periodic loading. The Journal of Strain Analysis for Engineering Design 51 (4), 270–278.
8. Barber, J. R. (2018). Contact mechanics (Vol. 250). Springer.
9. Bleich H. (1932). U¨ber die bemessung statisch unbestimmter stahl-tragwerke unter beru¨cksichtigung des elastisch-plastischenverhaltens des baustoffes. Bauingenieur; 19(20): 261–266
10. Bower, A. F. (2009). Applied mechanics of solids. CRC press.
11. Boussinesq, J. (1885). Application des potentiels a l'etude de l'equilibre et du mouvement des solides elastiques. Gauthier-Villars.
12. Broek, D. (2012). Elementary engineering fracture mechanics. Springer Science & Business Media.
13. Carrier, G. F., Krook, M., & Pearson, C. E. (2005). Functions of a complex variable: theory and technique. Society for Industrial and Applied Mathematics.
14. Dundurs, J (1967). Effect of elastic constants on stress in a composite under plane deformation. In: Journal of Composite Materials 1 (3), pp. 310–322.
15. Eshelby, J. D. (1951). The force on an elastic singularity. Philosophical Transactions of the Royal Society of London. Series A, Mathematical and Physical Sciences, 244(877), 87-112.

16. Erdogan, F., & Arin, K. (1976). Effect of friction in wedging of elastic solids. Journal of Elasticity, 6(3), 261-275.
17. Ewalds, H.L., Wanhill, R.J.H. (1984). Fracture mechanics. Delftse Uitgevers Maatschappij /Edward Arnold.
18. Flamant, A (1892). Sur la r´epartition des pressions dans un solide rectangulaire charge transversalement. In: CR Acad. Sci. Paris 114 (1892), pp. 1465–1468.
19. Filippi, S., Lazzarin, P., & Tovo, R. (2002). Developments of some explicit formulas useful to describe elastic stress fields ahead of notches in plates. International Journal of Solids and Structures, 39(17), 4543-4565.
20. Fine, B., Rosenberger, G. (1997). The fundamental theorem of algebra. Springer Science & Business Media, 70-71.
21. Fu, F. (2009). Progressive collapse analysis of high-rise building with 3-D finite element modeling method. Journal of constructional steel research, 65(6), 1269-1278.
22. Giannakopoulos, A. E., Lindley, T. C., & Suresh, S. (1998). Aspects of equivalence between contact mechanics and fracture mechanics: theoretical connections and a life-prediction methodology for fretting-fatigue. Acta materialia, 46(9), 2955-2968.
23. Hertz, H. (1881). "Uber die Ber¨uhrung fester elastischer K¨orper". In: ¨ J Reine Angew.
24. Hills, D. A., Dini, D. (2011). Characteristics of the process zone at sharp notch roots. International Journal of Solids and structures, 48(14-15), 2177-2183.
25. Hills, D. A., Nowell, D., and Sackfield, A. (2013). Mechanics of elastic contacts. Elsevier.
26. Hills, D. and Andresen, H. (2020). Fundamentals of Elastic Contacts. In: M. Paggi and D.A. Hills, ed., Modelling and Simulation of Tribological Problems in Technology (1st ed.). Springer Int. Publish.

27. Hills, D. A., Andresen, H. N. (2021). Mechanics of fretting and fretting fatigue (Vol. 266). Springer.

28. Johnson, K. L. (1987). Contact mechanics. Cambridge university press.

29. Kim, J. K., Cho, S. B. (2013). A superposition approach to the stress fields for various blunt V-notches. Fatigue & Fracture of Engineering Materials & Structures, 36(2), 139-153.

30. Kirsch, E.G.(1898). Die Theorie der Elastizität und die Bedürfnisse der Festigkeitslehre. Zeitschrift des Vereines Dtsch. Ingenieure 42, 797–807..

31. Knowles, J. K., Sternberg, E. (1978). On the failure of ellipticity and the emergence of discontinuous deformation gradients in plane finite elastostatics. Journal of Elasticity, 8(4), 329-379.

32. Koiter W. (1956). A new general theorem on shakedown of elastic-plastic structures. Proc Koninkl Ned Akad Wet B; 59: 24–34.

33. Kubair, D. V., & Bhanu-Chandar, B. (2008). Stress concentration factor due to a circular hole in functionally graded panels under uniaxial tension. International journal of mechanical sciences, 50(4), 732-742.

34. Lazzarin, P., and Tovo, R. (1996). A unified approach to the evaluation of linear elastic stress fields in the neighbourhood of cracks and notches. International Journal of Fracture, 78, 3-19.

35. Ma, L., Hills, D. A. (2022). Interaction of a parabolic notch with a generalized singularity. International Journal of Engineering Science, 176, 103685.

36. Ma, L., Hills, D. A. (2023). A wedge of arbitrary angle interacting with a generalized singularity. International Journal of Solids and Structures, 262, 112062.

37. Melan, E. (1936). Theorie statisch unbestimmter Systeme aus ideal-plastichem Baustoff .In: Sitzungsber. d. Akad. d. Wiss. 145, 195–218.

38. Moës, N., Dolbow, J., & Belytschko, T. (1999). A finite element method for crack growth without remeshing. International journal for numerical methods in engineering, 46(1), 131-150.
39. Muskhelishvili, N. I. (1953). Some basic problems of the mathematical theory of elasticity (Vol. 15). Groningen: Noordhoff.
40. Nagevadiya, B., Vaghasia, B., Rachchh, N., & Bhoraniya, R. (2019). Galerkin meshfree methods: A review and mathematical implementation aspects. International Journal of Applied and Computational Mathematics, 5(4), 105.
41. Nelson, E. (1961). A proof of Liouville's theorem. Proceedings of American Mathematical Society. AMS, 12, 995.
42. Neuber, H. (1958). Theory of Notch Stresses, Springer-Verlag. Berlin.
43. Nie, G. J., Batra, R. C. (2019). Reducing stress concentration factor by strengthening circular hole with functionally graded incompressible material layer. Thin-Walled Structures, 144, 106223.
44. Peigney, M. (2016). On shakedown of elastic-plastic bodies with temperature-dependent properties. In VII European Congress on Computational Methods in Applied Sciences and Engineering.
45. Rice, J., Paris, P., and Merkle, J. (1973). Some further results of J-integral analysis and estimates. In Progress in flaw growth and fracture toughness testing. ASTM International.
46. Sanders Jr, J. L. (1960). On the Griffith-Irwin fracture theory. Journal of Applied Mechanics. 27, 352-353
47. Savruk, M. P., & Kazberuk, A. (2006). Relationship between the stress intensity and stress concentration factors for sharp and rounded notches. Materials Science, 42(6), 725-738.

48. Sburlati, R. (2013). Stress concentration factor due to a functionally graded ring around a hole in an isotropic plate. International Journal of Solids and Structures, 50(22-23), 3649-3658.

49. Sinclair, G. B., Okajima, M., & Griffin, J. (1984). Path independent integrals for computing stress intensity factors at sharp notches in elastic plates. International Journal for Numerical Methods in Engineering, 20(6), 999-1008.

50. Sinclair, G. B., Beisheim, J. R., & Roache, P. J. (2016). Effective convergence checks for verifying finite element stresses at two-dimensional stress concentrations. Journal of Verification, Validation and Uncertainty Quantification, 1(4), 041003.

51. Zappalorto, M., Lazzarin, P., and Yates, J. R. (2008). Elastic stress distributions for hyperbolic and parabolic notches in round shafts under torsion and uniform antiplane shear loadings. International journal of solids and structures, 45(18-19), 4879-4901.

3. Shakedown of a plate with a circular hole

3.1 Introduction

The elastic plane containing a circular hole serves as our initial example of a plane with a defect. We assume that the hole's geometric size is relatively small compared to the plate, allowing us to consider the plate as infinitely large. This classic mechanical problem is notable for its stress concentration factor (SCF) being three. Analytical solutions for the stress field across the entire plate can be derived either by formulating a suitable Airy stress function that meets both the traction-free condition at the hole surface and the remote boundary condition, or by employing the complex variable method with appropriate potentials. Thus, the elastic approach to this problem is considered fully developed under monotonic loading, regardless of the loading modes.

However, in this thesis, we consider such a plane problem from an elasto-plastic perspective, focusing on its stability under cyclic loading. Specifically, we aim to explore the shakedown limit of the plate contains a circular hole. Shakedown analysis is crucial in practical engineering, especially in civil engineering, where construction codes are often developed in relation to the shakedown limit rather than the elastic limit. This enhances the material's effectiveness. Despite the critical role of shakedown theory in engineering design, its discussion in textbooks is limited. Therefore, analyzing the classic mechanical problem of a plate with a hole and discussing the approach to evaluate its shakedown limit holds both academic and educational value.

To evaluate the shakedown limit, we will rely on Melan’s lower bound theory (1936) as the foundation for our analytical analysis. We chose Melan’s theorem over other shakedown theories due to its conservative nature, ensuring safety, and its ease of application. It is important to note that Melan’s theory requires a comprehensive field check of the structure. Thus, our analytical analysis will be supplemented by finite element analysis to validate the

determined shakedown limit.

Analytically evaluating the shakedown limit involves proposing a feasible residual stress field for the entire plate. This residual stress field must remain within the yielding surface to avoid secondary yielding. The sum of the residual stress and the stress induced by the applied load must satisfy the following condition across the entire plate during shakedown:

$$\sigma_a(x, y) + \sigma_r(x, y) \leq \sigma_y$$

Here, σ_a , σ_r , and σ_y represent the stress induced by the applied load, the proposed residual stress, and the yield stress, respectively. Identifying the shakedown limit hinges on the residual stress, which is often challenging to determine pointwise analytically. However, we can start by proposing a stress field based on points subjected to the severest stress states and then perform finite element analysis to check if the shakedown limit found matches.

The following paper will begin by analyzing the shakedown limit when the cyclic load ranges between zero and its maximum, then progress to cases with various degrees of load reversal.

3.2 Paper: Shakedown of a plate with a circular hole[1]

Shakedown of a Plate with a Circular Hole - an educational problem

Yifeng Chen and David A. Hills

Abstract

The shakedown limit for an infinite plate containing a circular hole and subject to oscillatory arbitrary remote loading is found, first by using Melan's lower bound theorem, and secondly by using a finite element model. It is shown that in some cases the limit found from the Melan theorem using the solution for the residual state of stress for an over-pressurized hole provides the exact solution, specifically when the limiting factor is the reversal of the state of stress at a particular point, while in other cases the shakedown limit is rather higher.

1. Introduction

The method of shakedown analysis came into existence in the 1930s, first developed by Bleich [1] and Melan [2], which provided a conservative lower bound to the actual shakedown limit. Later, Koiter [3] supplied the basic concepts and determined an upper bound limit by using compatibility considerations. The fundamentals of the shakedown analysis for the engineering structure are well explained in König [4]. Mackenzie *et al.* [5] has further reviewed the elastic compensation method for elastic shakedown analysis, which concentrated on finite element implementation.

Today, Civil Engineering design codes for structural steelwork now invariably center on plastic

[1] Chen, Y., Hills, D. A. Shakedown of a plate with a circular hole: An educational problem. The Journal of Strain Analysis for Engineering Design. 2023;58(8):684-694.

design rules, which makes better use of material than elastic procedures, and implicit in those codes is the process of the shakedown. Most of the existing algorithms used for shakedown analysis in Civil Engineering were evaluated by Fuschi, Pisano and Weichert [6]. Although shakedown in skeletal frames is widely studied and understood, the application of shakedown principles to continuum problems is not usually treated in undergraduate courses and, indeed, there is little detail in textbooks on the process of the shakedown.

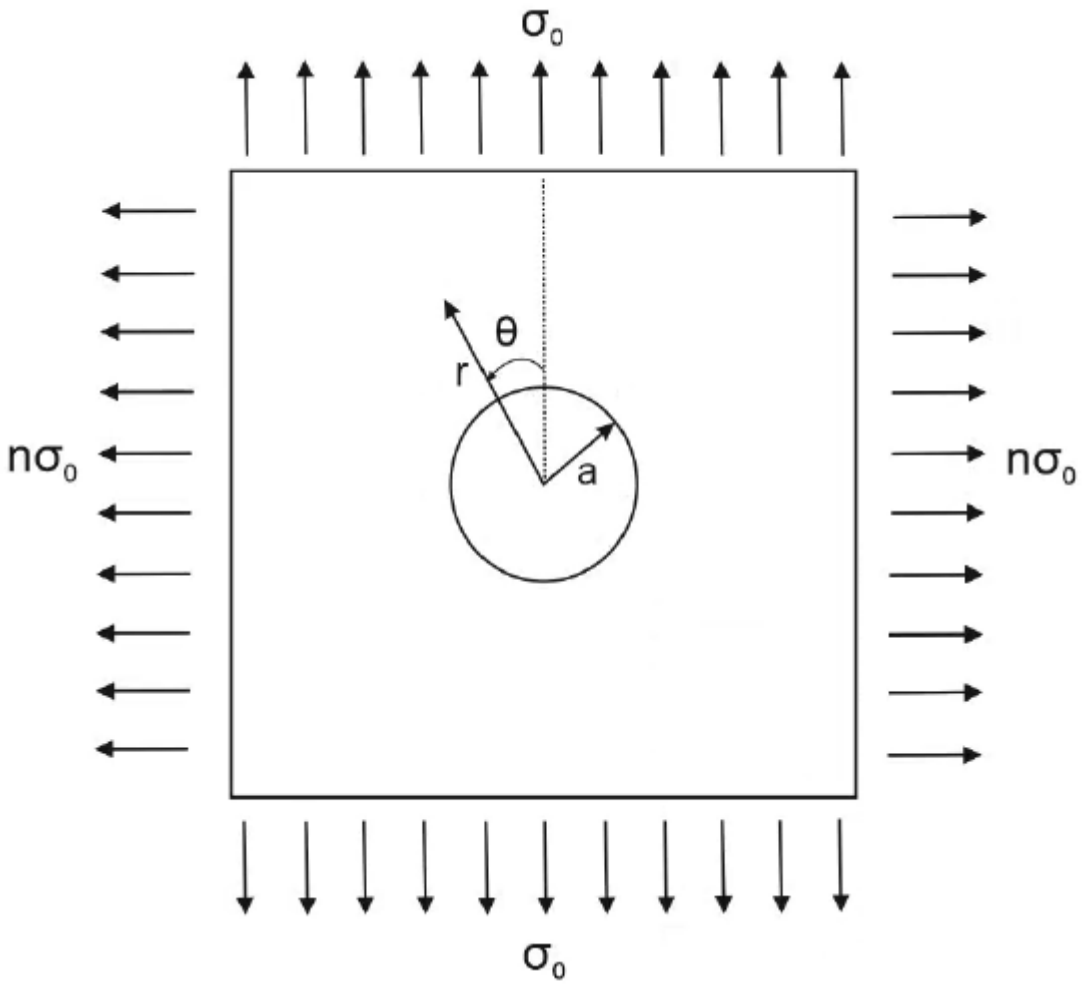


Figure 1: Geometry of a plate with a circular hole problem.

The shakedown analysis of a plate with a circular hole, shown in Figure 1, has been previously discussed by Muscat *et al.* [7]. This work applied the lower bound theorem developed by

Polizzotto [8], in which the applied load is decomposed to the steady state and cyclic load, and the shakedown limit will be the superposition of the responses of those two types of loads. Notice that in the shakedown limit calculation of the method mentioned in Muscat *et al*. [7], the inelastic stress field resulted by the steady state load is required. Because the inelastic response in most cases is not analytically feasible, finite element analysis is usually involved in Possi's theorem calculation.

In this paper, we will analyze the shakedown problem of a plate with a circular hole again, but the object of this paper is to provide a simple, practical illustration of the application of the lower bound theorem, due to Melan [9], and to investigate the strength of the problem generally. Melan's theorem may be stated as follows "If *some* residual state of stress may be found which, together with the applied stresses, results in an elastic state of stress everywhere and at all points in the loading cycle, the system will shake down in a finite number of cycles at at least the load assumed". The important thing is that we do not have to speculate what the exact form of the residual stress state is - that may be tricky - but only some self-consistent residual stress state which satisfies all free boundary conditions.

2. Formulation

The plate is subject to a general remote state of stress, Figure 1. We align the polar axis set with one of the principal directions ($\theta = 0$ with σ_0) and the other principal remote stress is given by $n\sigma_0$, where $-1 < n < 1$. The state of stress within the plate is a classical problem usually solved using an Airy stress function, and with the result [10].

$$\begin{Bmatrix}\sigma_{rr}\\ \sigma_{\theta\theta}\\ \sigma_{r\theta}\end{Bmatrix} = \frac{1}{2}\sigma_0 \begin{Bmatrix} 1-\frac{a^2}{r^2}+\cos 2\theta\left(\frac{3a^4}{r^4}-\frac{4a^2}{r^2}+1\right) \\ 1+\frac{a^2}{r^2}-\cos 2\theta\left(\frac{3a^4}{r^4}+1\right) \\ \sin 2\theta\left(\frac{3a^4}{r^4}-\frac{2a^2}{r^2}-1\right) \end{Bmatrix} + \frac{n}{2}\sigma_0 \begin{Bmatrix} 1-\frac{a^2}{r^2}-\cos 2\theta\left(\frac{3a^4}{r^4}-\frac{4a^2}{r^2}+1\right) \\ 1+\frac{a^2}{r^2}+\cos 2\theta\left(\frac{3a^4}{r^4}+1\right) \\ -\sin 2\theta\left(\frac{3a^4}{r^4}-\frac{2a^2}{r^2}-1\right) \end{Bmatrix}, \quad (1)$$

where a is the radius of the hole. The severest state of stress lies at the surface of the hole, where the tractions vanish, and the remaining stress component is given by

$$\sigma_{\theta\theta}(a,\theta) = \sigma_0(1+n) - 2\sigma_0(1-n)cos2\theta. \quad (2)$$

If we assume a state of plane stress, and that the material from which the plate is made satisfies a Von Mises yield condition, with a yield stress in pure shear k, the elastic limit is attained when

$$\sigma_{\theta\theta}^2 = 3k^2. \quad (3)$$

The exact points of the maximum and minimum values of $\sigma_{\theta\theta}$ at the edge of the hole are found by taking the derivative of equation (2) with respect to θ, and the maximum value ($\theta = \pi/2$) and the minimum value ($\theta = 0$) are:

$$\begin{aligned}\sigma_{\theta\theta}(a,\pi/2) &= \sigma_0(3-n)\\ \sigma_{\theta\theta}(a,0) &= \sigma_0(3n-1).\end{aligned} \quad (4)$$

The elastic limit for the problem is therefore found by substituting equation (4) into equation (3) and, in particular is given by $\sigma_0/k = \sqrt{3}/4$ ($n = -1$, pure shear), $\sigma_0/k = \sqrt{3}/3$($n = 0$, uniaxial tension), or $\sigma_0/k = \sqrt{3}/2$ ($n = 1$, cylindrical state of remote load). The general elastic

limit is given by $\sigma_0/k = \sqrt{3}/(3-n)$. Thus, result is included in Figure 2(a) as the yellow line (all other lines in figure 2(a) will be introduced in later sections).

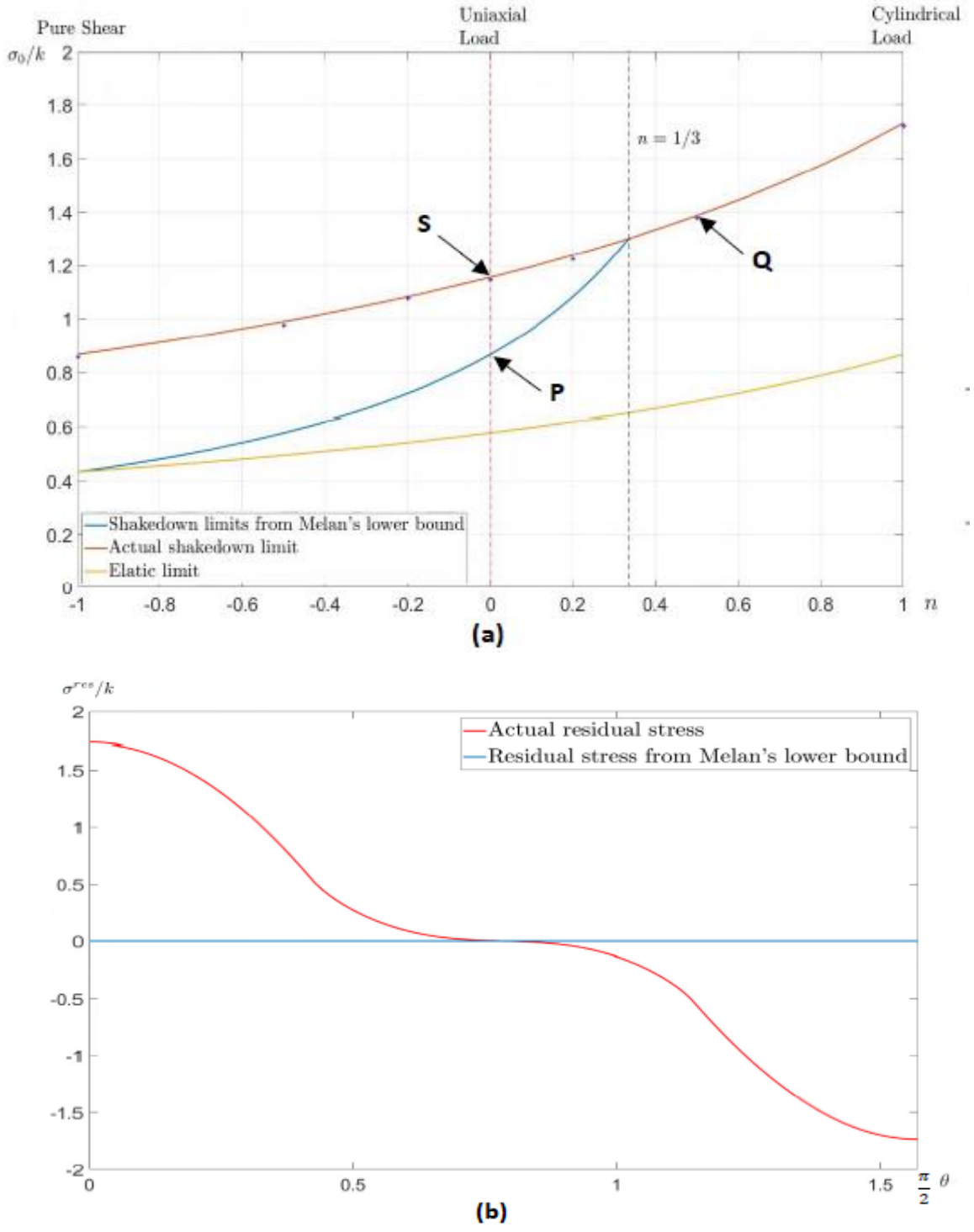


Figure 2. (a) Comparison between the elastic limit, actual shakedown limit and shakedown limit calculated by Melan's lower bound for the load-unload case. (b) for $n = -1$, comparison between the actual residual stress field at the edge of the hole, when the applied load reaches the actual shakedown limit $\sigma_0/k = \sqrt{3}/2$, and that implied by Melan's theorem when the lower bound shakedown limits $\sigma_0/k = \sqrt{3}/4$ applied.

3. Residual Stress Field

Clearly, except in the case when $n = 1$, the problem is not axi-symmetric, and neither the state of stress produced by the applied load nor any self-generated residual stress field will be symmetrical, but it is difficult to speculate on the form of the residual stress state in the general case, and even more difficult to form a potential solution to use. We therefore choose a very simple residual stress field, one which is axi-symmetric, and formed by the over-pressurization of the plate with a hole, followed by relaxation. The axi-symmetric solution has only one non-zero displacement, in the radial direction, and it is straightforward to solve for the state of stress after relaxation. This is a just a special case of the elastic-plastic analysis of thick-walled cylinder, when the outer radius is permitted to be infinitely big. After pressurization to a value of $p_0/k = \eta$ (and $1 < \eta < \frac{2+\sqrt{3}}{2}$), the residual stress state left is given by, for $r \leq r_p$:

$$\begin{aligned} \sigma_{rr}^{res}(r)/k &= 2\left(\ln\left(\frac{r}{a}\right)\right) - \eta\left(1 - \frac{a^2}{r^2}\right) \\ \sigma_{\theta\theta}^{res}(r)/k &= 2\left(\ln\left(\frac{r}{a}\right) + 1\right) - \eta\left(1 + \frac{a^2}{r^2}\right) \end{aligned} \tag{5}$$

and for $r > r_p$:

$$\begin{aligned} \sigma_{rr}^{res}(r)/k &= -\left(\frac{r_p}{r}\right)^2 + \eta\left(\frac{a}{r}\right)^2 \\ \sigma_{\theta\theta}^{res}(r)/k &= \left(\frac{r_p}{r}\right)^2 - \eta\left(\frac{a}{r}\right)^2 \end{aligned} \tag{6}$$

where

$$r_p = a\left(2 - \sqrt{2 - \eta}\right) \tag{7}$$

The residual stresses are plotted in Figure 3(a) ($\sigma_{rr}^{res}(r)$) and Figure 3(b) ($\sigma_{\theta\theta}^{res}(r)$). Note that if $\eta > \frac{2+\sqrt{3}}{2}$ upon relaxation there is secondary plastic flow, and we have not considered this case in detail.

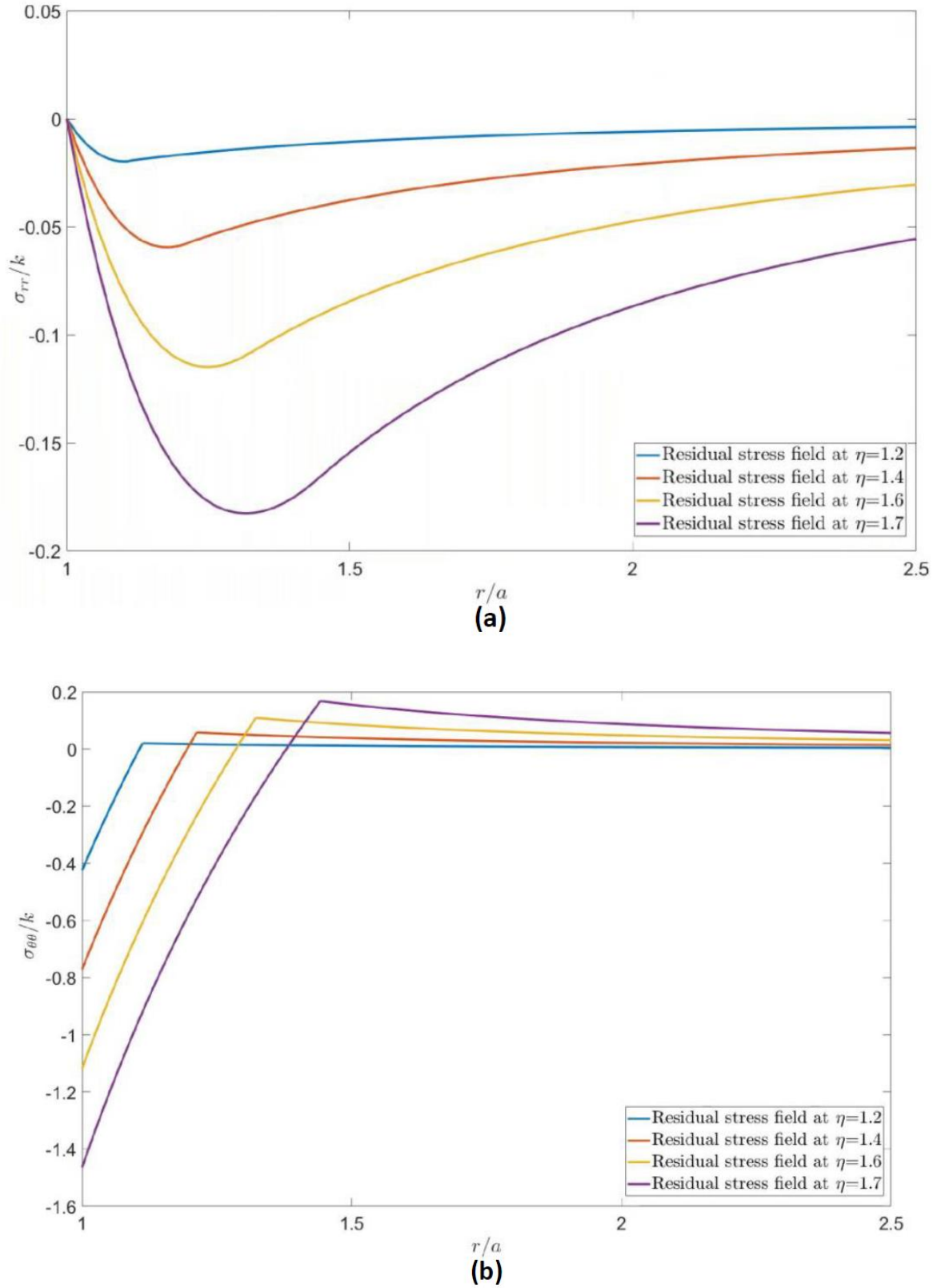


Figure 3. Residual stress (a) $\sigma_{rr}^{res}(r)$ (b) $\sigma_{\theta\theta}^{res}(r)$, generated by over-pressurized cylinder

4. Load-unload Case Analysis

Application of Melan's Theorem

It is important to note that Melan's theorem requires *all* points within the body to be within the elastic limit during the loading cycle for shakedown to be achieved, and therefore a full-field calculation is needed. But we may speculate what the optimum value of the residual stress field is by looking at **the edge of the hole**, where the severest state of stress occurs, and a picture will emerge. We shall now take a simple load-unload case where load varies between zero and σ_0 as an example to illustrate how we find the shakedown limit by finding the optimal residual stress at the edge of the hole using Melan's theorem (the residual stress fields then can be generated using equations (6)-(10) by matching $\sigma_{\theta\theta}(a)$ with the optimal residual stress we proposed at the edge of the hole). Additionally, the comparisons between the lower bound shakedown limits with the actual shakedown limits found by Finite Element Analysis (FEA) are also evaluated.

First, if we think of the problem of uniaxial tension applied to the plate ($n = 0$) we see from equations (4) and (5) that if residual stress has not been considered, point $(a, 0)$, where $\sigma_{\theta\theta}(a, \pi/2)/\sigma_0 = -1$, and point $(a, \pi/2)$, where $\sigma_{\theta\theta}(a, \pi/2)/\sigma_0 = 3$ have severe states of stress of opposite sign. So, if the magnitude of the axi-symmetric residual stress field on the edge of the hole is $\sigma_{\theta\theta}^{res}(a)/\sigma_0 = A$, the optimal choice of A is when

$$-1 + A = -(3 + A) \tag{8}$$

or $\sigma_{\theta\theta}^{res}(a)/\sigma_0 = -1$. According to Melan's theorem, the lower bound of the shakedown limit λ is therefore given by

$$\begin{aligned}\sigma_{\theta\theta}(a,\pi/2)+\sigma_{\theta\theta}^{res}(a) &= -\left(\sigma_{\theta\theta}(a,0)+\sigma_{\theta\theta}^{res}(a)\right)\\ &= 2\sigma_0 = 2\lambda k = \sqrt{3}k,\end{aligned} \tag{9}$$

or $\lambda = \sigma_0/k = \sqrt{3}/2$, i.e., a 50% increase on the elastic limit. When the applied load is removed fully the residual stress around the hole alone remains, but we know that that it is half the magnitude of the state of stress at the critical points in the presence of the load, so that there is no possibility of the component entering the plastic state because of the residual stress alone. Secondly, if we think about a state of remote applied pure shear ($n = -1$), again from equations (4)-(5), we see that $\sigma_{\theta\theta}(a,0) = -\sigma_{\theta\theta}(a,\pi/2)$, so that no residual stress of the character being considered can help, and so we expect the shakedown limit to be the same as the elastic limit, by the theorem.

When we have a cylindrical applied remote stress ($n = 1$), everywhere around the edge of the hole experiences a stress given by $\sigma_{\theta\theta}(a,\theta) = 2\sigma_0$ if residual stress has not been considered. The optimal choice of residual stress is therefore one which leads to incipient forwards slip when the maximum external load is applied and incipient reverse slip when the external load is removed, i.e., in the optimal case:

$$2\sigma_0 + \sigma_{\theta\theta}^{res}(a) = -\sigma_{\theta\theta}^{res}(a) = \sqrt{3}k. \tag{10}$$

the implied shakedown limit is given by $\lambda = \sigma_0/k = \sqrt{3}$, i.e. twice the elastic limit. Because the whole solution is axi-symmetrical, we might look forward to the actual shakedown limit being the same as that implied by the lower bound.

We extend the above reasoning to the entire range of n, [-1,1], bearing in mind that there are two key controlling points in the physical space, $(a,0)$ and $(a,\pi/2)$, to consider. In general, the net state of stress of those two points for the applied load σ_0 is displayed in Table 1. Also

bear in mind that the residual stress itself may not to exceed the elastic limit, $\pm\sqrt{3}k$, to avoid any secondary plastic flow. When $-1 \le n \le 1/3$, which includes both the uniaxial and pure shear loading cases, from equation (4), the most negative stress arose at $(a,0)$. Contribution from the applied stress together with the residual stress must not exceed the elastic limit in the reverse direction. As a result, the two extreme points during loading cycle are located at $(a,0)$ and $(a,\pi/2)$. The residual stress at the edge of the hole, therefore, needs to satisfy:

$$\sigma_{\theta\theta}(a,\pi/2) + \sigma_{\theta\theta}^{res}(a) = -\big(\sigma_{\theta\theta}(a,0) + \sigma_{\theta\theta}^{res}(a)\big) = \sqrt{3}k, \tag{11}$$

and hence, by substituting $\sigma_{\theta\theta}$ with equation (4), we have

$$\sigma_{\theta\theta}^{res}(a) = \frac{-\sqrt{3}(1+n)k}{2-2n} \tag{12}$$

$$\lambda = \sigma_0/k = \frac{\sqrt{3}}{2-2n} \quad -1 \le n \le 1/3 \tag{13}$$

The shakedown limit λ determined using Melan's theorem, for $-1 \le n < 1/3$, are plotted in Figure 2(a) as the blue line.

Table 1. Values of net stress $\sigma_{\theta\theta}(a,\theta)$ at $\theta = 0$ and $\theta = \pi/2$ for the applied load σ_0.

$\theta = 0$	$\theta = \pi/2$
$\sigma_0(3n-1) + \sigma_{\theta\theta}^{res}(a)$	$\sigma_0(3-n) + \sigma_{\theta\theta}^{res}(a)$

The illustrations of Melan's theorem may also be displayed by looking at trajectories in the deviatoric plane. The deviatoric yielding surface is a circle centered at the origin with radius $\sqrt{2}k$, and the projection of any stress σ to a deviatoric plane with a Cartesian coordinate system is transformed by the following equations:

$$|\sigma|_x = \sigma \cdot \frac{1}{\sqrt{2}}\begin{bmatrix}0\\-1\\1\end{bmatrix}, \quad |\sigma|_y = \sigma \cdot \frac{1}{\sqrt{6}}\begin{bmatrix}2\\-1\\-1\end{bmatrix}, \qquad (14)$$

Where $|\sigma|_x$ and $|\sigma|_y$ represent the x and y values of the stress σ on the deviatoric plane. We also represent the magnitude of any stress σ on the deviatoric plane as $|\sigma|_e$, so

$$|\sigma|_e = \sqrt{|\sigma|_x^2 + |\sigma|_y^2}. \qquad (15)$$

Taking $n = 0$ as an example, when the plate is loaded under the shakedown limit deduced by Melan's theorem (point *P* in the Figure 2(a), the magnitude of the elastic stress and axi-symmetrical residual stress at two controlling points on the deviatoric plane is shown in Table 2.

Table 2. Magnitude of elastic stress and residual stress on the deviatoric plane for n=0.

Elastic stress	Magnitude	Residual stress	Magnitude
$\sigma_{\theta\theta}(a,0) = -\frac{\sqrt{3}}{2}k$	$\lvert\sigma_{\theta\theta}(a,0)\rvert_e = \frac{\sqrt{2}}{2}k$	$\sigma_{\theta\theta}^{res}(a) = -\frac{\sqrt{3}}{2}k$	$\lvert\sigma_{\theta\theta}^{res}(a)\rvert_e = \frac{\sqrt{2}}{2}k$
$\sigma_{\theta\theta}(a,\pi/2) = \frac{3\sqrt{3}}{2}k$	$\lvert\sigma_{\theta\theta}(a,\pi/2)\rvert_e = \frac{3\sqrt{2}}{2}k$	$\sigma_{\theta\theta}^{res}(a) = -\frac{\sqrt{3}}{2}k$	$\lvert\sigma_{\theta\theta}^{res}(a)\rvert_e = \frac{\sqrt{2}}{2}k$

Therefore, for the case $n = 0$, by applying Melan's theorem, the deviatoric stress trajectories of the two controlling points for a load-unload cycle when the plate is loaded under the lower bound shakedown limit, are shown in Figure 4(a.1).

Next, in the case of $1/3 < n \leq 1$, positive stress arose at $(a,0)$, then the magnitude of the residual stress is no longer restricted. In other words, the residual stress at the edge of the hole

can be as small as the elastic limit in the reverse direction. Therefore, considering the critical point with maximum elastis stress, we have

$$\sigma_{\theta\theta}(a,\pi/2) + \sigma_{\theta\theta}^{res}(a) = \sigma_0(3-n) - \sqrt{3}k = \sqrt{3}k, \qquad (16)$$

hence the shakedown limits:

$$\lambda = \frac{2\sqrt{3}}{3-n} \quad 1/3 < n \leq 1 \qquad (17)$$

which has been plotted in Figure 4(a) as the red line on the right-hand side of the line "$n = 1/3$". In this case, the two extremes of the loading cycle are located at the same point (a,$\pi/2$), occurring at both the maximum applied load and the unload state. The same as above, for $1/3 < n \leq 1$, Melan's theorem can be further demonstrated by the trajectories in the deviatoric plane. Taking $n = 0.5$ as an example, when the plate is loaded under the shakedown limit determined by Melan's theorem (point Q in Figure 4(a)), the magnitude of the relevant stress on the deviatoric plane is displayed in Table 3.

Table 3. Magnitude of elastic stress and residual stress on the deviatoric plane for n=0.5.

Elastic stress	Magnitude	Residual stress	Magnitude
$\sigma_{\theta\theta}(a,0) = -\frac{2\sqrt{3}}{5}k$	$\lvert\sigma_{\theta\theta}(a,0)\rvert_e = \frac{2\sqrt{2}}{5}k$	$\sigma_{\theta\theta}^{res}(a) = -\sqrt{3}k$	$\lvert\sigma_{\theta\theta}^{res}(a)\rvert_e = \sqrt{2}k$
$\sigma_{\theta\theta}(a,\pi/2) = 2\sqrt{3}k$	$\lvert\sigma_{\theta\theta}(a,\pi/2)\rvert_e = 2\sqrt{2}k$	$\sigma_{\theta\theta}^{res}(a) = -\sqrt{3}k$	$\lvert\sigma_{\theta\theta}^{res}(a)\rvert_e = \sqrt{2}k$

The specific trajectories for the applied load moving between σ_0 and the unload state are plotted in the deviatoric plane are shown in Figure 5(a.1).

The shakedown limits derived above are found from a consideration of points on the edge of the hole only. For them to constitute a valid application of Melan's theorem, a full field

comparison of the state of stress after transient in a shake-down state, characterized by Von-Mises' parameter for all of the above cases are needed. The Von-Mises' stress is represented by the following equation in the plane stress condition:

$$\sigma_v = \sqrt{\sigma_{rr}^2 + \sigma_{\theta\theta}^2 - \sigma_{rr}\sigma_{\theta\theta} + 3\sigma_{r\theta}^2}. \tag{18}$$

It was first found that the critical points did indeed always lie on the surface of the hole. Example cases of the states of stress at what were judged to be the critical points in the loading cycle are shown in Figure 6 . Again, we take $n = 0$ as an typical example to represent the stress state behavior at critical points when $-1 \leq n \leq 1/3$, shown in Figure 6(a) (applied load $\sigma_0 = \lambda k$) and (b) (unload state). The above figures demonstrate that two critical locations are $(a,0)$ and $(a,\pi/2)$, and those points reach the yielding surface at maximum applied load state, i.e., σ_0. For the case $1/3 < n \leq 1$, we take $n = 0.5$ as an example, and the full field checks are shown in Figure 6(c) (applied load $\sigma_0 = \lambda k$) and (d) (unload state). Two extremes in this case occur at the same point $(a,\pi/2)$, happen at both load and unload states. Secondly, compared with the elastic solution, i.e., equation (1), all points in the plate are within the elastic limit $\sqrt{3}k$, which indicates that shakedown limit and the auxiliary stress field derived from Melan's theorem considering only the points on the edge of the hole are valid.

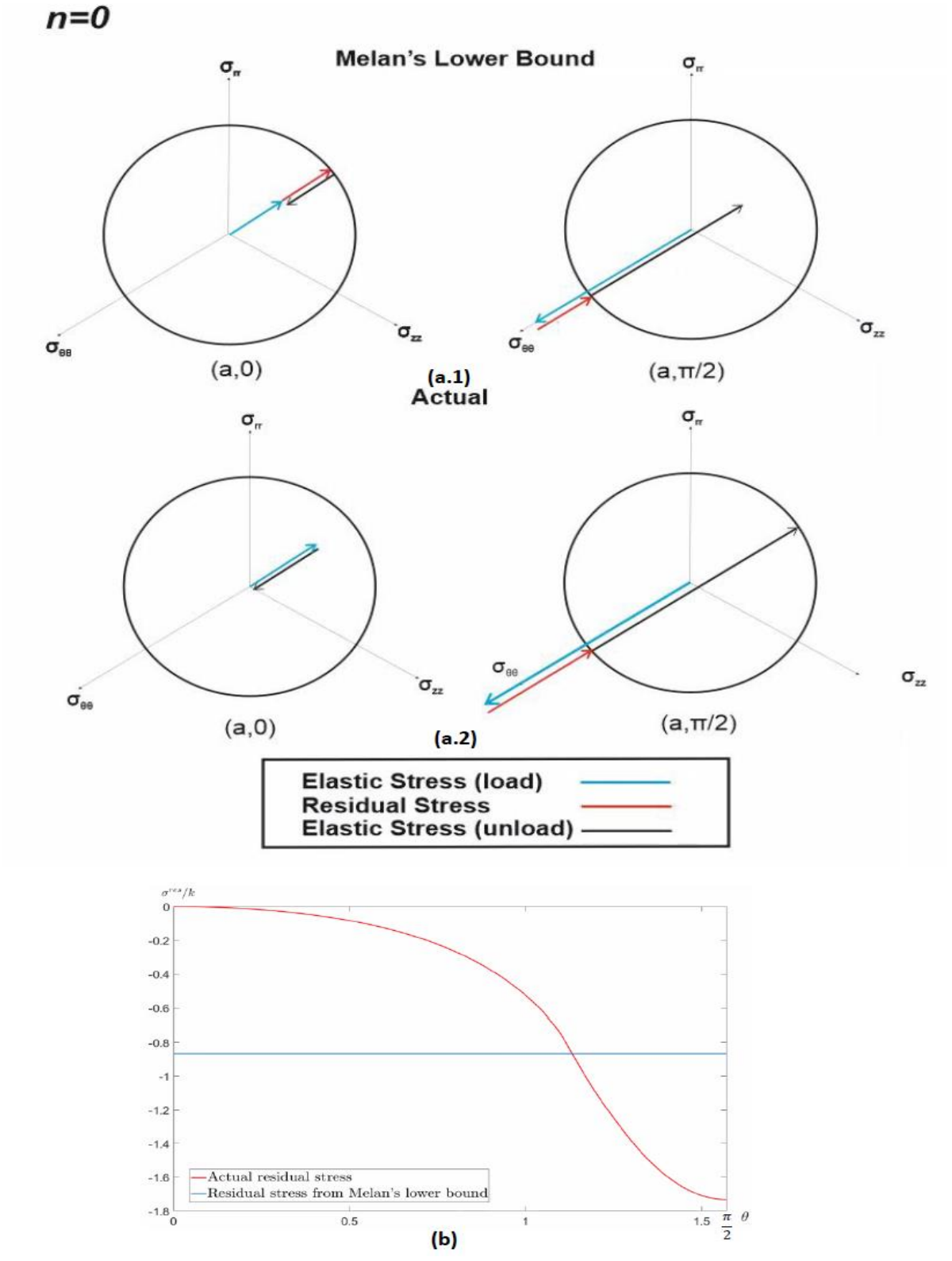


Figure 4. Load-unload case, n=0, when the applied load moves between an unloaded state and $\sigma_0 = \lambda k$*: (a.1) Elastic stress residual stress in the deviatoric plane for Melan's case. (a.2) Elastic stress, residual stress in the deviatoric plane for the actual case. (b) Comparison between the residual stress field at the edge of the hole in both actual and lower bound.*

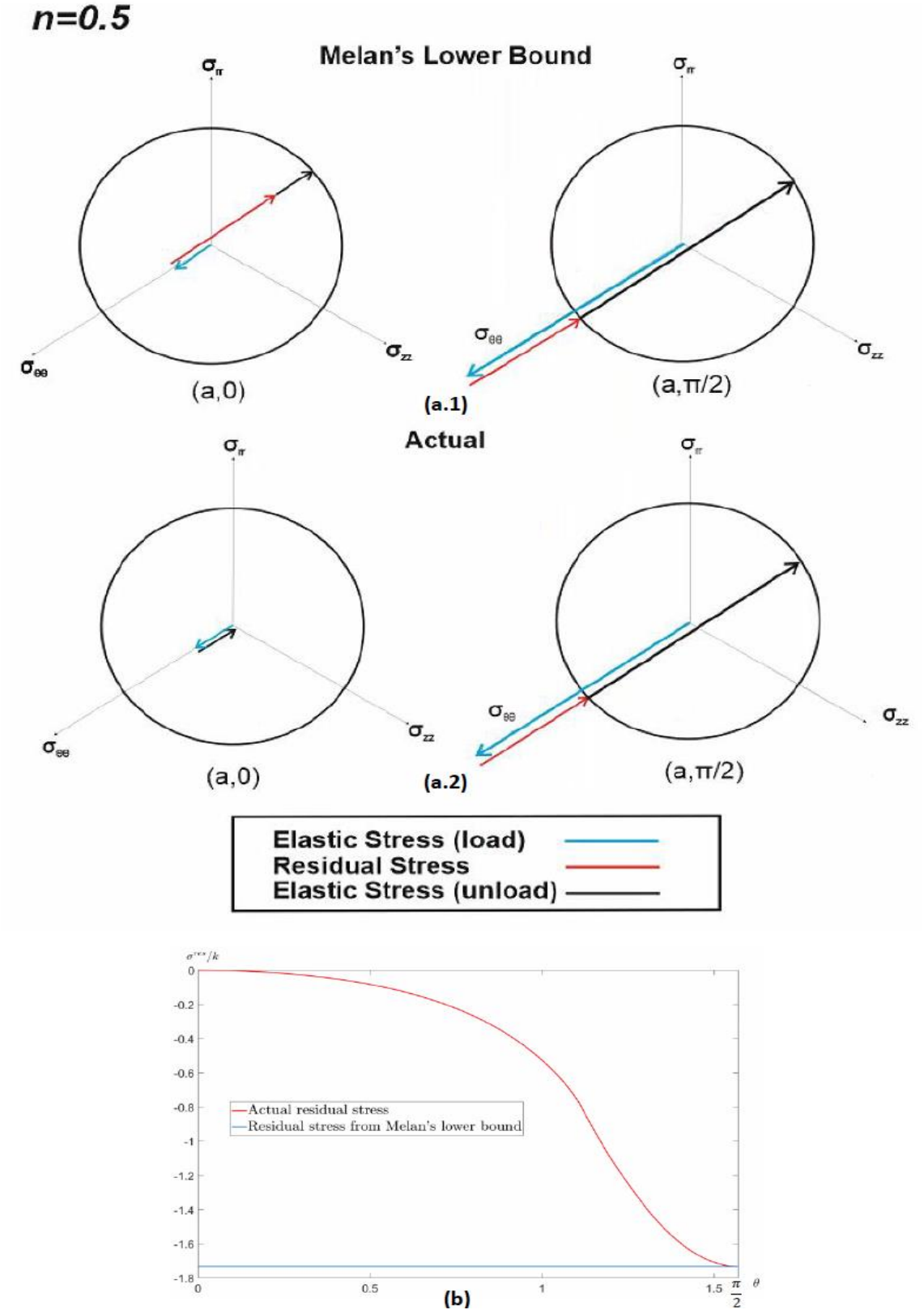


Figure 5. Load-unload case, n=0.5, when the applied load moves between an unloaded state and $\sigma_0 = \lambda k$: (a.1) Elastic stress residual stress in the deviatoric plane for Melan's case. (a.2) Elastic stress, residual stress in the deviatoric plane for the actual case. (b) Comparison between the residual stress field at the edge of the hole in both actual and lower bound.

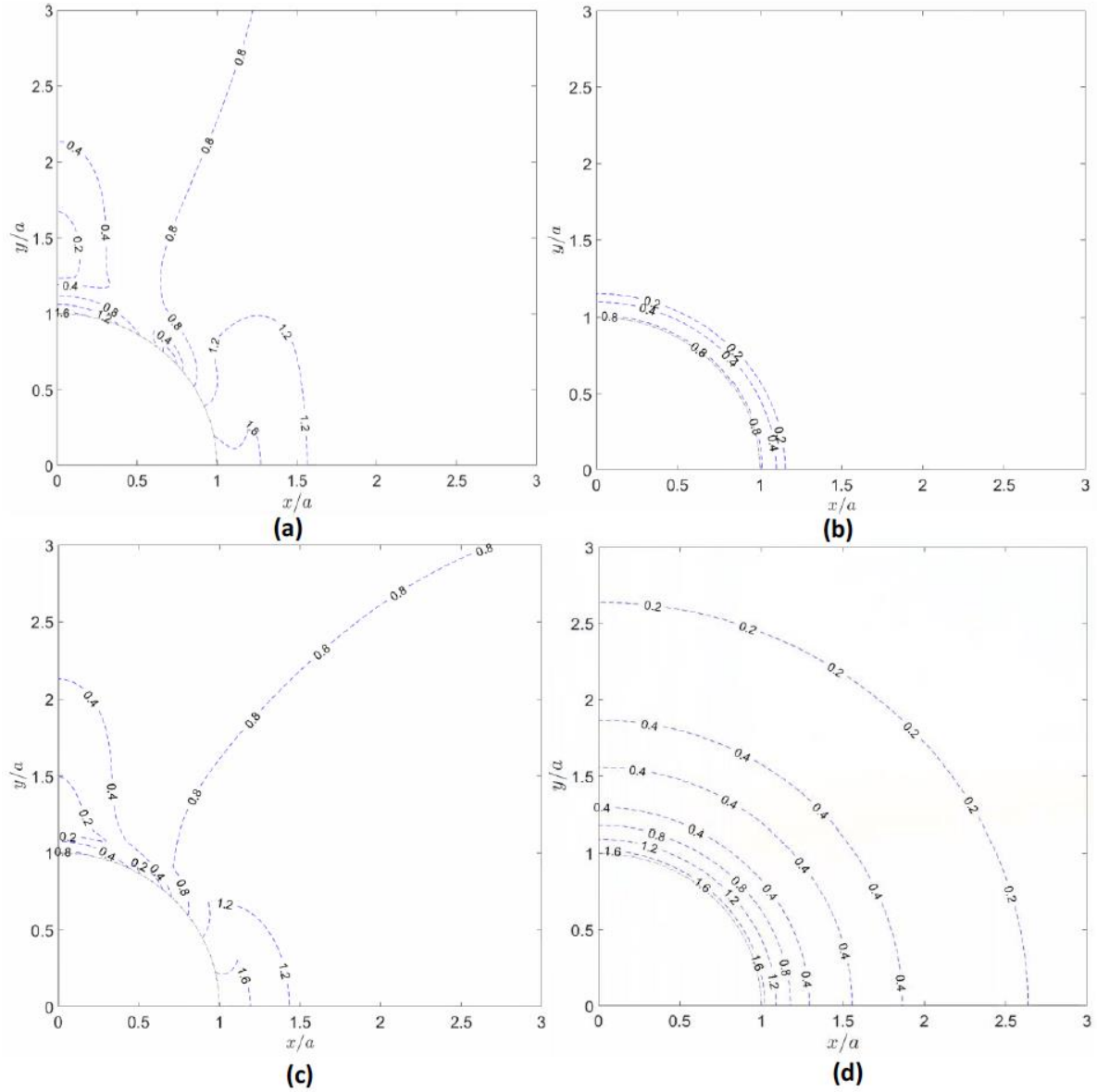


Figure 6. State of stress (σ_v/k) after transient in a shake-down state (applied laoad moving between an unloaded state and $\sigma_0 = \lambda k, n = 0$, (b) the unload state, $n = 0$, (c) applied load $\sigma_0 = \lambda k, n = 0.5$, (d) the unload state, $n = 0.5$

5. Marching in Time Solution

An elastic-plastic analysis of the problem in which the applied loads are shown in Figure 1 were exerted and the response tracked out as a function of time. The problem studied was analyzed using the commercial finite element program ABAQUS. The outer boundary was set at $r/a = 50$ and a carefully graded mesh was used. Convergence checks were also made assiduously. The material was assumed to have an elastic almost-perfectly plastic constitutive law with a gradient in the plastic range of $10^{-4}E$, where E is Young's modulus. The very small amount of work hardening was declared to be of the kinematic type. Loads were applied in ten steps and after the first cycle of load, all subsequent turning points were chosen to be at 95% of the initial value to avoid ambiguities which arise when a region is on the verge of entering the plastic state. The shakedown limits implied by the calculations described in $\mathsection3.1$ were probed by carefully advancing the range of load until cyclic plasticity was detected.

The shakedown limit found from FEA is shown in Figure 4(a) as the red line. Notice that the numerical values from FEA were consistent with that implied by Melan's theorem when the critical locations occur at the same point of both forward and reverse direction, i.e.,

$$\lambda = \frac{2\sqrt{3}}{3-n} = 2\sigma_E. \tag{19}$$

It is found that for the range $1/3 < n \leq 1$, the actual shakedown limit coincides with that found by Melan's theorem.

The reason that the lower bound results cannot track the actual shakedown limit when $-1 \leq n < 1/3$, is that the actual residual stress can change with the value of θ to eliminate the effect on the shakedown limit from other different points expect $(a, \pi/2)$. Therefore, the actual

shakedown limit calculation would focus only on the extremes produced by the point with severest stress state, i.e., $(a, \pi/2)$. But the axi-symmetrical auxiliary stress field always provides same residual stress in every different value of θ. Hence, when shakedown limits were calculated using the lower bound theorem, we need to consider the possibility that the auxiliary stress might result in the reverse direction plasticity at other different θs. The typical example would be the pure shear case, i.e., $n = -1$. The comparison between the axi-symmetrical residual stress implied by Melan's theorem when the lower bound shakedown limit applies, and the actual residual stress implied by the actual shakedown limit was plotted with respect to the values of θ, for points on the edge of the hole, indicated in Figure 4(b). In this case, no beneficial residual stress available from Melan's theorem because the axi-symmetrical residual stress is unable to deal with the situation that stress states at $(a, 0)$ and $(a, \pi/2)$ reach the elastic limit in both directions. The actual residual stress, however, can change with value of θ from negative elastic limit to positive elastic limit, hence it eliminates the effect of the reversed direction plasticity brought by points around $\theta = 0$ and then give the shakedown limit twice as that derived from Melan's theorem.

We will further illustrate that by comparing the stress trajectories at two controlling points in the deviatoric plane for the actual case and the case implied by Melan's theorem, again, for $n = 0$ and $n = 0.5$ respectively. Firstly, for $n = 0$, where the shakedown limit in the actual case is higher than that derived from Melan's theorem, in the actual case the magnitude of relevant stress on the deviatoric plane when the plate is subjected to the actual shakedown limit (point S in Figure 2(a)) are shown in Table 4, also the corresponding trajectories are shown in Figure 4(a.2). Additionally, when the plate is loaded under the shakedown limit implied by Melan's theorem and the actual shakedown limit, the specific comparison between the corresponding residual stress on the edge of the hole with respect to θ is shown in figure 4(b).

From both figures, in the actual case, residual stress varies from $(a, 0)$ to $(a, \pi/2)$, which enable larger shakedown limit to be obtained for $n = 0$

Table 4. Magnitude of elastic stress and residual stress on the deviatoric plane for n = 0, when plate is loaded under the actual shakedown limit.

Elastic stress	Magnitude	Residual stress	Magnitude
$\sigma_{\theta\theta}(a, 0)$ $= -\frac{2\sqrt{3}}{3}k$	$\lvert\sigma_{\theta\theta}(a, 0)\rvert_e$ $= \frac{2\sqrt{2}}{3}k$	$\sigma_{\theta\theta}^{res}(a, 0) = 0$	$\lvert\sigma_{\theta\theta}^{res}(a, 0)\rvert_e = 0$
$\sigma_{\theta\theta}(a, \pi/2)$ $= 2\sqrt{3}k$	$\lvert\sigma_{\theta\theta}(a, \pi/2)\rvert_e$ $= 2\sqrt{2}k$	$\sigma_{\theta\theta}^{res}(a, \pi/2)$ $= -\sqrt{3}k$	$\lvert\sigma_{\theta\theta}^{res}(a, \pi/2)\rvert_e$ $= \sqrt{2}k$

Secondly, for the case $n = 0.5$, the actual shakedown limit coincides with that derived from Melan's theorem. The same as above, when plates are loaded under the corresponding shakedown limit, the magnitude of relevant stress on the deviatoric plane in the actual loading case (point Q in Figure 2(a)), are shown in Table 5.

Table 4. Magnitude of elastic stress and residual stress on the deviatoric plane for n = 0.5, when plate is loaded under the actual shakedown limit.

Elastic stress	Magnitude	Residual stress	Magnitude
$\sigma_{\theta\theta}(a, 0)$ $= -\frac{2\sqrt{3}}{5}k$	$\lvert\sigma_{\theta\theta}(a, 0)\rvert_e$ $= \frac{2\sqrt{2}}{5}k$	$\sigma_{\theta\theta}^{res}(a, 0) = 0$	$\lvert\sigma_{\theta\theta}^{res}(a, 0)\rvert_e = 0$
$\sigma_{\theta\theta}(a, \pi/2)$ $= 2\sqrt{3}k$	$\lvert\sigma_{\theta\theta}(a, \pi/2)\rvert_e$ $= 2\sqrt{2}k$	$\sigma_{\theta\theta}^{res}(a, \pi/2)$ $= -\sqrt{3}k$	$\lvert\sigma_{\theta\theta}^{res}(a, \pi/2)\rvert_e$ $= \sqrt{2}k$

Additionally, the deviatoric stress trajectories for a load-unload cycle together with the relevant residual stress comparison on the edge of the hole are displayed in Figure 5(a.2) and Figure 5(b). Even though from the above two diagrams, the residual stresses are different at two controlling points in the actual case, but stress arose at other points except $(a, \pi/2)$ does not consider as the extreme stress state. It was found that, for the case $1/3 < n \leq 1$, both lower bound shakedown limit and the actual shakedown limit implied that two extremes of the loading cycle occur at the same point, $(a, \pi/2)$, and this also explained the coincidence of the two corresponding shakedown limits when $1/3 < n \leq 1$.

6. Varying Degrees of Load Reversal

The last example looked at in section 3 demonstrates that it is not just the state of stress at maximum applied load which matters, but also that at the opposite end of the loading cycle. The problems looked at so far have an applied load which implicitly varies between zero and σ_0, but in some cases the applied load may vary over a different range, say between $m\sigma_0$ and σ_0, where $-1 < m < 1$, so we will extend our considerations in section 3 to more general cases, defined in (m, n) space, where each varies over the interval $[-1\ 1]$. First, note that when the applied load is fully reversing $(m = -1)$ the state of applied stress fully reverses at every point, so that no residual state of stress can be beneficial.

Consider, next, a uniaxial state of stress $(n = 0)$, same as the above, there are two key controlling points in physical space, $(a, 0)$ and $(a, \pi/2)$, and two extremes of load range σ_0 and $m\sigma_0$ to consider. Hence, there will be four combinations that can be considered as possible

conditions for load extremes. The net state of stress at these four conditions are displayed in Table 2. Therefore, by applying Melan's theorem with axi-symmetrical auxiliary stress, in choosing an optimal residual stress field we are looking for the value of $\sigma_{\theta\theta}^{res}$ which minimises the absolute difference between any pair of entries in Table 2. We know, from reasoning in the last section, that when $m = 0$ (and presumably, close to zero) the biggest difference is between entries (2,1) and (2,2) in Table 2, and this continues to hold until $m < -1/3$. Otherwise, the limitation is between entries (1,2) and (2,2), and in this case we have that the optimal value for the residual stress is given by

$$2\sigma_{\theta\theta}^{res} = -3\sigma_0(m+1), \tag{20}$$

which gives a shakedown limit of $\sigma_0/k = 2\sqrt{3}/(3-3m) = 2\sigma_E/(1-m)$, where σ_E is the elastic limit.

Table 6. value of $\sigma_{\theta\theta}(a,\theta)$ at $\theta = 0$ and $\theta = \pi/2$ at two load extremes, for a uniaxial load ($n = 0$), when the applied load moves between σ_0 and $m\sigma_0$.

	$\theta = 0$	$\theta = \pi/2$
$m\sigma_0$	$-m\sigma_0 + \sigma_{\theta\theta}^{res}(a)$	$3m\sigma_0 + \sigma_{\theta\theta}^{res}$
σ_0	$-\sigma_0 + \sigma_{\theta\theta}^{res}$	$3\sigma_0 + \sigma_{\theta\theta}^{res}$

We now extend this reasoning to the case where both the remote loading is more general in character and the degree of load reversal is itself a parameter. The table just introduced now needs to be extended to include n in the general case. The net state of stress at load extremes for the general case is shown in Table 7.

Table 7. value of $\sigma_{\theta\theta}(a,\theta)$ at $\theta = 0$ and $\theta = \pi/2$ at load extremes, for general load combinations, when the applied load moves between σ_0 and $m\sigma_0$.

	$\theta = 0$	$\theta = \pi/2$
$m\sigma_0$	$\sigma_0 m(3n-1) + \sigma_{\theta\theta}^{res}$	$\sigma_0 m(3-n) + \sigma_{\theta\theta}^{res}$
σ_0	$\sigma_0(3n-1) + \sigma_{\theta\theta}^{res}$	$\sigma_0(3-n) + \sigma_{\theta\theta}^{res}$

When $n \leq 1/3$, which includes the case of uniaxial loading, $n = 0$, treated above, the biggest difference is between the entries (2,1) and (2,2) in Table 7, if $(3n-1)/(3-n) \leq m < 1$, otherwise it is between entries (1,2) and (2,2). Hence the optimal residual stress are:

$$-1 \leq n \leq 1/3 \begin{cases} 2\sigma_{\theta\theta}^{res} = -\sigma_0(m+1)(3-n), \\ \qquad\qquad -1 \leq m \leq \dfrac{3n-1}{3-n}; \\ 2\sigma_{\theta\theta}^{res} = -2\sigma_0(1+n), \\ \qquad\qquad \dfrac{3n-1}{3-n} < m \leq 1 \end{cases} \tag{21}$$

and the corresponding shakedown limits $\sigma_0/k = \lambda$ are:

$$-1 \leq n \leq 1/3 \quad \begin{cases} \lambda = \dfrac{2\sqrt{3}}{(3-n)(1-m)} = \dfrac{2}{1-m}\sigma_E, \\ \qquad\qquad -1 \leq m \leq \dfrac{3n-1}{3-n}; \\ \lambda = \dfrac{\sqrt{3}}{2-2n}, \\ \qquad\qquad \dfrac{3n-1}{3-n} < m \leq 1. \end{cases} \tag{22}$$

When $n > 1/3$, for $m < 0$ the extremes of the stress state in the loading cycle occur at the same point, i.e., at $(a,\pi/2)$, hence the biggest difference is between entries (1,2) and (2,2). physically when $m > 0$, we notice that at both external extremes, $(\sigma_0, m\sigma_0)$, the stress state at

$\theta = 0$ has the same sign as that at $\theta = \pi/2$ but is of smaller magnitude. Therefore, the biggest difference is between entries (1,1) and (2,2). The optimal residual stress is:

$$1/3 < n \leq 1 \quad \begin{cases} 2\sigma_{\theta\theta}^{res} = -\sigma_0(m+1)(3-n), \\ \qquad\qquad -1 \leq m \leq 0; \\ 2\sigma_{\theta\theta}^{res} = \dfrac{n-3}{3-n+3mn-m}\sigma_0, \\ \qquad\qquad 0 < m \leq 1. \end{cases} \tag{23}$$

and the corresponding shakedown limits are:

$$1/3 < n \leq 1 \quad \begin{cases} \lambda = \dfrac{2\sqrt{3}}{(3-n)(1-m)} = \dfrac{2}{1-m}\sigma_E, \\ \qquad\qquad -1 \leq m \leq 0; \\ \lambda = \dfrac{2\sqrt{3}}{3-n-3mn+m}, \\ \qquad\qquad 0 < m \leq 1. \end{cases} \tag{24}$$

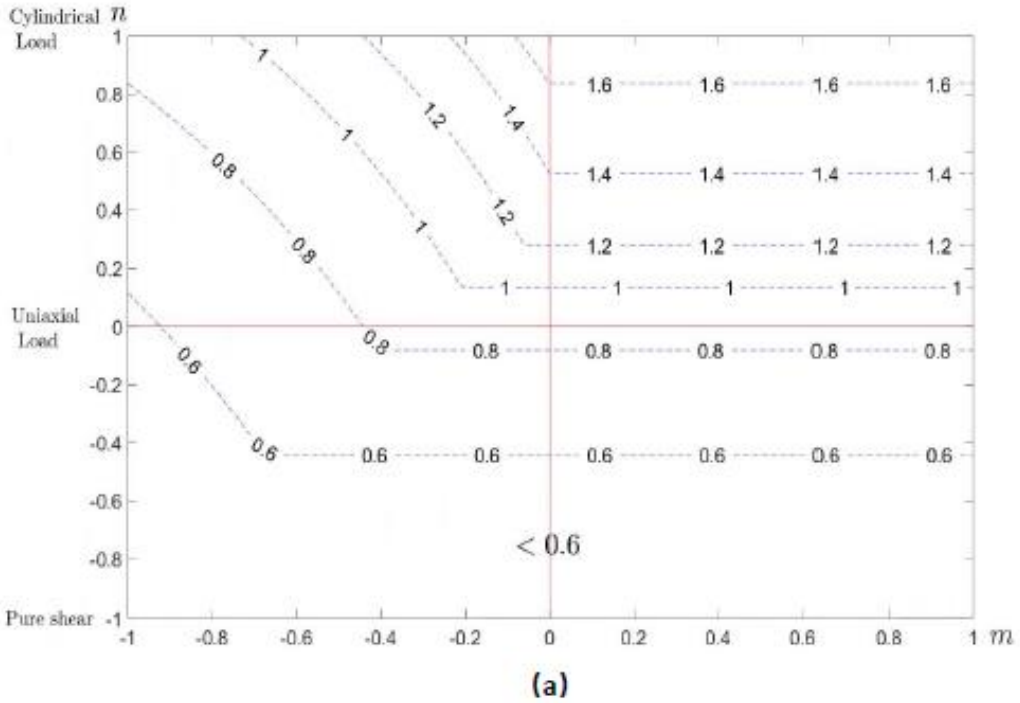
Notice that when (m,n) is (1,1), the shakedown limit was calculated as $\lambda = \infty$. However, in elastic perfectly plastic material, stress included secondary stress is bounded by the elastic limit. Therefore, the external load of σ_0 is limited by the following inequality:

$$\sigma_0(3n-1) - \sqrt{3}k \leq \sqrt{3}k, \tag{25}$$

or $\lambda \leq \frac{2\sqrt{3}}{3-n}$ which is smaller than $\frac{2\sqrt{3}}{3-n-3mn+m}$ for the range $1/3 < n \leq 1$ and $0 < m \leq 1$. And when (m, n) lies in this range, failure will be resulted by the secondary plastic strain instead of by the accumulated plastic strain. To summarize the above, the limitations of the external load for $1/3 < n \leq 1$ are:

$$1/3 < n \leq 1 \quad \begin{cases} \lambda = \dfrac{2\sqrt{3}}{(3-n)(1-m)} = \dfrac{2}{1-m}\sigma_E, \\ \qquad\qquad -1 \leq m \leq 0; \\ \lambda = \dfrac{2\sqrt{3}}{3-n}, \\ \qquad\qquad 0 < m \leq 1. \end{cases} \tag{26}$$

The contour plot of shakedown limits or applied load limits normalized by k, is shown in Figure 7(a) according to equations (22) and (24). Values of λ for special cases (Pure Shear, Uniaxial Load and Cylindrical load) are shown in Figure 7(b) with respect to m.



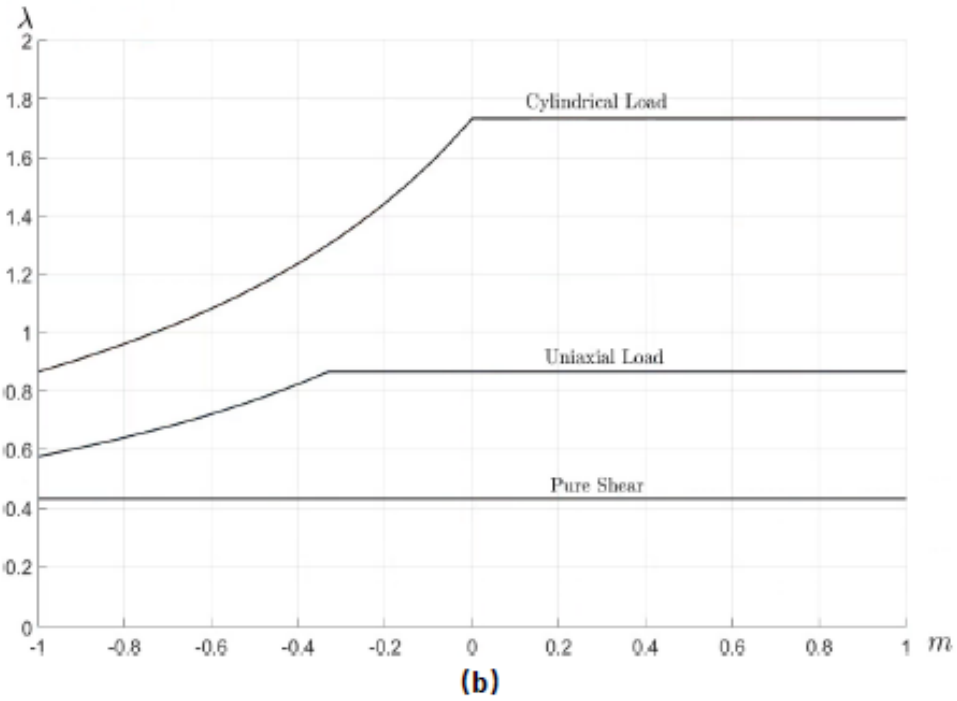


Figure 7. values of normalized shakedown/external load limits (λ) derived for Melan's theorem: (a) Contour plot of full (m, n) space, (b) for special case, pure shear, uniaxial load and cylindrical load $(n = -1,0,1)$

Apart from the above analysis using Melan's theorem, We also extend our FEA to the full (m,n) space. Firstly, for the range of m from -1 to 0, which includes the case we analysed in section 3, the numerical value of the shakedown limit proved to be consistent with

$$\lambda = \frac{2\sqrt{3}}{(3-n)(1-m)} = \frac{2}{1-m}\sigma_E. \tag{27}$$

Notice that this is the shakedown limit calculated by using entries (1,2) and (2,2) in Table 7. And again, this implies that in the actual case, two extremes of the loading cycle occur at the same point, hence the reason that explained under a certain range of n, lower bound shakedown limit is unable to track the actual shakedown limit in section 3 still holds. In other words, the coincidence between the shakedown limit in the actual case and that derived from Melan's theorem happens when two extremes during the cyclic loading occur at the same point. The range for the above coincidence happening is characterized by the first range of (m,n) in equation (22) and equation (24), i.e., $-1 \leq n \leq 1/3$ and $-1 \leq m \leq \frac{3n-1}{3-n}$; $1/3 < n \leq 1$ and $-1 \leq m \leq 1$, the above also can be rewritten as $-1 \leq m \leq 0$ and $n \geq \frac{3m+1}{3+m}$.

We need to be aware of the secondary plastic flow when considering the case $0 < m \leq 1$. As mentioned above, in this case, equation (24) does not continually provide the shakedown limit because the residual stress implied at $(a, \pi/2)$ is larger than the elastic limit for $0 \leq m \leq 1$ when $0 < m \leq 1$. Therefore, the maximum external load will be the shakedown limit implied by equation (23),

$$\lambda = \frac{2\sqrt{3}}{3-n}. \tag{28}$$

The maximum loads found from FEA are consistent with equation (26) by showing non-convergency at some internal points when the applied load is equal or greater than that

indicated in equation (25), and no accumulated plastic strain when the applied load is below that value. Therefore, for $0 < m \leq 1$, lower bound theorem can successfully calculate the actual shakedown limit when the axi-symmetrical residual stress at the edge of the hole equals to the elastic limit in the reversed direction, i.e., $-\sqrt{3}k$, which happens in the range $1/3 < n \leq 1$, indicated in equation (24).

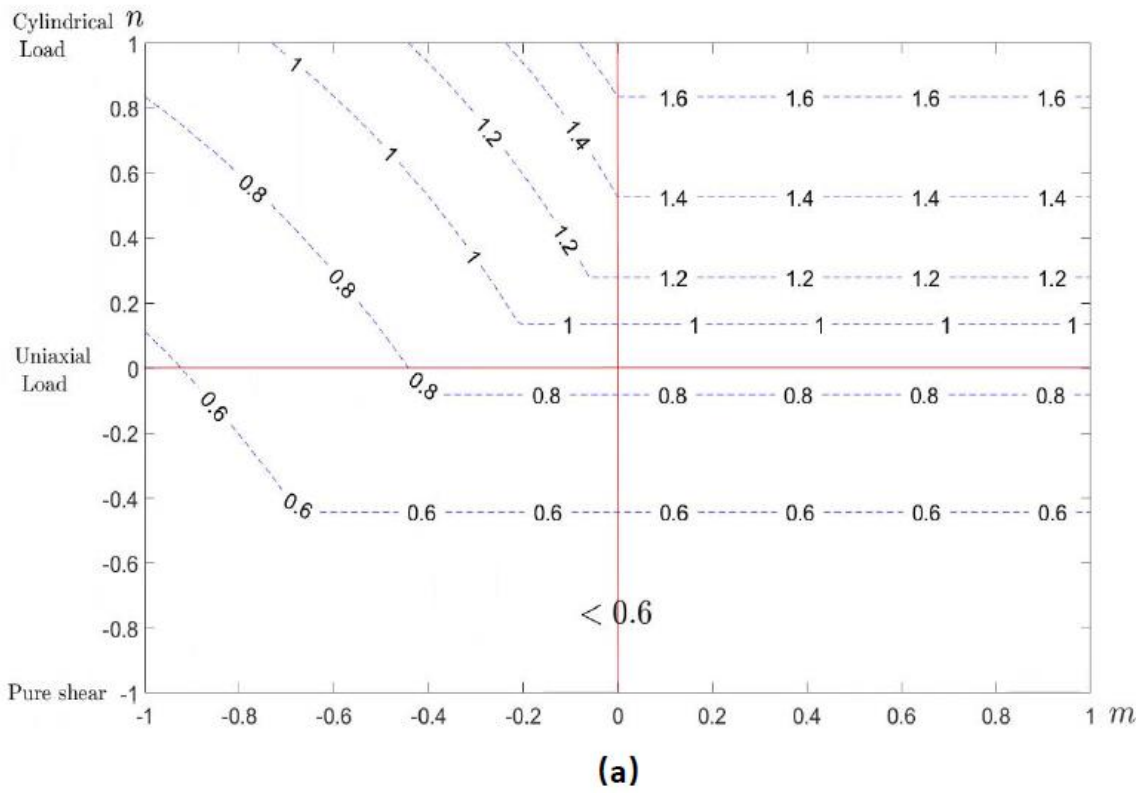
To summarize the above, from FEA, the estimated actual shakedown limits are the following for the full (m, n) space:

$$\begin{cases} \lambda^{actual} = \dfrac{2\sqrt{3}}{(3-n)(1-m)} = \dfrac{2}{1-m}\sigma_E, & -1 \leq m \leq 0; \\ \lambda^{actual} = \dfrac{2\sqrt{3}}{3-n}, & 0 < m \leq 1. \end{cases} \tag{29}$$

the above have been plotted in contours, in Figure 8(a). Additionally, the comparison between the actual shakedown/applied load limits and those calculated by Melan's lower bound, represented by the difference $e = (\lambda^{actual} - \lambda)/\lambda^{actual}$, is shown in Figure 8(b). The space of the coincidence is:

$$\{-1 \leq m \leq 0, n \geq \frac{3m+1}{3+m}\} \cup \{0 < m \leq 1, n \geq 1/3\}. \tag{30}$$

This space was indicated as the region marked by '$e = 0$'. Lastly, from the diagram, we can conclude that for the entire range of m, the shakedown limits produced by Melan's lower bound are getting closer to the exact solution with the increase of the value of n.



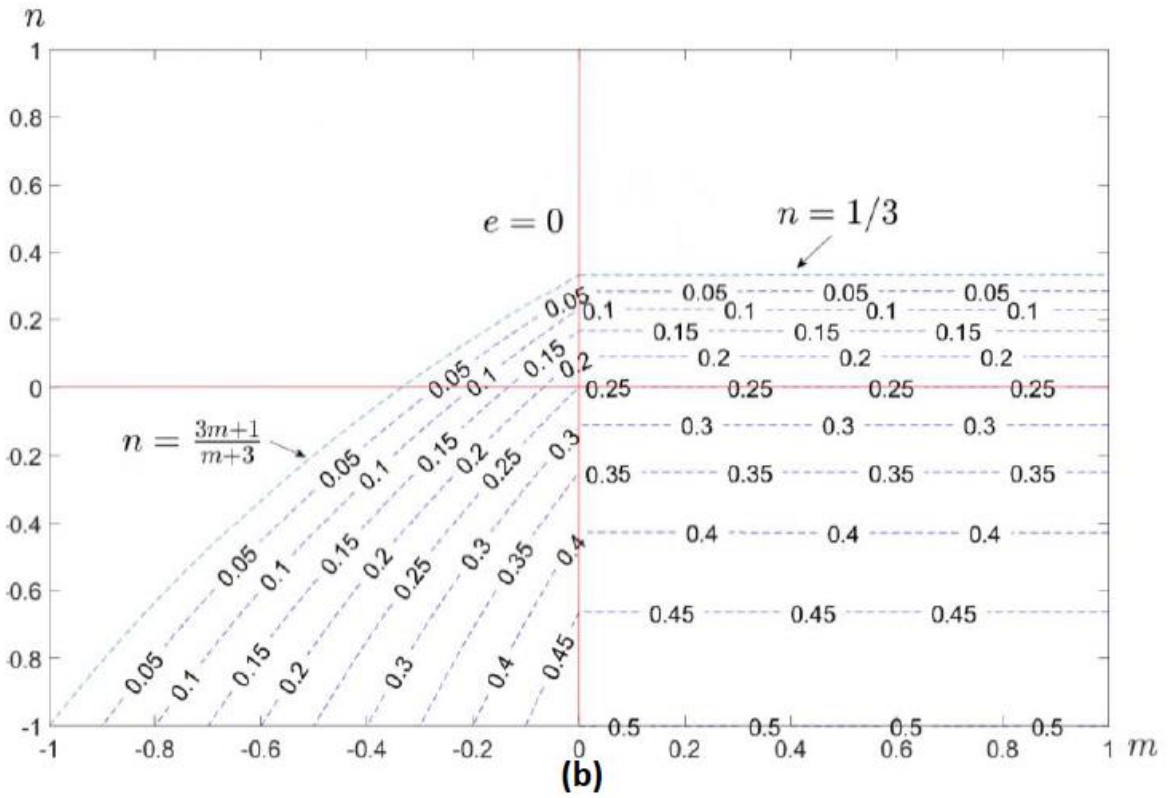


Figure 8.(a) values of normalized shakedown/external load limits (λ^{actual}) derived from finite element mode, (b) values of the difference e between the shakedown/external load limits found by Melan's theorem and actual case.

7. Conclusion

The paper provides valuable insight into the implementation of Melan's lower bound shakedown theorem applied to an accessible problem, viz. a circular hole in an infinite plate subject to an arbitrary remote stress. The often practically encountered limiting factors arising in what is essentially a "min-max" problem - finding the maximum value of the state of stress over the load cycle, and choosing the optimal residual stress state to achieve it - is done in way which minimizes the amount of mathematics needed.

The shakedown limit calculated by Melan's theorem is shown in equations (22) and (24), also indicated in Figure 7; and the actual shakedown limit predicted by FEA is shown in equation (29), plotted in Figure 8. In all the cases, the actual shakedown limit implies that the extremes of the loading cycle occur at the same point, $(a, \pi/2)$, so when the shakedown limit calculated using Melan's theorem implies the same, Melan's theorem can succesfully predict the actual shakedown limit. The range of the coincidence between the lower bound shakedown limit and the actual shakedown limit is characterized by equation (30).

3.3 Limitations of the paper

Melan's theorem of shakedown is a significant principle in structural mechanics and plasticity, providing conditions under which a structure subjected to cyclic loading will adapt without further plastic deformation. Despite its utility, several limitations constrain its application.

Firstly, the material behavior in Melan’s analysis assumes a linear elastic-perfectly plastic material. However, in the real world, complex material behaviors such as strain hardening and strain rate dependence need to be considered.

Secondly, Melan’s theorem doesn’t consider the residual stresses or pre-strain that remain in the material. These factors can significantly impact the accuracy of shakedown predictions. Additionally, Melan’s theorem is based on the principle of superposition, which means geometric non-linearity is not considered, and this property also affects the shakedown response.

Time-dependent effects like creep and fatigue are also excluded from Melan's theorem. In scenarios where structures are subjected to long-term loading or high-cycle fatigue, these effects are crucial, and their exclusion can lead to inaccurate predictions. Melan’s theorem is also typically used in simplified cyclic load scenarios, but in the real world, load responses can be very complicated.

The paper provides examples of using Melan’s theorem to find the shakedown limit by proposing an axi-symmetrical residual stress field. However, such a residual stress field changes from case to case. In reality, Melan’s lower bound theory cannot represent the actual shakedown response; its role is to act as a criterion to give engineers a quick check on structural stability.

Reference

[1] H. Bleich, “Über die bemessung statisch unbestimmter stahltragwerke unter berücksichtigung des elastisch-plastischen verhaltens des baustoffes,” *Bauingenieur*, vol. 19, no. 20, pp. 261–266, 1932.

[2] F. Bleich and E. Melan, *Die gewöhnlichen und partiellen differenzengleichungen der baustatik*. Springer-Verlag, 2013.

[3] W. Koiter, “A new general theorem on shakedown of elastic-plastic structures,” *Proc. Koninkl. Ned. Akad. Wet. B*, vol. 59, pp. 24–34, 1956.

[4] J. A. König, *Shakedown of elastic-plastic structures*. Elsevier, 2012.

[5] R. Hamilton, M. Muscat, and J. Boyle, “Shakedown analysis for complex loading using superposition. j,” *Strain Analysis*, vol. 37, no. 5, pp. 399–411, 2002.

[6] P. Fuschi, A. A. Pisano, D. Weichert, *et al.*, *Direct methods for limit and shakedown analysis of structures*. Springer, 2015.

[7] M. Muscat, R. Hamilton, and J. Boyle, “Shakedown analysis for complex loading using superposition,” *The Journal of Strain Analysis for Engineering Design*, vol. 37, no. 5, pp. 399–412, 2002.

[8] C. Polizzotto, “On the conditions to prevent plastic shakedown of structures: Part i—theory,” 1993.

[9] E. Melan, “Der spannungszustand eines mises-henckys chen kontinuums bei veraderlicher belastung,” *Sitzber Akad. Wiss. Wien Iia*, vol. 147, pp. 73–87, 1938.

[10] J. R. Barber, *Elasticity*. Springer, 2002.

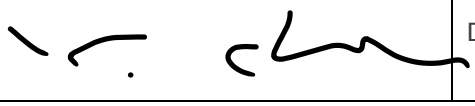
Statement of Authorship for joint/multi-authored papers for PGR thesis

To appear at the end of each thesis chapter submitted as an article/paper

The statement shall describe the candidate's and co-authors' independent research contributions in the thesis publications. For each publication there should exist a complete statement that is to be filled out and signed by the candidate and supervisor **(only required where there isn't already a statement of contribution within the paper itself).**

Title of Paper	Shakedown of a plate with a circular hole: An educational problem
Publication Status	✓Published □ Accepted for Publication □Submitted for Publication □Unpublished and unsubmitted work written in a manuscript style
Publication Details	Chen, Y., & Hills, D. A. (2023). Shakedown of a plate with a circular hole: An educational problem. The Journal of Strain Analysis for Engineering Design, 03093247231163205.

Student Confirmation

Student Name:	Yifeng Chen		
Contribution to the Paper	Perform essential FE analysis. Perform Theoretical deduction. Write up all the paper.		
Signature		Date	16/04/2024

Supervisor Confirmation

By signing the Statement of Authorship, you are certifying that the candidate made a substantial contribution to the publication, and that the description described above is accurate.

Supervisor name and title: Prof. John Huber		
Supervisor comments		
Signature 	Date	17/4/24

This completed form should be included in the thesis, at the end of the relevant chapter.

4. Finite height-crack problem

4.1 Introduction

Unlike the circular hole problem discussed in the previous chapter, a crack or a sharp notch is considered as a ‘singular’ feature in engineering design. This is because stress concentrates around it, leading to infinitely singular stress in elastic analysis. The method often used for analyzing stress around a singular feature is the asymptotic method, such as Williams’ solution, where stress is characterized as the product of the stress intensity factor and corresponding eigenfunctions. The 'plane with a defect' problem in this section is chosen to discuss a semi-infinite elastic plane containing a defect with singular features. However, instead of a general crack or sharp notches, which are extensively reviewed in the literature (see Section 2), we focus on a crack with a finite height, which is a sharp crack that has a finite height at its tip to form a ‘letterbox’ shape. This finite height crack contains two singular features and the interaction of the stress field around these two singular features may affect the mechanical behavior, specifically where the crack will initiate.

Before applying any analytical tool to this problem, we should start by discussing some key features of the finite height crack. First, the finite height of a crack is a local feature; hence, its influence on areas remote from the crack is minimal. This also means that the stress field will eventually converge to that of a sharp crack problem at an infinitely far distance. Additionally, the distance required for this convergence decreases with an increase in the applied load. This is because a heavier load pushes the yield violation front further away from the crack tip, making the sharp crack and finite crack appear more similar. Therefore, for a certain amount of load, the finite crack problem can be considered similar to the sharp crack problem. In this case, if crack initiation occurs, it will likely happen at the middle plane between the two notch corners, just as with a sharp crack. However, the load value for this sharp crack approximation remains unknown. To determine this load value, we compare the elastic

violation front (or the approximated plastic front) of the finite height crack, found via finite element method, to the analytical elastic violation front of the sharp crack under the same load. If the two closely match, we consider this approximation valid.

Secondly, if the applied load is very light, the interaction of the two notch corners is considered negligible, effectively making them two independent features. The load limit for the two notch corners to be considered as independent features is approximated by comparing the yield condition violation front with the geometric length feature, the crack height d. If the yield violation front is within 1/10 of the crack height, then the two notch corners can be considered independent, and fracture failure will likely occur at one of the notch corners.

Lastly, if the applied load lies between the 'crack approximation' limit and the 'independent notches' limit, this represents an intermediate case. In such a scenario, fracture failure will initiate somewhere between the mid-plane and the notch corners. This specific discussion is presented in the following paper.

4.2 Paper: Investigation of stress state around a finite-height crack[2]

Investigation of stress states around a finite-height crack

Yifeng Chen[a,] , George G. Adams[b] , David A. Hills[a3]

[a] Department of Engineering Science, University of Oxford, Parks Road, OX1 3PJ Oxford, United Kingdom

[b] Department of Mechanical Engineering, Northeastern University, Boston, MA 02115, USA

Abstract

This paper is concerned with the analysis of a crack that has a finite-height at its crack tip, loaded under Mode 1 and 2 loading. The stress field around the "crack-height" region has been analysed and local Williams' eigensolutions collocated using the H-integral. Results of the analysis help us to predict which one of the three possible places that fracture failure could occur is most likely, i.e., (1) at the middle plane of the crack tip collinear with the sharp crack problem), (2) at the "notch corner" or (3) at the intermediate plane between the notch corner and the middle plane (intermediate state). A practical example of an infinite plane with a rectangular shaped crack has also been shown to demonstrate the practical use of the results of this paper.

1. Introduction

A notch loaded under both mode 1 (tensile) and mode 2 (shear) loading, induces asymptotic stress fields when elastic which are described by Williams' solution [1], with explicitly known eigenvalue terms λ_1 and λ_2, in mode 1 and 2 loading respectively. The stress state can be represented under plane strain conditions by:

$$\begin{gathered}\sigma_{ij}(r,\theta) = K_1 r^{\lambda_{1N}-1} f_{ij}^{I}(\theta) + K_2 r^{\lambda_{2N}-1} f_{ij}^{II}(\theta) \\ \sigma_{zz} = v(\sigma_{rr} + \sigma_{\theta\theta}),\end{gathered} \tag{1}$$

where K_n are the stress intensity factors for a notch in mode *n* loading and can be found from:

$$\begin{aligned} K_1 &= \lim_{r\to 0} \sqrt{2\pi} r^{1-\lambda_{1N}} \sigma_{\theta\theta} \qquad \text{on } \theta = 0 \\ K_2 &= \lim_{r\to 0} \sqrt{2\pi} r^{1-\lambda_{2N}} \sigma_{r\theta} \qquad \text{on } \theta = 0 \end{aligned} \tag{2}$$

where $\theta = 0$ indicates the bisector of the notch and $f_{ij}^{n}(\theta)$ are the related eigenfunctions in mode *n* loading (listed in Hills and Dini [2]) scaled so that $f_{\theta\theta}^{I}(0) = 1$ and $f_{r\theta}^{II}(0) = 1$, and v is the Poisson's ratio. In this paper, all situations are evaluated in the plane strain condition, with $v = 0.3$.

To distinguish the general notch from a crack, we use the subscript *C* for the crack situation and *N* for the notch. When the angle of the notch becomes 2π (Figure 1. (a)), the notch will become a sharp crack with $\lambda_{1N} = \lambda_{1C} = 1/2$ and $\lambda_{2N} = \lambda_{2C} = 1/2$.

When the r term goes to zero in equation (1), the stresses will tend to infinity, which is unrealistic. Therefore, plastic deformation will inevitably occur near the crack tip. The plastic front in this paper is approximated by the contour that just violates the yield stress when

[2] Chen, Y., Adams, G. G., & Hills, D. A. (2023). Investigation of stress states around a finite-height crack. International Journal of Solids and Structures, 284, 112499.

[3] Corresponding author: *Tel*.: +44 1865 273811; *E-mail address*: David.Hills@eng.ox.ac.uk (David Hills).

assuming linear elastic behavior throughout. In terms of Von Mises' yield criterion, this region is expressed as points satisfying the following equation:

$$\sigma_v^2 = \sigma_{rr}^2 + \sigma_{\theta\theta}^2 + \sigma_{zz}^2 - (\sigma_{rr}\sigma_{\theta\theta} + \sigma_{\theta\theta}\sigma_{zz} + \sigma_{rr}\sigma_{zz}) + 3\sigma_{r\theta}^2 \geq \sigma_Y^2, \qquad (3)$$

where σ_Y is the yield stress in simple tension.

The true position of the plastic front could be redefined by numerical analysis, in which its shape depends on the strain hardening rate [3]. We will not consider this behavior due to its complexity and its dependency on details of plastic behavior. However, under the assumption of elastic perfectly plastic material behavior, in each case, for a semi-infinite notch or crack only, the elastic perfectly plastic condition will generate a self-similar plastic front. A comparison of the position of the normalized plastic front between the infinitely elastic problem with violation, and elastic perfectly plastic case, for a sharp crack loaded in mode 1, is shown in Figure 2. In the elastic perfectly plastic case, the normalized plastic front was found by the finite element method. Notice that the origin of the graph is located at the crack tip, and only the upper half of the front shape is shown due to the symmetry. From now on, we will focus on linear elastic analysis only; we shall discuss how the result changes when the material is elastic perfectly plastic in later sections.

Equations (1), (2) and (3) enable the position and shape of the yield front to be estimated. The implicit assumption in Williams' solution is a "perfectly sharp" crack which will experience an infinite stress in linear elastic stress analysis. In fact, inelastic deformation leads to a relaxation of crack tip stresses caused by the yielding phenomenon at the sharp crack tip. Therefore, the local stresses are constrained by the yield strength of the material. This implies that the elastic stress analysis becomes increasingly inaccurate as the inelastic region at the sharp crack tip becomes large and linear elastic fracture mechanics (LEFM) is no longer useful for predicting the field equations.

If we zoom in on the crack tip, it is not necessarily sharp. The most common approximation used in numerous works is an elliptical shaped crack tip, and the stress field around it has been discussed in [4]. Another approximation is a “finite-height crack” depicted in Figure 1 (b), where a finite-height, $2d$, will present between two right-angle ’V-notch’ corners. The nature of the crack tip depends on the scale of observation. Previous works, such as Budarapu et al. [5], have shown that in materials like silicon, the breakage of bonds can lead to a finite height at the crack tip. Although they used a multiscale analysis based on a discrete material model, at a certain observation scale, a finite-height crack tip approximation is better than a sharp crack analysis in continuum analysis. Additionally, when the specimen is loaded under mode 1 conditions, experimental results in Budarapu et al. [5] do not exhibit symmetrical Mode 1 behavior of the material around the crack-tip region. This asymmetry could be caused by either the perturbation of random molecule positions or the disturbance of the stress field due to the finite crack height.

Another mechanism that can result in a blunt crack tip is stress corrosion, which occurs when a material dissolves under stress near the sharp crack tip. This phenomenon has been previously discussed in Creager and Paris [6], but it should be noted that the analysis primarily focused on the assumption of an elliptical-shaped crack tip. In this paper, however, we present an analysis exploring an alternative possibility - a rectangular-shaped blunt crack.

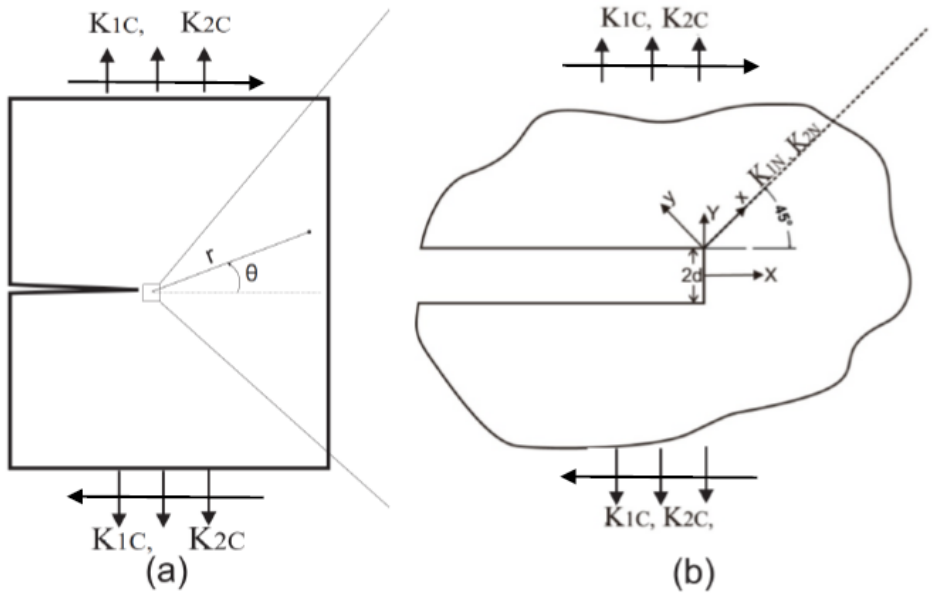


Figure 1: Illustration of crack problems with a finite-height.

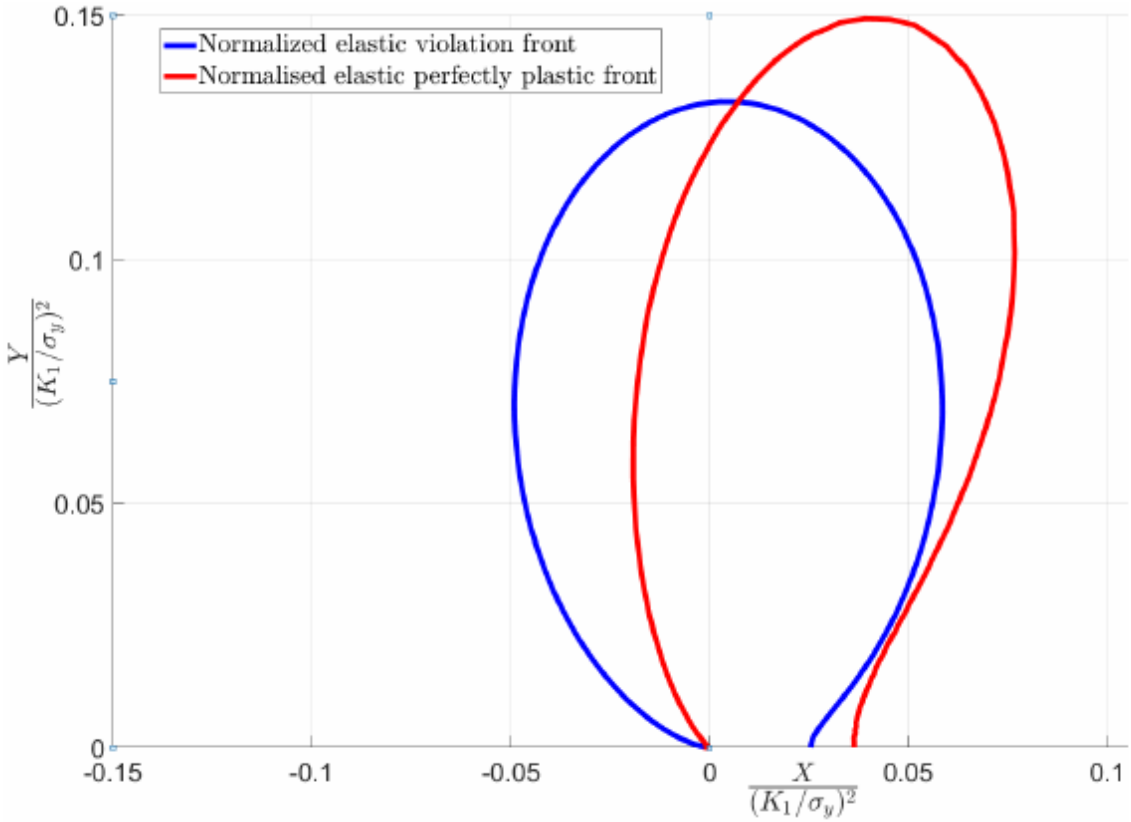


Figure 2: The comparison between the normalized elastic violation front and the normalized elastic perfectly plastic front.

The geometry of the finite-height crack was first studied by Rice [7]. The finite-height crack is constructed by inserting a rectangular rigid-plastic strip between the upper and lower halves of the crack plane. The purpose is to understand the nature of the end region near a sharp crack tip. Later, Andersson and Bergkvist [8] pointed out that Rice's model does not achieve the desired fracture criterion and crack geometry. Broberg [9] suggested another model by replacing the inserted strip with one that has the desired material property. In Andersson and Bergkvist [8], this model was further discussed by introducing a layer of thickness 2d, interrupted in the interval $-c_0 < x < c_0$, inserted between two semi-infinite media. The layer has been modeled as a continuous row of springs with a desired material stress-strain relationship. The purpose of this modeling approach is to investigate the non-linear force-deformation relationship and propose conditions for crack-tip instability.

The motivation for modeling non-linear cracks with an interrupted layer arises from both mathematical convenience and experimental observations. The interrupted layer acts as a transition zone between the crack tip and the surrounding material, allowing for a more tractable mathematical representation of the crack behavior. Furthermore, experimental evidence suggests that the plastic region often extends in a thin layer ahead of the crack tip.

The above work still focuses on 'building' a finite-height crack model to reveal the non-linear properties at the crack tip of a sharp crack. However, in this paper, we discuss the 2D plane problem that naturally contains a rectangular-shaped crack. This geometry was previously studied by Fett [10]. Apart from a finite-height crack, it also introduces a small one-dimensional crack located at the mid-plane, as shown in Figure 3(a). The geometry, similar to that proposed by Fett, has also been previously studied by Neal [11], who presented mathematical modeling for rectangular cutouts with a small one-dimensional crack located at the mid-plane of the left and right sides of the cutout. We also note that Rice [7] obtained results for the problem presented in Fett[10], by setting to zero the finite crack height. However, the

works constrain the location of crack propagation. Cracks can initiate at any position along the crack height. Golecki and Suzdalnitsky [12] also studied the finite-height crack in the form of a step notch, but local load was added perpendicular to the finite-height, instead of remote, global load.

Certainly, the presence of the crack height will distort the stress states proposed by equation (1), which leads to the main purpose of this paper: to compare the stress fields produced by the same applied load, between a finite-height crack and a sharp crack, and to quantify the stress states near one of the "notch corners". Note that when considering singularities, contour integral methods are often used to evaluate stress intensity factors (e.g. Sanders' integral [13] and J-integral [14]). All the foregoing integrals apply to a crack. In this paper, a contour integral method named the "H-integral" method [15], which is suited to numerical results, has been applied to compute the stress intensity factors near the right angle "notch corners".

The distorted stress states will give new possible places for fracture failure initialization. Those can be classified as three types: (a) At the middle plane of the crack tip (colinear with the sharp crack problem), (b) At the notch corners, (c) At an intermediate point between a notch corner and the middle plane of the crack tip (intermediate type). Those locations are also depicted in Figure 3. The conditions for the above three types of fracture failure initialization will also be explored in this paper.

Results of this paper will then be applied to an example problem, i.e. a mechanical part that has a rectangular-shaped hole, to demonstrate how the stress evaluated near the "notch corners" where the state of stress at remote points, $r >> d$, approximates the sharp crack fields under K_{1C} and K_{2C} loading and hence to derive the possible places for fracture failure initialization.

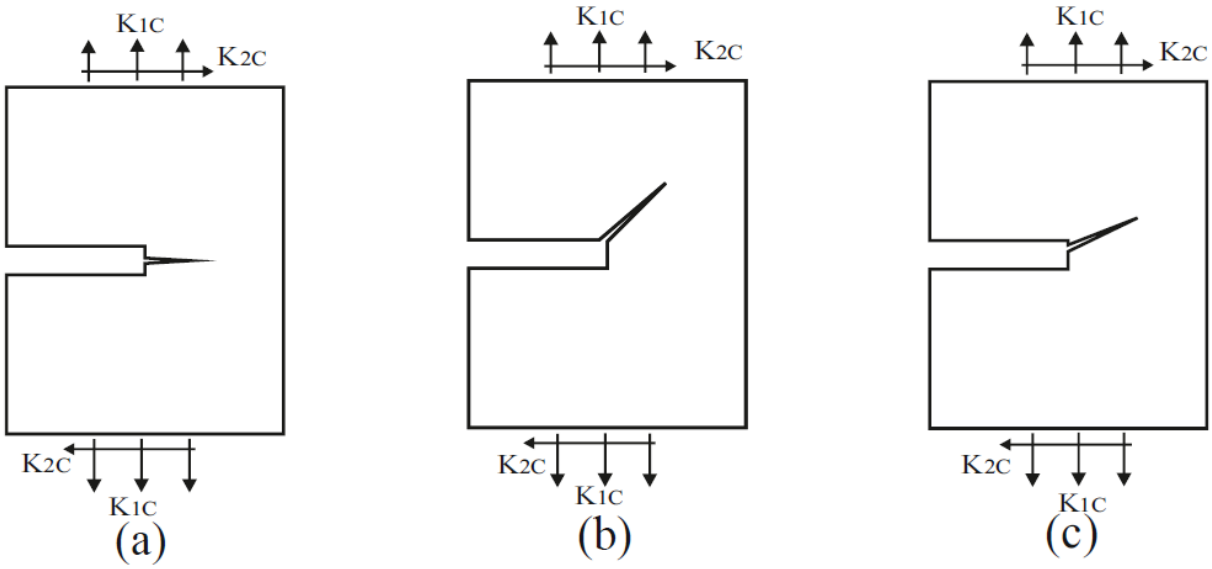


Figure 3: Illustration of possible crack initialization places: (a) at the middle plane, (b) at the notch corner, (c) intermediate type.

2. Heavy load case: sharp crack problem approximation

In the finite-height crack problem shown in Figure 1(b), the presence of the crack height can be considered a "local" geometric feature, so the influence of it will be insignificant at remote distances from the crack tip. Stress states of the finite-height crack problem will, therefore, eventually converge to that of the sharp crack problem as $r/d \to \infty$. For further analysis, the origin of the coordinate system of this problem is set at the middle point between the two notch corners. Additionally, the minimum distance from the origin required for this convergence to occur decreases with an increase of the applied load. This is because when the load increases, the yield condition violation front will move further from the crack tip to a larger value of r/d where the two problems get closer to one another.

Therefore, the influence of the finite-height of the crack on the near tip stress field will be less significant with heavier remote loads, represented by the stress intensity factors K_{1C} and K_{2C}

applied far from the crack tip. When those remote loads reach a certain level, the near crack asymptotic behaviour of the process zone can be considered to be sufficiently close to that of the sharp crack problem and fracture failure will be initialized at the middle plane, depicted in Figure 3(a). To quantify the loading required for such an approximation, the problem was analysed using the commercial finite element program ABAQUS, and we characterized the remote loading by the non-dimensional quantity L, i.e.,

$$L^2 = N_1^2 + N_2^2 \qquad (4)$$

where

$$N_1 = \frac{K_{1C}}{\sigma_Y \sqrt{d}}; \qquad N_2 = \frac{K_{2C}}{\sigma_Y \sqrt{d}} \qquad (5)$$

The displacements of remote points of the finite-height crack will also eventually converge to those deduced by the Williams' solution for a sharp crack. Therefore, for a chosen stress intensity factor, the sharp crack displacements at a remote distance can be used as boundary conditions in a Finite Element Analysis (FEA). The FEA experiments have been conducted by the controlling parameter L, and simulating within the "semi-infinite" plane problem the ratio of maximum radius of the model to the crack half-height is chosen to be 200, shown in Figure 1.

To judge whether the stress states around the finite-height crack can be considered sufficiently close to that of the sharp crack, the yield condition violation front shapes of both problems are compared. For the finite-height problem, the yield condition violation front was computed numerically by finding the minimum value of the radius that violates the Von Mises' yield criterion for each angle θ from $-\pi$ to π. For the sharp crack problem, the elastic violation front shape can be computed analytically in terms of Williams' solution together with violation of

the yield criterion. The discrepancy between shapes of the yield condition violation front between the two problems has been evaluated by the Mean Squared Fractional Error (MSFE):

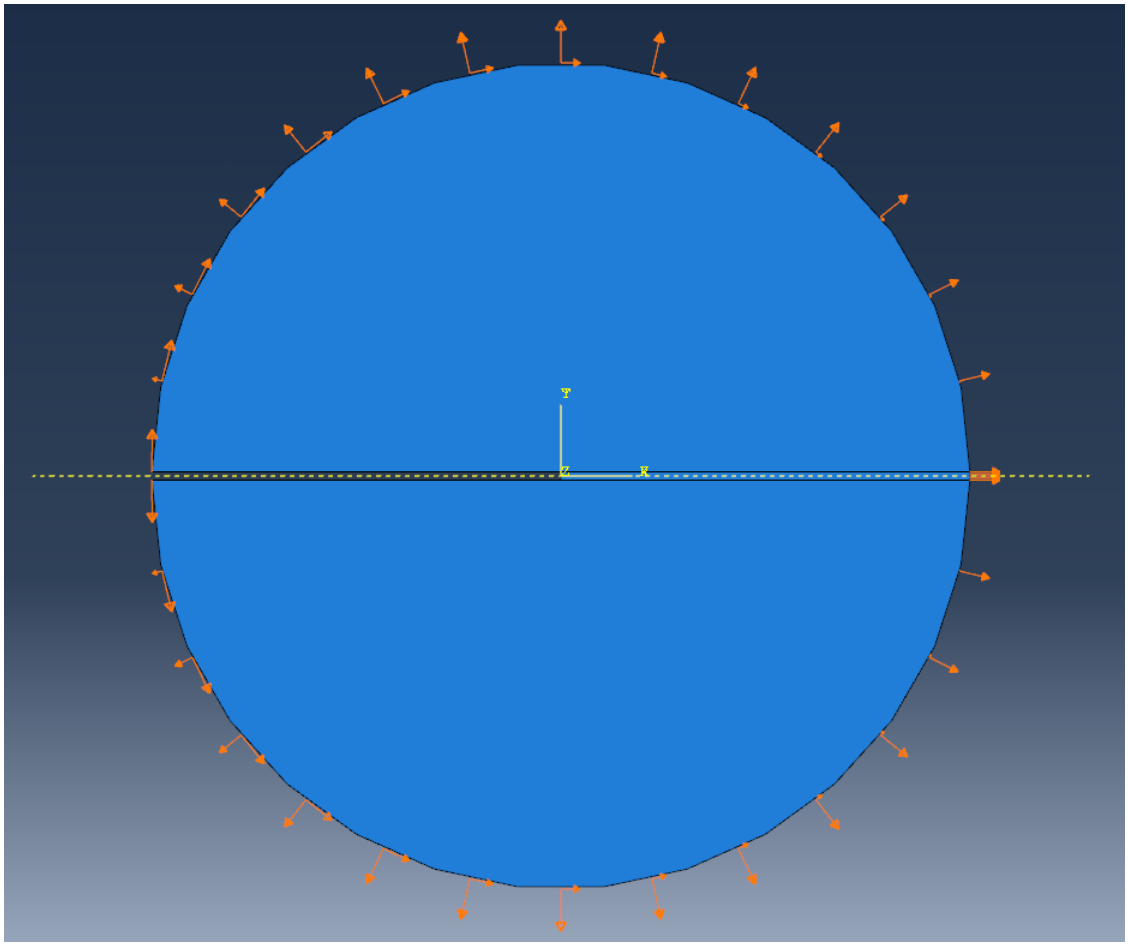


Figure 4: Illustration of finite element model with remote displacement added as boundary conditions.

$$MSFE = \frac{1}{n}\sum_{i=1}^{n}\frac{\left(r_{pFE}(\theta_i) - r_{pC}(\theta_i)\right)^2}{r_{pC}(\theta_i)^2} \tag{6}$$

where n discrete points at different direction θ_i are included in the calculations, $r_{pFE}(\theta_i)$ is the front radius obtained at θ_i by the numerical method, and $r_{pC}(\theta_i)$ is the analytical elastic violation front at the same angle with $r_{pFE}(\theta_i)$ for a sharp crack. Notice that points which give $r_{pC}(\theta_i) = 0$ (this also means no plastic radius, i.e., in mode 1 case at $\theta_i = \pm\pi$, see Figure 2.)

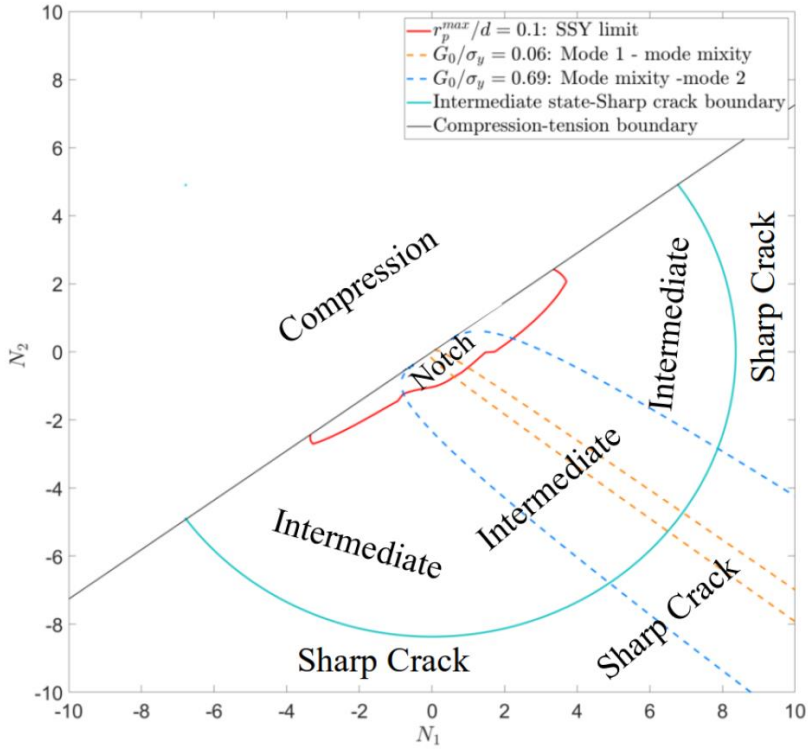
are excluded from this calculation because those points will give an infinite MSFE. If MSFE is smaller than 0.02, the two plastic front shapes, as well as their stress states near the finite-height crack tip, will be assumed to be sufficiently close.

Five sets of numerical experiments with values of $\frac{N_2}{N_1}$ equal to 0, 0.33, 0.5, 0.67 and infinity have been used to find the critical minimum value of L such that MSPE is smaller than 0.02. All numerical results indicate that this minimum value of L should be roughly 8.4, and $L = 8.4$ has been plotted in Figure 2 as the green line (all other lines in Figure 2 will be introduced in the later sections). Detailed comparison between the elastic violation fronts of the sharp crack and that the finite-height crack, for $\frac{N_2}{N_1}$ equals to 0, 0.5, and infinity are shown in Figure 3. The left-hand side of the Figure 3 ((a), (c), (e)) shows elastic violation front shapes with specific positions on the plate for both the sharp crack and the finite-height crack problem under the same loading for various mode mixity. Bearing in mind that the front shape is centrally symmetric, hence only the upper half of the FE model are compared. The right-hand side of the Figure 3 ((b), (d), (f)) plots the detailed comparison of the front shapes at different angles in a (r,θ) coordinate system.

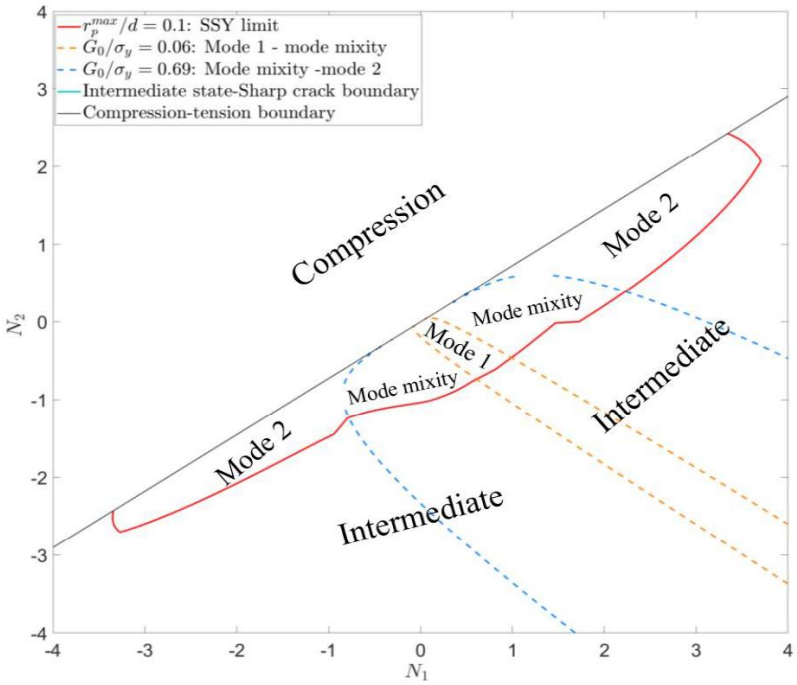
If a plastic FE analysis of the finite-height crack problem is conducted, the process zone in this case is seen to be larger than that predicted by the elastic solution since the stress field near the singularity must be redistributed. Additionally, FE experiments have been conducted using elastic perfectly plastic material. The results show that if plasticity is considered, the value of L for the sharp crack approximation will be increased compared with that of the elastic analysis in order to relax the stress at the singular notch corners, and in this case the value critical of L will generally be around 15. The actual value of L for the sharp crack approximation will also depend on the strain hardening rate when work hardening is introduced and will not be considered in this paper due to the complexity involved. We should expect that the critical

value of L for the sharp crack approximation to apply is between that critical value generated by linear elastic case and elastic perfectly plastic case, i.e., between 8.4 and 15. To maintain consistency with the analysis of later sections where LEFM is assumed to compute the "notch corner" stress intensity factor, we will use only the result $L = 8.4$, i.e., result derived from violation of the yield condition to characterize the crack approximation case.

In conclusion, in the linear elastic case, if $L \gtrapprox 8.4$, the stress states near the crack tip of a finite-height crack can be considered as that of a sharp crack, and fracture failure will be initiated at the middle plane between the two notch corners (Figure 3 (a)).



(a)



(b)

Figure 5: Asymptotic behaviour analysis for the top-notch corner: (a) scale $N_1 \in [-10,10]$ *and* $N_2 \in [-10,10]$*, (b) scale* $N_1 \in [-4,4]$ *and* $N_2 \in [-4,4]$.

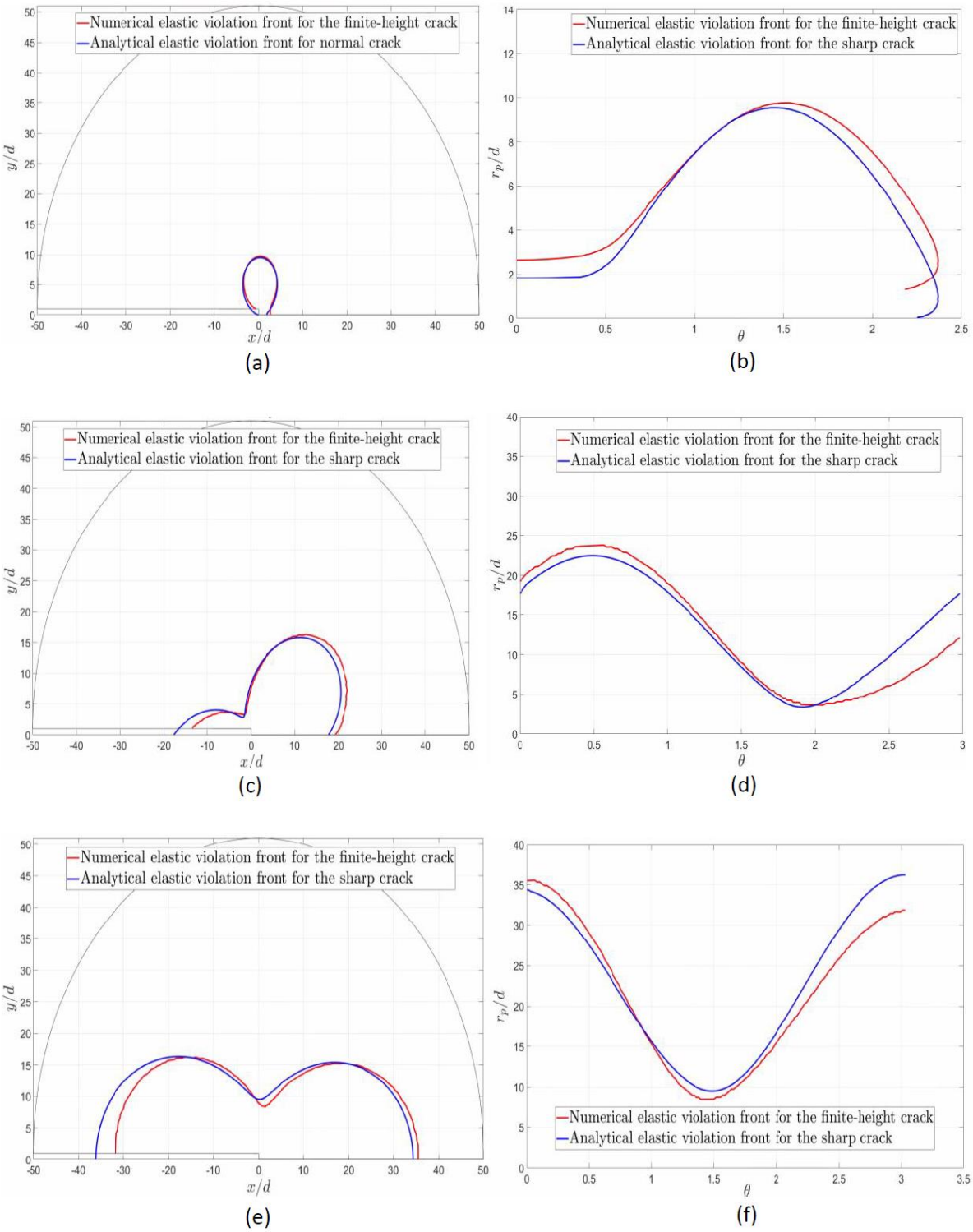


Figure 6: Elastic violation front comparisons between the numerical results for the finite-height crack and the analytical results for the sharp crack: (a)&(b) Pure mode 1 loading, $L^2 = 72$, *MSPE=0.0184; (c)&(d) Mixed-mode loading* ($K_1 = K_2$), $L^2 = 70.56$, *MSPE=0.0150 ; (e)&(f) Pure mode 2 loading,* $L^2 = 72$, *MSPE=0.0127.*

3. **Light Load case: Notch problem approximation**

When the load *L* is smaller than about 8.4, the presence of the finite-height starts to influence the stress states around the tip region and introduces other possibilities of fracture initialization. The interaction between multiple right-angle singular features was first studied by Hasebe and Ueda[16] They analyzed the stress of a square hole in an elastic plane using the conformal mapping technique and complex variable approach. However, the method is rather complicated, and the boundary condition differs from the present problem. In the present problem, notice that when *L* is sufficiently small, the stress field around two "notch corners" will be uncoupled. Based on the pure elastic analysis, the local stress states near the notch corners can be expressed in terms of local stress intensity factors for the right-angle notch corners, using a Cartesian coordinate system along the 45-degree line depicted in Figure 1(b).

The eigenvalues λ_{1N} and λ_{2N} at a general notch are calculated by [17]:

$$\begin{array}{ll} \lambda_{1N} sin2\alpha + sin(2\lambda_{1N}\alpha) = 0 & \text{Mode 1} \\ \lambda_{2N} sin2\alpha - sin(2\lambda_{2N}\alpha) = 0 & \text{Mode 2} \end{array} \tag{7}$$

where α is one half the notch angle in the solid. For a sharp crack, α is equal to π, and the eigenvalues are repeated 1/2 leading to stresses proportional to $K_{1C}/r^{1/2}$, and $K_{2C}/r^{1/2}$, according to equations (3) and (4).

For a right-angle notch, λ_{1N} is equal to 0.544 and λ_{2N} is 0.909. Therefore, the stresses related to mode 1 failure are proportional to $K_{1N}/r^{0.456}$ and the stresses related to mode 2 failure are proportional to $K_{2N}/r^{0.091}$.

A 2×2 non-dimensional matrix is proposed to relate the remote loading parameters to local stress intensity factors according to:

$$[K_{1_C} \quad K_{2_C}] \begin{bmatrix} A_{11} & \pm A_{12} \\ \pm A_{21} & A_{22} \end{bmatrix} = \left[K_{1_N} d^{\left(\lambda_{1_N} - \lambda_{1_C}\right)} \quad K_{2_N} d^{\left(\lambda_{2_N} - \lambda_{2_C}\right)}\right] = \left[K_{1_N} d^{0.044} \quad K_{2_N} d^{0.409}\right]$$

(8)

where A_{11}, A_{12}, A_{21} and A_{22} are dimensionless constants. Note that the "$\pm$" is added before the constants A_{12} and A_{21}, where the plus sign is taken for the top right-angle notch and the minus sign is for the bottom-notch. This is because the remote positive shear will induce local compression at the top-notch and local tension at the bottom-notch; whereas for global tension a local positive shear at the top-notch and negative shear at the bottom-notch will be induced.

Sinclair [15] has developed a path independent integral method called the "H-integral" method to calculate the stress intensity factor of a notch, an approach which is based on Betti's reciprocal theorem. This method has been shown to calculate the stress intensity factor with great accuracy. It states that for a closed contour around a notch, for example a contour around the right-angle notch, such as the one in Figure 4 indicated by black arrows, the stress intensity factor can be represented as:

$$K_{1(2)N} = \int_{\Sigma} \left(\sigma_{ij} u_i^* - \sigma_{ij}^* u_i\right) \eta_j ds \qquad (9)$$

where σ_{ij} represents the two-dimensional stress components on a given contour and those stresses can be extracted from the FE results; u represents the corresponding displacements; σ^* and u^* represent the complementary stress and displacement fields which satisfy the same equilibrium and constitutive equations as σ_{ij} and u; η_j is an outward pointing unit vector normal to the contour surface; and ds is the infinitesimal contour length. According to equation (1) and the constitutive law, stress and strain along the contour will behave as:

$$\sigma_{ij} = O\left(r^{\lambda-1}\right); \qquad u = O\left(r^{\lambda}\right) \qquad (10)$$

As the contour radius shrinks to zero, the integrand in equation (12) needs to behave as $O(r^{-1})$ so that the integral can recover the stress intensity factor as a constant. Hence we must have:

$$\sigma_{ij}^{*} = O\left(r^{-\lambda-1}\right); \qquad u^{*} = O\left(r^{-\lambda}\right) \qquad (11)$$

Notice that on the flanks of this contour, the integral will diverge because of the $1/r$ term when r goes to zero. However, if λ satisfies equation (7) then $-\lambda$ also does, and the complementary fields can be further required to be the eigenfunction themselves so that both $\sigma_{ij}n_j$ and $\sigma_{ij}^{*}n_j$ will be equal to zero on the flanks. Under the above conditions, the integral around the contour is equal to the integral performed only on the circular arc, and the appropriate participation factors are chosen in the complementary fields to recover the stress intensity factors K_{1N} and K_{2N}. Those complementary field are defined differently in modes 1 or 2 loadings and are listed in Sinclair [15]. Finally, because of symmetry, the H-integral method can be computed as twice the integral along half of the contour.

In the finite-height problem, the contour is chosen to be located around the top-notch, depicted in Figure 4. Using finite element analysis, the remote stress intensities were applied in the same way as the heavy load case, i.e., Figure 1. The stresses σ_{ij} and displacements u_{ij} were extracted along this contour. Since the H-integral method around notch corners is based on the local coordinate system, the stresses and the displacements along the contour obtained from the FE analysis must be rotated to the local coordinate system and then further decomposed into both local mode 1 and local mode 2 stresses and displacements separately. In the end, the decomposed stresses were carried into equation (9) to utilize the H-integral method for the local stress intensity factors of both mode 1 and mode 2, K_{1N} and K_{2N} separately. Note that because the FE results are avaliable only at discrete points, Simpson's method was used to find the approximate integral. Additionally, convergence checks were also made assiduously following the method derived by Beisheim, Sinclair and Roache [18]

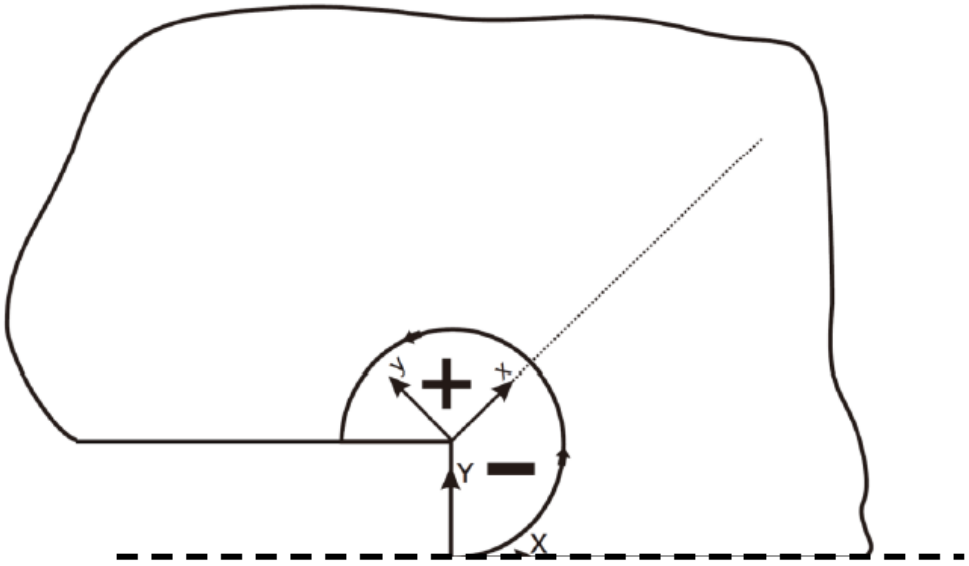


Figure 7: Illustration of the contour used in H-integral method for the finite-height crack problem.

According to the above steps, for the finite-height crack case we perform the H-integral method at the upper corner notch according to 45-degree coordinate system which gives the relation between the global loads and local stress intensity factors:

$$[K_{1_C} \quad K_{2_C}] \begin{bmatrix} 0.747 & \pm 0.284 \\ \pm 1.029 & 0.381 \end{bmatrix} = \left[K_{1_N} d^{0.044} \quad K_{2_N} d^{0.409}\right] \tag{12}$$

From equation (12), the top-notch corner is loaded under tension when $K_{1N} > 0$, hence

$$0.747K_{1C} - 1.029K_{2C} \geq 0, \tag{13}$$

otherwise, compressive stress will be generated at the notch corner on $\theta = 0$, leading to closure of an embryonic crack on that line. On the other hand, it can result in yielding, and the purpose of this paper is to discuss possible fracture failure initialization. The compression-tension boundary for the notch corner is shown in Figure 2 as the black line.

Hills and Dini [2], developed a method to characterize the asymptotic stress field around a notch. Instead of equation (1), they state that for a general notch the first two terms in a series expansion of the state of stress can be represented non-dimensionally as

$$\frac{\sigma_{ij}(r,\theta)}{G_0} = sgn(K_{1N})\left(\frac{r}{d_0}\right)^{\lambda_1-1} f_{ij}^{I}(\theta) + sgn(K_{2N})\left(\frac{r}{d_0}\right)^{\lambda_2-1} f_{ij}^{II}(\theta) \tag{14}$$

where

$$G_0 = |K_{1N}|^{\frac{\lambda_{2N}-1}{\lambda_{2N}-\lambda_{1N}}}|K_{2N}|^{\frac{\lambda_{1N}-1}{\lambda_{1N}-\lambda_{2N}}} \tag{15}$$

has the same dimension as the stress, and

$$d_0 = \left|\frac{K_{2N}}{K_{1N}}\right|^{\frac{1}{\lambda_{1N}-\lambda_{2N}}} \tag{16}$$

has the same dimension as length. Additionally, $sgn(x)$ is a signum function where

$$sgn(x) = \begin{cases} 1 & x > 0 \\ 0 & x = 0 \\ -1 & x < 0 \end{cases} \tag{17}$$

Equations (14)-(17) characterize the elastic field of mixed loading conditions by the magnitude (G_0) and mixity (d_0) of two notch stress intensity factors. Notice that even though this solution is universal, we can interprete it only if d_0 is finite. Hence the solution permits neither limits $K_1 \to 0$, $K_2 \to 0$ nor $\lambda_{1N}, \lambda_{2N} \to 1/2$ to be displayed.

For a loading condition characterized by G_0 and d_0, the implied radius of the elastic violation front at a given angle θ can be found by solving for r with $\sigma_{ij}(r,\theta)$ in equation (3) replaced by equation (16). This value of the elastic violation radius r will be denoted as r_p.

In Hills and Dini [2], for a right angle notch problem, r_p/d_0 has been plotted for different loading parameters G_0/σ_y. From that plot, the contour shapes of r_p/d_0 approach that of pure

mode 1 loading with decreasing values of G_0/σ_y. Since $\lambda_2 > \lambda_1$, when $r_p/d_0 << 1$, from equation (14), mode 1 loading term will be dominant. Therefore, a critical value of G_0/σ_y has been proposed such that when G_0/σ_y is smaller than this critical value, the elastic violation front and hence the asymptotic stress states can be considered as tending towards mode 1 loading around the notch. In the right-angle notch case, this critical value of G_0/σ_y for the pure mode 1 loading approximation has been found to be approximately 0.06. Notice that in Hills and Dini this condition for mode 1 asymptotic behaviour is represented as $G_0/k \leq 0.1$, where k is the yield stress in pure shear and $\sigma_y = \sqrt{3}k$.

When G_0/σ_y is gradually increased, with a corresponding increase of r_p/d_0, the mode 2 term tends to become the dominant factor and so the stress state around the notch will gradually change towards mode 2 loading of a right-angle notch. Similar to the above, a critical value of G_0/σ_y has been proposed such that when G_0/σ_y is greater than this value, the notch can be assumed loaded under pure mode 2, and this value has been justified as about 0.69 (in Hills and Dini this would be $G_0/k \geq 1.2$). Any value of G_0/σ_y between 0.06 to 0.69 can then be characterized as mixed mode in character

Therefore, considering the top right-angle notch in the finite-height crack problem, for a 45 degree Cartesion coordinate system depicted in Figure [fig:figure1](b), substituting values of K_{1N} and K_{2N} found from equation (13) into (14) and (15), G_0 and d_0 can be computed as functions of the non-dimensional loading parameters N_1 and N_2 related to the applied remote loads:

$$G_0/\sigma_y = |A_{11}N_1 + A_{21}N_2|^{(\lambda_{2N}-1)/(\lambda_{2N}-\lambda_{1N})} \times |A_{12}N_1 + A_{22}N_2|^{(\lambda_{1N}-1)/(\lambda_{1N}-\lambda_{2N})} \qquad (18)$$

and A_{11}, A_{12}, A_{21} and A_{22} are defined in equation (13), the local loading mixity is defined as

$$d_0 = d\left|\frac{A_{12}N_1 + A_{22}N_2}{A_{11}N_1 + A_{21}N_2}\right|^{\frac{1}{\lambda_{1N}-\lambda_{2N}}} \tag{19}$$

The local loading magnitude G_0 and mixity d_0 for the notch corner of the finite-height crack are represented by the remote loading parameter as N_1 and N_2 of corners. Additionally, if we define the remote applied load mixity as

$$\alpha = \frac{K_{2C}}{K_{1C}} \tag{20}$$

then we can also rewrite G_0/σ_y as

$$G_0 = L\sigma_y(1+\alpha^2)^{-1/2}|A_{11} + A_{21}\alpha|^{\frac{\lambda_{2N}-1}{\lambda_{2N}-\lambda_{1N}}}|A_{12} + A_{22}\alpha|^{\frac{\lambda_{1N}-1}{\lambda_{1N}-\lambda_{2N}}} \tag{21}$$

Next, if the stress fields of the two notch corners do not interfere with each other (the conditions for achieving this will be further discussed in the next section), the stress state around the two notch corners of the finite-height crack problem can be considered as that of the two independent general right-angle notches.

By representing G_0/σ_y with the applied load using equation (18), the critical value $G_0/\sigma_y = 0.06$ represents the pure mode 1 loading-mode mixity boundary with respect to applied loads parameter N_1 and N_2 has been plotted in Figure 2 as the orange dash line. $G_0/\sigma_y = 0.69$ represents the boundary of mode mixity/pure mode 2 has also been plotted in Figure 2 as the blue dash line.

In Figure 2, the black line separates the entire region into compression and tension regimes. Therefore, only the applied loads in the tension regime are of interest to us for predicting the fracture failure, i.e., below the black line.

Next, for the stress state near the top-notch corner which behaves as that of a general notch loaded in mode 1, the condition $G_0/\sigma_y \leq 0.06$ is represented by the region in between the two

orange dash lines. Hence, when the applied load lies within that region, the criterion that characterizes crack propagation for a right-angle notch under pure mode 1 1oading may be applied for crack propagation analysis, and this will be introduced in section 6.

Similarly, the blue dash line in Figure 2 separates the “Mode 2” region and “Mode Mixity” region. The region between the orange and the blue dash lines represents the range of applied loads that cause the mixed mode loading to arise at the top notch corner. Lastly, when the applied loads lie outside the blue line, almost pure notch mode 2 asymptotic stress field will be generated at the top-notch corner.

4. Non small scale yielding: intermediate state analysis

As in the previous section, when the non-dimensional load G_0/σ_y is small, notch mode 1 loading can be assumed at each notch corner. If the load is gradually increased, the stress state at the notch corner will gradually become that of the notch mode 2 loading. However, in the finite-height crack problem, with the increase of the applied loads, the possibility that the state of stress around each of the two corners interfere with each other exists. In this case, the notch corner cannot be considered as an independent right-angle notch and fracture failure will not be initialized from the notch corner. If fracture failure occurs in the region between the mid-plane of the crack tip and the notch corners, then this type of failure initialization is referred to as the intermediate state (Figure 3(c)). The requirements for this type of failure are the following two: first, the applied loads are enough to result in interference of the stress fields of the two notch corners. Second, the applied loads are not so large as to cause the stress state around the finite-height crack to be considered close to that of a sharp crack, this has been discussed in section 2, i.e., $L \leq 8.4$.

If there is no interference between the near-crack tip stress-states of the two notch corners, then this situation is defined as small scale yielding (SSY). Hence the remote loads will induce a

notch-like behaviour around each of the two notch corners. Whether the stress state can be characterized as SSY is estimated by comparing the maximum elastic violation radius r_p^{max} with the nearest salient geometric feature, i.e., crack half height d. Therefore, the characteristics of the notch tip process zone is displayed in Table 1.

Table 1. Characteristics of the notch tip process zone justified as two non-dimensional factors r_p^{max}/d and G_0/σ_y

	G_0/σ_y		
	0.06≤	0.58-0.69	≥0.69
$r_p^{max}/d \leq 0.1$	Mode 1	Mode Mixity	Mode 2
$r_p^{max}/d > 0.1$	Intermediate state or Sharp crack		

To compare the maximum elastic violation radius with d, we rewrite equation (15) as

$$\frac{\sigma_{ij}(r,\theta)}{L\sigma_y} = C_1\left(\frac{r}{d}\right)^{\lambda_{1N}-1} f_{ij}^1(\theta) + C_2\left(\frac{r}{d}\right)^{\lambda_{2N}-1} f_{ij}^1(\theta) \tag{22}$$

and

$$\begin{aligned} C_1 &= sgn(K_{1N})(1+\alpha^2)^{-1/2}|A_{11}+A_{21}\alpha| \\ C_2 &= sgn(K_{2N})(1+\alpha^2)^{-1/2}|A_{12}+A_{22}\alpha| \end{aligned} \tag{23}$$

Therefore, according to equation (22) and (23), for every applied load mix α, we can compute the loading magnitude L for $r_p^{max}/d = 0.1$, by equating the Von Mises parameter of $\sigma_{ij}(r,\theta)$ with σ_y. Hence, the ranges of N_1 and N_2 that satisfy $r_p^{max}/d \leq 0.1$ can be formed and are also shown in (N_1, N_2) space, plotted as the red line in Figure 2.

To summarize the above results, from Figure 2, first, if the applied load in (N_1, N_2) space lies within the SSY limit (the red line), each of the two corner notches at the finite-height crack can

be considered as an independent right angle notch, i.e., Figure 3(b) applies, and the criterion that justifies the loading modes in section 3 can be applied, shown as the blue and yellow lines. Secondly, if the applied loads lie in between the red line and the green line, i.e., the intermediate regime, fracture failure is predicted to occur at somewhere between the middle plane of the two notches and one of the notch corners, such as Figure 3(c). Finally, if the applied loads lie outside the region encircled by the green line, i.e., in the sharp crack regime, then the stress field around the finite height crack can be considered as that of the sharp crack, i.e., Figure 3(a).

5. Application to an example problem: an infinite plate with a rectangular shaped crack

Consider a configuration of an infinite plate that has a rectangular crack in which the crack dimensions are small compared to the size of the plate, as depicted in Figure 8. The rectangular crack has crack height $2d$ and crack length $2kd$, where $k \geq 1$. The plate is loaded under global load K_{1C} and K_{2C} which are, for example, $K_{1C} = \sigma_0\sqrt{2\pi kd}$, $K_{2C} = \tau_0\sqrt{2\pi kd}$ and σ_0, τ_0 are the remote tension and applied shear respectivly. K_{1C} and K_{2C} can also be transfered to N_1 and N_2 according to equation (5).

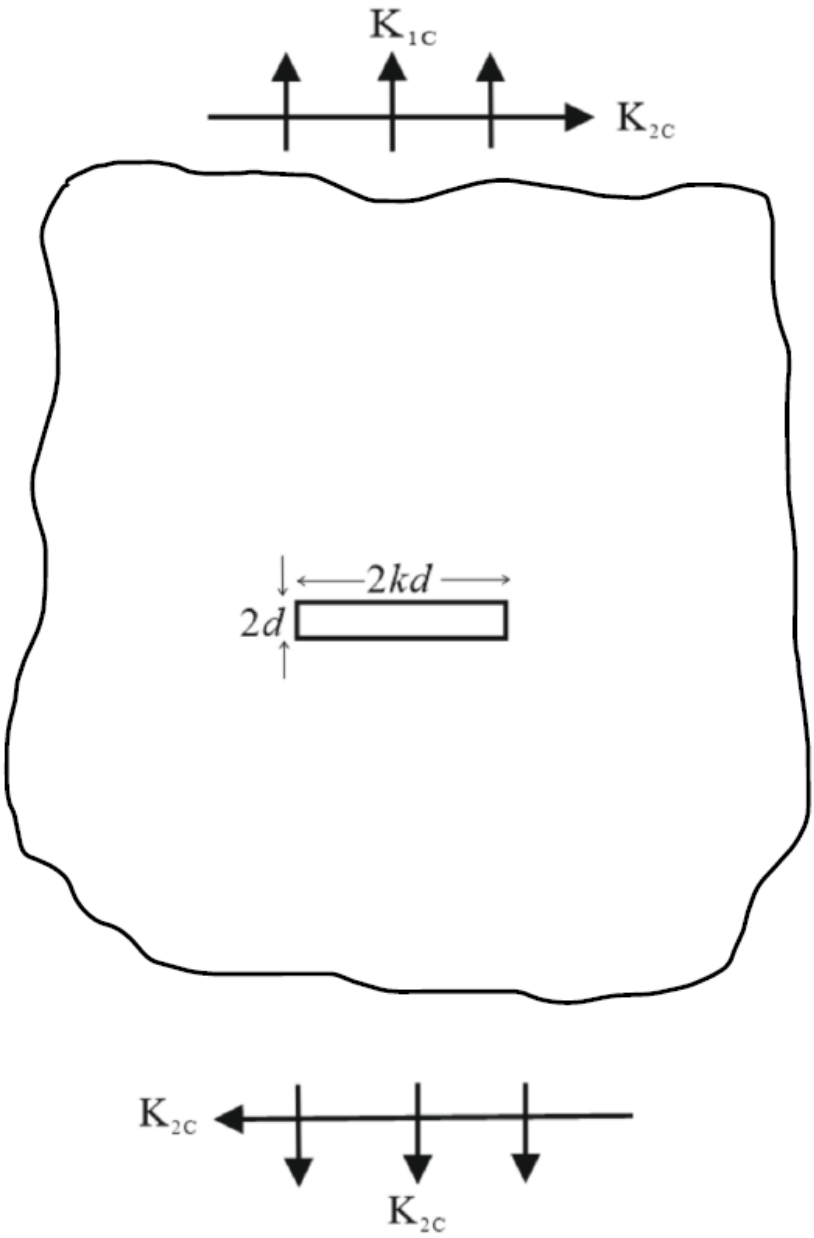


Figure 8: Illustration of a plate that has a rectangular crack

Before applying the criteria developed to the problem to identify where the crack will initialize, we need to ensure the process zone of the left-side notch pair of corners does not interfere with that of the right-side notch pair, i.e., $r_p^{max} < 0.1kd$ say. As in section 4, by applying equation (21), $r_p^{max}/d \leq 0.1k$ has been plotted for different value of k, shown in Figure 6.

Figure 6 shows the range of global load for different values of k that we can assume the notch pairs at the left and right side of the crack are “independent”. For a specific value of k, if the applied load is in the “independent” range, we can use the criteria developed, to justify the place of crack initiation, whereas if the load is outside the above range, the process zones of left and right sides of the crack will interfere (see Figure 5). The latter case is a much more complicated situation and out of this paper’s consideration.

We will provide an example case to illustrate this concept. When considering the case where $k = 20$, to apply the results obtained in the present paper, we need to ensure that the global loading falls within the range circled by the blue line labeled ‘$k = 20$’. If we look at the right upper notch corners (This is also equivalent to the left lower notch corners due to the symmetry), here are three examples with typical values of N_1 and N_2:

- If $N_1 = 1$ and $N_2 = -0.5$, the crack will initiate at the "notch corner" with Mode 1 loading characteristics.
- If $N_1 = 4$ and $N_2 = -4$, the crack will initiate between the mid-plane and the "notch corner," representing an intermediate state.
- If $N_1 = 7$ and $N_2 = -7$, the finite-height crack can be considered as a sharp crack, and crack initiation will occur at the mid-plane.

However, for the range outside that circled by ‘$k = 20$’ line in Figure 6, the present paper cannot provide suggestions for crack initiation. This is because the stress field on the left and right sides of the rectangular crack will interfere with each other. Notice that the above are examples of $N_2 < 0$, when $N_2 > 0$, the critical corners will swap, from upper right and lower left corners to upper left and lower right corners.

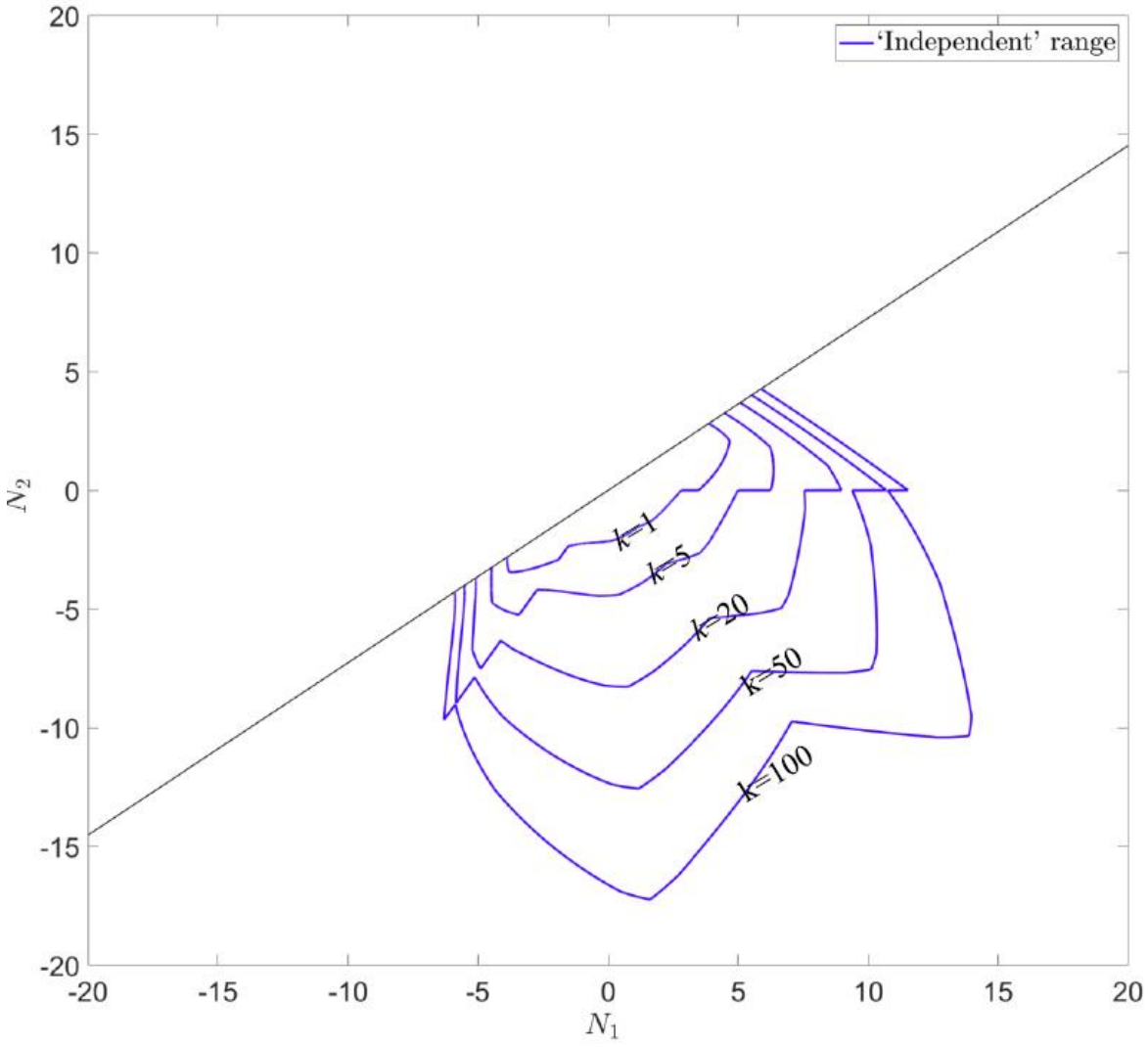


Figure 9: Global load range for independent notch pairs

6. Critical stress intensity factor of the notch mode 1 loading approximation

Consider a notch loaded under pure mode 1 loading. Adams and Hills [19] developed a crack growth criterion which can be represented as a function of the fracture toughness and yield strength of the material. For a general notch, the tangential stress at the bisector can be expressed as:

$$\sigma_{\theta\theta} = \frac{K_{1N}}{\sqrt{2}} r^{\lambda_1 - 1} \tag{24}$$

Critical values of K_{1N}, K_{1Nc} has been developed such that when $K_{1N} \geq K_{1Nc}$, fracture failure will start to propagate from the notch tip. This K_{1Nc} is referred to as critical stress intensity factor for a general notch.

The expression of K_{1Nc} in terms of notch opening angle β, yield stress σ_y, fracture toughness K_{Ic}, and the mode 1 loading eigenvalue λ_{1N}, is represented non-dimensionally as:

$$\frac{K_{1Nc}\left(\sigma_y/K_{1c}\right)^{1-2\lambda_1}}{K_{Ic}/\sqrt{\pi}} = 1 + 0.038393\beta^2 - 0.027857\beta^3 + 0.024207\beta^4. \tag{25}$$

For the 90-degree notch case, $\beta = \pi/2$, $\lambda_1 = 0.54484$, and equation (28) can be simplified to get the following expression for K_{1Nc} in terms of intrinsic material properties:

$$K_{1Nc} = 1.134K_{Ic}^{2-2\lambda_1}\sigma_y^{2\lambda_1-1}/\sqrt{\pi} = 1.134K_{Ic}^{0.911}\sigma_y^{0.090}/\sqrt{\pi} \tag{26}$$

So far we have defined a criterion for crack propagation at a notch tip under pure mode 1 loading. In the finite-height crack case, if the remote loading has been predicted to result in notch Mode 1 asymptotic behaviour at the notch corner (mode 1 region in Figure 2), the critical stress intensity factor at the notch corner for crack growth is $K_{1N} \geq K_{1Nc}$. The expression of K_{1N} can be obtained from equation (13). Rewrite the criterion for fracture failure growth in terms of global stress intensity factors as

$$K_{1N} = (A_{11}K_{IC} + A_{21}K_{2C})d^{\lambda_{1C}-\lambda_{1N}} \geq K_{1Nc} \tag{27}$$

and simplify to get

$$1.168K_{IC} - 1.608K_{2C} \geq K_{1c}^{0.911}\sigma_y^{0.090}d^{0.0448} \tag{28}$$

as the analytical criteria for failure growth at the notch corners.

7. Conclusion

For a finite-height crack problem, the characteristics of the near crack-tip asymptotic behaviour are controlled by two non-dimensional loading parameters $K_{1c}/(\sigma_y\sqrt{d})$ and $K_{2c}/(\sigma_y\sqrt{d})$. Three different types of fracture failure initialization are proposed: (1). at the notch corner, (2) at the middle plane between notch corners, (3) at an intermediate state. Those failure types can be predicted with the help of Figure 2.

Considering fracture criteria, when the applied load lies in the "sharp crack" region, fracture toughness can be straightly imposed in the conventional manner because the stress states of the finite-height crack is very similar at the process zone edge to that of the sharp crack. Inside the "sharp crack" critical line, the criterion developed for the crack growth has been found only for the pure mode 1 notch-like approximation, states in equation (28).

The method used in this paper, which analyses a plane that contains more than one singularity can be also applied to the case of a rigid inclusion. Because the rigid inclusion never has a zero-thickness, but previous studies often assume of that type, i.e., [20] [21], hence the shape can be assumed as that of a finite-height crack. The analytical model in the rigid inclusion would need to consider the singularities at the bi-material interface, and this has been developed in [22], a more realistic stress behaviour could be generated by adopting the analysis in this paper.

4.3 Clarification

The statement made in this section aims to provide clarifications regarding the attached paper to avoid any misunderstandings.

In the attached paper, it is novel that the finite-height crack is analyzed energetically, and predictions of fracture failure positions are made according to different loading combinations. However, these predictions about where the crack will initiate around the finite-height feature might not always be practical.

When the load is very light, the two right-angle notches will act independently, and we expect the two singular notch features to dominate. Therefore, in this case, fracture failure will inevitably start at one of the notches. The crack propagation can be predicted as in the case of a loaded rectangular notch. However, when the load is heavy, the elastic violation front will be large compared to the crack height, making the height negligible. In this scenario, the finite-height crack can be treated as a sharp crack, but this does not necessarily mean that fracture failure will occur along the line of symmetry. Instead, it always occur at the point of maximum shear stress, which is one of the notch corners, with its propagation resembling the case of a plate containing a sharp crack under load.

Regarding the intermediate state, the paper proposes a function related to the load states. This function differentiates the loading state from those where the two notches can be treated independently, i.e., r_p/d>0.1. This condition again does not imply that a crack will initiate somewhere along the crack height. In such a case, the crack will always initiate at the location with the maximum shear stress, which is, once again, one of the notch corners. However, in the intermediate state, the propagation of the crack cannot be straightforwardly considered as either like a sharp notch or a loaded notch corner. The crack starting at one of the notch corners will be influenced by the other notch corner, making its propagation difficult to predict.

Another clarification needed is about the similarity between sharp notches and right-

angle notches, defined by the mean squared percentage error (MSPE) of the two plastic fronts being smaller than 0.02. Although the value of 0.02 might be applicable in this case, a more scientific approach to choosing this number should be based on both the accuracy of the measurements and the salient geometric feature. When the average difference at selected data points of the two plastic radii is within the minimum scale of the measurement or within the length of the crack height, we can consider the difference sufficiently small and thus negligible.

Reference

[1] M. L. Williams, "Stress singularities resulting from various boundary conditions in angular corners of plates in extension," *Journal of Applied Mechanics*, vol. 19, no. 4, pp. 526–528, 1952.

[2] D. A. Hills and D. Dini, "Characteristics of the process zone at sharp notch roots," *International Journal of Solids and Structures*, vol. 48, no. 14–15, pp. 2177–2183, 2011.

[3] J. R. Rice and G. F. Rosengren, "Plane strain deformation near a crack tip in a power-law hardening material," *Journal of the Mechanics and Physics of Solids*, vol. 16, no. 1, pp. 1–12, 1968.

[4] I. N. Sneddon, "The distribution of stress in the neighborhood of a crack in an elastic solid," *Philosophical Transactions of the Royal Society of London, Series A*, vol. 187, no. 1009, pp. 1934–1990, 1946.

[5] P. R. Budarapu, J. Reinoso, and M. Paggi, "Concurrently coupled solid shell-based adaptive multiscale method for fracture," *Computer Methods in Applied Mechanics and Engineering*, vol. 319, pp. 338–365, 2017.

[6] M. Creager and P. C. Paris, “Elastic field equations for blunt cracks with reference to stress corrosion cracking,” *International journal of fracture mechanics*, vol. 3, pp. 247–252, 1967.

[7] J. R. Rice, “Proceedings of the first international conference on fracture,” *The Japanese Society of Strength and Fracture of Materials*, vol. 1, p. 309, 1965.

[8] H. Andersson and H. Bergkvist, “Analysis of a non-linear crack model,” *Journal of the Mechanics and Physics of Solids*, vol. 18, no. 1, pp. 1–28, 1970.

[9] K. B. Broberg, “Critical review of some theories in fracture mechanics,” *International Journal of Fracture Mechanics*, vol. 4, pp. 11–19, 1968.

[10] T. Fett, “The stress intensity factor for small cracks at the root of a notch,” *International journal of fracture*, vol. 54, no. 4, pp. R57–R64, 1992.

[11] D. M. Neal, “Stress intensity factors for cracks emanating from rectangular cutouts,” *International Journal of Fracture Mechanics*, vol. 6, pp. 393–400, 1970.

[12] J. J. Golecki and J. D. Suzdalnitsky, “Crack initiation at the rectangular step notch surface under combined loading,” *Archive of Applied Mechanics*, vol. 71, pp. 640–648, 2001.

[13] J. L. Sanders Jr, “On the Griffith-Irwin fracture theory,” *Journal of Applied mechanics*, vol. 27, pp. 352–353, 1960.

[14] J. R. Rice, P. C. Paris, and J. G. Merkle, “Some further results of j-integral analysis and estimates,” in *Progress in flaw growth and fracture toughness testing*, ASTM International, 1973, pp. 231–245.

[15] G. B. Sinclair, M. Okajima, and J. H. Griffin, “Path independent integrals for computing stress intensity factors at sharp notches in elastic plates,” *International Journal for Numerical Methods in Engineering*, vol. 20, no. 6, pp. 999–1008, 1984.

[16] N. Hasebe and M. Ueda, “Crack originating from a corner of a square hole,” *Engineering Fracture Mechanics*, vol. 13, no. 4, pp. 913–923, 1980.

[17] J. R. Barber, *Elasticity*. Springer, 1992.

[18] J. R. Beisheim, G. B. Sinclair, and P. J. Roache, “Effective convergence checks for verifying finite element stresses at three-dimensional stress concentrations,” *Journal of Verification, Validation and Uncertainty Quantification*, vol. 3, no. 3, p. 034501, 2018.

[19] G. G. Adams and D. A. Hills, “Analytical representation of the non-square-root singular stress field at a finite angle sharp notch,” *International Journal of Solids and Structures*, vol. 51, no. 25–26, pp. 4485–4491, 2014.

[20] L. Argani, D. Bigoni, and G. Mishuris, “Dislocations and inclusions in prestressed metals,” *Proceedings of the Royal Society A: Mathematical, Physical and Engineering Sciences*, vol. 469, no. 2154, p. 20120752, 2013.

[21] M. Goudarzi, F. Dal Corso, D. Bigoni, and A. Simone, “Dispersion of rigid line inclusions as stiffeners and shear band instability triggers,” *International Journal of Solids and Structures*, vol. 210, pp. 255–272, 2021.

[22] M. Paggi and A. Carpinteri, “On the stress singularities at multimaterial interfaces and related analogies with fluid dynamics and diffusion,” *Applied Mechanics Reviews*, vol. 61, no. 2, 2008.

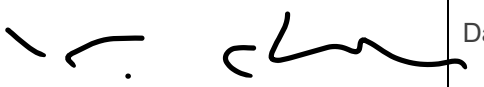
Statement of Authorship for joint/multi-authored papers for PGR thesis

To appear at the end of each thesis chapter submitted as an article/paper

The statement shall describe the candidate's and co-authors' independent research contributions in the thesis publications. For each publication there should exist a complete statement that is to be filled out and signed by the candidate and supervisor **(only required where there isn't already a statement of contribution within the paper itself).**

Title of Paper	Investigation of stress states around a finite-height crack.
Publication Status	✓Published □ Accepted for Publication □Submitted for Publication □Unpublished and unsubmitted work written in a manuscript style
Publication Details	**1.** Chen, Y., Adams, G. G., & Hills, D. A. (2023). Investigation of stress states around a finite-height crack. International Journal of Solids and Structures, 284, 112499.

Student Confirmation

Student Name:	Yifeng Chen		
Contribution to the Paper	Perform essential FE analysis. Perform Theoretical deduction. Write up all the paper.		
Signature		Date	16/04/2024

Supervisor Confirmation

By signing the Statement of Authorship, you are certifying that the candidate made a substantial contribution to the publication, and that the description described above is accurate.

Supervisor name and title: Prof. John huber		
Supervisor comments		
Signature 	Date	17/4/24

This completed form should be included in the thesis, at the end of the relevant chapter.

5. Anti-plane wedge interacting with a singularity

5.1. Introduction

In the previous chapter, we discussed a finite-height crack where the interaction between two right-angle notches was considered. The analytical method used to characterize the singular features of the sharp notch is the asymptotic method, namely Williams' solution. In this chapter, we return to the basics and attempt to study the wedge problem using an alternative approach: the complex variable solution.

Although the asymptotic method is well-documented in numerous literatures and effectively characterizes the stress field near the singular feature, its drawback is that the solution relies only on the most significant term of the Airy stress function expansion. Therefore, it is approximate in nature, and information is lost regarding points not located close to the singular feature. Ma and Hills (2022) sought to solve this problem in an alternative way. They realized that all applied load conditions, whether displacement or force, could be decomposed into the integration of singular dislocations or singular forces. Thus, they aimed to develop the method more fundamentally, that is, to solve the problem for a wedge interacting with a singularity. Their solution employs Neuber's conformal mapping technique (Neuber, 1958) to transform the wedge plane into a half-plane, thereby eliminating any geometric singularity. They then applied the argument of analytic continuation to fully address the problem. This section will follow the method developed by Ma and Hills (2022) and extend the solution to a wedge interacting with an anti-plane singularity, aiming to create a complete 'toolbox' for the complex variable solution method in wedge problems.

Therefore, the 'plane with a defect' problem chosen for this section is the basic anti-plane wedge problem. We will discuss the stress field behavior when it interacts with an anti-plane singular feature (anti-plane singular stress, screw dislocation). The closed-form solution will be presented in the form of complex potential that can be directly applied to equations

(2.18)-(2.20) for stress field calculation. This solution will then be further evaluated by comparison with some classical cases, and an application of this method will be illustrated.

5.2. Paper: A generalized anti-plane singularity within a semi-infinite wedge of arbitrary angle[4]

Abstract

The state of stress arising within an elastic wedge generated by an anti-plane singularity present within it is studied. An analytical solution is derived with a unified generic approach. The singularity may represent either an anti-plane concentrated force or a screw dislocation. To validate the general solution, two degenerate cases are presented. Further, the image force present on the screw dislocation due to the wedge free boundary is obtained. It is found that when the screw dislocations are placed in the vicinity of the wedge surface, the image force will drive dislocations to the free boundary where they will be annihilated. This implies that a dislocation-free zone may exist along the free surface of the wedge. To demonstrate the application of the fundamental solutions, a formulation for a slip band under anti-plane loading with Green's function method is provided. The solutions developed in this study may be used as building blocks to model the damage of material near a V-notch under versatile anti-plane load conditions or torsional loading.

Keywords: Singularity, wedge, V-notch, screw dislocation, anti-plane concentrated force, conformal mapping.

1. Introduction

The solid shown in Fig. 1 is generally called a 'wedge' when its internal angle is lies between 0 and 2π, whereas it is usually named a 'V-notch' when the internal angle is between π and 2π. Since the only difference between the two cases is the value of the angle,

[4] Ma, L., Chen, Y., & Hills, D. A. (2023). A generalized anti-plane singularity within a semi-infinite wedge of arbitrary angle. The Journal of Strain Analysis for Engineering Design, 03093247231190684.

in this study, for simplicity, we will not differentiate between the two cases and call the configuration a ‘wedge’.

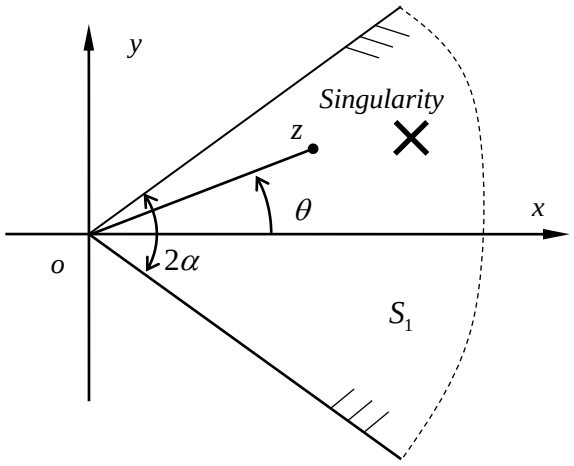


Fig. 1 The configuration of a wedge interacting with an anti-plane singularity denoted by the cross sign. The singularity is arbitrarily located within the wedge, the *x*-axis is set along the bisector line of the wedge, and the wedge internal angle is within the range $0 < 2\alpha < 2\pi$.

The wedge is a common feature necessarily figuring in many mechanical components, including, for example, grooves for retention clips, or power transmission, as in the spline. Also, wedge-shaped crack problems are observed more often in practice, compared with parallel slits. A knowledge of the stress field within wedges is essential during design and fatigue assessment. The wedge problem is of special importance in elastic mechanics because of its fundamental significance, its widespread application, and its theoretical challenge. To determine the stress distribution within a wedge for various kinds of load condition, great efforts have been put into studying this topic so that wedge mechanics turns to be one of the most classical problems in elasticity. [1-4]

In the literature, studies of the wedge under *anti-plane* loading have been conducted for a long time[4,5-7]. Three approaches have been employed to cater for various anti-plane load conditions: (*i*) The first one is Williams expansion approach,[8-11] which approximates the *real* stress function of the problem in a simple form to calculate the stress concentration factor at

V-notch tips; (*ii*) The second is one which takes the *complex* stress function of the problem in finite representative terms, [12-17] which has been used to approximate the stress distribution; (*iii*) The third one is the Mellin transform technique[18-20], which may be used to examine crack problems within wedges. It should be pointed out that, in theory, the Mellin transform is a rigorous and feasible approach to find exact solutions; however, when applied in practice, analytical solutions can be derived only for several very simple problems, and generally, numerical methods have to be further employed for common problems[20,21]. Here, we mainly present typical developments in cases subject to *anti-plane* loading, and the detailed review on these approaches applied to the cases under '*in-plane*' loading has been separately given in a recent work[22].

The work described above represents progress in our understanding of the problems under *anti-plane* loading, but some remaining challenges still exist. First, strictly speaking, the aforementioned analyses have been mostly conducted in an asymptotic or approximate sense. It is hard to treat various anti-plane load conditions, including spatially varying far-field loads, and near-field loads such as body forces or imposed displacement loads in the neighborhood of notches. Secondly, micromechanics analysis in literature just focuses tightly on the dislocation-wedge interaction problems. These are very powerful in applications but lack a generic approach to develop the solutions for the generalized singularity-wedge problem, such as when the singularity represents an anti-plane force or a more complex strain nucleus such as point-wise defined residual strain. These challenges demand a rigorous and thorough analysis of the generalized singularity-wedge problem. In this paper the interaction of a wedge with a generalized *anti-plane* singularity is studied, which complements the recent efforts in establishing the corresponding solution for in-plane loading[22].

The aim of this study is to propose a generic approach to treating wedge problems, and then specifically to develop a fundamental solution for a wedge interacting with a generalized

anti-plane singularity. The singularity may be either an out-of-plane concentrated force or a screw dislocation, or various combinations of them, which may lead to a moment load, a residual stress (or strain) state, and so on[23].

The basic geometry we will consider is shown in Fig. 1, in which, the singularity is arbitrarily located within the infinite wedge solid. The analysis procedure is outlined as follows: first, the complex formulation for anti-plane deformation and the generalized anti-plane singularity is presented, and the specific model is provided. Afterwards, the solution for the interaction between the wedge and the singularity is derived. Subsequently, two degenerate cases are presented: first a half-plane solid containing a concentrated body force, and secondly a semi-infinite crack interacting with a singularity. Later on, the image force present on the screw dislocation is derived, and the application of the fundamental solutions with Green's function method is demonstrated through a slip band formulation. Finally conclusions are drawn.

2. The complex framework and its form for a generalized anti-plane singularity

In this section, complex variable formulae for anti-plane problems and boundary conditions are introduced. The generalized singularity model is introduced which provides a basic concept for subsequent analysis.

The complex potential formulae

In the anti-plane shear deformation of an isotropic elastic material, the in-plane displacements vanish, i.e. $u = v = 0$, and the out-of-plane displacement is $w = w(x, y)$. The two anti-plane shear stress components σ_{13} and σ_{23} (the only non-zero stress components), and the single stress function ϕ can be expressed in terms of a holomorphic function $f(z)$ of the complex variable $z = x_1 + ix_2 (= x + iy)$ as[24]:

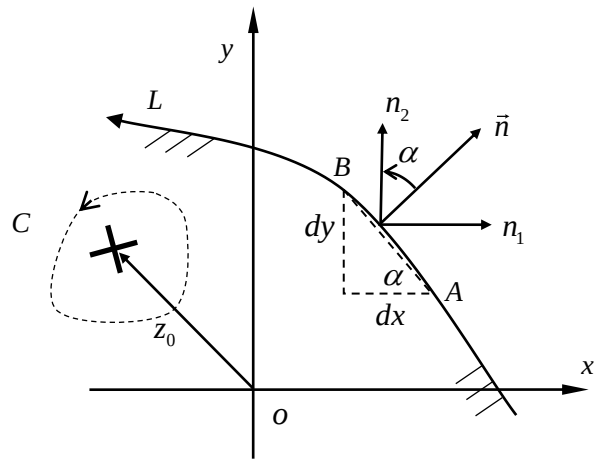


Fig. 2 Framework for anti-plane deformation of a generalized singularity (shown here by a cross sign) embedded within a plane solid whose boundary is *L*.

$$\begin{cases}\sigma_{23} + i\sigma_{13} = \mu f'(z) \\ \phi + i\mu w = \mu f(z)\end{cases}, \tag{1}$$

where $i = \sqrt{-1}$, and μ is the shear modulus. The two stress components are derived for the stress function ϕ as follows

$$\sigma_{13} = -\phi_{,2} \quad \sigma_{23} = \phi_{,1}, \tag{2}$$

where the comma followed by a subscript 1 (or 2) indicates differentiation with respect to x_1 (or x_2). The resultant traction t_3, along the x_3-direction on a boundary *L*, with material present on the left-hand side shown in Fig. 2, can be written as

$$t_3 = \sigma_{i3}n_i = \sigma_{13}n_1 + \sigma_{23}n_2 = -\frac{\mu}{2}\frac{\partial[f(z)+\bar{f}(\bar{z})]}{\partial s} = -\frac{\partial \phi}{\partial s}. \tag{3}$$

where $n_1 = \frac{\partial y}{\partial s}, n_2 = -\frac{\partial x}{\partial s}$ are components of the surface unit normal. Thus, the resultant force acting on an arc $\widehat{AB}$ is

$$T_3 = \int_A^B t_3\, ds = -\frac{\mu}{2}\left[f(z) + \bar{f}(\bar{z})\right]\Big|_A^B = -\phi|_A^B\,. \tag{4}$$

Eqs. (1) and (4) will be frequently used in the following manipulation.

The complex potential for singularities

A generalized anti-plane singularity, located at z_0 in an infinite plane, which may be a screw dislocation or an anti-plane concentrated force, has a complex variable potential which may be expressed as[24]

$$f_0(z) = A\, ln(z - z_0) = \frac{(F_z + i\mu b_z)}{2\pi\mu i} ln(z - z_0), \tag{5}$$

where b_z is the Burgers vector while F_z is the out-of-plane concentrated force in z- direction. If $F_z = 0$, it degenerates to the complex variable potential for a screw dislocation in an infinite solid:

$$f_0(z) = \frac{b_z}{2\pi} ln(z - z_0), \tag{6}$$

while if $b_z = 0$, it degenerates to the solution for an out-of-plane concentrated force as

$$f_0(z) = \frac{F_z}{2\pi\mu i} ln(z - z_0). \tag{7}$$

With Eq. (5) established, the complex potential for an anti-plane concentrated moment or an anti-plane eigenstrain nucleus may also be derived[25,26]. For example, the complex potential for a point-wise anti-plane eigenstrain located at the point $z_0 = x_0 + iy_0$ in an infinite plane is[23]

$$f_0(z) = -\frac{\varepsilon_{23}^0 - i\varepsilon_{13}^0}{\pi(z - z_0)} = -\frac{\varepsilon_{23}^0(x_0, y_0) - i\varepsilon_{13}^0(x_0, y_0)}{\pi[z - (x_0 + iy_0)]}, \tag{8}$$

where ε_{13}^0 and ε_{23}^0 are anti-plane eigenstrains.

In the following manipulation, we will take the generalized singularity expressed in terms of Eq. (5). The results for other generalized singularities can be derived in the same way.

3. Formulation

Consider the wedge shown in Fig. 1, where a generalized anti-plane singularity is located in the material. For this geometry, the complex potentials within the elastic solid, identified as S_1 can be constructed from

$$f(z) = f_0(z) + f_1(z), z \in S_1, \tag{9}$$

where $f_0(z)$ represents the complex potential of a generalized anti-plane singularity in an infinite plane, as given by Eq. (5), and $f_1(z)$ is a regular perturbed complex potential in S_1,

which will be determined from the free surface boundary condition. It should be pointed out that $f_1(z)$ will reflect the presence of material, the geometric surface boundary conditions, and incorporate the presence of the singularity.

We introduce a *one-to-one* conformal mapping function for everywhere, except the point $z = 0$, as follows

$$\begin{cases} z = x + iy = re^{i\theta} = w(\zeta) = (-i\zeta)^q, \theta \in (-\alpha, \alpha), \\ \zeta = u + iv = \rho e^{i\varphi} = w^{-1}(z) = iz^{\frac{1}{q}}, \varphi \in (0, \pi) \end{cases}, (z \neq 0), q = \frac{2\alpha}{\pi}, 0 < q \leq 2. \quad (10)$$

This maps the configuration in Fig. 1 (or Fig. 3a) into the one shown in Fig. 3b.

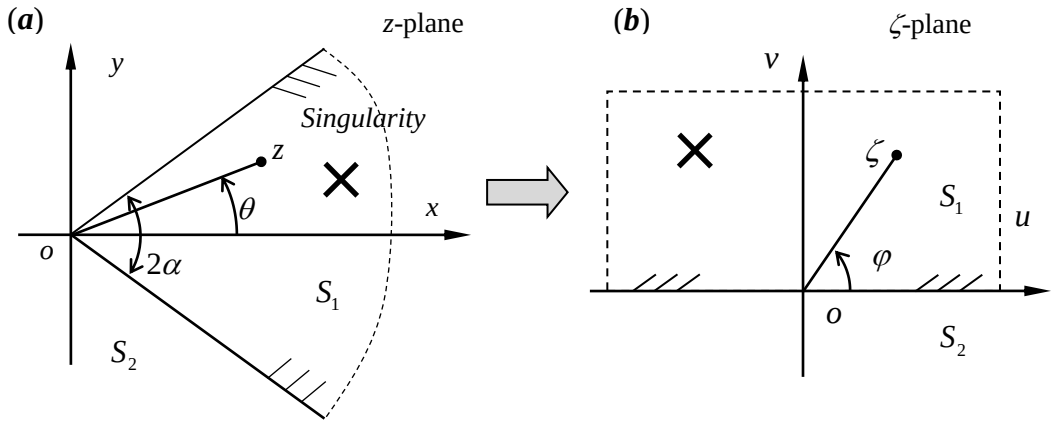


Fig. 3 (a) physical model, where the singularity located within the wedge, *x* axis is set along the bisector line of the wedge, (b) auxiliary plane

It may be observed from Fig. 3 that the material S_1 in Fig. 3a is mapped onto the upper plane in Fig. 3b, while the void in Fig. 3a is mapped onto the lower plane in Fig. 3b. The free surface is mapped into the *u*-axis in ζ-plane.

In terms of the mapping, Eq. (4) can be rewritten as

$$T_3 = -\frac{\mu}{2}\left[\hat{f}(\zeta) + \overline{\hat{f}(\zeta)}\right], \quad (11)$$

and Eq. (9) will be transformed to

$$\hat{f}(\zeta) = \hat{f}_0(\zeta) + \hat{f}_1(\zeta), \zeta \in S_1, \quad (12)$$

in which, accordingly,

$$\hat{f}_0(\zeta) = f_0\big(w(\zeta)\big) = A\,ln((-i\zeta)^q - (-i\zeta_0)^q). \tag{13}$$

Because Eq. (10) is a *one-to-one* conformal mapping (except the point $z = 0$), and there is only one singularity in ζ -plane, the potential $\hat{f}_0(\zeta)$ can be split into a *singular* term together with a *regular* term as

$$\begin{aligned}\hat{f}_0(\zeta) &= A\ln\left((-i\zeta)^q - (-i\zeta_0)^q\right) = A\ln(\zeta-\zeta_0) + A\ln\left(\frac{(-i\zeta)^q - (-i\zeta_0)^q}{(\zeta-\zeta_0)}\right), \\ &= \hat{f}_{0s}(\zeta) + \hat{f}_{0r}(\zeta)\end{aligned} \tag{14}$$

where

$$\hat{f}_{0s}(\zeta) = A\,ln(\zeta - \zeta_0), \quad \hat{f}_{0r}(\zeta) = A\,ln\left(\frac{(-i\zeta)^q-(-i\zeta_0)^q}{(\zeta-\zeta_0)}\right), \ (\zeta_0 \neq 0), \tag{15}$$

in which $\hat{f}_{0s}(\zeta)$ is singular at $\zeta = \zeta_0$, whilst $\hat{f}_{0r}(\zeta)$ is regular when $\zeta \in S_1$, and its value at $\zeta = \zeta_0$ should be understood as the limiting value in the auxiliary plane Fig. 3b.

The following operation is conducted within the ζ -plane in Fig. 3b. According to Liouville's theorem[27], it is logically assumed that the function $\hat{f}_1(\zeta)$ is regular within S_1 and singular within S_2, while $\bar{\hat{f}}_1(\zeta)$ is regular within S_2 and singular within S_1in Fig. 3b. With the traction-free condition on the notch surface ($Im(\zeta) = v = 0$) in Fig. 3b, inserting Eq. (12) into Eq. (11) leads to

$$\hat{f}_0(\zeta) + \hat{f}_1(\zeta) + \overline{\hat{f}_0(\zeta)} + \overline{\hat{f}_1(\zeta)} = 0, \ (\zeta = u). \tag{16}$$

Further, by substituting Eqs. (14) into (16), it follows that

$$\hat{f}_{0s}(u) + \hat{f}_{0r}(u) + \hat{f}_1(u) + \overline{\hat{f}_{0s}}(u) + \overline{\hat{f}_{0r}}(u) + \overline{\hat{f}_1}(u) = 0. \tag{17}$$

This result may be rearranged to give

$$\hat{f}_{0r}(u) + \hat{f}_1(u) + \overline{\hat{f}_{0s}}(u) = -\hat{f}_{0s}(u) - \overline{\hat{f}_{0r}}(u) - \overline{\hat{f}_1}(u). \tag{18}$$

Eq. (18) is a typical boundary value problem in terms of complex variables with a specific mapping, from which $\hat{f}_1(\zeta)$ is to be determined. Once solved, the primitive function$f_1(z)$ in Eq. (9) will be fixed.

4. Solution

By applying the standard analytic continuation argument to Eq. (18) and according to Liouville's theorem[27], we may obtain

$$\begin{cases}\hat{f}_{0r}(\zeta)+\hat{f}_1(\zeta)+\overline{\hat{f}_{0s}}(\zeta)=0,\zeta\in S_1\\ \hat{f}_{0s}(\zeta)+\overline{\hat{f}_{0r}}(\zeta)+\overline{\hat{f}_1}(\zeta)=0,\zeta\in S_2\end{cases}. \tag{19}$$

Thus, $\hat{f}_1(\zeta)$ is found to be

$$\hat{f}_1(\zeta)=-\hat{f}_{0r}(\zeta)-\overline{\hat{f}_{0s}}(\zeta),\zeta\in S_1. \tag{20}$$

In terms of Eq. (15), Eq. (20) may be rewritten as

$$\hat{f}_1(\zeta)=-A\,ln\left(\frac{(-i\zeta)^q-(-i\zeta_0)^q}{(\zeta-\zeta_0)}\right)-\bar{A}\,ln(\zeta-\bar{\zeta}_0),\zeta\in S_1. \tag{21}$$

It can be verified that the solution (21) is regular for $\zeta\in S_1$. By inserting $\zeta=iz^{\frac{1}{q}}$ into Eq. (21), we obtain

$$f_1(z)=-A\,ln\frac{(z-z_0)}{\left(iz^{\frac{1}{q}}-iz_0^{\frac{1}{q}}\right)}-\bar{A}\,ln\left(iz^{\frac{1}{q}}+i\bar{z}_0^{\frac{1}{q}}\right),z\in S_1. \tag{22}$$

Solution (22) is regular in the wedge area in Fig. 3a, and by substituting it into Eq. (9), the solution for the wedge interacting with a generalized singularity is revealed, viz.

$$f(z)=f_0(z)+f_1(z)=A\,ln(z-z_0)-A\,ln\frac{(z-z_0)}{\left(iz^{\frac{1}{q}}-iz_0^{\frac{1}{q}}\right)}-\bar{A}\,ln\left(iz^{\frac{1}{q}}+i\bar{z}_0^{\frac{1}{q}}\right). \tag{23a}$$

or

$$f(z)=A\,ln\left(iz^{\frac{1}{q}}-iz_0^{\frac{1}{q}}\right)-\bar{A}\,ln\left(iz^{\frac{1}{q}}+i\bar{z}_0^{\frac{1}{q}}\right). \tag{23b}$$

where $z=re^{i\theta}\neq 0,z_0=r_0e^{i\theta_0}\neq 0;\theta,\theta_0\in(-\alpha,\alpha)$. It can be also written in the form,

$$f(z)=A\,ln\left(z^{\frac{1}{q}}-z_0^{\frac{1}{q}}\right)-\bar{A}\,ln\left(z^{\frac{1}{q}}+\bar{z}_0^{\frac{1}{q}}\right), \tag{23c}$$

in which, the constant involved is ignored as it does not influence the stress field. If the singularity represents a screw dislocation, the stress due to it becomes

$$\sigma_{23}+i\sigma_{13}=\mu f^{'}(z)=\mu\frac{A}{q}z^{\frac{1}{q}-1}\left(\frac{1}{z^{\frac{1}{q}}-z_0^{\frac{1}{q}}}-\frac{1}{z^{\frac{1}{q}}+\bar{z}_0^{\frac{1}{q}}}\right), \tag{24}$$

where $A=\frac{b_z}{2\pi}$. This result is completely consistent with the one by Ohr *et al.*[6], which was obtained by a '*trial-and-error method*'.

Solution (23) is the key result of this study. It should be restated that: (*i*) the angle of the wedge can be any value $\alpha\in(0,\pi)$, which allows this solution to cover any scenario, regardless of whether it is an ordinary wedge or a V-notch; (*ii*) the singularity may represent either a concentrated force or a dislocation; (*iii*) the singularity can be at any point within the wedge except the point $z=0$. These desirable properties provide great flexibility in its use. In particular, when a screw dislocation within a V-notch is being modelled, this solution can be treated as a kernel function to model V-notch damage within the notch root region.

Additionally, it should be explained that the procedure described in previous sections may be treated as a generic approach for developing other fundamental solutions. For example, the singularity may be thought of as representing a point-wise residual strain.

5. Solutions for typical cases

We obtained the general solution (23). In this section, as shown in Fig. 4, two degenerate cases are presented to demonstrate its generality, and, to provide confidence in its reliability. The concentrated force acting at the vertex of wedge will also be also developed.

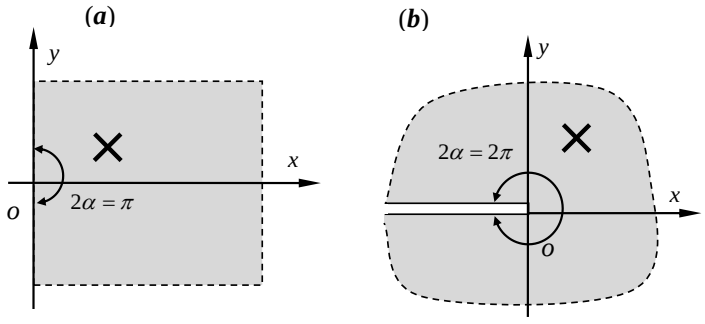


Fig. 4 Typical cases: (*a*) A half plane solid, (*b*) A semi-infinite crack, respectively, interacting with a singularity.

A half plane solid interacting with a singularity

By setting $\alpha = \frac{\pi}{2}$, the wedge problem becomes a semi-infinite plane solid including a singularity (see Fig. 4a). From Eq. (10), we see that

$$q = \frac{2\alpha}{\pi} = 1, \tag{25}$$

and then Eq. (23) becomes

$$f(z) = A\,ln(z - z_0) - \bar{A}\,ln(z + \bar{z}_0), \tag{26}$$

where $z = re^{i\theta}, z_0 = r_0 e^{i\theta_0}, \theta, \theta_0 \in \left(-\frac{\pi}{2}, \frac{\pi}{2}\right)$. This is the exact solution for the interaction between a singularity and a half plane.

For this case, we may take the limit $z_0 \to 0$, and when the singularity represents a concentrated anti-plane force

$$A = \frac{F_z}{2\pi\mu i}, \tag{27}$$

So that Eq. (26) becomes

$$f(z) = \frac{F_z}{\pi\mu i} ln\, z. \tag{28}$$

Inserting Eq. (28) into Eq. (1), we get the fundamental solution for the anti-plane case, complementing the well-known Flamant solution for the in-plane case.

A semi-infinite crack interacting with a singularity

By setting $\alpha = \pi$, the wedge problem turns to be a semi-infinite crack interacting with a singularity (see Fig. 4b). From Eq. (10), we have

$$q = \frac{2\alpha}{\pi} = 2, \tag{29}$$

and Eq. (23) becomes

$$f(z) = A\,ln\left(z^{\frac{1}{2}} - z_0^{\frac{1}{2}}\right) - \bar{A}\,ln\left(z^{\frac{1}{2}} + \bar{z}_0^{\frac{1}{2}}\right), \tag{30}$$

where $z = re^{i\theta}, z_0 = r_0 e^{i\theta_0}; \theta, \theta_0 \in (-\pi, \pi)$, and the singularity is located at z_0.

The conventional stress intensity factor induced by the singularity may be defined as

$$K_{III} = \lim_{r\to 0}\sqrt{2\pi r}(\sigma_{23} + i\sigma_{13})_{\theta=0}. \quad (31)$$

Substituting Eq. (30) into the second equation of Eq. (1), and then supplying the stress expression to Eq. (31), after a straightforward manipulation, we find

$$K_{III} = \lim_{r\to 0}\sqrt{2\pi r}(\sigma_{23} + i\sigma_{13})_{\theta=0} = \lim_{r\to 0}\sqrt{2\pi r}\mu f'(z)_{\theta=0} = -\sqrt{\frac{\pi}{2}}\mu\left(\frac{A}{z_0^{\frac{1}{2}}} + \frac{\bar{A}}{\bar{z}_0^{\frac{1}{2}}}\right). \quad (32)$$

Whether the singularity is a screw dislocation or a concentrated anti-plane force, its stress intensity factor can be immediately found. For example, when it represents a screw dislocation,$A = \frac{b_z}{2\pi}$, we can have

$$K_{III} = -\sqrt{\frac{\pi}{2}}\mu\left(\frac{A}{z_0^{\frac{1}{2}}} + \frac{\bar{A}}{\bar{z}_0^{\frac{1}{2}}}\right) = -\frac{\mu b_z}{2}\sqrt{\frac{1}{2\pi}}\left(\frac{1}{z_0^{\frac{1}{2}}} + \frac{1}{\bar{z}_0^{\frac{1}{2}}}\right). \quad (33)$$

This result is completely consistent with the one by Thomson and Sinclair[28]. If the screw dislocation is located at *x*-axis, Eq. (33) turns to

$$K_{III} = -\mu b_z\sqrt{\frac{1}{2\pi x_0}}. \quad (34)$$

Eq. (33) can be treated as the Green's function to evaluate the crack tip stress intensity factor due to the presence of a cloud of screw dislocations in the vicinity of crack tip.

A concentrated force acting at the tip of a wedge

Because the mapping function introduced in this study is not conformal at the point $z = 0$, this case is not found in literature and it must be treated separately. We now consider the case of a concentrated force acting at the vertex of a wedge.

From consideration of Eq. (23c), we can see that the complex function for this case is

$$f(z) = C\,ln\,z^{\frac{1}{q}} - \bar{C}\,ln\,z^{\frac{1}{q}} = \frac{iC_0}{q}ln\,z, \quad (35)$$

in which C_0 is a real number, to be specified. Inserting Eq. (35) into the second equation of Eq. (1), we may get

$$\phi + i\mu w = \mu f(z) = \frac{i\mu C_0}{q} ln\, z = \frac{i\mu C_0}{q} ln\, r\, e^{i\theta} = \frac{i\mu C_0}{q}(ln\, r + i\theta), \tag{36}$$

and by using Eq. (4),

$$T_3 = \int_A^B t_3\, ds = -\phi|_A^B = -Re\left[\frac{i\mu C_0}{q}(ln\, r + i\theta)\right]|_A^B = \left[\frac{\mu C_0}{q}\theta\right]|_A^B = \frac{2\alpha\mu C_0}{q} = -F_z. \tag{37}$$

We have now fixed C_0 so that

$$C_0 = -\frac{qF_z}{2\alpha\mu}. \tag{38}$$

Therefore, Eq. (35) becomes

$$f(z) = \frac{iC_0}{q} ln\, z = \frac{F_z}{2i\alpha\mu} ln\, z. \tag{39}$$

It may be verified that Eq. (39) automatically satisfies the free-traction boundary condition. This is the complementary solution to the one developed in previous sections.

6. The image force on a screw dislocation due to the configuration of the wedge

In this section, we will analyze the image force on a screw dislocation due to the configuration of the wedge, which may be evaluated through the vector *path-independent* integral J_i, which was originally introduced by Eshelby[29]. The integrals J_1 and J_2 may be written as:

$$J_i = \oint_C \left(\omega m_i - T_j \frac{\partial u_j}{\partial x_i}\right) ds = \oint_C \left(\omega m_i - T_3 \frac{\partial w}{\partial x_i}\right) ds\,, \quad (i = 1,2) \tag{40}$$

where m_i is the vector normal to the integral path *C* in Fig. 5, T_3 is the resultant traction acting on integral path and w are displacement on it in anti-plane direction, the strain energy density can be expressed as $\omega = \int_0^{\varepsilon_{ij}} \sigma_{ij} d\varepsilon_{ij}$. It should be pointed out thatJ_1 and J_2 are the components of the image force acting on the singularity in *x*-direction and *y*-direction, respectively, as shown in Fig. 5.

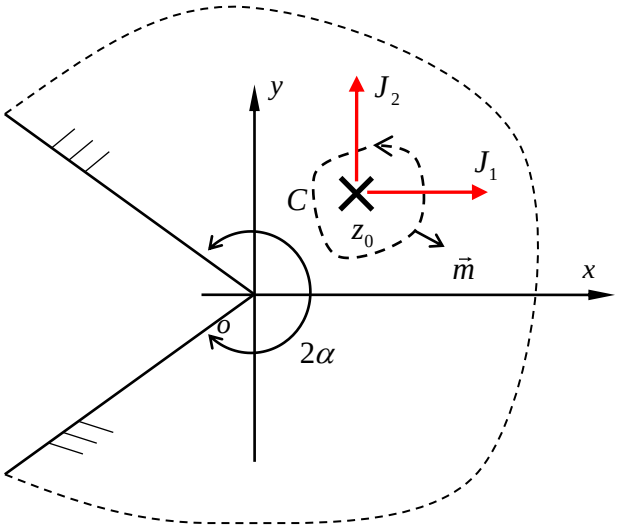


Fig. 5 The image force on a screw dislocation due to the configuration of the wedge

Alternatively, the combination of the two integrals can be expressed in terms of the complex potential as[30]

$$J_1 - iJ_2 = -\frac{\mu i}{2}\oint_C [f'(z)]^2 dz. \tag{41}$$

From Eq. (23c), we know that

$$f'(z) = \frac{A}{\left(z^{\frac{1}{q}} - z_0^{\frac{1}{q}}\right)}\frac{1}{q}z^{\frac{1}{q}-1} - \frac{\bar{A}}{\left(z^{\frac{1}{q}} + \bar{z}_0^{\frac{1}{q}}\right)}\frac{1}{q}z^{\frac{1}{q}-1}, \tag{42}$$

where $A = \frac{b_z}{2\pi}$. By substituting Eq. (42) into Eq. (41), then by using $z = (-i\zeta)^q$ to perform the integration in the ζ -plane, after that, by replacing ζ by $\zeta = iz^{\frac{1}{q}}$, finally, the image force is found to be

$$J_1 - iJ_2 = -\frac{\mu i}{2}\oint_C [f'(z)]^2 dz = -\frac{\mu {b_z}^2}{2\pi q\left(z_0^{\frac{1}{q}} + \bar{z}_0^{\frac{1}{q}}\right)} z_0^{\frac{1}{q}-1} \tag{43}$$

In consideration of $z_0 = r_0 e^{i\theta_0}$ and $q = \frac{2\alpha}{\pi}$, the expressions for J_1 and J_2 may be separately written in terms of real quantities as

$$\begin{cases} J_1 = -\frac{\mu {b_z}^2}{8\alpha\, cos\left(\frac{\pi\theta_0}{2\alpha}\right)} \frac{1}{r_0} cos\left[\left(\frac{\pi}{2}-\alpha\right)\frac{\theta_0}{\alpha}\right] < 0 \\ J_2 = \frac{\mu {b_z}^2}{8\alpha\, cos\left(\frac{\pi\theta_0}{2\alpha}\right)} \frac{1}{r_0} sin\left[\left(\frac{\pi}{2}-\alpha\right)\frac{\theta_0}{\alpha}\right] \end{cases}. \tag{44}$$

It is found from Eq. (44) that $J_1 < 0$, and the direction of J_2 always points to the free surface as $\alpha < \frac{\pi}{2}$, while the direction of J_2 points to the line of geometric symmetry, the *x*-axis, as $\alpha > \frac{\pi}{2}$. When either $\alpha = \frac{\pi}{2}$ or the screw dislocation is exactly located on the *x*-axis, we also find that $J_2 = 0$, and J_1 becomes

$$J_1 = -\frac{\mu {b_z}^2}{8\alpha\, cos\left(\frac{\pi\theta_0}{2\alpha}\right)} \frac{1}{r_0} < 0. \tag{45}$$

The image force on the screw dislocation results from the presence of the free boundary. It is a persistent force that tends to drive the dislocation out of the substrate towards the free surface. When the dislocation is located near the surface, the image force will be large enough to overcome the material internal resistance (the Peierls force) to impel it out of the substrate, which will result a dislocation-free layer. However, when the dislocation is located deeply inside of the substrate, the image force on the dislocation rapidly decreases, and it may be verified that when $r_0 \to \infty$ in Eq. (44) and $\theta_0 \neq \pm\alpha$, the image forces $J_1 \to 0$ and $J_2 \to 0$.

This may shed some light on the mechanism of wedge-singularity interaction and at the same time, it may be regarded as a test to validate the derivation of the general solution.

7. Application: formulation for a slip band under anti-plane loading

In this section, to demonstrate the application of fundamental solutions, a slip band (crack) subjected to some anti-plane loading shown in Fig. 6 will be formulated with Green's function method.

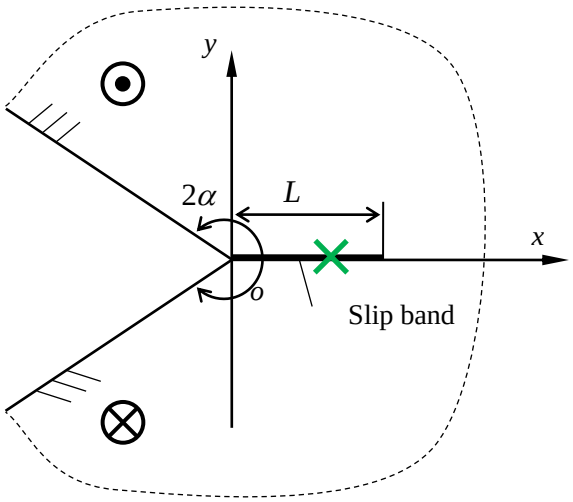


Fig .6 A slip band at the root of a V-notch under anti-symmetric loading

From Eq. (24), a screw dislocation is located at point t on x-axis, and the stress along the x-axis excited by the dislocation is

$$\sigma_{23} = \mu\frac{A}{q}z^{\frac{1}{q}-1}\left(\frac{1}{z^{\frac{1}{q}}-z_0^{\frac{1}{q}}}-\frac{1}{z^{\frac{1}{q}}+\bar{z}_0^{\frac{1}{q}}}\right) = -\frac{\mu}{2\pi q}x^{\frac{1}{q}-1}\left(\frac{1}{t^{\frac{1}{q}}-x^{\frac{1}{q}}}+\frac{1}{x^{\frac{1}{q}}+t^{\frac{1}{q}}}\right)b_z. \tag{46}$$

Then the traction along x-axis excited by a slip band shown in Fig. 6 can be formulated through a continuous dislocation distribution technique as[31]

$$\sigma_{23}^{dis}(x) = -\frac{\mu}{2\pi q}x^{\frac{1}{q}-1}\int_0^L\left(\frac{1}{t^{\frac{1}{q}}-x^{\frac{1}{q}}}+\frac{1}{x^{\frac{1}{q}}+t^{\frac{1}{q}}}\right)B(t)dt, \tag{47}$$

where dislocation density function $B(t) = \frac{db_z}{dt}$. On the other hand, if the traction distribution along x-axis due to some external loading is given as $\sigma_{23}^{appl}(x)$, and the internal friction force along the slip band can be ignored, any infinitesimal dislocation segment in the slip band will be always in equilibrium. It requires

$$\sigma_{23}^{dis}(x) + \sigma_{23}^{appl}(x) = 0. \tag{48}$$

Substituting Eqs. (47) into (48) leads to

$$\frac{1}{\pi}\int_0^L\left(\frac{1}{t^{\frac{1}{q}}-x^{\frac{1}{q}}}+\frac{1}{x^{\frac{1}{q}}+t^{\frac{1}{q}}}\right)B(t)dt = \frac{2q}{\mu}x^{1-\frac{1}{q}}\sigma_{23}^{appl}(x). \tag{49}$$

It can be seen from Eq. (49) that the singular integral equation looks a bit complex because of its singularity form, but at any rate the equation can be transformed into a singular integral equation of the first kind through the method of variable transformation. In a same way, the more complex slip band cases can be formulated, and the traction on the slip band due to external loads can be also evaluated through the Green's function method. More detailed discussion will not be presented here. In the following, to show how to solve Eq. (49) and calculate the stress intensity factor at the slip band tip, without loss of generality, we present a simple case as shown in Fig. 7.

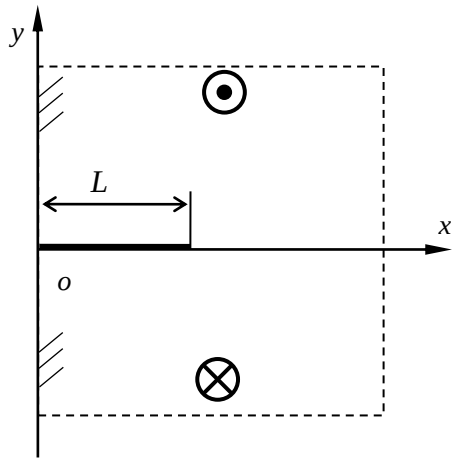


Fig. 7 A slip band developed from a half-plane edge under an anti-symmetric tearing load.

For this case, $\alpha = \frac{\pi}{2}$, and $q = \frac{2\alpha}{\pi} = 1$, and Eq. (49) becomes

$$\frac{1}{\pi}\int_0^L \left(\frac{1}{t-x} + \frac{1}{x+t}\right) B(t)dt = \frac{2}{\mu}\sigma_{23}^{appl}(x). \tag{50}$$

This is a case where a surface crack is subjected to anti-plane loading.

Eq. (50) can be written into a standard form as

$$\frac{1}{\pi}\int_{-1}^1 \left(\frac{1}{T-X} + \frac{1}{(X+T+2)}\right) Q(T)dT = \frac{2}{\mu}\sigma_{23}^{appl}\left(\frac{L(X+1)}{2}\right) = f(X), \tag{51}$$

where $X = \frac{2}{L}x - 1, T = \frac{2}{L}t - 1$, $Q(T) = B\left(\frac{L}{2}(T+1)\right)$. With considering the physical

significance of the slip band, $Q(T)$ can be written as a product of a weight function $(1-T)^{-\frac{1}{2}}(1+T)^{\frac{1}{2}}$ and a regular function $g(T)$ as

$$Q(T) = (1-T)^{-\frac{1}{2}}(1+T)^{\frac{1}{2}}g(T). \tag{52}$$

The numerical algorithm to Eq. (51) has been well studied[32,33], which is

$$\sum_{i=1}^{n} \frac{2(1+T_i)}{2n+1}\left[\frac{1}{T_i - X_j} + \frac{1}{(X_j + T_i + 2)}\right] g(T_i) = f(X_j) \tag{53}$$

where

$$T_i = cos\left(\frac{2i-1}{2n+1}\pi\right), i = 1,2,3 \ldots, n$$

$$X_j = cos\left(\frac{2j}{2n+1}\pi\right), j = 1,2,3 \ldots, n\ . \tag{54}$$

The regular function $g(X)$ can be numerically solved from Eq. (53), which implies that the traction distribution along the slip band is also obtained.

According to the conventional definition, the stress intensity factor at the slip band tip can be defined as

$$K_{III} = \lim_{x \to L^+} \sqrt{2\pi(x-L)}\left[\sigma_{23}^{dis}(x) + \sigma_{23}^{appl}(x)\right] = \lim_{x \to L^+} \sqrt{2\pi(x-L)}\,\sigma_{23}^{dis}(x). \tag{55}$$

Inserting Eqs. (47) into (55) leads

$$\begin{aligned} K_{III} &= -\lim_{x \to L^+} \sqrt{2\pi(x-L)}\,\frac{\mu}{2\pi}\int_0^L \left(\frac{1}{t-x} + \frac{1}{x+t}\right) B(t)\,dt \\ &= -\lim_{x \to L^+} \sqrt{2\pi(x-L)}\,\frac{\mu}{2\pi}\int_0^L \frac{B(t)}{t-x}\,dt \\ &= -\lim_{X \to 1^+} \sqrt{\pi L(X-1)}\,\frac{\mu}{2\pi}\int_{-1}^{1} \frac{Q(T)}{T-X}\,dT \end{aligned} \quad . \tag{56}$$

Further, replacing $Q(T)$ in Eq. (56) by Eq. (52), one can derive

$$
\begin{aligned}
K_{III} &= -\lim_{X\to 1^+}\sqrt{\pi L(X-1)}\,\frac{\mu}{2\pi}\int_{-1}^{1}\frac{(1-T)^{-\frac{1}{2}}(1+T)^{\frac{1}{2}}\,g(T)}{T-X}\,dT \\
&= -\lim_{X\to 1^+}\sqrt{\pi L(X-1)}\,\frac{\mu}{2\pi}\left\{\int_{-1}^{1}\left(\frac{1+T}{1-T}\right)^{\frac{1}{2}}\frac{\left[g(T)-g(X)+g(X)\right]}{T-X}\,dT\right\} \\
&= -\lim_{X\to 1^+}\sqrt{\pi L(X-1)}\,\frac{\mu}{2\pi}\left\{\int_{-1}^{1}\left(\frac{1+T}{1-T}\right)^{\frac{1}{2}}\frac{1}{T-X}\,dT\right\}g(X) \qquad . \quad (57) \\
&= -\lim_{X\to 1^+}\sqrt{\pi L(X-1)}\,\frac{\mu}{2\pi}\left\{\pi-\pi\sqrt{\frac{1+X}{X-1}}\right\}g(X) \\
&= \mu\sqrt{\frac{\pi L}{2}}\,g(1)
\end{aligned}
$$

The general case shown in Eq. (49), where the notch opening angle is arbitrary, can be treated as this procedure, after it is transformed into a standard singular integral equation of the first kind.

8. Concluding remarks

In this study, using the complex conformal mapping technique, the analytical solution for a semi-infinite wedge, interacting with a generalized anti-plane singularity, has been derived. The singularity may be thought of as representing either a screw dislocation or a concentrated anti-plane force. To verify its correctness, a half plane solid and an infinite crack, respectively, interacting with a singularity have been presented. The image force on the screw dislocation due to the wedge configuration has been obtained, from which the dislocation-free zone can be predicted.

To demonstrate the application of the fundamental solutions, a slip band at the root of a V-notch under anti-plane loading has been formulated through Green function method. The solutions developed can be used as building blocks to model V-notch damage problems and the wedge under complex load conditions. Moreover, the generic approach developed in this study may be also used to solve other similar problems.

References

1. Timoshenko SP, Goodier JN, Theory of Elasticity, McGraw Hill, 1951.
2. Neuber H, *Theory of Notch Stresses: Principles for Exact Calculation of Strength with Reference to Structural Form and Material.* Berlin: Springer-Verlag, 1958.
3. Barber JR. *Elasticity.* Springer, 2010.
4. Savruk MP, Kazberuk A. Stress concentration at notches. Springer, 2017.
5. Rushton KR. Stress concentrations arising in the torsion of grooved shafts. *Int J Mech Sci* 1967; 9: 697-705.
6. Ohr SM, Chang SJ, Thomson R. Elastic interaction of a wedge crack with a screw dislocation. *J Appl Phys* 1985; 57:1839-1843.
7. Zappalorto M, Lazzarin P. A new version of the Neuber rule accounting for the influence of the notch opening angle for out-of-plane shear loads. *Int J Solids Struct* 2009; 46: 1901-1910.
8. Williams ML. Stress singularities resulting from various boundary conditions in angular corners of plates in extension. *J Appl Mech* 1952; 19: 526-528.
9. Noda N, Takase Y. Generalized stress intensity factors for V-shaped notch in a round bar under torsion, tension and bending. *Eng Fract Mech* 2003; 70: 1447-1466.
10. Noda N, Takase Y. Stress concentration formula useful for all notch shape in a round bar (comparison between torsion, tension and bending). *Int J Fatigue* 2006; 28: 151-163.
11. Savruk MP, Kazberuk A, Tarasiuk G. Distribution of stresses over the contour of rounded V-shaped notch under antiplane deformation. *Mater Sci* 2012; 47: 717-725.
12. Williams ML. The complex variable approach to stress singularities. *J Appl Mech* 1956; 23: 477-478.
13. Kim, JK, Cho SB. A superposition approach to the stress fields for various blunt V-notches. *Fatigue Fract Eng Mater. Struct* 2012; 36: 139-153.

14. Kim JK, Cho SB. Superposition approach of the stress fields for blunt V-notches under anti-plane shear loading. *International Journal of Precision Engineering and Manufacturing* 2013; 14: 605-612.
15. Qian J, Hasebe N. Property of eigenvalues and eigenfunctions for an interface V-notch in antiplane elasticity. *Eng Fract Mech* 1997; 56: 729-734.
16. Zappalorto M, Lazzarin P, Filippi S. Stress field equations for U and blunt V-shaped notches in axisymmetric shafts under torsion. *Int J Fract* 2010; 164: 253-269.
17. Zappalorto M, Lazzarin P, Yates JR. Elastic stress distributions for parabolic and parabolic notches in round shafts under torsion and uniform antiplane shear loadings. *Int J Solids Struct* 2008; 45; 4879-4901.
18. Tranter CJ. The use of the Mellin transform in finding the stress distribution in an infinite wedge. *Quart J Mech Appl Math* 1948; 1: 125-130.
19. Sneddon IN. *Fourier transforms*. New York: McGraw-Hill, 1951.
20. Faal RT, Fotuhi AR, Fariborz SJ, Daghyani HR. Antiplane stress analysis of an isotropic wedge with multiple cracks. *Int J Solids Struct* 2004; 41: 4535-4550.
21. Theocaris PS, Tsamasfyros G, Andrianopoulos N. The problem of the infinite wedge. *Acta Mechanica* 1979; 34: 63-87.
22. Ma LF, Hills DA. A generalized singularity interacting with a wedge of arbitrary angle. *Int J Solids Struct* 2023; 262-263: 112062.
23. Ma LF. Fundamental formulation for anti-plane eigenstrain problems. *Mech Mater* 2022; 165: 104188.
24. Ma LF, Chen YF, Hills DA. A parabolic notch interacting with a generalized antiplane singularity. *J Appl Mech* 2022; 89: 091001.
25. Rose LRF. The mechanics of transformation toughening. *Proc R Soc Lond* A 1987; 412: 169-197.

26. Ma LF. Fundamental formulation for transformation toughening. *Int J Solids Struct* 2010; 47: 3214-3220.
27. Nelson E. A proof of Liouville's theorem. *Proc Amer Math Soc* 1961; 12: 995.
28. Thomson RM, Sinclair JE. Mechanics of cracks screened by dislocations. *Acta Metall* 1982; 30: 1325-1334.
29. Eshelby JD. The force on an elastic singularity. *Philosophical Transactions of the Royal Society of London* A 1951; 244: 87-112.
30. Budiansky B, Rice JR. Conservation laws and energy-release rates. *J Appl Mech* 1973; 40: 201-203.
31. Hills DA, Kelly PA, Dai DN, Korsunsky AM. *Solution of Crack Problems: The Distributed Dislocation Technique*, Kluwer Academic Publishers, Dordrecht, the Netherlands, 1996.
32. Erdogan F, Gupta GD, Cook TS. On the numerical solution of singular integral equations. 368-425. In: Methods of analysis and solutions of crack problems. Groningen: Noordhoff, 1973.
33. Ma LF, Korsunsky AM. An efficient numerical method for the solution of sliding contact problems. *International Journal for Numerical Methods in Engineering*, 2005; 64: 1236-1255.

Statement of Authorship for joint/multi-authored papers for PGR thesis

To appear at the end of each thesis chapter submitted as an article/paper

The statement shall describe the candidate's and co-authors' independent research contributions in the thesis publications. For each publication there should exist a complete statement that is to be filled out and signed by the candidate and supervisor **(only required where there isn't already a statement of contribution within the paper itself).**

Title of Paper	A generalized anti-plane singularity within a semi-infinite wedge of arbitrary angle
Publication Status	✓Published □ Accepted for Publication □Submitted for Publication □Unpublished and unsubmitted work written in a manuscript style
Publication Details	Ma, L., Chen, Y., & Hills, D. A. (2023). A generalized antiplane singularity within a semi-infinite wedge of arbitrary angle. *The Journal of Strain Analysis for Engineering Design*, 03093247231190684

Student Confirmation

Student Name:	Yifeng Chen		
Contribution to the Paper	Review essential literature. Deduce the basic equations of the paper that forms the final solutions. Check the calculations for the final examples and discuss with the main author about the application of the examples. Review the submitted version.		
Signature: 		Date	21/12/2023

Supervisor Confirmation

By signing the Statement of Authorship, you are certifying that the candidate made a substantial contribution to the publication, and that the description described above is accurate.

Supervisor name and title: Prof. Lifeng Ma		
Supervisor comments This paper involves a significant amount of calculation with complex algebra. Yifeng has been instrumental in deducing the solution that leads to the final formula. He also made considerable efforts to revise the solution and compare it with classic problems. Therefore, I agree to include this paper as a part of his final thesis.		
Signature: 	Date	2023 Dec 23

6. Parabolic Notch interacting with anti-plane singularity

6.1. Introduction

In the last chapter, we developed a complex variable method for analyzing the interaction between a wedge, or a sharp notch, and an anti-plane singularity. In actual engineering design, sharp notches are typically avoided due to their singular nature. Therefore, this chapter will focus on a case of 'plate with a defect' problem with more practical use, that is a blunt notch interacting with an anti-plane singularity. We will discuss the scenario in which the blunt notch forms the shape of a parabolic curve and deduce the stress potential related to it.

The procedure for addressing this problem closely mirrors that of the previous chapter, involving conformal mapping followed by the application of the analytical continuation argument. The conformal mapping transforms the parabolic notch onto a half-plane. Subsequently, the analytical continuation argument is employed to solve for the complex potential using the zero-traction boundary condition. The example cases considered in this chapter include a parabolic notch subjected to a pair of concentrated forces where the stress field is explored; and a parabolic notch containing a screw dislocation, where the driving force is calculated in relation to its position from the tip of the parabolic notch.

6.2. Paper：A Parabolic Notch Interacting with a Generalized Anti-plane Singularity[5]

Abstract

In this study, the interaction of a parabolic notch with a generalized anti-plane singularity is studied and its analytical solution is derived. The singularity may be either an anti-plane concentrated force or a screw dislocation, and separate solutions for each of these are found. The driving force present on the screw dislocation due to the notch free boundary is obtained. It is found that a dislocation-free zone may exist beneath the notch root surface when the screw dislocation is placed on the notch geometric symmetry axis, as the driving force will pull dislocations to the free boundary where they will be annihilated. The solutions developed in this study may be used as building blocks to model the damage of material near a parabolic notch under anti-plane load conditions, and therefore serve as a step in quantifying crack nucleation conditions, which is the novelty of the current study.

Keywords： Singularity, parabolic notch, screw dislocation, anti-plane concentrated force, conformal mapping.

1. Introduction

A notch is a common feature necessarily figuring in many mechanical components, possibly included for practical requirements such as component assembly (the grooves needed for retention clips, for example) or power transmission, as in the shaft spline. A knowledge of the stress fields ahead of notches is essential during design and fatigue assessment. To understand the stress distribution near notches, great efforts have been put into studying this topic. There are two fundamental classes: ‘sharp’ and ‘blunt’.

[5] Ma, L., Chen, Y., & Hills, D. A. (2022). A Parabolic Notch Interacting with a Generalized Anti-plane Singularity. Journal of Applied Mechanics, 89(9), 091001.

Considering the sharp notch first and also ‘in-plane’ loading, Williams [1] developed a method for expanding the Airy stress function as an eigenfunction series, presenting an asymptotic solution for the distribution of stress around a sharp V-notch. Traditional notch stress intensity factors are the multipliers on first symmetric and anti-symmetric terms in Williams’ solution. The factors can be thought of as the extensions of the conventional stress intensity factors used for cracked components. But, the most important property of the solution found is that the eigensolutions provide very precise information about stress gradients and the spatial distribution of stresses; they therefore provide a lot of information about the neighbourhood in which cracks may potentially start, and it is straightforward to represent the environment present in a complicated prototype in a laboratory experiment to a very high degree of fidelity.

Now, turning to *blunt* notches and again ‘in-plane’ loading, Neuber [2] dealt with the stress *concentration* for a blunt notch using the first term in a series expansion of Airy biharmonic potential functions. The simple stress concentration factor was adopted to directly characterize the stress field of blunt notches *at a point* (see, e.g., [3-7]). It seems that this approach is perceived to be simpler in practical engineering so that it has been widely employed (e.g., [8-12]). It is attractive because of its simplicity, but a lot of information is lost by this approach. In particular, there is no information about the gradients of stress, nor their spatial distribution.

Approaching the problem from the opposite direction, by taking advantage of the Kolosov-Muskhelishvili complex variable formulae [13], the sharp V-notch was investigated with finite representative complex terms by Carpenter [14-17]. And, following Carpenter’s efforts, by combining the Kolosov-Muskhelishvili approach with Neuber’s conformal mapping [2,13], a substantial attempt to provide a unified approach to the analysis of cracks, sharp and blunt V-notches was proposed by Lazzarin and Tovo [18]. In order to improve the

accuracy of the approach and its application, much further work has been done (see, e.g., [19-21]). In these studies notch problems are treated by a stress function series expansion, or by employing a series terms to find asymptotic or approximate solutions.

In addition to the in-plane deformation, notches under anti-plane load or torsion loading have even been received particular attention since the excellent pioneering investigations of stress fields around grooves or cracks [22-25]. Torsion of circular shafts is, of course, a problem in which a surface notch undergoes, locally, pure anti-plane loading. In more general problems notches may experience complicated states of stress which, locally, comprise an in-plane pair of loads (opening and shear) together with an anti-plane contribution.

Within the framework of a geometrically plane assumption, studies of both the sharp V-notch and blunt V-notch under anti-plane loading has been conducted for a long time (see, e.g., [26-32]). The stress distributions near the root of an elliptically cylindrical notch under torsional loading has been documented (see, e.g., [33, 34]). Elastic stress distributions for hyperbolic, parabolic and more generalized notches in round shafts under torsion and uniform anti-plane shear loading have been analyzed [35, 36]. Recently, a unified solution approach for a large variety of anti-plane shear and torsion notch problems has been performed by Salviato and Zappalorto [37]. The main approaches employed in these studies are either direct approximate elastic solutions, or the complex potential method used in combination with all kinds of transform into curvilinear coordinates (see, e.g., [2]).

The work described above represents very considerable progress in our understanding of the problems but some remaining challenges still exist. Firstly, strictly speaking, the aforementioned analysis has been conducted in an asymptotic or approximate sense. It is hard to cover various load conditions, including the far-field loads, and the near-field loads such as acting body force loads and displacement loads in the neighborhood of notches. Secondly, apart from some finite element simulations, the damage such as crack initiation, crack propagation,

or plastic deformation, occurred near the root of notches due to high stress concentration, can be modelled in terms of continuous dislocation distribution through Green's function method, which is able to reflect the physical damage mechanism. However, at present, its kernel function is hard to be established. These challenges demand a rigorous and thorough analysis on the blunt notch problems. As a first step, in this paper the parabolic notch is studied, and the effect of generalized singularity, producing an anti-plane stress field in its neighbourhood, is found. This complements our recent efforts in establishing the corresponding solution for in-plane loading [38].

The aim of this complementary study is to develop a fundamental solution for a parabolic notch interacting with a generalized anti-plane singularity. The singularity may be either an out-of-plane concentrated force or a screw dislocation, or various combinations of them, which may lead to a moment load, a residual stress (or strain) state, and so on (see, e.g., [39]). The intended application of the results is two-fold; first, as a means of generating a wide range of equivalent remote loads in a simple and versatile way, and secondly, to provide the possibility of analyzing local notch root plasticity in a way which correctly tracks out the plastic flow rules.

Following this strategy, we use complex variable methods to derive closed-form solutions to the problem of a parabolic notch interacting with the anti-plane singularity. The basic geometry we will consider is shown in Fig. 1, in which, the generalized anti-plane singularity is arbitrarily located within the infinite notched solid.

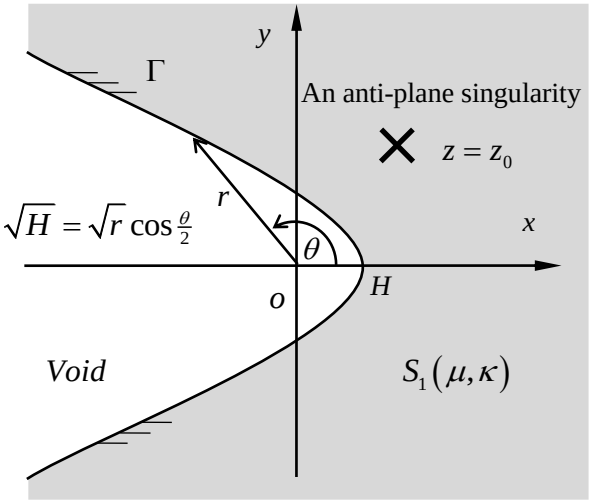


Fig. 1 The configuration of a parabolic notch interacting with a generalized anti-plane singularity which is located at an arbitrary point within solid S_1, and the void is located at the left side.

The procedure followed is outlined as follows: first, the complex formulae for anti-plane deformation and the generalized anti-plane singularity are presented in §2, and the basic model is formulated in §3. The solution for the interaction between a parabolic notch and an anti-plane singularity is derived in §4. Subsequently, in §5, two examples are analyzed: first a parabolic notch interacting with a pair of concentrated forces, and secondly a parabolic notch interacting with a screw dislocation. The force present on the dislocation is derived. Finally conclusions are drawn in §6.

2. The complex framework and its form for a generalized anti-plane singularity

In this section, complex variable formulae for out-of-plane problems and boundary conditions are introduced. The general singularity model is introduced which provides a basic

concept for subsequent analysis.

2.1 The complex potential formulae

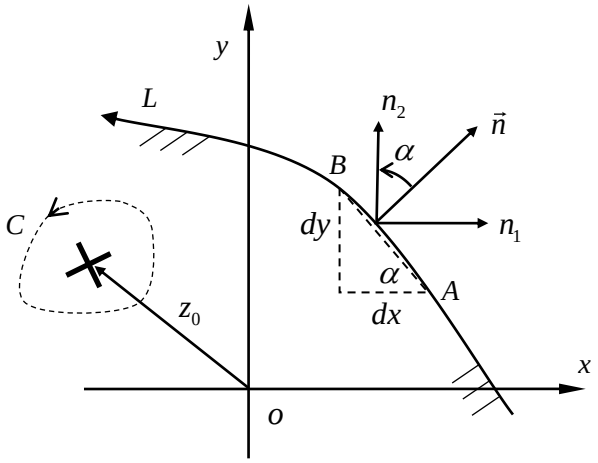


Fig. 2 The framework of anti-plane deformation and a generalized anti-plane singularity (shown here by a cross sign) embedded within a plane solid whose boundary is *L*.

In the anti-plane shear deformation of an isotropic elastic material, the in-plane displacements are $u = v = 0$, and the out-of-plane displacement is $w = w(x, y)$. The geometric equations, the constitutive equation and the equilibrium equation are as follows

$$\gamma_{13} = \frac{\partial w}{\partial x}, \gamma_{23} = \frac{\partial w}{\partial y}, \sigma_{13} = \mu\gamma_{13}, \sigma_{23} = \mu\gamma_{23}, \frac{\partial \sigma_{13}}{\partial x} + \frac{\partial \sigma_{23}}{\partial y} = 0, \tag{1}$$

where γ_{13} and γ_{23} are strains, σ_{13} and σ_{23} are anti-plane shear stresses, and μ is the shear modulus. From (1) we get

$$\frac{\partial^2 w}{\partial^2 x} + \frac{\partial^2 w}{\partial^2 y} = 0. \tag{2}$$

Its formal solution can be expressed in terms of a holomorphic function $f(z)$ of the complex variable $z = x_1 + ix_2 (= x + iy)$ as

$$w = -\frac{i}{2}\left[f(z) - \bar{f}(\bar{z})\right], \tag{3}$$

where $i = \sqrt{-1}$.

With the help of (3), the two stress components can be rewritten as

$$\begin{cases}\sigma_{13}=\mu\dfrac{\partial w}{\partial x}=-\dfrac{i}{2}\mu\left[f'(z)-\overline{f}'(\bar{z})\right]\\ \sigma_{23}=\mu\dfrac{\partial w}{\partial y}=\dfrac{\mu}{2}\left[f'(z)+\overline{f}'(\bar{z})\right]\end{cases}. \tag{4}$$

Now, we consider traction boundary condition shown in Fig. 2. Let t_3 be the nonzero traction component along the x_3-direction on a boundary L, with material present on the left-hand side. The resultant traction can be written as:

$$t_3=\sigma_{i3}n_i=\sigma_{13}n_1+\sigma_{23}n_2=\sigma_{13}\frac{\partial y}{\partial s}-\sigma_{23}\frac{\partial x}{\partial s}, \tag{5}$$

where $n_1=\frac{\partial y}{\partial s}, n_2=-\frac{\partial x}{\partial s}$ are components of the surface unit normal. In consideration of the equilibrium equation in (1), the two stress components can be related to a stress function ϕ as

$$\sigma_{13}=-\phi_{,2}\quad \sigma_{23}=\phi_{,1}. \tag{6}$$

So Eq. (5) can be reformulated as

$$t_3=\sigma_{i3}n_i=\sigma_{13}n_1+\sigma_{23}n_2=-\phi_{,2}\frac{\partial y}{\partial s}-\phi_{,1}\frac{\partial x}{\partial s}=-\frac{d\phi}{ds}. \tag{7}$$

Alternatively, because

$$\begin{cases}n_1=\dfrac{\partial y}{\partial s}=\dfrac{\partial(z-\bar{z})}{2i\partial s}=\dfrac{1}{2}\left(-i\dfrac{\partial z}{\partial s}+i\dfrac{\partial \bar{z}}{\partial s}\right)\\ n_2=-\dfrac{\partial x}{\partial s}=-\dfrac{\partial(z+\bar{z})}{2\partial s}=-\dfrac{1}{2}\left(\dfrac{\partial z}{\partial s}+\dfrac{\partial \bar{z}}{\partial s}\right)\end{cases}, \tag{8}$$

Eq. (5) can be rewritten as

$$t_3=\sigma_{i3}n_i=\sigma_{13}n_1+\sigma_{23}n_2=-\frac{\mu}{2}\frac{\partial[f(z)+\bar{f}(\bar{z})]}{\partial s}. \tag{9}$$

Thus by combining (7) and (9), we have

$$t_3=-\frac{\mu}{2}\frac{\partial[f(z)+\bar{f}(\bar{z})]}{\partial s}=-\frac{\partial\phi}{\partial s}. \tag{10}$$

The resultant force acting on an arc $\overset{\frown}{AB}$ is (see, Fig. 2)

$$T_3=\int_A^B t_3\,ds=-\frac{\mu}{2}\left[f(z)+\bar{f}(\bar{z})\right]\Big|_A^B=-\phi\Big|_A^B. \tag{11}$$

Furthermore, using the above formulae, we can obtain

$$\begin{cases}\sigma_{23}+i\sigma_{13}=\mu f'(z)\\ \phi+i\mu w=\mu f(z)\end{cases}, \tag{12}$$

where the constant is discarded during the operation. Eqs. (11) and (12) will be frequently used in the following manipulation.

2.2 The complex potential for singularities

A generalized anti-plane singularity, located at z_0 in an infinite plane, which may be a screw dislocation or an anti-plane concentrated force, has a complex variable potential which may be expressed as

$$f_0(z) = A\, ln(z - z_0), \tag{13}$$

where *A* is a complex number, to be determined by one of the following singularity conditions

$$\begin{cases} b_z = \oint_{z_0} dw \\ F_z = -\oint_{z_0} dT_3 = \oint_{z_0} d\phi \end{cases} \tag{14}$$

The contour of integration should enclose the singularityz_0, and in the first equation b_z is the Burgers vector while in the second F_z is the out-of-plane concentrated force in *z*- direction. Inserting Eq. (13) into the last equation in (12), and considering (14), we obtain

$$f_0(z) = \frac{(F_z + i\mu b_z)}{2\pi\mu i} ln(z - z_0). \tag{15}$$

If $F_z = 0$, it degenerates to the complex variable potential for a screw dislocation in infinite solid:

$$f_0(z) = \frac{b_z}{2\pi} ln(z - z_0), \tag{16}$$

while if $b_z = 0$, it degenerates to the solution for an out-of-plane concentrated force as

$$f_0(z) = \frac{F_z}{2\pi\mu i} ln(z - z_0). \tag{17}$$

With (15) established, the complex potential for an anti-plane concentrated moment or an anti-plane eigenstrain nucleus may also be derived (see e.g., [39-41]).

3. Formulation

3.1 Physical problem

Consider a parabolic notch with a surface Γ which extends to infinity, as shown in Fig. 1, where a generalized anti-plane singularity is located in the substrate material. The parabolic surface can be described by the following function in a polar coordinate set, as set out by [35]

$$h = \sqrt{H} = \sqrt{r}\, cos\frac{\theta}{2}, \tag{18}$$

where h and H are constant numbers, and H has a length dimension. Its corresponding expression in rectangular coordinate system is

$$x = H - \frac{y^2}{4H}, \text{ or } \left(\frac{x}{H}\right) = 1 - \frac{1}{4}\left(\frac{y}{H}\right)^2 . \tag{19}$$

This implies that a series of parabolic notches can be described in a standard expression.

For this geometry, the complex potentials within the elastic solid, identified asS_1 can be constructed from

$$f(z) = f_0(z) + f_1(z), z \in S_1, \tag{20}$$

where $f_0(z)$ represents the complex potential of a generalized anti-plane singularity in an infinite plane shown in Eq. (15), and $f_1(z)$ is a regular perturbed complex potential in S_1, which will be determined from the free surface boundary condition. It should be pointed out that $f_1(z)$ will reflect the material presence, the geometric surface boundary conditions, and incorporate the presence of the singularity.

3.2 Conformal mapping

To solve the physical problem, it is convenient to map the physical configuration onto an auxiliary configuration in which the surface is mapped into a straight line, so that the traditional complex variable techniques can be employed to solve the problem. To this end we introduce the mapping function as follows

$$\begin{cases} z = x + iy = re^{i\theta} = \omega(\zeta) = (-i\zeta + h)^2, h > 0 \\ \zeta = \omega^{-1}(z) = i\left(z^{\frac{1}{2}} - h\right) = u + iv, h = \sqrt{H} \end{cases}. \tag{21}$$

We find that

$$v = \sqrt{r}\cos\frac{\theta}{2} - h, \;\; u = -\sqrt{r}\sin\frac{\theta}{2}. \tag{22}$$

The mapping functions (21) map the physical z-plane in Fig. 3a onto the auxiliary ζ-plane in Fig. 3b. It may be observed from Fig. 3 that the material S_1 in Fig. 3a is mapped onto the upper plane in Fig. 3b, while the void in Fig. 3a is mapped onto the lower plane in Fig. 3b. The free surface is mapped into the u-axis in ζ-plane.

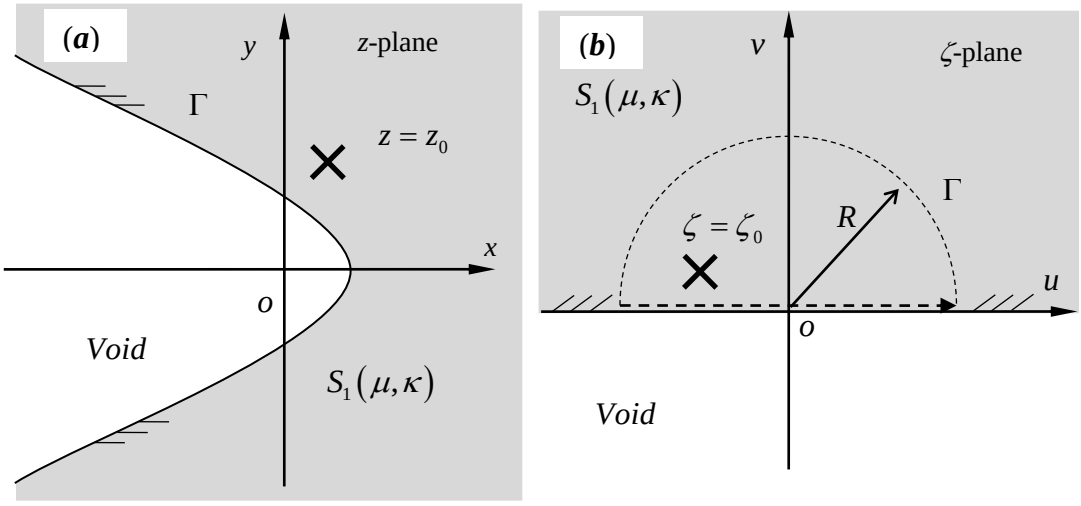


Fig. 3 A parabolic notch in an infinite plane interacting with a singularity located in material S_1 (right-side): (a) physical model, (b) auxiliary plane

In terms of the mapping, Eq. (11) can be rewritten as

$$T_3 = -\frac{\mu}{2}\left[\hat{f}(\zeta) + \overline{\hat{f}(\zeta)}\right], \tag{23}$$

and Eq. (20) will be transformed to

$$\hat{f}(\zeta) = \hat{f}_0(\zeta) + \hat{f}_1(\zeta), \zeta \in S_1, \tag{24}$$

in which, accordingly,

$$\begin{aligned}\hat{f}_0(\zeta) &= f_0\left(\omega(\zeta)\right) = A\ln\left(\left(-i\zeta+h\right)^2-\left(-i\zeta_0+h\right)^2\right)\\ &= A\ln\left(\zeta_0-\zeta\right)+A\ln\left(\zeta+\zeta_0+2hi\right)\end{aligned}. \tag{25}$$

According to Liouville's theorem, it is logically assumed that the function $\hat{f}_1(\zeta)$ is regular within S_1 and singular within S_2, while $\bar{\hat{f}}_1(\zeta)$ is regular within S_2 and singular within S_1in Fig. 3b.

With the traction-free condition on the notch surface ($Im(\zeta) = v = 0$) in Fig. 3b, inserting (24) into Eq. (23) leads to

$$\hat{f}_0(\zeta) + \hat{f}_1(\zeta) + \overline{\hat{f}_0(\zeta)} + \overline{\hat{f}_1(\zeta)} = 0, (\zeta = u). \tag{26}$$

Further, by substituting (25) into (26), it can be rearranged to give

$$\begin{aligned}A\,ln(\zeta_0 - u) + A\,ln(u + \zeta_0 + 2hi) + \hat{f}_1(u) + \bar{A}\,ln(\bar{\zeta}_0 - u)\\ + \bar{A}\,ln(u + \bar{\zeta}_0 - 2hi) + \overline{\hat{f}_1}(u) = 0.\end{aligned} \tag{27}$$

Eq. (27) is a typical boundary value problem in terms of complex variables with a specific mapping, from which $\hat{f}_1(\zeta)$ is to be determined. Once it is solved, the primitive function$f_1(z)$ in Eq. (20) will be fixed.

4. Solution

In this section, some integral formulae will be presented. By virtue of these identities, Eq. (27) will be solved.

4.1 Integral formulae: Cauchy's integral formula and integral formulae for holomorphic function with singularities

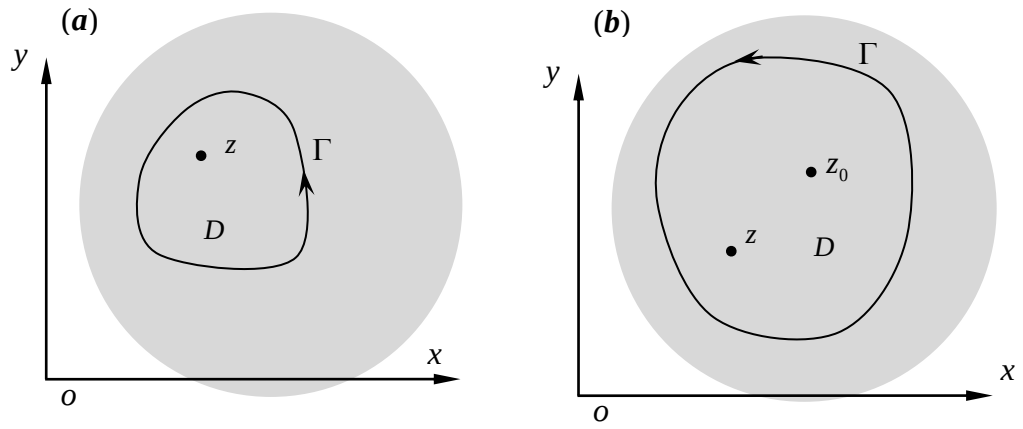


Fig. 4 Integral formulae and function holomorphism in a complex plane: (*a*) function holomorphism in a domain, (*b*) function holomorphism in a domain but with a singularity in the integral contour.

Cauchy's integral formula would play a key role in the following manipulation. It can be described as: A holomorphic function $f(z)$ defined on a domain D enclosed by a curve Γ is completely determined by its values on the boundary Γ (see Fig. 4a)

$$f(z)=\begin{cases}\frac{1}{2\pi i}\oint_{\Gamma}\frac{f(t)dt}{(t-z)}, (z\in D)\\ 0, \qquad\qquad (z\notin D)\end{cases}. \tag{28}$$

and it also results in integral formulas for all derivatives of the holomorphic function as

$$f^{(n)}(z)=\begin{cases}\frac{n!}{2\pi i}\oint_{\Gamma}\frac{f(t)dt}{(t-z)^{n+1}}, (z\in D)\\ 0, \qquad\qquad (z\notin D)\end{cases} n\geq 0. \tag{29}$$

On the other hand, if there is a singularity within the holomorphic plane, as shown in Fig. 4b, $\lim_{t\to z_0} f(t)=\infty$, and the singularity is enclosed within the contour, we can prove that [38]

$$\frac{n!}{2\pi i}\oint_{\Gamma}\frac{f(t)dt}{(t-z)^{n+1}}=\begin{cases}Cf(\infty), (z\in D, n=0)\\ 0, (z\in D, n\geq 1)\end{cases}. \tag{30}$$

where C is a finite constant and $f(\infty)$ is a constant at infinity. For convenience, we suppose that $\lim_{z\to\infty} f(z)=0$ which does not influence the stress analysis in this study. So that

$$\frac{n!}{2\pi i}\oint_{\Gamma}\frac{f(t)dt}{(t-z)^{n+1}}=0, (z\in D, n\geq 0)\ . \tag{31}$$

4.2 Solution

Because $\hat{f}_0(\zeta)$ and $\bar{\hat{f}}_1(\zeta)$ are non-holomorphic while $\bar{\hat{f}}_0(\zeta)$ and $\hat{f}_1(\zeta)$ are holomorphic within the upper plane in Fig. 3b, multiplying both sides of Eq. (27) by $\frac{1}{2\pi i}\frac{du}{(u-\zeta)}$and performing the integration along the contour Γ in the upper plane in Fig. 3b as $R \to \infty$, and considering (29) and (31), we obtain

$$\hat{f}_1(\zeta) + A\, ln(\zeta + \zeta_0 + 2hi) + \bar{A}\, ln(\bar{\zeta}_0 - \zeta) = 0, \tag{32}$$

which gives

$$\hat{f}_1(\zeta) = -A\, ln(\zeta + \zeta_0 + 2hi) - \bar{A}\, ln(\bar{\zeta}_0 - \zeta). \tag{33}$$

This is the perturbed potential solution in the auxiliary plane. It can be verified that it is regular in the upper ζ-plane, which completely complies with the preceding assumption.

Now, by substituting $\zeta = i\left(\sqrt{z} - h\right)$ from (21) into (33), it follows that

$$f_1(z) = -A\, ln\left[i\left(\sqrt{z} + \sqrt{z_0}\right)\right] - \bar{A}\, ln\left[-i\left(\sqrt{\bar{z}_0} + \sqrt{z} - 2h\right)\right]. \tag{34}$$

After discarding the constants involved in the above expression, which do not influence the stress expression in (12), the solution (20) for the singularity-notch interaction problem is finally seen to be

$$f(z) = f_0(z) + f_1(z) = A\, ln(z - z_0) - A\, ln\left(\sqrt{z} + \sqrt{z_0}\right) - \bar{A}\, ln\left(\sqrt{\bar{z}_0} + \sqrt{z} - 2h\right). \tag{35}$$

By inserting the function $f(z)$ into (12), the stress and displacement fields can be found.

It should be mentioned that the analytic solution for a screw dislocation interacting with a parabolic elastic inhomogeneity has been recently derived by Wang and Schiavone [42]. Their solution was expressed as a complex variable series.

5. Examples: Analytical solution for the parabolic notch interacting with singularities

In §4, we have obtained the general solution. In this section we present two examples, as shown in Fig. 5: (*a*) a parabolic notch under two opposing concentrated anti-plane forces which

are symmetrically distributed along the two sides of symmetric line *x*-axis, and (*b*) a parabolic notch interacting with a screw dislocation. The first example is to numerically verify the foregoing equation manipulation. The second is to investigate the configuration-force acting on the screw dislocation. For simplicity, but without loss of the generality, we here set $H = 1$, which would imply that other variables involved such as z, z_0 Burgers vector b_z, and F_z would be simultaneously treated as being divided by *H* (see Eq. (21), $H = h^2$).

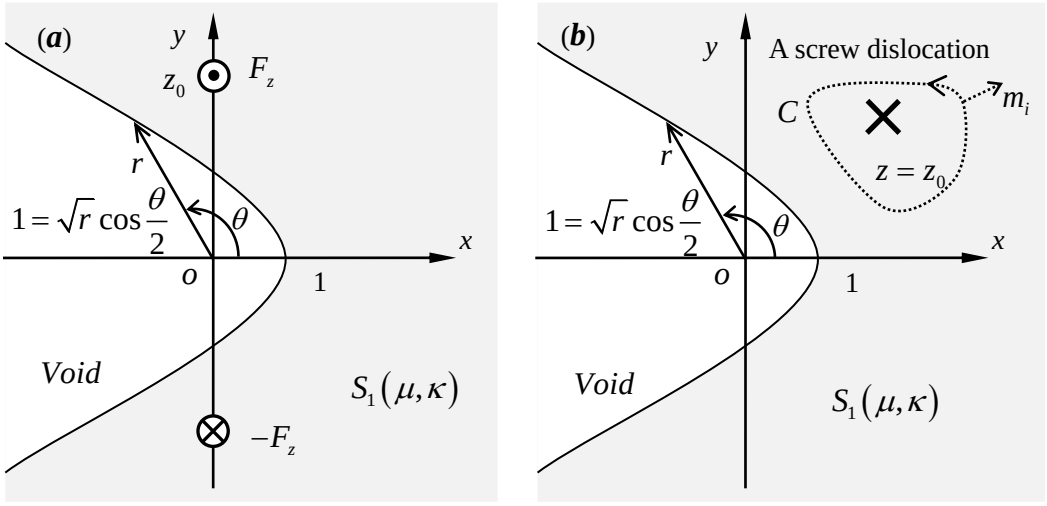


Fig. 5 Examples: (*a*) a parabolic notch under two opposed concentrated anti-plane forces which are symmetrically distributed along the two side of symmetric line *x*-axis; (b) a parabolic notch interacting with a screw dislocation.

5.1 Stress field excited by the two concentrated forces (see Fig. 5a)

Since there are two singularities which are symmetrically distributed as shown in Fig. 5a, the complex potential solution for the problem can be assembled as

$$f(z) = \frac{F_z}{2\pi\mu i}\left[ln(z-z_0) - ln\left(\sqrt{z}+\sqrt{z_0}\right) + ln\left(\sqrt{\bar{z}_0}+\sqrt{z}-2\right)\right]$$
$$-\frac{F_z}{2\pi\mu i}\left[ln(z-\bar{z}_0) - ln\left(\sqrt{z}+\sqrt{\bar{z}_0}\right) + ln\left(\sqrt{z_0}+\sqrt{z}-2\right)\right] \quad (36)$$

and its derivative is

$$f'(z)=\frac{F_z}{2\pi\mu i}\left[\begin{matrix}\frac{1}{(z-z_0)}-\frac{1}{(z-\bar{z}_0)}+\frac{1}{2\sqrt{z}(\sqrt{z}+\sqrt{\bar{z}_0})}-\frac{1}{2\sqrt{z}(\sqrt{z}+\sqrt{z_0})}\\+\frac{1}{2\sqrt{z}(\sqrt{\bar{z}_0}+\sqrt{z}-2)}-\frac{1}{2\sqrt{z}(\sqrt{z_0}+\sqrt{z}-2)}\end{matrix}\right]. \quad (37)$$

Inserting Eq. (37) into the first equation of (12), the stress field will be immediately derived. To provide an illustration of the stress distribution, we take $z_0 = 6i$ in Fig. 5a. The stress distributions induced are plotted in Fig. 6, in which the normalized stresses are defined as$\bar{\sigma}_{i3} = \frac{2\pi\sigma_{i3}}{F_z}$. It can be observed from Fig. 6 that: (*i*) the stress $\bar{\sigma}_{13}$is anti-symmetrically distributed about *x*-axis so that its value is always 0 along the *x*-axis; (*ii*) the stress $\bar{\sigma}_{23}$is symmetrically distributed about *x*-axis and the stress is concentrated around the notch throat. These stress distribution patterns partially demonstrate the reliability of the above solutions we derived.

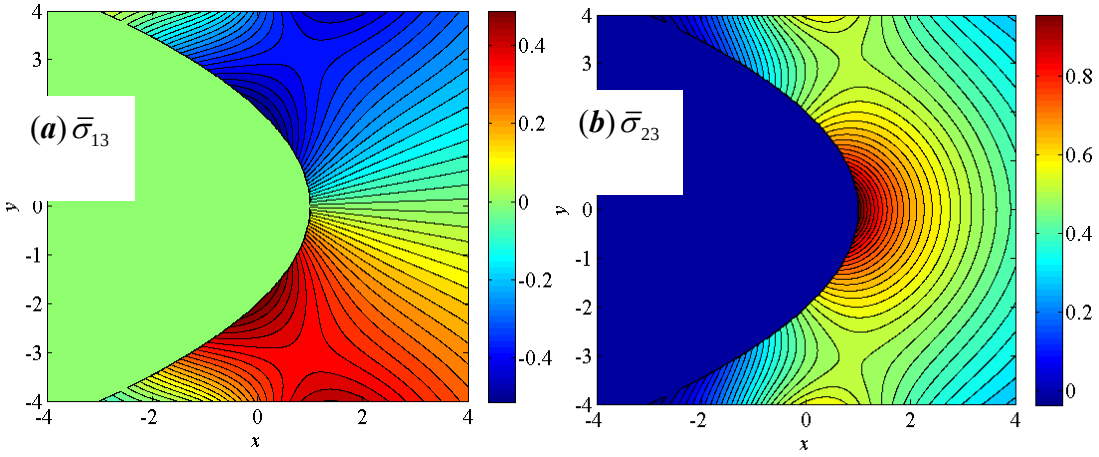


Fig. 6 Normalized stress distribution at the notch throat due to two opposite concentrated anti-plane forces respectively acting at the points (0,6) and (0,-6);

$$(a)\ \bar{\sigma}_{13}=\frac{2\pi\sigma_{13}}{F_z},\ (b)\ \bar{\sigma}_{23}=\frac{2\pi\sigma_{23}}{F_z}$$

5.2 The driving force on the dislocation (see Fig. 5b)

As shown in Fig. 5b, a screw dislocation is embedded within the substrate and the complex potential solution for this problem will be

$$f(z)=f_0(z)+f_1(z)=A\,ln(z-z_0)-A\,ln\left(\sqrt{z}+\sqrt{z_0}\right)-\bar{A}\,ln\left(\sqrt{\bar{z}_0}+\sqrt{z}-2\right) \quad (38)$$

where $A=\frac{b_z}{2\pi}$ and the Burgers vector b_z should be understood by being normalized by H as

before.

The presence of a curved free surface or an external force causes a force to act on the singularity, and this may be evaluated through the vector integral J_i, which was originally introduced by Eshelby [43], and later on its component $J = J_1$ was independently introduced into fracture mechanics by Cherepanov [44] and Rice [45]. The integrals J_1 and J_2 can be written as:

$$J_i = \oint_C \left(w m_i - T_j \frac{\partial u_j}{\partial x_i} \right) ds = \oint_C \left(w m_i - T_3 \frac{\partial w}{\partial x_i} \right) ds\,, \quad (i = 1,2) \tag{39}$$

where m_i is the vector normal to the integral path *C* in Fig. 5b, T_3 are the resultant forces acting on integral path and w are displacement on it in anti-plane direction, the strain energy density can be expressed as $w = \int_0^{\varepsilon_{ij}} \sigma_{ij} d\varepsilon_{ij}$. It should be pointed out that (*i*) both J_1 and J_2 are path-independent integrals, i.e. each integral has an identical value for any integral path enclosing the singularity, and (*ii*) J_1 and J_2 are the components of the driving force acting on the singularity in *x*-direction and *y*-direction, respectively.

Alternatively, the combination of the two integrals can be expressed in terms of the complex potential as [46]

$$J_1 - iJ_2 = -\frac{\mu i}{2} \oint_C [f'(z)]^2 dz. \tag{40}$$

By substituting Eq. (38) into Eq. (40), the driving force is found to be

$$\begin{aligned} J_1 - iJ_2 &= -\frac{\mu i}{2} \oint_C \left[\frac{A}{(z - z_0)} - \frac{A}{2\sqrt{z}\left(\sqrt{z} + \sqrt{z_0}\right)} - \frac{\bar{A}}{2\sqrt{z}\left(\sqrt{\bar{z}_0} + \sqrt{z} - 2\right)} \right]^2 dz \\ &= -\mu\pi \left[\frac{A^2}{2z_0} + \frac{A\bar{A}}{\sqrt{z_0}\left(\sqrt{\bar{z}_0} + \sqrt{z_0} - 2\right)} \right] \end{aligned}. \tag{41}$$

If we write $z_0 = re^{i\alpha}$, the expressions for J_1 and J_2 can be separately written as

$$\begin{cases} J_1 = -\frac{\pi\mu A^2}{2}\left(\frac{\cos\alpha}{r} + \frac{2\cos\psi}{R}\right) \\ J_2 = -\frac{\pi\mu A^2}{2}\left(\frac{\sin\alpha}{r} + \frac{2\sin\psi}{R}\right) \end{cases}, \tag{42}$$

where

$$\begin{cases} R = \left[\left(r + r\cos\alpha - 2\sqrt{r}\cos\frac{\alpha}{2}\right)^2 + \left(r\sin\alpha - 2\sqrt{r}\sin\frac{\alpha}{2}\right)^2\right]^{\frac{1}{2}} \\ tan\,\psi = \frac{\left(r\sin\alpha - 2\sqrt{r}\sin\frac{\alpha}{2}\right)}{\left(r + r\cos\alpha - 2\sqrt{r}\cos\frac{\alpha}{2}\right)} \end{cases}. \tag{43}$$

It can be found from Eqs. (42) and (43) that, if $-\delta \le \alpha \le \delta$, where δ is a small positive number, $J_1 < 0$, and the direction of J_2 is always pointing to the geometric symmetric line *x*-axis.

If the dislocation is exactly located on the *x*-axis and no external force applied, we also find that $J_2 = 0$, and the normalized J_1 becomes

$$\bar{J}_1 = \frac{2}{\mu\pi A^2} J_1 = -\left(\frac{1}{x} + \frac{1}{\sqrt{x}-1} - \frac{1}{\sqrt{x}}\right). \tag{44}$$

By using Eq. (44), the driving force J_1 on the screw dislocation versus its location on *x*-axis in Fig. 5b is drawn and shown in Fig. 7.

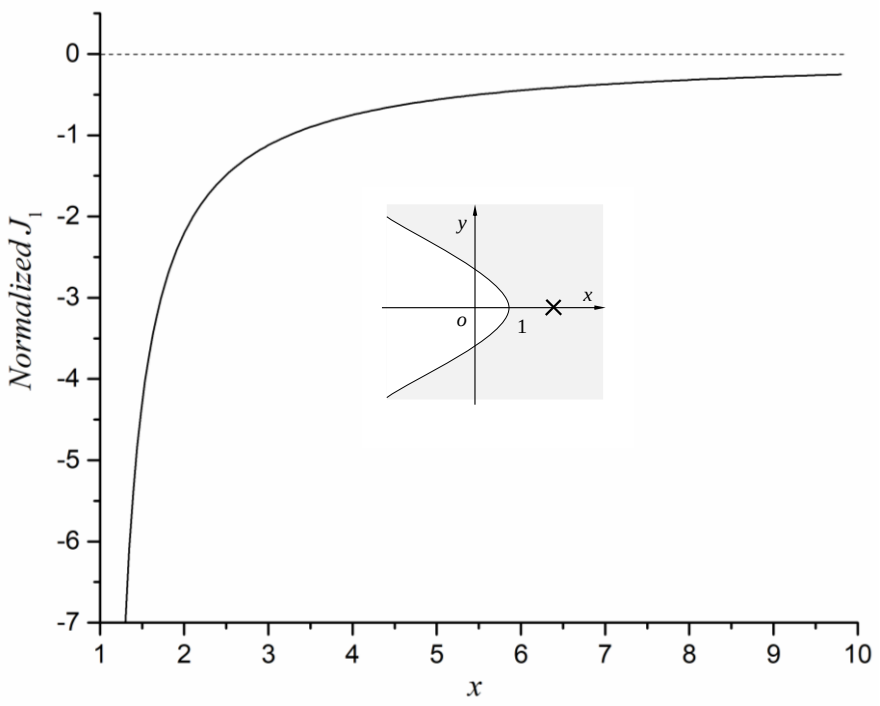


Fig. 7 The driving force J_1 on the screw dislocation versus its location along *x*-axis (The inset is the physical configuration of notch showing the screw dislocation position.)

It is observed from Fig. 7 that the driving force on the screw dislocation resulting just from the presence of the free boundary has a drastic variation with *x*. It is a persistent force that tends

to drive the dislocation out of the substrate towards the free surface. When the dislocation is located near the surface, the driving force will be large enough to overcome the material internal resistance to impel it out of the substrate, which may result a dislocation-free area. However, when the dislocation is located deeply inside of the substrate, the driving force on the dislocation rapidly decreases, and it may be verified that when $x \to \infty$ in Eq. (44), the driving force $J_1 \to 0$.

The two examples we considered in this section are just the simplest scenarios of the parabolic notch interacting with singularities, but they may be regarded as tests to validate the derivation of the general solution, and at the same time, they may shed some light on the mechanism of notch-singularity interaction.

6. Concluding remarks

In this study, using the complex conformal mapping technique, the analytical solution for a parabolic notch in a plane infinite solid, interacting with a generalized anti-plane singularity has been derived. The singularity may be thought of as representing either a screw dislocation or a concentrated anti-plane force. To demonstrate its application and validate its correctness, a parabolic notch separately interacting with concentrated forces and a screw edge dislocation have been investigated in detail. The driving force on the screw dislocation has been obtained, from which the dislocation-free zone can be predicted.

The solutions developed can be used as building blocks to model the parabolic notch damage problems such as crack initiation and propagation, with the distributed dislocation technique [47], and the parabolic notch under complex load conditions simulated with Green's function method. Moreover, the approach developed in this study may be also used to solve further hyperbolic notch-singularity interaction problems. These are the evident novelties of the current study in comparison with the results in literature.

References

[1] Williams, M.L., 1952, “Stress singularities resulting from various boundary conditions in angular corners of plates in extension,” J. Appl. Mech., **19**, pp. 526-528.

[2] Neuber H., 1958, Theory of Notch Stresses: Principles for Exact Calculation of Strength with Reference to Structural Form and Material. Berlin: Springer-Verlag.

[3] Creager, M., and Paris, P. C., 1967, “Elastic field equations for blunt cracks with reference to stress corrosion cracking, ” Int. J. Fract. Mech., **3**, pp. 247-252.

[4] Savruk, M. P., and Kazberuk, A., 2006, “A relationship between the stress intensity and stress concentration factors for sharp and rounded notches,” Mater. Sci., **42**, pp. 725-738.

[5] Kim, J. K., and Cho, S. B., 2012, “A superposition approach to the stress fields for various blunt V-notches,” Fatigue Fract. Eng. Mater. Struct., 36, pp.139-153

[6] Radaj, D., 2014, “State-of-the-art review on extended stress intensity factor concepts,” Fatigue Fract. Eng. Mater. Struct., **37**, pp. 1-28

[7] Bahrami, B., Ayatollahi, M. R., and Mirzaei, A. M., 2019, “Analysis of stresses and displacements in the vicinity of blunt V-notches by considering higher order terms,” Fatigue Fract. Eng. Mater. Struct., **42**, pp. 1760-1774.

[8] Kullmer, G., and Richard, H. A., 2006, “Influence of the root radius of crack-like notches on the fracture load of brittle components,” Arch. Appl. Mech., **76**, pp. 711-723.

[9] Gómez, F. J., Elices, M., Berto, F.， and Lazzarin, P., 2007, “Local strain energy to assess the static failure of U-notches in plates under mixed mode loading,” Int. J. Fract., **145**, pp. 29-45.

[10] Livieri, P., and Segala, F., 2007, “Analytical evaluation of J-integral for elliptical and parabolic notches under mode I and mode II loading, ” Int. J. Fract., **148**, pp. 57-71.

[11] Zappalorto, M., and Lazzarin, P., 2014, “Some remarks on the Neuber rule applied to a control volume surrounding sharp and blunt notch tips,” Fatigue Fract. Eng. Mater. Struct., **37**, pp. 349-358.

[12] Wang, X., and Schiavone, P., 2021, “Elastic field for a blunt crack represented by a parabolic cavity in a generally anisotropic elastic material,” Eng. Fract. Mech., **251**, pp. 107763.

[13] Muskhelishvili, N.I., 1953, Some basic problems of the mathematical theory of elasticity. Noordhoff, Groningen.

[14] Carpenter, W. C., 1984a, “Calculation of the fracture mechanics parameters for a general corner,” Int. J. Fract., **24**, pp. 45-58.

[15] Carpenter, W. C., 1984b, “Mode I and Mode II stress intensities for plates with cracks of finite opening, ” Int. J. Fract., **26**, pp. 201-204.

[16] Carpenter, W. C., 1994, “Comments on the eigenvalue formulation of problems with cracks, V-notched cracks, and corners,” Int. J. Fract., **68**, pp. 75-87.

[17] Carpenter, W. C., 1995, “Insensitivity of the reciprocal work contour integral method to higher order eigenvectors,” Int. J. Fract., **73**, pp. 93-108.

[18] Lazzarin, P., and Tovo, R., 1996, “A unified approach to the evaluation of linear elastic stress fields in the neighborhood of cracks and notches” Int. J. Fract., **78**, pp. 3-19.

[19] Filippi, S., Lazzarin, P., and Tovo, R., 2002, “Developments of some explicit formulas useful to describe elastic stress fields ahead of notches in plates,” Int. J. Solids Struct., **39**, pp. 4543-4565.

[20] Lazzarin, P., Zappalorto, M., and Berto, F., 2011, “Generalised stress intensity factors for rounded notches in plates under in-plane shear loading,” Int. J. Fract. , **170**, pp. 123-144

[21] Mirzaei, A.M., Ayatollahi, M.R., Bahrami, B., and Berto, F., 2020, "Elastic stress analysis of blunt V-notches under mixed mode loading by considering higher order terms, " Applied Mathematical Modelling, **78**, pp. 665-684.

[22] Filon, L.N.G., 1900, "On the resistance to torsion of certain forms of shafting with special reference to the effect of keyways," Philos. Trans. R. Soc. A, **193**, pp. 309-352.

[23] Shepherd, W.M., 1932, "The torsion and flexure of shafting with keyways or cracks," Proc. R. Soc. Lond. A, **138**, pp. 607-634.

[24] Wigglesworth, L.A., 1939, "Flexure and torsion of an internally cracked shaft," Proc. R. Soc. Lond. A, **170**, pp. 365-391.

[25] Wigglesworth, L.A., and Stevenson, A.C., 1939, "Flexure and torsion of cylinders with cross-sections bounded by orthogonal circular arcs, " Proc. R. Soc. Lond. A, **184**, pp. 391-414.

[26] Rushton, K.R., 1967, "Stress concentrations arising in the torsion of grooved shafts," Int. J. Mech. Sci., **9**, pp. 697-705.

[27] Ohr, S. M., Chang, S.J., and Thomson, R., 1985, "Elastic interaction of a wedge crack with a screw dislocation," J. Appl. Phys., **57**, pp. 1839-1843.

[28] Noda, N., and Takase, Y., 2003, "Generalized stress intensity factors for V-shaped notch in a round bar under torsion, tension and bending," Eng. Fract. Mech., **70**, pp. 1447-1466.

[29] Noda, N., and Takase, Y., 2006, "Stress concentration formula useful for all notch shape in a round bar (comparison between torsion, tension and bending)," Int. J. Fatigue, **28**, pp. 151-163.

[30] Savruk, M.P., Kazberuk, A., and Tarasiuk, G., 2012, " Distribution of stresses over the contour of rounded V-shaped notch under antiplane deformation," Mater. Sci., **47**, pp. 717-725.

[31] Kim, J.-K., and Cho, S.-B., 2013, "Superposition approach of the stress fields for blunt V-notches under anti-plane shear loading," International Journal of Precision Engineering and Manufacturing, **14**, pp. 605-612.

[32] Savruk, M. P., and Kazberuk, A., 2017, Stress concentration at notches, Springer.

[33] Smith, E., 2004, "The elastic stress distribution near the root of an elliptically cylindrical notch subjected to mode III loadings," Int. J. Eng. Sci., **42**, pp. 1831-1839.

[34] Lazzarin, P., Zappalorto, M., and Yates, J.R., 2007, "Analytical study of stress distributions due to semi-elliptic notches in shafts under torsion loading," Int. J. Eng. Sci., **45**, pp. 308-328.

[35] Zappalorto, M., Lazzarin, P., and Yates, J.R., 2008, "Elastic stress distributions for parabolic and parabolic notches in round shafts under torsion and uniform antiplane shear loadings," Int. J. Solids Struct., **45**, pp. 4879-4901.

[36] Zappalorto, M., and Lazzarin, P., 2009, "A new version of the Neuber rule accounting for the influence of the notch opening angle for out-of-plane shear loads," Int. J. Solids Struct., **46**, pp. 1901-1910.

[37] Salviato, M., and Zappalorto, M., 2016, "A unified solution approach for a large variety of antiplane shear and torsion notch problems: Theory and examples," Int. J. Solids Struct., **102-103**, pp. 10-20.

[38] Ma, L.F., and Hills, D.A., 2022. "Interaction of a parabolic notch with a generalized singularity," Int. J. Eng. Sci., **176**, pp. 103685.

[39] Ma, L.F., 2022, "Fundamental formulation for anti-plane eigenstrain problems," Mech. Mater., **165**, pp. 104188.

[40] Rose, L.R.F., 1987, "The mechanics of transformation toughening," Proc. R. Soc. Lond. A, **412**, pp. 169-197.

[41] Ma, L.F., 2010, “Fundamental formulation for transformation toughening,” Int. J. Solids Struct., **47**, pp. 3214-3220.

[42] Wang, X., and Schiavone, P., 2021, “A screw dislocation located outside, inside or on the interface of a parabolic elastic inhomogeneity,” Arch. Mech., **73**, pp. 219-235.

[43] Eshelby, J.D., 1951, “The force on an elastic singularity,” Philosophical Transactions of the Royal Society of London A, **244**, pp. 87-112.

[44] Cherepanov, G.P., 1967, “The propagation of cracks in a continuous medium,” Journal of Applied Mathematics and Mechanics, **31**, pp. 503-512.

[45] Rice, J.R., 1968, “A path independent integral and the approximate analysis of strain concentration by notches and cracks,” J. Appl. Mech., **35**, pp. 379-386.

[46] Budiansky, B., and Rice, J.R., 1973, “Conservation laws and energy-release rates,” J. Appl. Mech., **40**, pp. 201-203.

[47] Hills, D. A., Kelly, P. A., Dai, D. N., and Korsunsky, A. M., 1996, Solution of Crack Problems: The Distributed Dislocation Technique, Kluwer Academic Publishers, Dordrecht, the Netherlands.

6.3. Validation of the results

From Chapter 5, the potential function characterizes the stress field of a wedge interacting with a singularity is represented as:

$$f(z) = A\,ln\left(z^{\frac{1}{q}} - z_0^{\frac{1}{q}}\right) - \bar{A}\,ln\left(z^{\frac{1}{q}} + \bar{z}_0^{\frac{1}{q}}\right) \tag{6.1}$$

In the case of dislocation

$$A = b_z/2\pi \tag{6.2}$$

We simplify the case by assuming that the opening angle of the wedge is π, to represent a half space, the potential function can be simplified as:

$$f(z) = b_z/2\pi\,ln(z - z_0) - b_z/2\pi\,ln(z + \bar{z}_0) \tag{6.3}$$

If dislocation locates at the axis of symmetry with distance l, by neglecting the singular part in potential function, and applying the following equation

$$\sigma_{23} + i\sigma_{13} = \mu f'(z) \tag{6.6}$$

the image force acting on the dislocation is

$$\sigma_{23} = \mu b_z/2\pi\frac{1}{2l} = \frac{\mu b}{4\pi l} \tag{6.5}$$

Which matches the results in Hirth and Lothe (1982) about the image for on dislocation in a half space.

Consider another popular case, that is when $q = 2$ in equation (6.1) to represent a crack, the potential function for a crack can be represented as

$$f(z) = A\,ln\left(z^{\frac{1}{2}} - z_0^{\frac{1}{2}}\right) - \bar{A}\,ln\left(z^{\frac{1}{2}} + \bar{z}_0^{\frac{1}{2}}\right). \tag{6.6}$$

The crack configuration can also be represented considering a parabolic notch case, the potential function for a parabolic notch interacting with a screw dislocation is

$$f_p(z) = A\,ln(z - z_0) - A\,ln\left(\sqrt{z} + \sqrt{z_0}\right) - \bar{A}\,ln\left(\sqrt{\bar{z}_0} + \sqrt{z} - 2h\right). \tag{6.7}$$

For a crack, $h = 0$, it can be simplified as

$$f(z) = A\,ln\left(z^{\frac{1}{2}} - z_0^{\frac{1}{2}}\right) - \bar{A}\,ln\left(z^{\frac{1}{2}} + \bar{z}_0^{\frac{1}{2}}\right) \tag{6.8}$$

which matches equation (6.6). The match show the consistency of the potential function in wedge and parabolic notch cases.

According to equation (6.6), the stress field of a crack contains a screw dislocation can be represent as

$$\sigma_{23} = \mu b_z / 2\pi \sqrt{\frac{l}{z}} \frac{1}{z - x} = \frac{\mu b}{4\pi l} \tag{6.9}$$

The result matches the stress predicted in Majumdar and Burns (1981).

Both Chapter 5 and 6 predicts a dislocation free zone, this agrees with the prediction in Majumdar and Burns (1983), Change and Ohr (1981). However, the dislocation free zone size in the above two literatures is predicted using force balancing strategy, which is different from energetical calculation in Chapter 5 and 6. The calculation of the dislocation free zone size using energetical method is complicated and beyond the scope of this thesis.

Bibliograpy:

Chang, S.J., & Ohr, S.M. (1981). Dislocation-free zone model of fracture. Journal of Applied Physics, 52, 7174–7181.

Hirth, J. P., Lothe, J., & Mura, T. (1983). Theory of dislocations. Journal of Applied Mechanics, 50(2), 476-477.

Majumdar, B. S., & Burns, S. J. (1981). Crack tip shielding—an elastic theory of dislocations and dislocation arrays near a sharp crack. Acta Metallurgica, *29*(4), 579-588.

Majumdar, B. S., & Burns, S. J. (1983). A Griffith crack shielded by a dislocation pile-up. International Journal of Fracture, *21*, 229-240.

Statement of Authorship for joint/multi-authored papers for PGR thesis

To appear at the end of each thesis chapter submitted as an article/paper

The statement shall describe the candidate's and co-authors' independent research contributions in the thesis publications. For each publication there should exist a complete statement that is to be filled out and signed by the candidate and supervisor **(only required where there isn't already a statement of contribution within the paper itself).**

Title of Paper	A Parabolic notch Interacting with a Generalized Anti-plane singularity
Publication Status	✓Published □ Accepted for Publication □Submitted for Publication □Unpublished and unsubmitted work written in a manuscript style
Publication Details	Ma, L., Chen, Y., & Hills, D. A. (2022). A Parabolic Notch Interacting With a Generalized Anti-plane Singularity. *Journal of Applied Mechanics*, *89*(9), 091001.

Student Confirmation

Student Name:	Yifeng Chen		
Contribution to the Paper	Deduce the basic equations of the paper for anti-plane loading in Parobolic notch. Check the calculations for the final examples. Plot the stress field graph. Review the submitted version.		
Signature: 		Date	21/12/2023

Supervisor Confirmation

By signing the Statement of Authorship, you are certifying that the candidate made a substantial contribution to the publication, and that the description described above is accurate.

Supervisor name and title: Dr. Lifeng Ma		
Supervisor comments Like the last chapter, which involved anti-plane calculations. Yifeng is becoming familiar with the anti-plane formula and has therefore taken on the task of basic formula deduction. He also assisted with the plotting of the stress field and checked the final revision. I agree to include this paper as part of his PhD work.		
Signature: 	Date	2023 Dec 23

7. Analysis of elastic prismatic contact of finite length

7.1. Introduction

The plane problem is often regarded as a means to grasp the fundamental mechanisms in solid mechanics, rather than a direct criterion for practical applications. This is due to the inherently three-dimensional nature of real-world mechanical bodies, where the effects in the third dimension — the 'into-the-page' direction — can cause the solutions derived from plane problems to differ from those in realistic cases. In the industry, stress analysis is more safely and conveniently conducted through numerical methods, such as the finite element technique.

For researchers, a crucial question concerning the application of plane problem solutions to real-life scenarios is how these solutions will be altered by incorporating the third dimension. Specifically, if we extend the plane problem into the out-of-plane direction with a finite extent, how will each plane along that extent exhibit behavior that diverges from the reference analytical solution?

In this section, our objective is to tackle this issue by examining a new variant of the plane problem: the contact problem. We will extend the plane contact problem into the out-of-plane direction to form a prismatic body and employ finite element analysis to evaluate each plane along the extension. The behavior of these planes will then be compared with the reference plane solution to elucidate the differences.

Two contact cases will serve as illustrative examples. The first is the uncoupled common-edge problem, which can be viewed as a monolithic body due to the symmetry, thus making it simpler to analyze and offering greater computational efficiency. The second example is the Hertzian contact, characterized by a bounded contact pressure profile that improves the accuracy of the finite element analysis and possesses greater applicability in practice.

The conclusions drawn from this study have broader implications for all problems

involving the extension of a plane over a finite length or those featuring prismatic geometry. A fundamental understanding of these issues will be developed by proposing a corrective solution, one that can adjust the stress field of the plane problem to match specific planes within the finite extent.

Before beginning our analysis, it's important to discuss the general characteristics of this problem. In the finite extent contact problem, the traction-free ends do not form a plane shape in the deformed configuration; that is, the out-of-plane displacement for the end-plane varies from point to point. However, the mid-plane of this contact problem will present a planar shape due to symmetry. Consequently, the end effect will influence the overall behavior of the contact, but according to Saint-Venant's principle, this effect cannot persist throughout the entire extent, as the self-balancing effect is limited in distance during propagation. Understanding how the end effect propagates and the extent of its influence is also a focal point of this section.

7.2. Paper: Analysis of a Prismatic Elastic Contact of Finite Length[6]

Analysis of a Prismatic Elastic Contact of Finite Length

Yifeng Chen [a], David A. Hills [a], John E. Huber [a7], Lifeng Ma [b]

[a] Department of Engineering Science, University of Oxford, Parks Road, OX1 3PJ Oxford, UK

[b] Department of Mechanical, Material and Manufacturing Engineering, University of Nottingham, University Park, NG7 2RD, UK

Abstract

This paper is concerned with a contact problem which is geometrically two dimensional, but of finite extent in a third dimension. Two different contact models (common edge contact and incomplete contact) are analysed, using a finite element model to investigate the 3D end effects. The object is to take the 2D plane strain solution in each model as a reference, and to show how it must be modified to allow for the 3D finite extent contact problem with free end faces. It is shown that the in-plane stress distribution at the mid-plane matches the solution to the 2D plane strain problem. Additionally, the end effect is evaluated using the finite element results to show how it decays with distance from the free end. The decay is exponential and governed by a dominant length-scale of the problem. For a common edge contact, this length-scale is the contact width. However, for a Hertzian contact, the contact width varies in the third dimension and the governing length scale is the radius of curvature, typically much larger than the contact width.

Keywords: Contact of Finite Length, Finite Element Analysis, End Effects, Saint-Venant's Principle

1. Introduction

Prismatic elastic contacts of finite length are frequently found in engineered components, including splined shafts, gears and turbine blade roots. In order to gain a general understanding of such contacts, a two-dimensional (2D) analysis may be used. However, all such contacts in practice have ends, and the end effects may significantly influence contact pressure. There is thus a requirement to understand how the solution of prismatic contact problems differs from the solution to a corresponding 2D problem.

One way to observe the end effect in prismatic contacts is by conducting fretting tests, where it is found that the contact or wear scar varies in the thickness direction, despite prismatic component geometry [1]. Fretting tests commonly employ pads pressed into a traditional dog-bone-shaped tensile test specimen, as shown in Figure 1 (see also [2] and [3]). These tests aim to reveal the fretting fatigue strength of the material. The pads have prismatic geometry with a cross-section that may be either flat-and-rounded in form or circular. A significant amount of effort has been invested in analyzing the behavior of these contacts in partial slip. The analysis has commonly been conducted under plane conditions, i.e. where there are no permitted gradients of stress or strain components in the out-of-plane direction. The tests themselves are intended to match these conditions: care is taken to use pads of prismatic geometry, and to match the through-thickness length of the pads to that of the dog-bone specimen. However, it is inevitable that there are deviations from prismatic contact conditions due to imperfection and the nature of incomplete contact. The singular solution due to slight mismatch of through-thickness length typically has little effect in practical experimental conditions. By contrast, the end effect due to the free surfaces can intrude far into the contact, making it essential to account

[6] Chen, Y., Hills, D.A., Huber, J.E., Ma, L. (2024). Analysis of Elastic Plane Contact with a Finite Length, Journal paper submitted to European Journal of Mechanics A/Solids.
[7] Corresponding author: *E-mail address* john.huber@eng.ox.ac.uk (John E. Huber).

for this effect. The objective of the current work is to analyse the end effect due to the free surfaces at the ends of prismatic contacts.

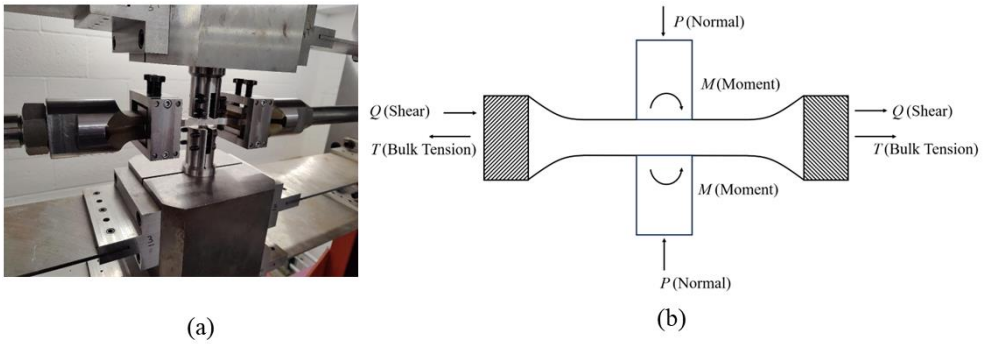


Figure 1: (a) Experimental apparatus for fretting tests. (b) Idealisation of the key part of the test.

The structure of the paper is as follows: First, general properties of prismatic contacts are considered, and it is shown that the elastic fields can be decomposed into those due to bodies constrained in plane strain and an additional set of corrective fields due to the end effect. Then, geometries are explored. The target problem is a Hertzian contact in which a cylinder is pressed against a flat surface. Noting that this problem is complicated by the non-prismatic contact profile, a common edge contact problem in which symmetric anvils are pressed together is first explored. This has the advantage that the problem geometry defines the contact width; combined with symmetry, a result is that the elastic pair can be treated as a monolithic body, which is computationally efficient to model while revealing key features of the problem. The analysis uses the finite element method for a 3D evaluation of stress fields and compares the results with a 2D plane strain solution. The decay-rate of the end-effects is evaluated for both Hertzian and common-edge contacts, and it is shown that this follows an oscillatory exponential decay, typical of the Saint-Venant decay for end effects. A detailed comparison between the Hertzian contact and the common-edge contact is given.

2. Theoretical background

2.1. Prismatic body with uniform loading

We begin by examining a monolithic and homogeneous prismatic body of arbitrary cross section, with length $2L$ much greater than the leading dimension of the cross-section. The body is elastic and is subjected to a uniform distributed normal force P and shear force Q per unit length. This body is additionally constrained by fixed frictionless planes at $z = 0$ and $z = L$, such that the through-thickness displacement u_z is zero everywhere, as depicted in Figure 2(a). The condition $u_z = 0$ effectively ensures that each cross-sectional plane along its length satisfies the plane strain condition, i.e. $\epsilon_{zz} = 0$ everywhere, thereby maintaining an identical in-plane stress state in all these cross-sections. In addition to the applied loads P and Q, the geometry shown in Figure 2(a) sustains a non-uniform stress distribution perpendicular to the x-y plane, $\sigma_{zz}^{\mathrm{PS}}(x, y)$, where the superscript PS stands for plane strain. This ensures that the through-thickness strain components ϵ_{zz} vanish. The distribution of $\sigma_{zz}^{\mathrm{PS}}(x, y)$ is characterized by:

$$\sigma_{zz}^{\mathrm{PS}}(x, y) = \nu \left(\sigma_{xx}^{\mathrm{PS}}(x, y) + \sigma_{yy}^{\mathrm{PS}}(x, y) \right) \tag{1}$$

where ν is Poisson's ratio. By considering the applied loads P and Q and the stress $\sigma_{zz}^{\mathrm{PS}}(x, y)$ separately, the plane strain case can be decomposed into two parts. The first part is the target problem, defined by a prismatic body loaded by P and Q, of finite extent, with both ends being free, as shown in Figure 2(b). The second part is a corrective solution defined by the same body, loaded with the plane strain through-thickness stress, as illustrated in Figure 2(c). Note that the target problem is a classic prismatic bar problem, and the analytical solution is discussed in Barber [4] using Papkovich–Neuber solution. This solution will not be applied

in this paper due to its mathematical complexity, instead superposition principle is applied to illustrate the stress state behavior.

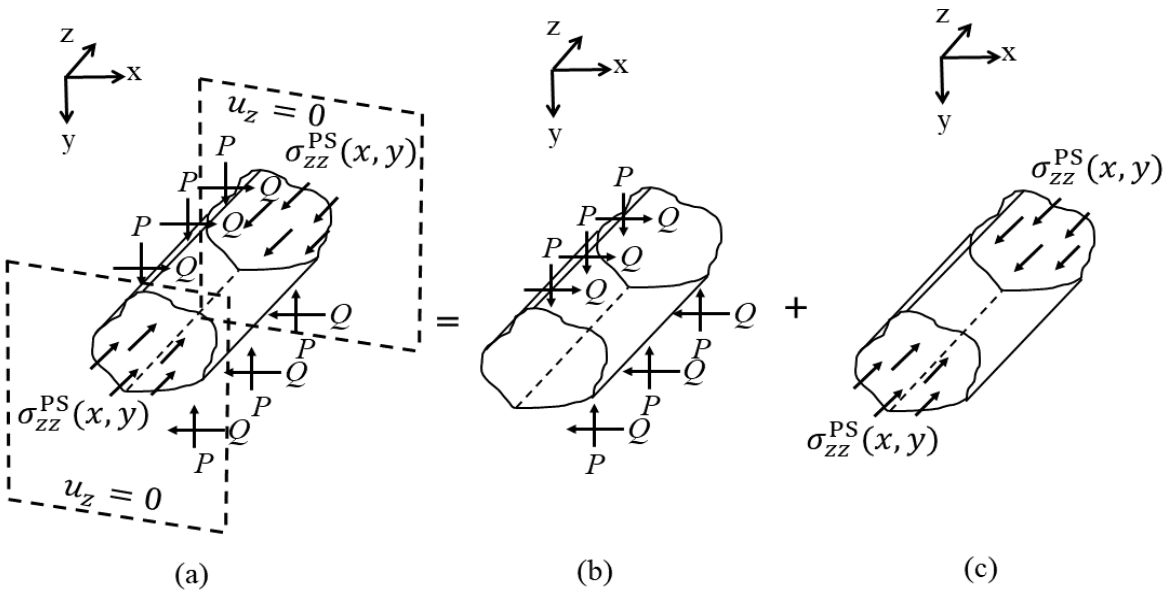


Figure 2: An arbitrary prismatic body of finite length (a) loaded by applied loads P and Q in plane strain; (b) loaded by applied loads P and Q with free ends (our target); (c) loaded by the through-thickness stress $\sigma_{zz}^{PS}(x,y)$ (corrective solution).

We refer to the problem shown in Figure 2(b) as the 'finite length problem', which is found in many practical situations. In the corrective solution, σ_{zz} varies with position (x, y, z), but the variation in the x-y plane decays with distance z along the length, according to Saint-Venant's principle [5]. Since σ_{zz} has a non-zero average over the x-y plane, this stress field decays towards the average value as the centre ($z = L$) is approached.

Let σ_{zz}^{a} be the average of stress $\sigma_{zz}^{\mathrm{PS}}(x,y)$ over the x-y plane, given by:

$$\sigma_{zz}^{\mathrm{a}} = \frac{1}{A_0}\int_{A_0} \sigma_{zz}^{\mathrm{PS}}(x,y)\ \mathrm{d}A \tag{2}$$

where A_0 is the cross-sectional area of the prismatic body. Also define $\sigma_{zz}^{\mathrm{b}}(x,y)$ as the self-balancing complementary stress field given by

$$\sigma_{zz}^{\mathrm{PS}}(x,y) = \sigma_{zz}^{\mathrm{b}}(x,y) + \sigma_{zz}^{\mathrm{a}}. \tag{3}$$

Then, according to Saint-Venant's principle, $\sigma_{zz}(x,y,z)$ in the corrective solution, makes a transition from $\sigma_{zz}^{\mathrm{b}}(x,y) + \sigma_{zz}^{\mathrm{a}}$ at the ends of the prismatic body, to σ_{zz}^{a} at $z = L$. The propagation of $\sigma_{zz}(x,y,z)$ is illustrated in Figure 3, which shows a non-uniformly distributed stress gradually changes to a uniformly distributed stress at the mid-plane. The decay of the zero-resultant stress σ_{zz}^{b} is the free end-effect investigated in this paper. The region of this decay is typically short compared to the length $2L$. Hence there is a transient region, wherein the stress state is dependent on the z co-ordinate, followed by a steady-state region, where no end-effect is presented, and the stress state is practically constant along the z-axis.

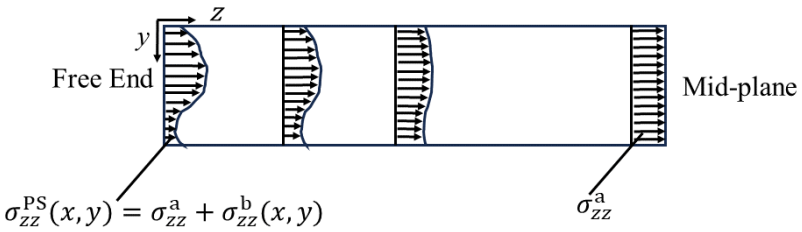


Figure 3: Illustration of the propagation of $\sigma_{zz}(x,y,z)$ in the corrective solution, from the non-uniform distribution $\sigma_{zz}^{PS}(x,y)$ at the free-end to a uniform distribution at the mid-plane σ_{zz}^{a}.

The mid-plane is of particular interest, because it is guaranteed to remain plane in the loaded state, due to symmetry. Also, it represents the steady-state behavior beyond the transient region. Noting the superposition shown in Figure 2, the mid-plane stress field is given by subtracting σ_{zz}^{a} from the plane strain solution. Therefore, the stress field at the mid-plane σ_{ij}^{M} can be expressed as:

$$\sigma_{ij}^{\mathrm{M}} = \sigma_{ij}^{\mathrm{PS}} \quad \text{for } i,j \in \{x,y\},$$

$$\sigma_{zz}^{\mathrm{M}} = \sigma_{zz}^{\mathrm{PS}} - \sigma_{zz}^{\mathrm{a}} = \sigma_{zz}^{\mathrm{b}},$$

$$\sigma_{xz}^{\mathrm{M}} = \sigma_{yz}^{\mathrm{M}} = 0. \quad (4)$$

Note that the in-plane stress fields $\sigma_{xx}^{\mathrm{M}}, \sigma_{yy}^{\mathrm{M}}$ and σ_{xy}^{M} are the same as those calculated in the plane strain condition.

2.2. Prismatic contact problem

Next, consider a contact made by two prismatic bodies of the same length, $2L$, where $2L$ is much larger than the leading dimension of the cross section of the prismatic body, under uniform load. The conclusion that the in-plane components of σ^{M} equal those of σ^{PS} may not hold in this problem. This is because, firstly, the contact pressure may vary with the z co-ordinate in a contact problem: thus, the requirement that the loading is independent of z may not be satisfied. Secondly, the contact pressure, especially in incomplete contact, is not linearly related to the applied load; thus, strictly, the principle of superposition is invalid and equations (4)-(6) are not applicable.

Nevertheless, if we impose the corrective stress field, $-\sigma_{zz}^{\mathrm{PS}}(x, y)$, at both ends of a prismatic contact under plane strain condition, then a finite length contact problem is constructed because of the match of the free-end boundary conditions, as depicted in Figure 4, using a Hertzian contact as an example. In this case, the stress field at the mid-plane of the finite length contact problem can be evaluated by using two cases: The first case is the prismatic contact under plane strain: here the stress distribution across any plane along the length will be the same as that in the plane strain analytical solution, since the through-thickness displacement, $u_z(x, y)$, is zero in every plane. The second case is the corrective stress added at the both ends, which will be governed by Saint-Venant's principle. This means that there is still a decaying end-effect and the stress state at the mid-plane is equivalent to a uniform stress distribution $-\sigma_{zz}^{\mathrm{a}}$ imposed on a plane strain contact.

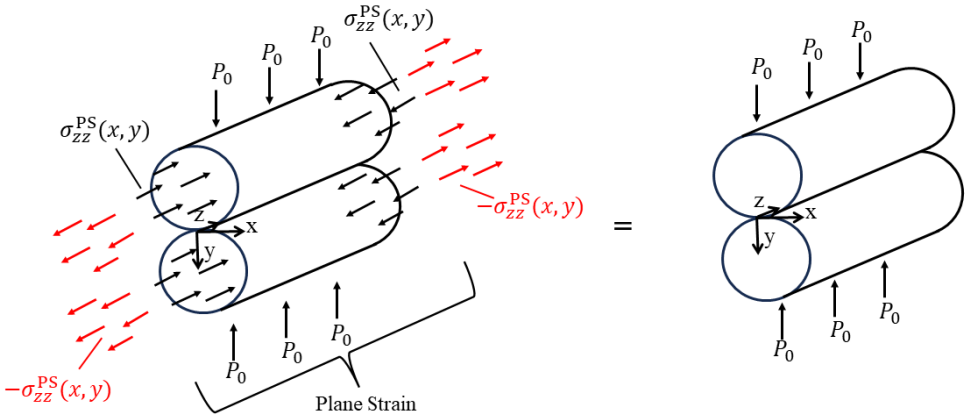


Figure 4: Illustration of the finite length contact problem, constructed by imposing the corrective stress field, $-\sigma_{zz}^{PS}(x,y)$ (indicated in red) onto a prismatic contact under plane strain.

Therefore, the contact pressure at the mid-plane can be calculated analytically by making use of the plane strain Flamant solution, with an additional out-of-plane uniform stress $-\sigma_{zz}^{a}$, as depicted in Figure 5. Linear superposition can then be used to construct the solution for a general contact pressure distribution. Considering first this problem, the in-plane stress field in Cartesian coordinates is identical to the Flamant solution and the through-thickness stress component is expressed as:

$$\sigma_{zz}(x,y) = \nu\left(\sigma_{xx}(x,y) + \sigma_{yy}(x,y)\right) - \sigma_{zz}^{a}. \tag{5}$$

Therefore, the corresponding strains can be computed as:

$$\begin{aligned} \epsilon_{xx} &= \frac{1}{E}\left(\sigma_{xx}(1-\nu^2) + \sigma_{yy}\nu(1+\nu) + \frac{\sigma_{zz}^{a}}{\nu}\right), \\ \epsilon_{yy} &= \frac{1}{E}\left(\sigma_{yy}(1-\nu^2) + \sigma_{xx}\nu(1+\nu) + \frac{\sigma_{zz}^{a}}{\nu}\right). \end{aligned} \tag{6}$$

Using the Flamant solution, and integrating the strains to get the displacement field on the contact interface:

$$
\begin{aligned}
u(x) &= -P\left[\frac{2(1-\nu)(1+\nu)}{\pi E}\right]\mathrm{sgn}(x) + Q\left[\frac{(1-2\nu)(1+\nu)}{2E}\right]\ln|x| + \frac{x\sigma_{zz}^{a}}{\nu} + c_1\frac{(1+\nu)}{E} \\
v(x) &= -P\left[\frac{2(1-\nu)(1+\nu)}{\pi E}\right]\ln|x| - Q\left[\frac{(1-2\nu)(1+\nu)}{2E}\right]\mathrm{sgn}(x) + c_2\frac{(1+\nu)}{E}
\end{aligned}
\tag{7}
$$

where $u(x)$ and $v(x)$ are the horizontal and vertical displacements, c_1 and c_2 are arbitary constants of integration, and

$$
\mathrm{sgn}(x) = \begin{cases} 1 & \text{if } x > 0 \\ 0 & \text{if } x = 0 \\ -1 & \text{if } x < 0 \end{cases}
$$

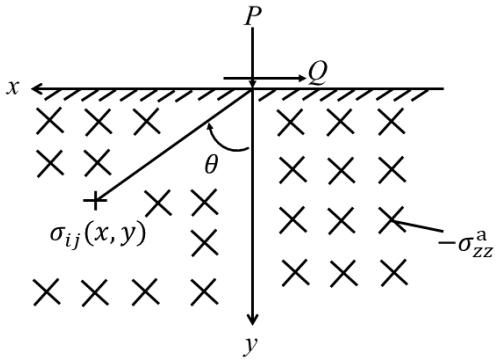


Figure 5: Flamant problem with the plane loaded by an additional out-of-plane uniform stress distribution $-\sigma_{zz}^{a}$.

We will now extend the above results to the case that the surface is subjected to a distributed normal load $p(\xi)\mathrm{d}$ and a distributed shear load $q(\xi)\mathrm{d}$, where ξ is the x-coordinate for the load. The displacement gradients can be deduced as:

$$
\begin{aligned}
\frac{\partial u}{\partial x} &= \frac{(1-2\nu)(1+\nu)}{E}p(x) + \frac{2(1-\nu)(1+\nu)}{\pi E}\int_{\text{contact}}\frac{q(\xi)\,\mathrm{d}\xi}{x-\xi} + \frac{\sigma_{zz}^{a}}{\nu} \\
\frac{\partial v}{\partial x} &= \frac{2(1-\nu)(1+\nu)}{\pi E}\int_{\text{contact}}\frac{p(\xi)\,\mathrm{d}\xi}{x-\xi} - \frac{(1-2\nu)(1+\nu)}{E}q(x)
\end{aligned}
\tag{8}
$$

$$If we introduce contacting bodies 1 and 2, with material properties E_1, ν_1 and E_2, ν_2, the relative surface vertical displacement is $h(x) = v_1(x) - v_2(x)$ and the relative surface horizontal displacement is $g(x) = u_1(x) - u_2(x)$. The governing equation relating contact stress and relative displacement can then be expressed as:

$$\begin{aligned} \frac{1}{\alpha}\frac{\partial h}{\partial x} &= -\frac{1}{\pi}\int \frac{p(\xi)d\xi}{x-\xi} - \beta q(x) \\ \frac{1}{\alpha}\frac{\partial g}{\partial x} &= -\frac{1}{\pi}\int \frac{q(\xi)d\xi}{x-\xi} + \beta p(x) + \gamma\sigma_{zz}^{a} \end{aligned} \tag{9}$$

where α and β are Dundurs' first and second constant and $\gamma = 1/\nu_1 - 1/\nu_2$.

Equation (9) show the displacement gradient at the contact interface for the mid-plane of the finite length contact problem, and the only difference compared with those in a plane strain contact solution is the additional $\gamma\sigma_{zz}^{a}$ in the horizontal displacement gradient (see [6] and [7] for plane strain displacement gradients). There are special cases in which equations in (9) are uncoupled, i.e., $\beta = 0$ or $q(x) = 0$. Another special case arises when the two contacting bodies have the same Poisson's ratio, i.e., $\gamma = 0$. In these cases, we can expect that at the mid-plane, the contact pressure $p(x)$ will be the same as that in the plane strain solution.

The theoretical analysis provides insight into the problem, but some aspects remain unknown, such as how far the free end effect penetrates along the length direction and what the decay pattern of this free end effect is. Two finite element experiments related to the contact problem are next conducted to further explore these aspects and to validate the theoretical findings.

3. Finite length, common-edge contact

The eventual objective is to solve problems such as that depicted in Figure 6. This illustrates a Hertzian contact between a cylinder of finite length, $2L$, with radius $R \ll L$, and a plate of length $2L$, made from elastically similar material. A line force of magnitude P_0 per unit length,

constant along the z-axis, is applied. The degree of lateral constraint in the problem varies: on and near the central plane the value of the through-thickness displacement is zero, whereas at the free ends, $z = 0,2L$, the tractions σ_{zz}, σ_{zx} and σ_{zy} must vanish over all values of (x, y). The contact patch is not rectangular, complicating the problem significantly. Therefore, as a preliminary exercise, we propose to examine a problem where this feature is absent, namely a common-edge contact between symmetric anvils.

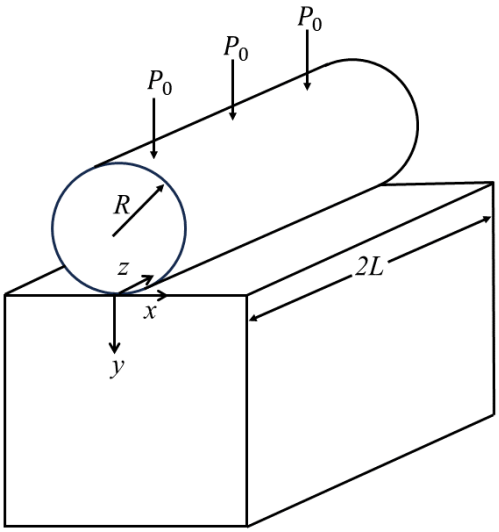


Figure 6: Hertzian contact of finite length.

A suitable common-edge contact problem is shown in Figure 7(a), which depicts two identical, filleted, flat-ended, frictionless anvils, each having a length of $2L$. The anvils are pressed together by a uniformly distributed line force of magnitude P_0 per unit length. For convenience, the height and width of the cross-section are chosen to be the same, denoted as $2w$. The value of w is required to be greater than twice the radius of the fillet, denoted as r, to ensure a moderate pressure gradient along the x direction in the contact. Thus, the contact half-with is equal to $a = w - r > r$. This is also convenient for finite element mesh construction.

Additionally, we require $L \gg w$, so that the end effect will fully decay within the length of the anvils.

The choice of this common edge contact was made in preference to alternatives such as a convex (incomplete or non-conformal) contact of any profile or a complete (conformal) contact of finite width pressed onto a wider block. This is because any prismatic incomplete contact would display the non-constant contact with phenomenon we wish to isolate. Therefore, the contact problem would not be prismatic in the deformed state. Meanwhile, a complete contact between blocks of different widths would show a singular edge contact pressure, and this, too, obscures some of the key features of the problem. The chosen contact is defined by both bodies simultaneously and has finite contact pressure everywhere; pressure gradients are modest, and the effects of differing degrees of axial constraint are isolated from other features. Because the bodies are identical it follows that no out-of-plane shear tractions σ_{zx}, or σ_{zy}), will arise at any point. Indeed, because the interfacial traction is compressive everywhere it follows that a monolithic finite element model of the pair may be studied, avoiding the need for explicit representation of a contact. The combined geometry is familiar, comprising symmetric semicircular notches in a rectangular section; stress concentration factors are typically less than 2.75 and are available in standard tables [8].

The commercial finite element (FE) package Abaqus FEA was used to analyse the end effect and validate the results of the theoretical analysis. Using symmetry, only one-eighth of the full geometry was represented in the numerical model. The geometry and loading of the FE model are depicted in Figure 7(b). Three different sets of numerical experiments with constant width $w = 10$ mm but varying length $L \geq 10w$ and varying characteristic radius r have been examined, see Table 1. The model codes shown in Table 1 are used subsequently to refer to each model.

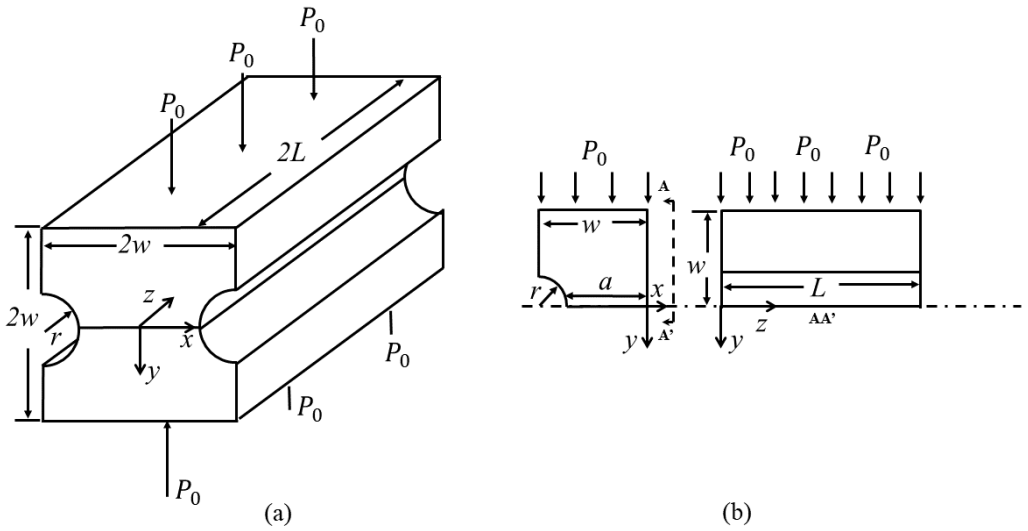


Figure 7: (a) Finite length, common edge contact, (b) finite element model of finite length, common edge contact.

Table 1. FE models with different parameters for finite length, common edge contact: P_0 is the load per unit length, L is the half-length, r is the fillet radius and a is the contact half-width.

common edge models; $w = 10$ mm

model code	P_0 [MPa mm]	L [mm]	r [mm]	a [mm]
P2000L100r2.5a7.5	2000	100	2.5	7.5
P2000L200r2.5a7.5	2000	200	2.5	7.5
P2000L100r5a5	2000	100	5	5

3.1. Results and analysis of the finite length, common-edge contact

As mentioned before, each whole model behaves as a monolithic body with prescribed boundary conditions, independent of z. Therefore, through the analysis in Section 2.2, we expect that the stress field in plane strain, and in the mid-plane of the finite length problem will be the same for this geometry. Additionally, we aim to observe how the free end effect propagates by taking a 2D plane strain solution as a reference and comparing it with the state of stress of the plane cross-section at each z co-ordinate.

The analysis of the FE results starts by extracting the contact pressure at the mid-plane and end-plane from the finite element experiments mentioned in Table 1. These contact pressures are then compared with the corresponding plane strain solution. In all three models of Table 1, it can be observed that the finite, common edge contact exhibits lower pressure at the free end than the reference plane strain solution, but at the mid-plane, the pressure profiles coincide, as expected. An example of this comparison, from model P2000L100r2.5a7.5, is shown in Figure 8. Here, the mid-point contact pressure (minimum pressure) in the plane strain common edge contact is denoted by p_{m0} and this value is subsequently used to normalize $p(x)$ in all numerical experiments.

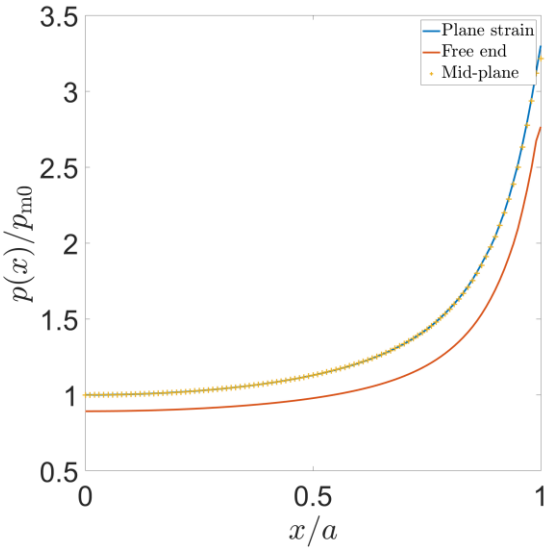


Figure 8: Contact pressure comparison between the plane strain solution, the mid-plane and the free end-plane of a finite length, common edge contact: model P2000L100r2.5a7.5.

The analysis of FE results proceeds by extracting the direct stress component normal to the mid-plane, $\sigma_{zz}^{\mathrm{M}}(x,y)$, and comparing with $\sigma_{zz}^{\mathrm{PS}}(x,y)$, the plane strain solution. The latter is directly extracted from a plane strain finite element model. The comparison reveals that the difference between these two out-of-plane stresses is uniform in the x-y plane, and the value of this difference agrees with the average provided by equation (2). This can be analytically expressed as

$$\sigma_{zz}^{\mathrm{a}} = \frac{1}{A_0}\int_{A_0} \sigma_{zz}^{\mathrm{PS}}(x,y)\ \mathrm{d}A_0 = \frac{\nu}{A_0}\int_{A_0} \sigma_{yy}^{\mathrm{PS}}(x,y)\ \mathrm{d}A_0 = \frac{\nu P_0 w}{A_0} \qquad (10)$$

for the plane geometry shown in Figure 7(a). The agreement validates the corrective solution proposed in Section 2.

The variation of contact force per unit length at each plane, $P(z)$, indicates how the applied load is distributed along the contact surface. Consequently, it can be used to evaluate the behaviour of the transient region. $P(z)$ is defined as the integral of the contact pressure across the contact half-width, i.e.

$$P(z) = \int_{-a}^{a} p(x)\ \mathrm{d}x. \tag{11}$$

This quantity can be normalized by the applied force per unit length P_0; the quantity $P(z)/P_0$ is used to observe the decay of the end effect.

It can be anticipated that the end effect will propagate inward only for a limited distance. Determining this range in terms of the geometric length feature is one of the key objectives of this paper. A suitable candidate for the nondimensionalization of the length over which the end effect diminishes is the contact half-width, a (an alternative would be feature radius r).

Figure 9(a) shows results from models P2000L100r2.5a7.5 and P2000L200r2.5a7.5. These two models have the same x-y plane geometry, differing only in their length, L. This shows that the results are independent of L with $L \gg r, a$. These results also indicate that the length is divided into a transient region and a steady state region, with the transient region having length about $4a$. Note that Figure 9(b) shows corresponding results from a Hertzian contact model, for later use.

The range of the end effect varies when the geometry in the x-y plane changes, as shown in Figure 10, where the cross-section of the models is characterized by their a/r ratio. Note that $a/r \to \infty$ corresponds to the scenario where two identical blocks are pressed against each other, resulting in a contact patch that remains unchanged along the length. Consequently, in cases of common edge contact, a larger a/r ratio is expected to yield a smaller end-effect range. In simple terms, smaller grooved features produce a more confined transient region.

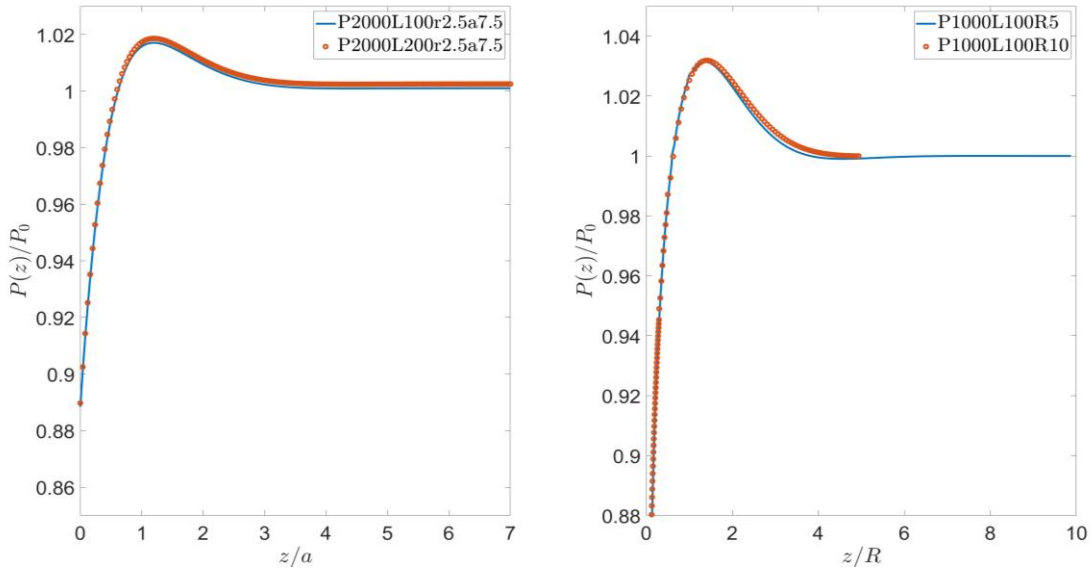


Figure 9: The variation of $P(z)/P_0$ with z from different models: (a) finite length, common edge contact; results show similarity when z is normalized by contact half-width a; (b) finite length, Hertzian contact, results show similarity when z is normalized by contact indenter radius R.

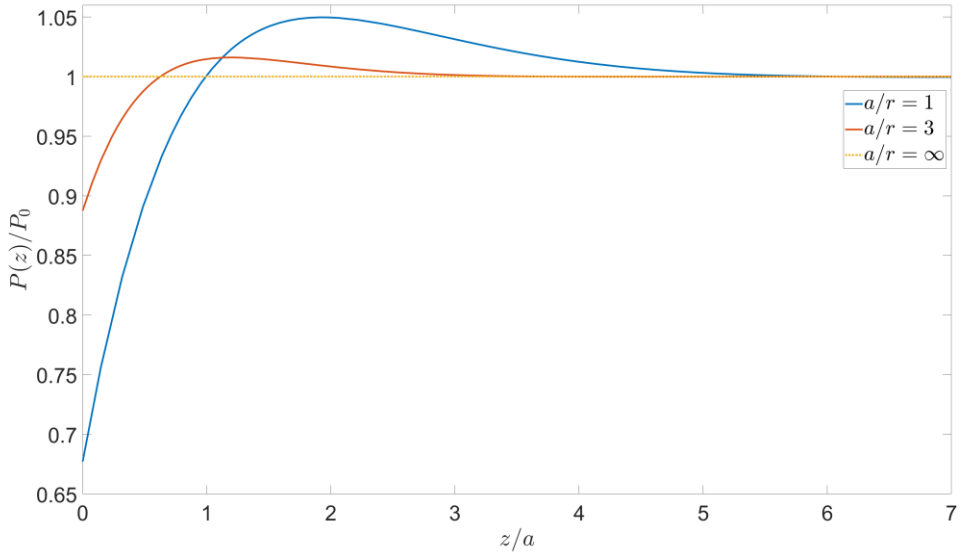


Figure 10: Common edge contact: contact force per unit distribution of models with $a/r = 1,3,\infty$.

Numerous studies have demonstrated that the decay pattern of a self-equilibrating end effect follows an oscillating exponential function, see [9] and [10]. The data in Figure 10 were found to fit an oscillating exponential function of the form

$$P(z)/P(0) = A\exp\big(-\lambda(z/a)\big)\sin(\omega(z/a) + \phi) + 1 \tag{12}$$

where λ is the decay constant, ω is the angular frequency of the oscillation and ϕ is a phase shift. Using the Levenberg-Marquardt non-linear least squares fitting algorithm [11] (See Appendix for details), the following fitting functions were identified:

$$P(z)/P(0) = 0.562\exp\big(-0.944(z/a)\big)\sin(0.617(z/a) - 0.612) + 1$$

for the model with feature $a/r = 1$ and

$$P(z)/P(0) = 0.195\exp\big(-1.560(z/a)\big)\sin(0.983(z/a) - 0.615) + 1$$

For $a/r = 3$ Both fitted curves show maximum error less than 0.1%. While the common edge contact is a simpler case than the target problem of Hertzian contact, the results given indicate the robustness and accuracy of our method to decompose the contact problem into a generalized plane strain case at the mid-plane and a corrective solution.

4. Finite length, Hertzian contact

We next proceed to study the frictionless, finite length, Hertzian contact, represented as two parallel frictionless identical cylinders pressed onto each other with their ends aligned, as shown in Figure 11(a). The cylinders have length $2L$, radius $R \ll L$ and are pressed together by a uniform line force P_0. This is a type of convex contact, and hence will display a non-constant contact width. This model shares the same through-thickness (3D) effect with the cylinder on plane model of Figure 6. However, the current model is computationally efficient, being identical to a cylinder pressed against a rigid surface (Figure 11(b)). Due to symmetry,

only one-eighth of the 3D model is required. For all of the FE experiments, we take Poisson's ratio $\nu = 0.3$.

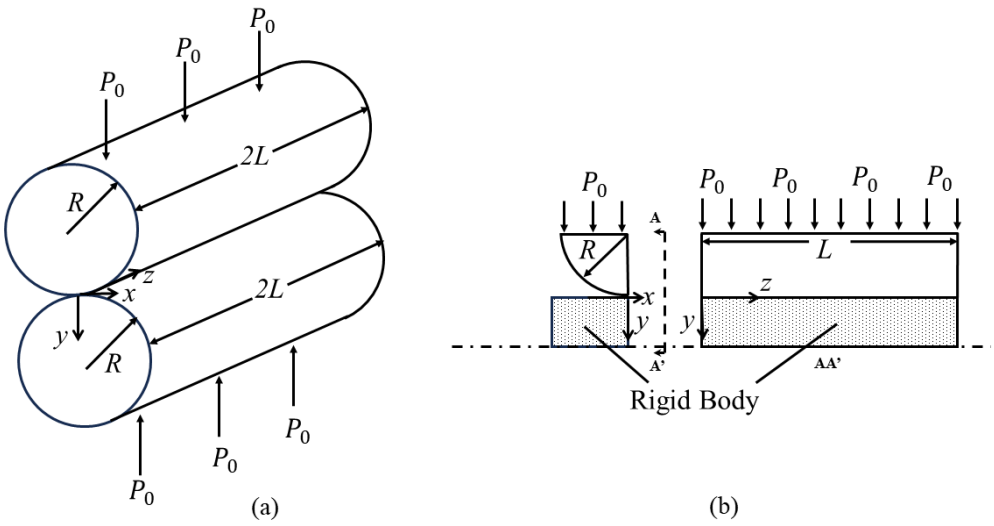


Figure 11: (a) Frictionless, finite length, Hertzian contact, (b) FE model of finite length, Hertzian contact.

In computational experiments, it was observed that the contact pressure gradient in the length direction is very steep near the free end. Consequently, a finer mesh was used for this region. Another challenge with the mesh design is that, to maintain 'conformal' contact, the contact width needs to be small compared to the in-plane geometry. To accurately capture the contact pressure profile in such a small area, fine mesh is required for the region close to $y = 0$. The meshing strategy is illustrated in Figure 12.

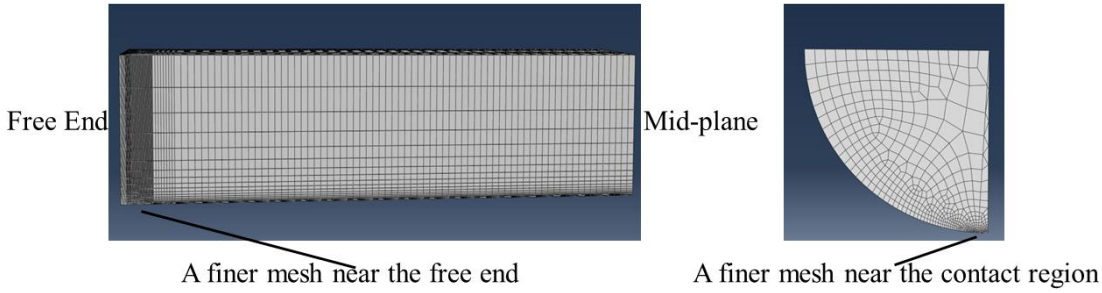


Figure 12: Finite element mesh for the finite length, Hertzian contact.

To control the variables involved in the numerical experiments systematically, eight different sets of numerical experiments with different loads P_0 (hence different contact half width in the plane strain case), different length L and different cylinder radius R were examined, see Table 2.

Table 2. FE model parameters for Hertzian contact models.

Hertzian contact models

model code	P_0 [MPa mm]	L [mm]	R [mm]
P2000L100R5	2000	100	5
P1000L100R5	1000	100	5
P2000L100R10	2000	100	10
P1000L100R10	1000	100	10
P2000L100R2.5	2000	100	2.5
P1000L100R2.5	1000	100	2.5
P2000L200R2.5	2000	200	2.5
P1000L100R2.5	1000	200	2.5

4.1. Results and analysis of finite, Hertzian contact

The solution for a plane strain Hertzian contact, with indenter radius R and force per unit length P_0 is used as a reference. Its contact half-width, a_0, and pressure profile $p(x)$ are:

$$a_0^2 = \frac{4(1-\nu^2)RP_0}{\pi E} \quad p(x) = -\frac{2P_0}{\pi a_0}\sqrt{1-(x/a_0)^2} = p_{m0}\sqrt{1-(x/a_0)^2} \qquad (13)$$

where p_{m0} is the maximum contact pressure.

We begin by comparing the contact pressures at the mid-plane and at the free-end to the reference solution. Unlike the common edge contact, superposition of load-cases is not available because the contact pressure is non-linearly related to load. Instead, the methods of section 2.2 are applied. Since the two bodies are uncoupled and elastically similar, we anticipate, from the discussion in Section 2, that the contact pressure profile at the mid-plane will be similar to that of the plane strain contact. To verify this expectation, the contact pressure distributions at the mid-plane and the free-end were extracted for all eight models and compared with the plane strain solution. Two examples of such comparisons, from models P1000L100R10 and P1000L100R5, are shown in Figure 13.

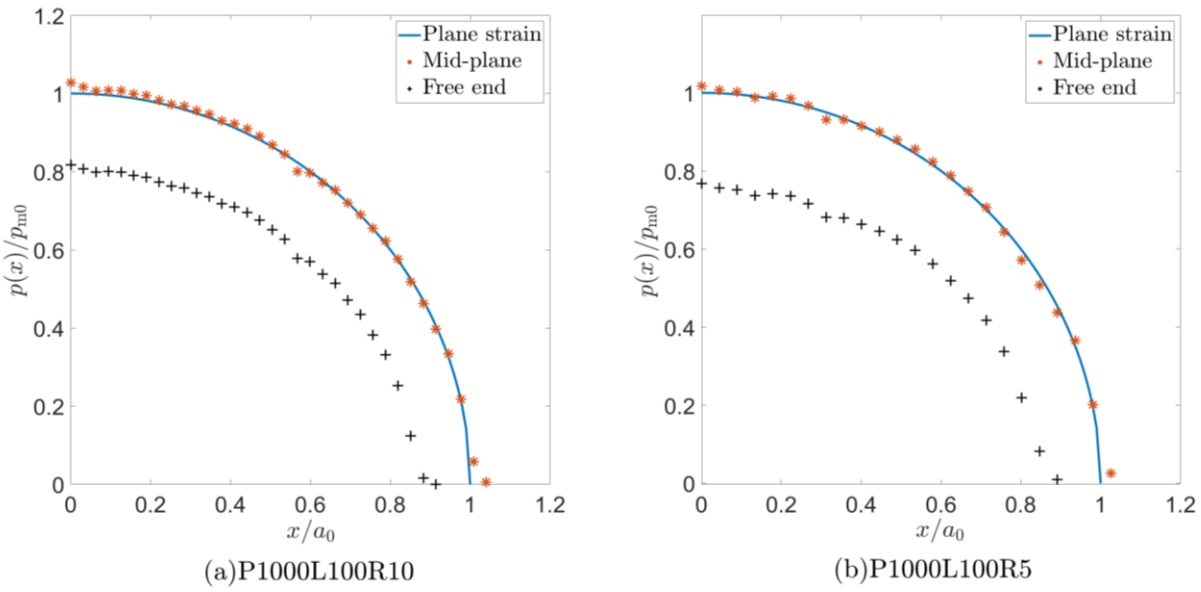


Figure 13: Contact pressure comparison between the plane strain analytical solution and the FE calculation at the mid-plane and free-end of a finite length, Hertzian contact.

In Figure 13, the FE data are normalized by the mid-point (maximum) pressure p_{m_0}; spatial position is normalized by the analytical contact half-width a_0. The FE data have limited accuracy due to discontinuity at the contact interface, however, it is evident that the mid-plane data closely matches the plane strain case. At the free end, both the contact pressure and the contact half-width are smaller than those observed in plane strain, indicating the presence of

an end-effect. The contact pressure distribution near the free-end is difficult to model accurately due to steep pressure gradients and slight mis-alignment of the two contacting bodies at the free end. Nevertheless, estimations of the stress state close to the end can be made by fitting an end-effect decay equation, as used in section 3.

The decay of the end effect has been discussed in section 2.2. This shows that the stresses of the finite length contact problem can be recovered by adding $-\sigma_{zz}^{\mathrm{PS}}(x,y)$ to both ends of the plain strain prismatic contact, so that the free end boundary condition is achieved. The expression of $\sigma_{zz}^{\mathrm{PS}}(x,y)$ can be evaluated using the Muskhelishvili potential [12], as discussed by Hills *et al.* [6].

The propagation of $-\sigma_{zz}^{\mathrm{PS}}(x,y)$ along the cylinders is subject to Saint-Venant's principle. This implies that in the finite length, Hertzian contact, the out-of-plane stress $\sigma_{zz}(x,y,z)$ changes from zero at the free end to $\sigma_{zz}^{b}(x,y)$ at the mid-plane, where $\sigma_{zz}^{b}(x,y)$ is defined in equation (3). Furthermore, the uniform stress, σ_{zz}^{a}, defined as the difference between the plane strain solution $\sigma_{zz}^{\mathrm{PS}}(x,y)$ and the mid-plane solution $\sigma_{zz}^{b}(x,y)$ can be expressed as:

$$\sigma_{zz}^{\mathrm{a}} = \frac{1}{A_0}\int_{A_0} \sigma_{zz}^{\mathrm{PS}}(x,y)\ \mathrm{d}A = \frac{\nu}{A_0}\int_{A_0} \sigma_{yy}^{\mathrm{PS}}(x,y)\ \mathrm{d}A \backslash = \frac{\nu}{A_0}\int_0^R \int_0^{\sqrt{R^2-y^2}} \sigma_{yy}^{\mathrm{PS}}(x,y)\ \mathrm{d}x\mathrm{d}y$$

$$= \frac{\nu R P_0}{2A_0} = \frac{2\nu P_0}{\pi R} \tag{14}$$

or

$$\frac{\sigma_{zz}^{\mathrm{a}} R}{P_0} = \frac{2\nu}{\pi} \tag{15}$$

For $\nu = 0.3$ this value is about 0.191.

To visualize the end-effect propagation, the resultant stress, $\sigma_{zz}^{\mathrm{R}}(x,y) = \sigma_{zz}(x,y) - \sigma_{zz}^{\mathrm{PS}}(x,y)$, was computed using the FE data, with the plane strain solution calculated using the

Muskhelishvili potential. The resultant stress $\sigma_{zz}^{\mathrm{R}}(x,y)$ is expected to match the plane strain corrective stress $-\sigma_{zz}^{\mathrm{PS}}(x,y)$ at the free end, and decay to a uniform stress distribution, $-\sigma_{zz}^{a}$ in the steady state region. Figure 14 shows the resultant stress on planes located at $z = 0$, R, $2R$, $3R$, $4R$ and at the mid-plane ($z = 10R$) of model P1000L100R10. As expected, the stress converges to a uniform distribution, with normalized magnitude about equal to 0.19, matching the prediction of equation (15)

Note that, unlike the common edge contact, the half-width of the Hertzian contact is not constant along the length. Thus, it is not a suitable dimension for normalization of the z co-ordinate. The only remaining geometric dimension is the indenter radius R. From the FE results, it is found that all eight models show similar forms of $P(z)/P_0$ when z is normalized as z/R; example results for models P1000L100R5 and P1000L100R10 were shown in Figure 9(b). The calculation of $P(z)/P_0$ was performed using equation (17) via Simpson's rule with a step size of approximately $a_0/40$. Figure 9(b) also clearly indicates that the length divides into a transient region and steady state region, with the transient region covering about $5R$ of the length.

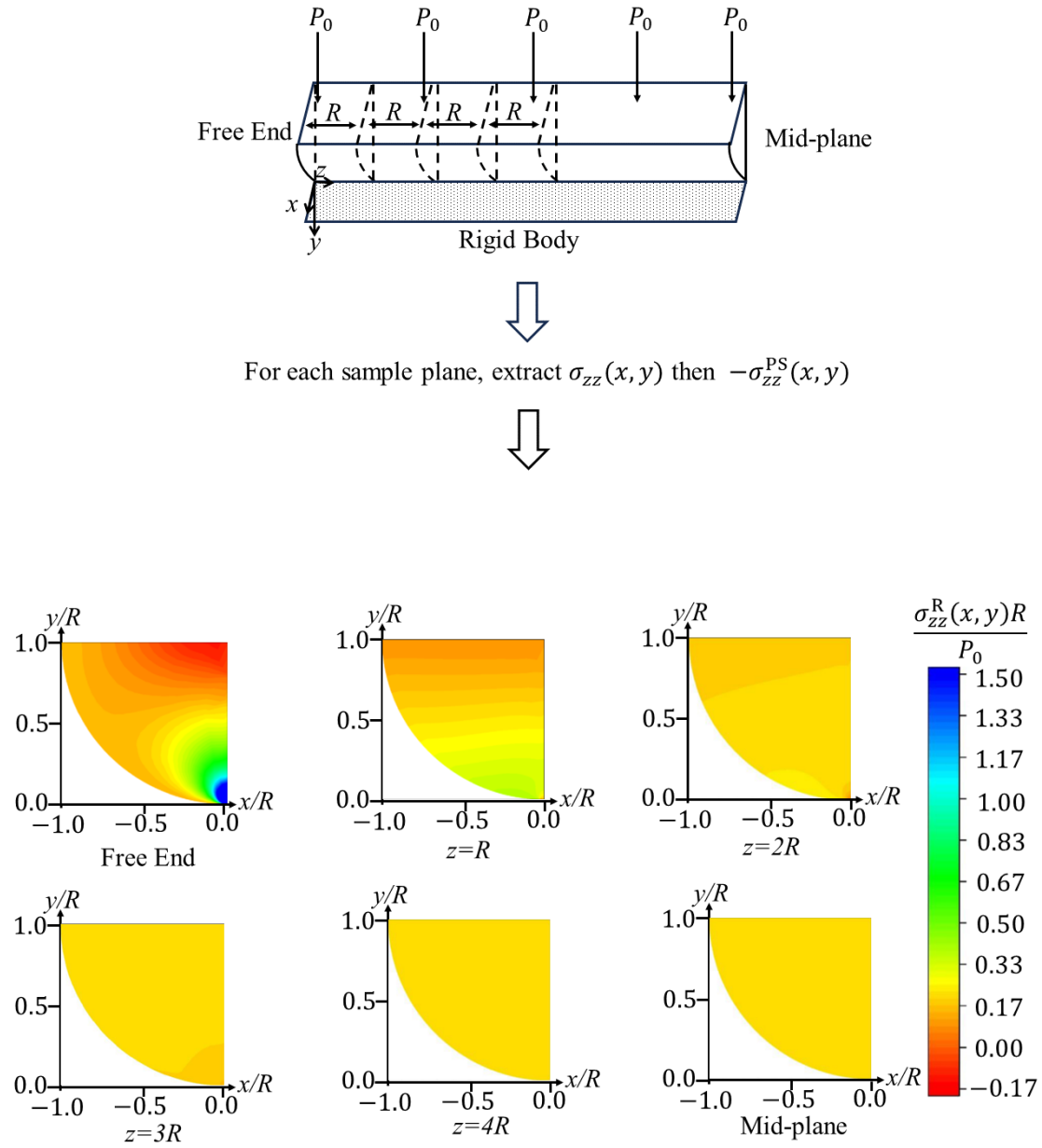


Figure 14: Illustration of the modified through-thickness stress distribution, σ_{zz}^{R}, at sample planes in a finite length, Hertzian contact.

The $P(z)$ data were processed to remove two sources of error. Firstly, steep pressure gradients close to the free end were not captured well by the FE model; the affected points were excluded from subsequent curve fitting. Secondly, quadrature error from Simpson's rule resulted in the steady state $P(z)/P_0$ not settling to unity, so the data were scaled to force $P(z) = P_0$ at $z = L$. Figure 15 shows a comparison between the raw data and the post-processed data.

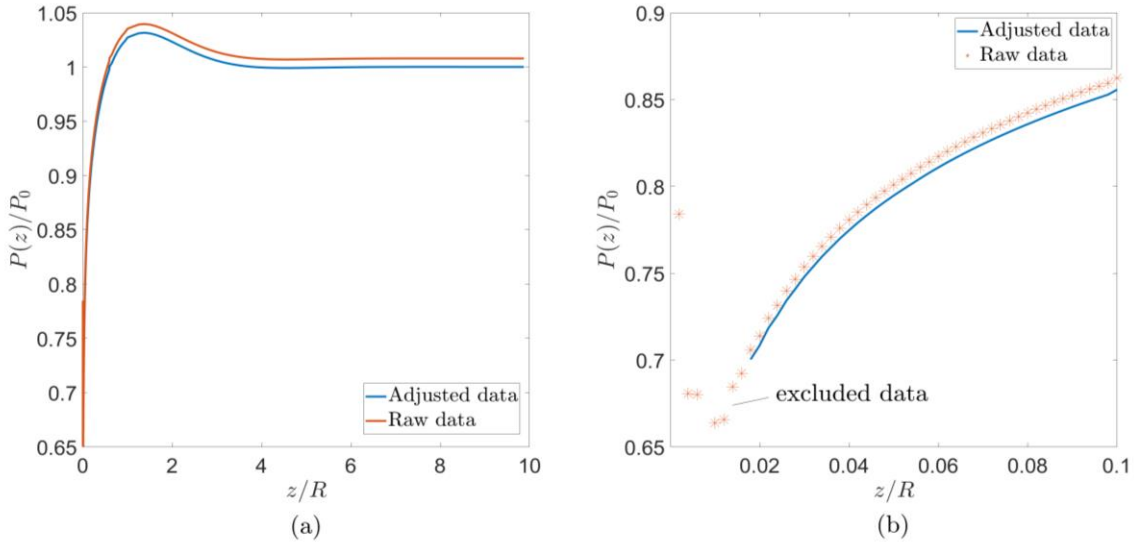


Figure 15: Illustration of the raw data and the post-processed data of normalized contact force per unit length: (a) scale $z/R \in [0\ 10]$; (b) scale $z/R \in [0\ 0.1]$.

The normalized and adjusted data were fitted to an oscillating exponential decay using the Levenberg-Marquardt algorithm (see Appendix) resulting in

$$P(z)/P(0) = -0.289\exp\big(-1.245(z/R)\big)\sin(0.864(z/R) + 2.611) + 1 \qquad (16)$$

with maximum error smaller than 0.1% for all $z/R > 0.06$. The contact half-width $a(z)$ could not be directly identified from the FE data due to limited mesh resolution. However, using the maximum contact pressure, it was possible to recover the contact half-width, noting the square root bounded distribution of contact pressure, i.e.

$$P(z) = p_{\mathrm{m}}(z)\int_{-a(z)}^{a(z)} \sqrt{1 - \big(x/a(z)\big)^2}\,\mathrm{d}x = \frac{\pi p_{\mathrm{m}}(z)a(z)}{2} \qquad (17)$$

where $p_{\mathrm{m}}(z)$ is the maximum contact pressure at position z along the length. Hence

$$a(z) = \frac{2P(z)}{\pi p_{\mathrm{m}}(z)}$$

The contact half-width and maximum contact pressure are plotted as functions of z along with fitted oscillatory exponential decays in Figure 16(a) and (b). The curve fits have the form

$$a(z)/a_0 = -0.143\exp\big(-1.246(z/R)\big)\sin(0.864(z/R) + 2.611) + 1 \qquad (18)$$

for the contact half-width, and for the maximum contact pressure

$$p_{\mathrm{m}}(z)/p_0 = -0.150\exp\big(-1.273(z/R)\big)\sin(0.864(z/R) + 2.611) + 1 \qquad (19)$$

Note that the oscillatory frequencies and phase shifts are closely matched between equations (16), (18) and (19); this is expected because they are produced by the transient of the same end effect.

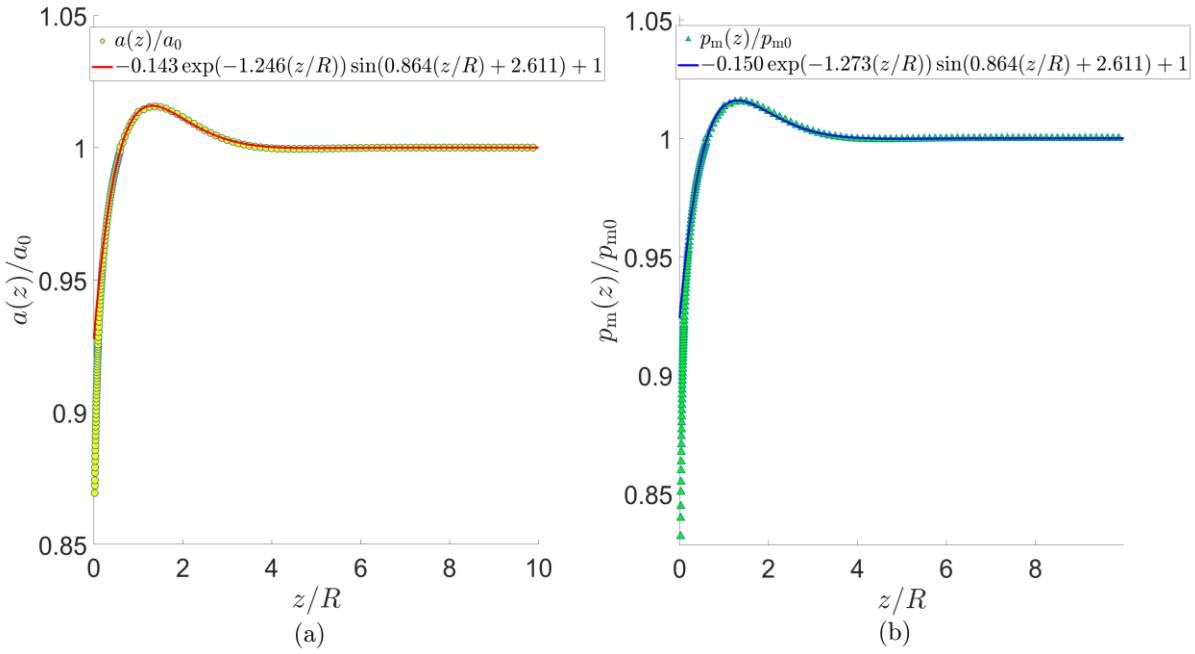


Figure 16: Propagation of (a) contact half-width and (b) maximum contact pressure along the length of the contact

From Figure 16, it can be observed that the transient region extends approximately to $5R$, and the contact pressure reaches a maximum at $z/R = 1.3$. The maximum contact force per unit length is $1.03P_0$ and the maximum contact pressure is $1.02p_{\mathrm{m0}}$. The above findings have

generality. The decay functions can also be extrapolated to $z = 0$ indicating that the force per unit length at the free end is about $0.86P_0$ while the free end contact has a maximum pressure of $0.92p_{m0}$ and a contact half-width of $0.93a_0$.

It is important to note that when applying the above results to the problem of a cylindrical pad in contact with an elastically similar flat surface, as shown in Figure 6, the relative curvature must be considered, denoted as κ. When two contacting bodies are identical cylinders, $\kappa = 2/R$; whereas $\kappa = 1/R$ refers to the case where the indenter is in contact with an elastically similar flat surface. Therefore, it can be concluded that, in the case of a finite length Hertzian contact, the transient region lasts about $10/\kappa$.

Noting that for Hertzian contacts, typically, $R \gg a$, this means that the penetration of the end effect in the length dimension is much greater that the contact width. In this respect the Hertzian contact differs qualitatively from the common edge contact, where the end effect typically penetrates less than $5a$ along the length. The numerical models also indicate that Saint-Venant's principle relates to a geometric feature size that is independent of load: in the Hertzian contact the load-dependent contact half-width does not affect the decay of the end-effect.

6. Conclusion

This paper analyzes the free-end effects found in prismatic contacting bodies. Two types of contacts were used as examples: a common edge contact and a Hertzian contact. Numerical experiments confirmed that the free-end effect is characterized by a transient region, governed by an oscillatory exponential decay of contact pressure. Towards the mid-plane, a steady-state is reached, corresponding to a modified plane strain solution of the corresponding 2D problem. The paper clearly shows observations of the pressure distribution and the end-effect, with results that have generality for the Hertzian case. The transient region of the Hertzian case has been found to be about 10 times the inverse curvature of the cross-sectional geometry.

Additionally, this work analyzes the steady-state portion of the finite length problem, as observed at the mid-plane. The mid-plane stress state can be recovered by imposing a uniform anti-plane stress onto the plane strain solution. This uniform stress corresponds to the average through-thickness stress in the plane strain case. In the case of a monolithic prismatic body (i.e. not a contact) of sufficient length, the in-plane stress field of the mid-plane is the same as that in the plane strain condition. In a finite length contact problem, the above statement still holds if the two contacting bodies are uncoupled or elastically similar.

Finally, expressions for the decay of the end effect were provided. This enables the propagation of the force per unit length, the maximum contact pressure, and the contact half-width to be predicted. The paper provides insight and understanding potentially valuable in the analysis of contact fretting, and prismatic contacts found in a variety of engineered components.

Acknowledgement

Special thanks are given to Professor J.R. Barber from the University of Michigan for his kind suggestions on the exponential decay pattern of the end-effect.

Appendix: Nonlinear fitting algorithm

This appendix outlines the algorithm used to fit the numerical data. The expected form is an oscillatory exponential decay given by:

$$y = A\exp(-\lambda x)\sin(\omega x + \phi) + 1, \qquad (23)$$

where y is the dependent variable, x is the independent variable, and A, λ, ω, and ϕ are the parameters to be estimated.

This can be expressed as $y = f(x;\Theta)$, where $\Theta = [A, \lambda, \omega, \phi]$ represents the vector of parameters to be estimated. The objective of the fitting process is to find the parameter values

that minimize the difference between the observed data points and the values of function f. This is typically achieved by minimizing a cost function, defined as the sum of squared errors (SSE):

$$\mathrm{SSE}(\Theta) = \sum_{i=1}^{n} [y_i - f(x_i; \Theta)]^2,$$

where y_i and x_i are the observed values of the dependent and independent variables, respectively, and n is the number of observations.

The fitting process involves an optimization algorithm that iteratively adjusts the parameters Θ to minimize the SSE. The Levenberg-Marquardt algorithm [11] is a damped least square optimization algorithm that interpolates between the Gauss-Newton algorithm and gradient descent, using

$$\Theta_{new} = \Theta_{old} + \left(J^T J + \gamma \cdot \mathrm{diag}(J^T J)\right)^{-1} J^T [y - f(z; \Theta_{old})] \qquad (25)$$

where J is the Jacobian matrix of partial derivatives of f with respect to the parameters, γ is a damping factor that adjusts the algorithm's behavior between the Gauss-Newton and gradient descent methods, and $\mathrm{diag}(J^T J)$ is the diagonal matrix of $J^T J$.

The fitting process was implemented using the curve_fit function in Python, using $\Theta = [1, 1, 1, 1]$ as an initial guess and iterating the Levenberg-Marquardt algorithm until a stable Θ is found.

Reference

[1] L. Blades, J. P. Truelove, R. Paynter, and D. A. Hills, “Experimental investigation of the effects of load path on the life of fretting fatigue contacts,” *Tribology International*, vol. 188, p. 108858, 2023.

[2] J. P. Truelove, D. A. Hills, and L. E. Blades, “Flat and rounded contacts: Modelling the effect of a moment with application to fretting fatigue tests,” *The Journal of Strain Analysis for Engineering Design*, vol. 58, no. 2, pp. 91–97, 2023.

[3] A. De Pannemaecker, S. Fouvry, J. Y. Buffiere, and M. Brochu, “Modelling the fretting fatigue crack growth: From short crack correction strategies to microstructural approaches,” *International Journal of Fatigue*, vol. 117, pp. 75–89, 2018.

[4] J. R. Barber, “Three-dimensional elasticity problems for the prismatic bar,” *Proceedings of the Royal Society A: Mathematical, Physical and Engineering Sciences*, vol. 462, no. 2070, pp. 1877–1896, 2006.

[5] A. E. H. Love, *A treatise on the mathematical theory of elasticity*. Cambridge University Press, 2013.

[6] D. A. Hills, D. Nowell, and A. Sackfield, *Mechanics of elastic contacts*. Elsevier, 2013.

[7] K. L. Johnson, *Contact mechanics*. Cambridge University Press, 1987.

[8] R. J. Roark, *Formulas for stress and strain*. McGraw-Hill, 1975.

[9] J. Wu, *Exponential decay for the saint-venant’s principle*. University of Illinois at Urbana-Champaign, 1984.

[10] R. A. Toupin, “Saint-Venant’s principle,” *Archive for Rational Mechanics and Analysis*, vol. 18, no. 2, pp. 83–96, 1965.

[11] K. Levenberg, “A method for the solution of certain non-linear problems in least squares,” *Quarterly of Applied Mathematics*, vol. 2, no. 2, pp. 164–168, 1944.

[12] N. I. Muskhelishvili, “Some basic problems of the mathematical theory of elasticity,” *Noordhooff, Groningen*,

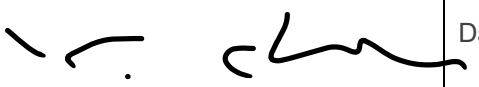
Statement of Authorship for joint/multi-authored papers for PGR thesis

To appear at the end of each thesis chapter submitted as an article/paper

The statement shall describe the candidate's and co-authors' independent research contributions in the thesis publications. For each publication there should exist a complete statement that is to be filled out and signed by the candidate and supervisor **(only required where there isn't already a statement of contribution within the paper itself).**

Title of Paper	Shakedown of a plate with a circular hole: An educational problem
Publication Status	□ Published □ Accepted for Publication ✓Submitted for Publication □Unpublished and unsubmitted work written in a manuscript style
Publication Details	Chen, Y., Hills, D. A., Huber, J., Ma, L. (2023). Analysis of elastic prismatic contact of finite length.

Student Confirmation

Student Name:	Yifeng Chen		
Contribution to the Paper	Perform essential FE analysis. Perform Theoretical deduction. Write up all the paper.		
Signature		Date	16/04/2024

Supervisor Confirmation

By signing the Statement of Authorship, you are certifying that the candidate made a substantial contribution to the publication, and that the description described above is accurate.

Supervisor name and title: Prof. John Huber			
Supervisor comments			
Signature		Date	17/4/24

This completed form should be included in the thesis, at the end of the relevant chapter.

8. Conclusion and Future Work

This thesis is primarily concerned with plane problems that include defects. These defects will be one of the following: a circular hole, a finite-height crack, a sharp notch, or a parabolic notch. It discusses both fracture and shakedown problems in these contexts. The main focus is on the development and discussion of analytical tools for addressing these problems. Additionally, it involves the use of finite element analysis or classical problems as benchmarks to validate the analytical methods. The final section extends the discussion to 3D problems by considering the extension of plane problems in the out-of-plane direction to form a prismatic body, analyzing the end effect and its propagation distance

In Chapter 3, we discuss the shakedown problem in a plate containing a circular hole. Melan's theorem was applied to compute the analytical shakedown limit, which was then compared with the results from point-wise finite element analysis. The findings indicate that the actual shakedown limit coincides with the analytical limit within a certain range. Beyond this range, the analytical shakedown limit serves as a lower bound and provides a good approximation. The principles of the shakedown problem discussed here can be extended to other types of plane problems, offering more illustrative examples. Although shakedown limits are more efficient compared to the elastic limits, Melan's calculation still has certain limitations, which are discussed at the end of Chapter 3. It is challenging to propose a full-field residual stress; hence, finite element analysis (FEA) is always used together with analytical methods to validate the shakedown limits and provide insights into stress behavior.

Chapter 4 introduces the finite-height crack problem under mode 1 and mode 2 loading conditions. The results establish criteria to identify the interaction of two notch corners based on various applied load combinations. The chapter concludes that when the load falls within a certain range, the two notch corners of the finite-height crack can be considered independently. In other scenarios, the interaction between the notches needs to be considered. This finite-

height crack problem can be extended to a solid inclusion problem. Given that the inclusion thickness is never zero, the finite-height crack serves as an example of an inhomogeneous inclusion, termed ‘free inclusion’ (Dobrovolskii, 2010). Thus, it is anticipated that the results and methods used in the finite-height crack problem will contribute to developing a unified approach for solid inclusion scenarios. As mentioned in the previous section, even though three states of notch corner interaction can be identified, this does not mean that a crack will necessarily initiate accordingly. In fact, cracks should always initiate at the location with maximum principal stress, which is typically around the notch corners. However, the three states proposed in the paper represent three scenarios that the finite height crack can be simulated to. Therefore, the behaviour of an initiated crack under certain load combinations can be predicted accordingly.

The results of Chapter 4 can also be validated by performing tensile tests on a mechanical part with finite-height crack feature. The observations can be made by 1) Loading the finite-height crack to the criteria that can be considered as a sharp crack; the finite-height crack should fail in a manner consistent with sharp crack behaviour, and the crack propagation can be calculated analytically. 2) Increasing the finite-crack height and loading the finite crack to failure under different load combinations. By observing the propagation of the crack near the notch corners, it can be determined if the two notch corners can be considered independently. Therefore, by combining the criteria proposed by experimental results and the predictions in the paper, we can validate the findings of the paper.

Chapters 5 and 6 introduce complex variable solutions for analyzing wedge or parabolic notch problems that interact with anti-plane singularities. These solutions are in the form of complex potentials, compatible with the general anti-plane potential stress relations (equations 2.18-2.20). Because the applied loading conditions, which include both force and displacement, can be treated as the integration of singular elements, these solutions are broadly applicable to

a variety of anti-plane problems. Together, these chapters, along with the work by Ma and Hills (2022&2023), create a comprehensive 'toolbox' for problems involving a plane interacting with a singular feature

In the case of the wedge, as illustrated in Chapter 5, the stress is found to be in the order of $z^{\frac{1}{q}-1}$, aligning with results found in numerous studies, such as those by Ohr *et al.* (1985), which again shows the results are valid. Further work can be considered based on the application of this developed solution. The solution can be extended to an anti-plane loaded sharp notch, particularly a right-angle notch, which is commonly seen in rotational grooved shafts. It's noteworthy that the grooved shaft geometry can also be linked to the finite-height crack problem, and the anti-plane solution can further complement the work in Chapter 4. A rotational shaft loaded under torque can be modeled as a right-angle notch, loaded by two opposing singular forces of equal magnitude F, spaced a distance l apart, resulting in a torque value $\tau = Fl$. The anti-plane wedge solution in this scenario provides insights into the stress field distribution, enabling the identification of key features such as the plastic front and potential sites for crack initiation.

For the parabolic notch problem, similar to the wedge problem, closed-form potential functions have been derived to represent the stress field when the plate interacts with a singular feature. These functions enable the determination of the stress concentration factor for a parabolic notch with various notch opening geometries. Chapter 6 also presents an application involving a parabolic notch containing a screw dislocation, where the driving force is plotted against the distance from the notch tip. The driving force of the dislocation is closely related to the dislocation emission problem in crystalline materials. Consequently, the direction of emission for a screw dislocation can be further determined using the solution derived in Chapter 6.

Chapter 7 explores a plane problem that extends in the out-of-plane direction, forming a

prismatic body. The problem has been studied through two contact geometries: a finite common edge contact and a finite Hertzian contact, using the finite element method. The results initially address the coincidence between the mid-plane in finite length contact and the reference plane strain solution, then proceed to characterize the end effect and propose a formula for its propagation. This formula captures the complex exponential nature of the end effect, and its accuracy benefits from finer finite element analysis. There is also an interest in the generality of the end effect propagation function, particularly in whether this function is applicable to all types of plane problems with finite extension. This could be further investigated by examining planes with different geometrical configurations. Although the primary reason for choosing these two geometries is their lack of singular features, additional research could include the effects of singularity. Lastly, regarding the contact problem, further studies could involve an inverse problem: determining the geometry of a three-dimensional contact body that generates a rectangular contact patch in cases of incomplete contact. The results found in this chapter can be validated by lab fretting tests, the experiments is comprised of a curved prismatic pad and a flat prismatic dog-bone. The end-effect is predicted to have an internal maximum close to the free end in the paper, a pressure gauge could use to measure this maximum or it can be observed by the wear scar distribution.

Bibliography

1. Dobrovolskii, I. P. (2010). An inclusion problem. Mechanics of solids, *45*, 726-732.
2. Ma, L., Hills, D. A. (2022). Interaction of a parabolic notch with a generalized singularity. International Journal of Engineering Science, 176, 103685.
3. Ma, L., Hills, D. A. (2023). A wedge of arbitrary angle interacting with a generalized singularity. International Journal of Solids and Structures, 262, 112062.
4. Ohr, S. M., Chang, S.J., and Thomson, R. (1985), Elastic interaction of a wedge crack with a screw dislocation, Journal of Applied Physics, 57, 1839-1843.

Declaration of Competing interesting

The authors declare that they have no known competing financial interests or personal relationships that could have appeared to influence the work reported in this paper.